Interaction of Proteins with Multivalent Polyelectrolytes

vorgelegt von

M.Sc.

Jacek Walkowiak

an der Fakultät II – Mathematik und Naturwissenschaften

der Technischen Universität Berlin

zur Erlangung des akademischen Grades

Doktor der Naturwissenschaften

- Dr. rer. nat. -

genehmigte Dissertation

Promotionsausschuss:

Vorsitzender: Prof. Dr. Arne Thomas
Gutachter: Prof. Dr. Matthias Ballauff
Gutachter: Prof. Dr. Michael Gradzielski
Gutachter: Prof. Dr. Alexander Böker

Tag der wissenschaftlichen Aussprache: 09.09.2020

Berlin 2020

ABSTRACT

In the present work the thermodynamics of protein adsorption to charged polyelectrolytes is explored. Unravelling interactions of proteins with highly charged polyelectrolytes as *e.g.* DNA is a central topic in biophysics since many years.[1,2] It is now well-established that ionic interactions play a major role for the strength of binding as expressed through the thermodynamic binding constant K_b. Moreover, counterion release has been identified as the driving force for binding: Patches of positively charged amino acid residues located on the surface of the protein act as multivalent counterions that compensate the charge of the polyelectrolyte.[1–3] In this way a concomitant number of counterions condensed to the polyelectrolyte are released.[3]

The first part of this thesis contributes to the understanding of counterion condensation that determines the effective charge of a polyelectrolyte. The interaction between dendritic polyglycerol sulfate (dPGS) and divalent ions (Mg^{2+} and Ca^{2+}) were analyzed by combination of experiment (isothermal titration calorimetry (ITC)) and theory (non-linear penetrable Poisson-Boltzmann (PPB) model). The discussed lack of ion-specific effects upon adsorption of divalent ions to dPGS and a clear competition between mono- and divalent ions allows a better understanding of the fundamentals of polyelectrolyte-protein (PE-P) interaction that are presented in the following chapters.

In the second part, a comprehensive thermodynamic study of the PE-P interaction is presented. Starting form a linear (heparin) and low molecular weight (β cyclodextrin sulfate (β-CD-S)) polyelectrolytes up to a polyelectrolyte brushes - a detailed picture of the binding driving forces is given. A quantitative analysis of the thermodynamic processes involved in the interaction of the model glycosaminoglycan (GAG) - heparin and lysozyme is presented. The binding constant K_b was determined by ITC as the function of temperature and ionic strength adjusted through the concentration c_s of added salt. The dependence on salt concentration c_s was used to determine the net number of released counterions. Moreover, the binding constant at a reference salt concentration of 1M $K_b(1M)$ was determined by extrapolation. The dependence on temperature of K_b was used to dissect the binding free energy ΔG_b into the respective enthalpies ΔH_b and entropies ΔS_b together with the specific heat capacity change ΔC_p. A strong enthalpy-entropy cancellation (EEC) was found similar to the results for many other systems.[4–9] The binding free energy ΔG_b could furthermore be split up into a part ΔG_{ci} due to counterion release and a residual part ΔG_{res}. The latter quantity reflects specific contributions as *e.g.* salt bridges, van der Waals interactions or hydrogen bonds. The entire analysis shows that heparin-lysozyme interactions are mainly caused by counterion release, that is, *ca.* three counterions are being released upon binding of one lysozyme molecule. The presented approach was then applied in studies of β-CD-S - lysozyme binding. In that case also, three counterions released during the adsorption are the main driving force of the analyzed process. The reported approach of quantifying interactions between GAGs and CDs with proteins is in general applicable and suitable to provide new insights in the physical modulation of biomolecular signals.

Subsequently, the analysis of the PE-P interaction is extend in order to obtain the full thermodynamic information on the binding of protein to polyelectrolyte brushes. Thus, a thermodynamic study of the adsorption of human serum albumin (HSA) onto spherical polyelectrolyte brushes (SPB) is presented. The SPBs are composed of a solid polystyrene core bearing long chains of poly(acrylic acid) (PAA). ITC measurements done at different temperatures and ionic strengths lead to a full set of thermodynamic binding constants together with the enthalpies and entropies of binding. The adsorption of HSA onto SPBs is described with a two-step model with a binding constant K_b on the order of 10^5 and 10^4 M^{-1} for the first

and second binding step, respectively. The free energy of binding ΔG_b depends only weakly on temperature because of a marked compensation of enthalpy by entropy. Studies of the adsorbed HSA by Fourier transform infrared spectroscopy (FT-IR) demonstrates no significant disturbance in the secondary structure of the protein. The quantitative analysis demonstrates that counterion release is the major driving force for adsorption. A comparison with the analysis of previously discussed systems demonstrates that EEC is a general phenomenon dominated by released counterion that always accompanies the binding of proteins to polyelectrolytes.

The last part of this thesis presents a quartz crystal microbalance with dissipation (QCM-D) study of HSA adsorption onto a planar polyelectrolyte brush (PPB). This allows a quantitative comparison with calorimetric studies of HSA-SPB interaction. For this, the preparation of a PAA brush, polymerized by atom transfer radical polymerization (ATRP) of *tert*-butyl acrylate (*t*BA) and subsequent acid hydrolysis, on the flat gold surfaces of QCM crystals is presented. The PAA brush was characterized by FT-IR spectroscopy, ellipsometry and water contact angle analysis. The interaction of the brush with HSA was studied for a range of ionic strengths and pH conditions. The quantitative analysis showed a strong adsorption of protein molecules onto the brush. By increasing the ionic strength a fraction of the initially adsorbed HSA was released. A comparison with recent calorimetric studies related to the binding of HSA to polyelectrolytes allowed to analyze the QCM data based on the results of the thermodynamic analysis of the PE-P binding process.[10–13]

KEYWORDS: Polyelectrolyte, polyelectrolyte brush, protein, ITC, QCM-D, thermodynamic, counterion release, enthalpy-entropy cancellation.

ZUSAMMENFASSUNG

In der vorliegenden Arbeit wird die Thermodynamik der Proteinadsorption an geladenen Polyelektrolyten untersucht. Die Untersuchung von Wechselwirkungen von Proteinen mit hoch geladenen Polyelektrolyten, wie z. DNA ist seit vielen Jahren ein zentrales Thema in der Biophysik.[1,2] Es ist mittlerweile bekannt, dass ionische Wechselwirkungen eine wichtige Rolle für die Bindungsstärke spielen, die durch die thermodynamische Bindungskonstante K_b ausgedrückt wird. Darüber hinaus wurde die Freisetzung von Gegenionen als treibende Kraft für die Bindung identifiziert: Positiv geladene Aminosäurereste auf der Oberfläche des Proteins wirken als multivalente Gegenionen, die die Ladung des Polyelektrolyten kompensieren.[1–3] Auf diese Weise wird eine Anzahl von am Polyelektrolyten kondensierten Gegenionen freigesetzt.[3]

Der erste Teil dieser Arbeit trägt zum Verständnis der Gegenionenkondensation bei, die die effektive Ladung eines Polyelektrolyten bestimmt. Die Wechselwirkung zwischen dendritischem Polyglycerinsulfat (dPGS) und zweiwertigen Ionen (Mg^{2+} und Ca^{2+}) wurde durch Kombination von Experiment (isotherme Titrationskalorimetrie (ITC)) und Theorie (nonlinear penetrable Poisson-Boltzmann (PPB) -Modell) analysiert. Das Fehlen ionenspezifischer Effekte auf die Adsorption zweiwertiger Ionen an dPGS und eine klare Konkurrenz zwischen ein- und zweiwertigen Ionen ermöglichen ein besseres Verständnis der Grundlagen der Wechselwirkung zwischen Polyelektrolyt und Protein (PE-P), die in den folgenden Kapiteln vorgestellt werden.

Im zweiten Teil wird eine umfassende thermodynamische Untersuchung der PE-P-Wechselwirkung vorgestellt. Ausgehend von linearen (Heparin) und niedermolekularen (β-Cyclodextrinsulfat (β-CD-S)) Polyelektrolyten bis hin zu Polyelektrolytbürsten wird ein detailliertes Bild der Bindungsantriebskräfte gegeben. Eine quantitative Analyse der thermodynamischen Prozesse, die an der Wechselwirkung des Modells Glycosaminoglycan (GAG) - Heparin und Lysozym beteiligt sind, wird vorgestellt. Die Bindungskonstante K_b wurde durch ITC als Funktion der Temperatur und der Ionenstärke bestimmt, die durch die Konzentration c_s des zugesetzten Salzes eingestellt wurden. Die Abhängigkeit von der Salzkonzentration c_s wurde verwendet, um die Nettozahl der freigesetzten Gegenionen zu bestimmen. Darüber hinaus wurde die Bindungskonstante bei einer Referenzsalzkonzentration von 1 M $K_b(1\ M)$ durch Extrapolation bestimmt. Die Abhängigkeit von K_b von der Temperatur wurde verwendet, um die freie Bindungsenergie ΔG_b in die jeweiligen Enthalpien ΔH_b und Entropien ΔS_b zusammen mit der spezifischen Wärmekapazitätsänderung ΔC_p zu zerlegen. Eine starke Enthalpie-Entropie-Aufhebung (EEC) wurde ähnlich wie bei vielen anderen Systemen gefunden.[4–9] Die freie Bindungsenergie ΔG_b konnte aufgrund der Freisetzung von Gegenionen und eines Restteils ΔG_{res} in einen Teil ΔG_{ci} aufgeteilt werden. Die letztere Größe spiegelt spezifische Beiträge *wie z.* Salzbrücken, Van-der-Waals-Wechselwirkungen oder Wasserstoffbrücken wider. Die gesamte Analyse zeigt, dass Heparin-Lysozym-Wechselwirkungen hauptsächlich durch die Freisetzung von Gegenionen verursacht werden. Bei der Bindung eines Lysozymmoleküls werden drei Gegenionen freigesetzt. Der vorgestellte Ansatz wurde dann in Studien zur Bindung von β-CD-S - Lysozym angewendet. Auch in diesem Fall sind drei während der Adsorption freigesetzte Gegenionen die Hauptantriebskraft des analysierten Prozesses. Der beschriebene Ansatz zur Quantifizierung von Wechselwirkungen zwischen GAGs und CDs mit Proteinen ist allgemein anwendbar und geeignet, um neue Erkenntnisse über die physikalische Modulation biomolekularer Signale zu gewinnen.

Anschließend wird die Analyse der PE-P-Wechselwirkung erweitert, um die vollständigen thermodynamischen Informationen über die Bindung von Protein an Polyelektrolytbürsten zu erhalten. Daher wird eine thermodynamische Untersuchung der Adsorption von Humanserumalbumin (HSA) an kugelförmigen Polyelektrolytbürsten (SPB) vorgestellt. Die SPBs bestehen aus einem festen Polystyrolkern, der lange Ketten aus Poly(acrylsäure) (PAA) trägt. ITC-Messungen, die bei unterschiedlichen Temperaturen und Ionenstärken durchgeführt werden, führen zu einem vollständigen Satz thermodynamischer Bindungskonstanten, zusammen mit den Enthalpien und Entropien der Bindung. Die Adsorption von HSA an SPBs wird mit einem zweistufigen Modell mit einer Bindungskonstante K_b in der Größenordnung von 10^5 und 10^4 M^{-1} für den ersten bzw. zweiten Bindungsschritt beschrieben. Die freie Bindungsenergie ΔG_b hängt aufgrund einer deutlichen Kompensation der Enthalpie durch Entropie nur schwach von der Temperatur ab. Untersuchungen der adsorbierten HSA durch Fourier-Transformations-Infrarotspektroskopie (FT-IR) zeigen keine signifikante Störung der Sekundärstruktur des Proteins. Die quantitative Analyse zeigt, dass die Freisetzung von Gegenionen die Hauptantriebskraft für die Adsorption ist. Ein Vergleich mit der Analyse zuvor diskutierter Systeme zeigt, dass die EEC ein allgemeines Phänomen ist, das von der Freisetzung von Gegenionen dominiert wird und immer mit der Bindung von Proteinen an Polyelektrolyte einhergeht.

Der letzte Teil dieser Arbeit präsentiert eine Quarzkristall-Mikrowaage mit Dissipation (QCM-D) zur HSA-Adsorption auf einer planaren Polyelektrolytbürste (PPB). Dies ermöglicht einen quantitativen Vergleich mit kalorimetrischen Studien der HSA-SPB-Wechselwirkung. Hierzu wird die Herstellung einer PAA-Bürste vorgestellt, die durch Atomtransfer-Radikalpolymerisation (ATRP) von *tert*-Butylacrylat (*t*BA) und anschließende Säurehydrolyse auf den flachen Goldoberflächen von QCM-Kristallen polymerisiert wird. Die PAA-Bürste wurde durch FT-IR-Spektroskopie, Ellipsometrie und Wasserkontaktwinkelanalyse charakterisiert. Die Wechselwirkung der Bürste mit HSA wurde für eine Reihe von Ionenstärken und pH-Bedingungen untersucht. Die quantitative Analyse zeigte eine starke Adsorption von Proteinmolekülen an der Bürste. Durch Erhöhen der Ionenstärke wurde ein Teil des anfänglich adsorbierten HSA freigesetzt. Ein Vergleich mit kürzlich durchgeführten kalorimetrischen Studien zur Bindung von HSA an Polyelektrolyte ermöglichte die Analyse der QCM-Daten auf der Grundlage der Ergebnisse der thermodynamischen Analyse des PE-P-Bindungsprozesses.[10–13]

SCHLAGWÖRTER: Polyelektrolyt, Polyelektrolytbürste, Protein, ITC, QCM-D, thermodynamisch, Gegenionenfreisetzung, Enthalpie-Entropie-Aufhebung.

Table of Contents

1. Introduction

1.1. Polyelectrolytes in Inhibition and / or Enhancement of Protein Adsorption

The interaction of proteins with synthetic polyelectrolytes (PEs) in aqueous solution has been a long-standing subject in colloid and polymer science and the number of papers on this subject is hard to overlook.[3,14–17] Thus, polyelectrolytes may form complex coacervates with proteins of opposite charge and the formation of these complexes is strongly depending on the ionic strength in the system.[17,18] It is now well-established that ionic interactions play a major role for the strength of binding as expressed through the thermodynamic binding constant K_b. Often complex formation is followed by precipitation and phase separation[14,17–19] and possible non-equilibrium states may render the thermodynamic analysis a difficult task. At the same time, the interaction of highly charged biopolymers as *e.g.* DNA or RNA with specific proteins has been under intense scrutiny because of its obvious biological relevance.[2,7,28,20–27] Work along these lines has revealed that binding is often brought about by *counterion release*:[1–3,29–31] A patch of positively charged groups on the surface of the protein interacts with the highly charged biopolymer. Thus, this patch now balances the charge of the polyelectrolyte so that the counterions condensed to it may be released. The gain of entropy gained by release of the condensed counterions presents a strong driving force for binding that is even operative under physiological conditions. The increase of entropy thus effected scales with the number of released counterions and the logarithm of the binding constant, $log\ K_b$ is predicted to be proportional to the logarithm of the salt concentration, $log\ c_s$ in the system. Counterion release has been identified as major driving force for the binding of many natural[2,30] and synthetic polyelectrolytes[3] to proteins.[3,32,33] The release or uptake of water must be regarded as a second entropic factor that may come into play as well.

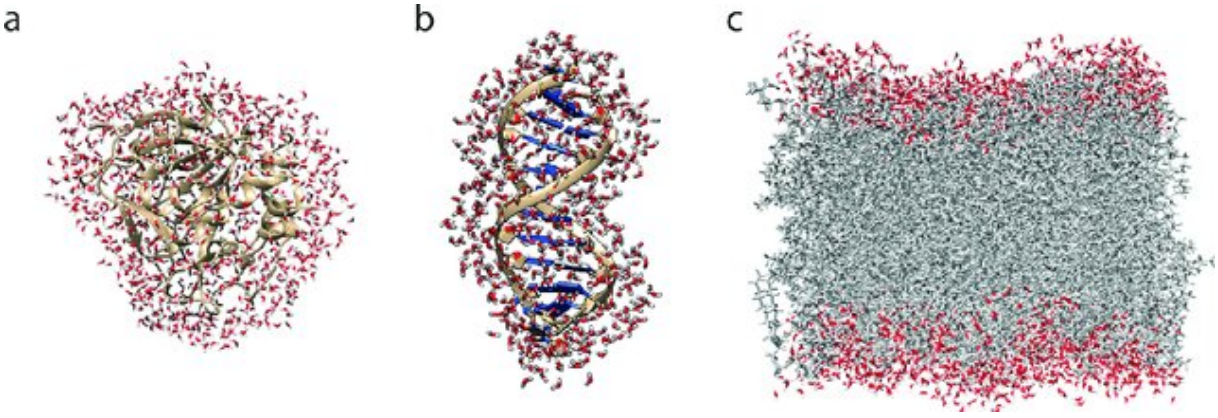

Figure 1. Hydration shell of **(a)** protein, **(b)** DNA and **(c)** phospholipid bilayer (snapshots from simulation described in ref. [34–36]).

Water molecules may be bound to the surface of proteins and released upon complexation.[37–40] Osmotic stress experiments have been used to probe this effect and there is quite a number of papers that report on such experiments showing that the release of water can be an important factor.[37,40–45] Many years ago, Tanford pointed out that the activity of water is inevitably bound to the activity of the added salt ions by virtue of the Gibbs-Duhem relation.[46] Hence, changing the activity of salt ions necessary to probe the dependence of the binding of counterion release

will change the water activity as well and shift possible contributions to K_b that are due to the release of water. Record *et al*.[2] included this effect in their general analysis while Ha *et al*.[47] and Mascotti and Lohman[48] performed the first experiments showing that counterion release may be accompanied by water release. Evidently, the change of water activity should become more decisive at higher salt concentration. Thus, in a series of experiments, Bergqvist, Ladbury, and their associates demonstrated that protein binding to DNA in halophilic bacteria can only be treated quantitatively when invoking this effect.[44,49–51] In particular, plots of *log* K_b vs. *log* c_s are found to be highly non-linear and the weakening of complex formation between DNA and the protein may be even reversed at high salt concentrations (see the discussion of this point in ref.[49]). However, as already pointed out by Tanford,[46] the change of water activity may be very small for salt concentration c_s over the order of 0.001 to 0.01 M used normally in experiments related to counterion release. Hence, the effect of water release may go unnoticed in such an experiment. Osmotic stress experiments may be a way to circumvent this problem.[37,40] However, the polymer or the solute added to the system in order to decrease the activity of water may not be inert and different agents have been shown to lead to considerably different results.

In a number of recent studies it has been shown that the counterion release effect can be analyze in detail by a combination of calorimetric investigations with molecular dynamics (MD) simulations: [3,12,13,31,52,53] First, the complex formation of human serum albumin (HSA) with single chains of poly(acrylic acid) (PAA) was investigated:[52] In this study, isothermal titration calorimetry (ITC) was used to study the complex formation in aqueous solution, varying both temperature and ionic strength.[52] The experimental studies were combined with MD simulation with explicit counterions. Both experimental data as well as simulations led to the conclusion that counterion release is fully dominating the formation of the 1:1 complex of PAA and HSA. Moreover, the experimental K_b coincides with the calculated one within the limits of error. The free energy of binding, ΔG_b was found to depend hardly on temperature whereas the directly measured enthalpy, ΔH^{ITC} varied strongly with T. Thus, binding of HSA to PAA-chains is accompanied by a marked cancellation of enthalpy and entropy that is a common feature for proteins interacting with natural polyelectrolytes.[28,54–56] Secondly, the interaction of dendritic polyglycerolsulfate (dPGS) with various proteins was investigated in aqueous solution by ITC,[12,13,31] with ionic strength and temperature as two decisive variables.[13,53] The binding constant K_b was then compared to the results of MD-simulations on a quantitative level. In this case, good agreement of theory and experiment was also found.[31]

While considering the interaction between proteins and natural / synthetic polymers, structures such as polymer brushes must be discussed. These systems can be described in general as polymer chains densely grafted by one end to an interface.[17] Interactions of proteins with such structures have been, for many years now, a subject of significant interest and investigation in colloid and polymer science.[14–17,19,57,58] In many cases polymer brushes are studied to control the protein adsorption onto surfaces[59,60]. This becomes more complex when the brush is composed of charged polymer chains, *i.e.*, polyelectrolytes.[15,61–65] Surfaces modified with polyelectrolyte brushes have been frequently investigated as they are related to “smart” or stimuli responsive surface coatings[66] and biosensors.[67] Furthermore, polyelectrolyte brushes can be applied to prevent biofouling.[62] It is known that proteins adsorbed and immobilized onto polyelectrolyte brushes retain their conformation[68] as well as their (enzymatic) activity.[69,70]

Understanding protein adsorption to polyelectrolyte brushes is therefore obviously needed for nanotoxicology and nanomedicine.[71]

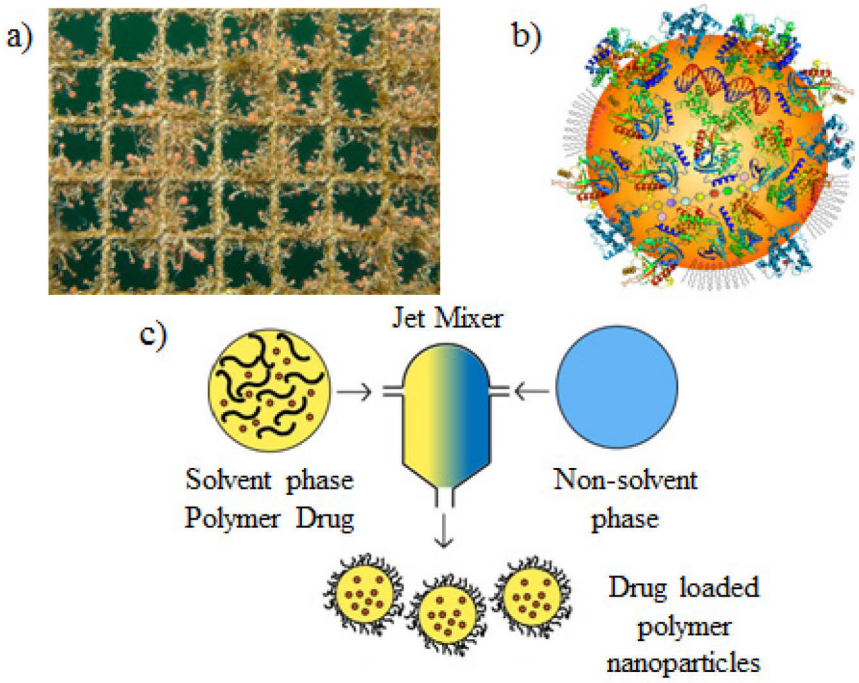

Figure 2. Multiple interaction of proteins with materials for which prevention or enhancement of interaction with polyelectrolyte brushes are applicable. **(a)** biofouling **(b)** protein corona on the surface of a nanoparticle and **(c)** drug encapsulation.[72] Pictures reprinted from: https://www.slideshare.net/ANJUNITHIKURUP/protein-corona-associated-with-nanoparticles and https://www.sintef.no/en/ocean/initiatives/biofouling/#/.

Proteins can be taken up or released from polyelectrolyte brushes depending on salt concentration.[3,73] As discussed above this is related to the counterion release mechanism.[2] Thus the effective degree of ionization and the charge distribution in the polyelectrolyte brush - which strongly depends on the salt concentration and pH of the solution[74] - is crucial for protein adsorption. The characterization of polyelectrolyte brushes and their stimulus response to changes in salt concentration and pH has been the focal point of a large number of articles. The effect of grafting density on brush conformation,[75,76] the hysteretic memory of brushes,[74] the ion specific effects on brush conformation[77] and the interactions with proteins[62,75,78] have been studied in detail. Delcroix *et al*. studied the pH- and salt- dependent polymer conformation and protein adsorption on several polymer brushes.[79] In particular, they defined a protocol for systematic evaluation of the change of polymer conformational upon protein adsorption by quartz crystal microbalance with dissipation monitoring (QCM-D). Recent work of Henzler *et al*. showed that thermodynamics and driving forces of the β-Lactoglobulin (BLG) adsorption on spherical polyelectrolyte brushes (SPBs) with long chains of poly(styrene sulfonate) can be well studied by ITC.[3,80] The resulting complexes of the SPB and the protein stay stable in solution and can be studied by a wide variety of methods including small angle X-ray scattering (SAXS).[73,81] Recently, a first theoretical study on the interaction of proteins with SPBs has been given.[82]

2. Objective of the Thesis

The study described in this thesis is dedicated to the investigation of the mechanism and the analysis of the driving forces upon polyelectrolyte-protein (PE-P) interaction. The main interest of this study is to gain detailed thermodynamic information of protein binding. Well-defined polyelectrolytes (PEs) with different morphologies *e.g.* linear PEs and polyelectrolyte brushes were used to investigate these complex interactions. The formation of PE-P complexes was specifically altered by changes in the physicochemical properties of the surrounding solution such as, salt concentration, pH and temperature. The studies of PE-P interactions presented in this work include:

A) The analysis of the counterion condensation to polyelectrolytes. Here the ion-specific effects and the competition between monovalent and divalent cations upon binding to dendritic polyglycerol sulfate (dPGS) were analyzed. Calorimetric studies in this regard, based on the two component ligand binding (TCLB) model were directly compared with theoretical approach based on the non-linear penetrable Poisson-Boltzmann (PPB) model. The lack of ion-specific effects and a clear competition between mono- and divalent ions upon binding to dPGS contribute to a better understanding of the fundamentals of polyelectrolyte-protein (PE-P) interaction.

B) In another set of experiments the interaction of proteins with linear and low-molecular weight polyelectrolytes is presented. Here a comprehensive investigation of the binding of lysozyme (Lys) to heparin (Hep) and sulfated β-Cyclodextrin (β-CD-S) is discussed. This investigation is based on the analysis of the binding constant K_b as the function of salt concentration c_s and temperature. The dependence on c_s can be used to analyze the release of counterions and water molecules upon binding. The dependence of K_b on T, on the other hand, leads to the enthalpy of binding ΔH_b. The present analysis is based on the interrelation of K_b with two variables and not on the dependence on c_s only. The comprehensive analysis of K_b thus affected allows to discuss the marked enthalpy-entropy cancellation (EEC) that is found for the present system. Various contributions to the enthalpy and entropy of binding are discussed. The related EEC includes not only the contribution of counterion release but also of the release of water.

C) Finally, the study of PE-P interactions was extended to include binding of proteins with polyelectrolyte brushes of planar and spherical geometry. A full thermodynamic analysis of the interaction of human serum albumin (HSA) with a spherical polyelectrolyte brush (SPB) bearing chains of poly(acrylic acid) (PAA) is discussed. Isothermal titration calorimetry (ITC) was used to determine the binding constants at different ionic strength and temperature. In order to ensure that the heat signal is not due to a partial unfolding upon binding, additional Fourier transform infrared spectroscopy (FT-IR) - studies of the complexes were performed. Additionally a quartz crystal microbalance with dissipation monitoring (QCM-D) study of HSA adsorption onto a planar PAA brush is described. This allows a quantitative comparison with calorimetric studies of the same problem. In that way precise structural information can be combined with thermodynamic information.

3. Fundamentals and Theory

3.1. Polyelectrolytes

Polyelectrolytes (PEs) are linear or branched polymers containing charged groups with dissociable counterions within their monomer units. Based on the structural properties of these units, PEs vary in terms of their flexibility in solution. Classification of PEs excludes proteins due to their high structural organization, with emphasis on their tertiary structure that leads to unique solution behavior. Nevertheless other biomolecules, *e.g.* DNA and in general short ionic polypeptides that can be characterized by well-defined secondary structures along with limited flexibility are often included in the overall broad group of polyelectrolytes. PEs are intensively studied for their interaction with charged surfaces. The number of experimental and theoretical work describing polyelectrolyte adsorption to such surfaces as well as the resulting bound state is hard to overlook.[83] PEs due to their conformation flexibility can interact with flat surfaces as well as with colloidal particles.

Over past years interactions between PEs and proteins were extensively studied by combined experiment and theory in order to elucidate physicochemical fundamentals of this process.[3] A special experimental effort with corresponding theoretical analyses has been paid to the interaction of PEs with variety of oppositely charged particles such as micelles, liposomes, and inorganic colloids.[84,85] Moreover, binding takes place even when PE and protein are a like-charged. This is a consequence of protein charge anisotropy, resulting from the asymmetric distribution of charged amino acid residues often clustered on the protein exterior forming so called charged protein patch. This allows PEs to interact electrostatically with regions of opposite charge on the protein surface.

A particular subgroup of PEs is constituted by glycosaminoglycans (GAGs). These linear and flexible bio-polysaccharides occur on the surface of cells, in connective tissues, and in the extracellular matrix. From a structural point of view GAGs can be described as highly heterogeneous due to the disaccharide building blocks, type of sulfation, pattern of sulfation and the overall chain length. Such structural diversity is a consequence of the non-template driven biosynthesis of these molecules which allows structural modifications of GAGs in response to variable physiological stimuli.[86] One of the consequences of such structural diversity, despite of clear influence on physicochemical characteristics of GAGs is their ability to interact with numerous proteins.[87,88] Their interactions with proteins are widely studied and in detail described in several reviews[87,89–91] yet recognition of GAGs as polyelectrolytes still has not a high profile.

3.1.1. Linear and Low Molecular Polyelectrolytes

3.1.1.1. Heparin

Heparin is commonly used as blood anticoagulant[92] and plays a fundamental role in cell signaling as it occurs on the surface of most cells by being proteoglycan sidechains.[93] Heparin is related to processes such as angiogenesis[94] and cancer.[95] It has been identified as a selective regulator of ligand-receptor interactions.[96] Special attention is paid to heparin in surgery and in

treatment of long-term diseases. Here, it is essential to modulate the amount of heparin available in the blood plasma to prevent from bleeding and overdose.[97]

From a structural point of view heparin is a linear GAG that consists of repeating, variably sulfated disaccharide units of uronic acid and glucosamine (see **Figure 3**). Variable substitutions with *N*- and *O*-sulfo and *N*-acetyl groups, as well as the epimerization of the uronic acid are the cause of variation in the structure of the main disaccharide unit of a native heparin.[88] Pharmaceutical heparin, commonly used as macromolecular drug[98] is a highly sulfated type of native heparin (see Figure 3) found in mast cell granulates.[88] A great deal of current interest is paid to study the heparin-protein binding in which highly sulfated type (Hep) plays a dominant role.[87,99,100] Although PE-P complexation is not exclusively ionic in nature, Hep is a very useful model for studying this process in detailed.[99]

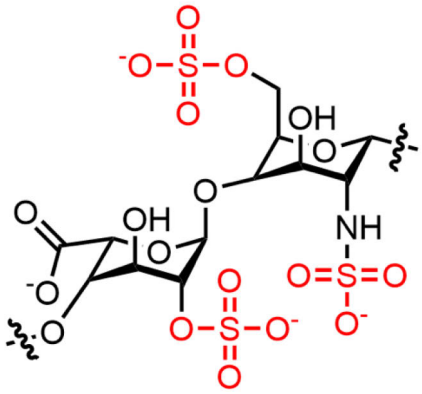

Figure 3. Chemical structure of highly sulfated major repeating unit of heparin: 2-O-sulfated iduronic acid and 6-O-sulfated, N-sulfated glucosamine, IdoA(2S)-GlcNS(6S).[87]

3.1.1.2. Sulfated β-Cyclodextrin

Rapid progress in development of therapeutic polymers is confronted by the challenges of the effective drug delivery. Major obstacles for polymers as drug candidates are solubility, stability and membrane permeability.[101] Many attempts of improving bioavailability of poorly-soluble drugs, was based on the complexation with solubilizing agents.[102] In this regard cyclodextrins (CDs) are able to eliminate some of the limitations of polymer drug candidates and improve their delivery.[103]

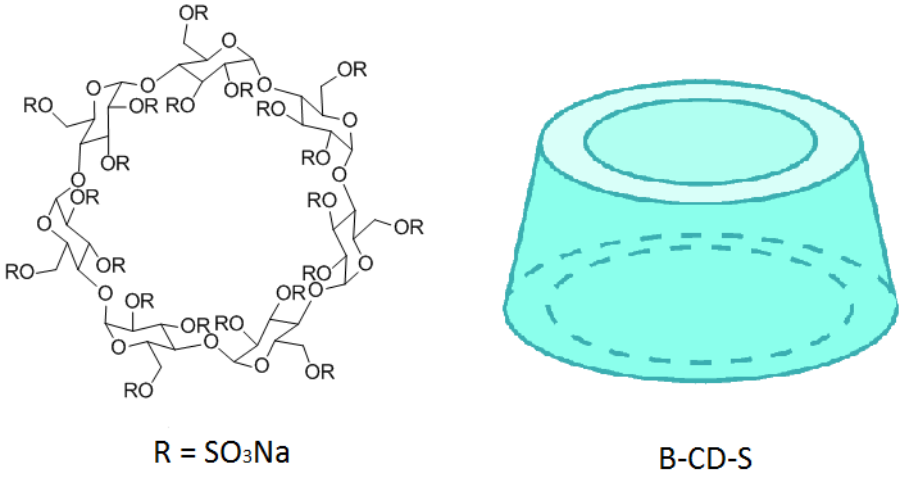

Figure 4. Chemical structure and schematic representation of a spatial structure of β-CD-S.

CDs are cyclic oligosaccharides shaped of a truncated cone or torus.[104] Their structure (see **Figure 4**) is characterized by hydrophobic cavity accessible for variety of compounds. Hydroxyl groups located on the face of the structure ensure water solubility.[105] Complexation of hydrophobic drugs with CDs was applied in separation methods[106–108] and pharmaceutical chemistry.[109] There are more than 30 available drugs with improved stability and solubility due to CDs complexation.[109,110] Special attention was paid to sulfated cyclodextrins (S-CDs). There were studied as an alternative for heparin in repairing process and used in direct measurement of lipoprotein cholesterol in serum.[111] β-CD-S which is composed of seven *α*-1,4-linked glucose units presented a lack of hemolytic activity in early studies on binding to erythrocytes[112] which resulted in increasing interest of this particular CD.

3.1.2. Hyperbranched Polyelectrolytes

Hyperbranched macromolecules can be in general described as composed of randomly branched structures that consist of one focal point and at least two branching points.[113] This class of polymers has become intensively investigated due to its biomedical applications. One of the medically most promising class of hyperbranched macromolecules is represented by dendritic polyglycerol sulfate (dPGS).

3.1.2.1. Dendritic Polyglycerol Sulfate (dPGS)

This compound was investigated originally as potential alternative for heparin, exhibiting interesting properties such as anti-inflammatory activity suitable for variety of applications.[114] **Figure 5** shows the structure of an idealized dPGS molecule.

Dernedde *et al*. showed a high anti-inflammatory effect of dPGS *in vivo*.[115] By varying the size of dPGS as well as the degree of its sulfation they obtained a detailed relationship of dPGS structure and activity. They evidenced a strong binding of dPGS to P- and L- selectin with clear correlation between binding affinity, increasing size and degree of sulfation.

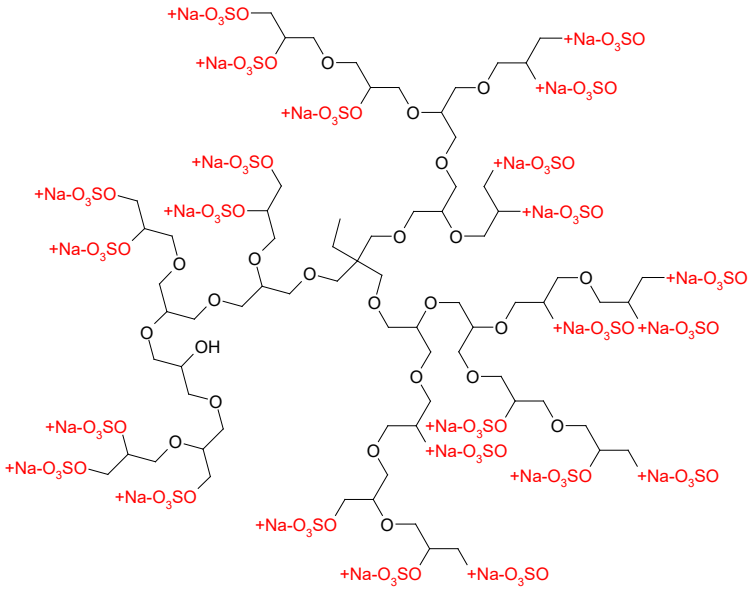

Figure 5. Idealized structure of dPGS.

Finally, it was found that dPGS by binding to, and inhibition of P- and L- selectins that cause the leukocyte extravasation diminishes the inflammatory response. Over the recent years the effect of dPGS was studied against multiple diseases associated with inflammatory events such as osteoarthritis,[116–120] rheumatoid arthritis[116] and neurological disorder.[121,122] In all these studies dPGS appeared as a promising candidate for medical treatment.

3.1.3. Polyelectrolyte Brushes

Polyelectrolyte (PE) brushes arise when long linear polyelectrolyte chains are densely grafted to a solid surface.[123] Depending if the PE chains are attached to a planar[123–125] or curved as *e.g.* spherical surface,[126–132] a planar- or spherical polyelectrolyte brush will be generated. The brush structure results from a sufficiently dense grafting of the chains which means that the length of the PE chain is much larger than the average distance between two neighboring chains grafted on the surface. In a more tangible way it can be formulated that the average distance (D) between neighboring grafted chains should be smaller than two times of the gyration radius (R_g) of a free PE chain (see **Figure 6**).[133]

Depending on the residual groups of grafted PE chains, two types of brushes can be distinguished. The *Quenched brush* is a result of attachment of a strong polyelectrolyte as *e.g.* poly(styrene sulfonic acid). In this case the charges along the chain are independent of the pH in the system.[134] Upon grafting a weak polyelectrolyte as *e.g.* poly(acrylic acid), an *annealed brush* will result. Here the degree of ionization of the chains depends on the pH within the brush layer.[74] At high pH the acid groups of monomeric units are dissociated leading to a highly charged system. Consequently, at low pH the acid groups are fully protonated and the system behaves similar to a neutral brush. An increasing interest in PE brushes is due to the fact, that the strong electrostatic interactions between charged and densely grafted chains allow a wide use of these systems, especially when compared to brushes of grafted, uncharged polymers.[15,135]

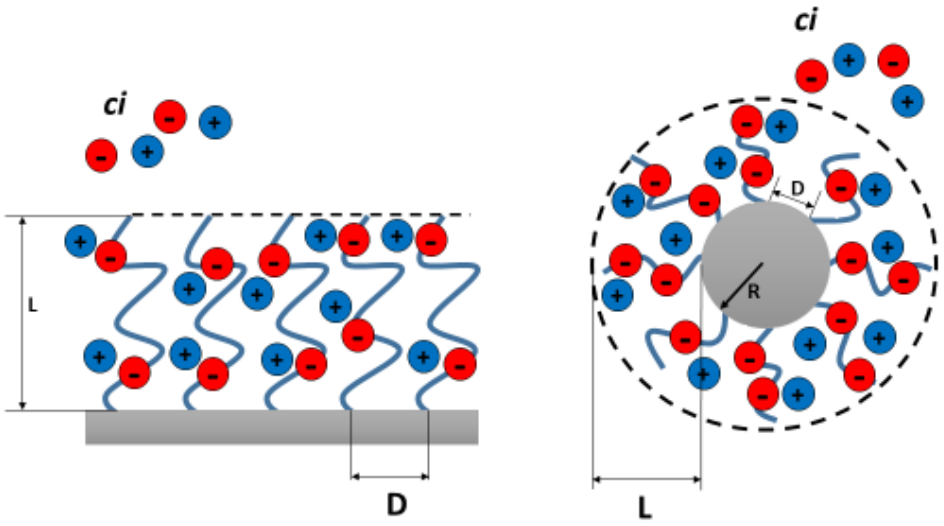

Figure 6. Schematic representation of the structure of the Planar- and Spherical Polyelectrolyte Brush with grafted anionic PE chains on their surface. *R* – radius of spherical substrate surface, *L* – the contour length of the attached chains, *ci* – counterions.

It has been shown that the confinement of a large number of counterions compensating the charge of polyelectrolyte chains within the brush layer constitute an essential property of these systems.[136,137] As a consequence of that, the PE chains will be stretched by the high osmotic pressure of the counterions retained within the brush layer. The resulting *osmotic brush* exists in a salt-free solution (see **Figure 7**).

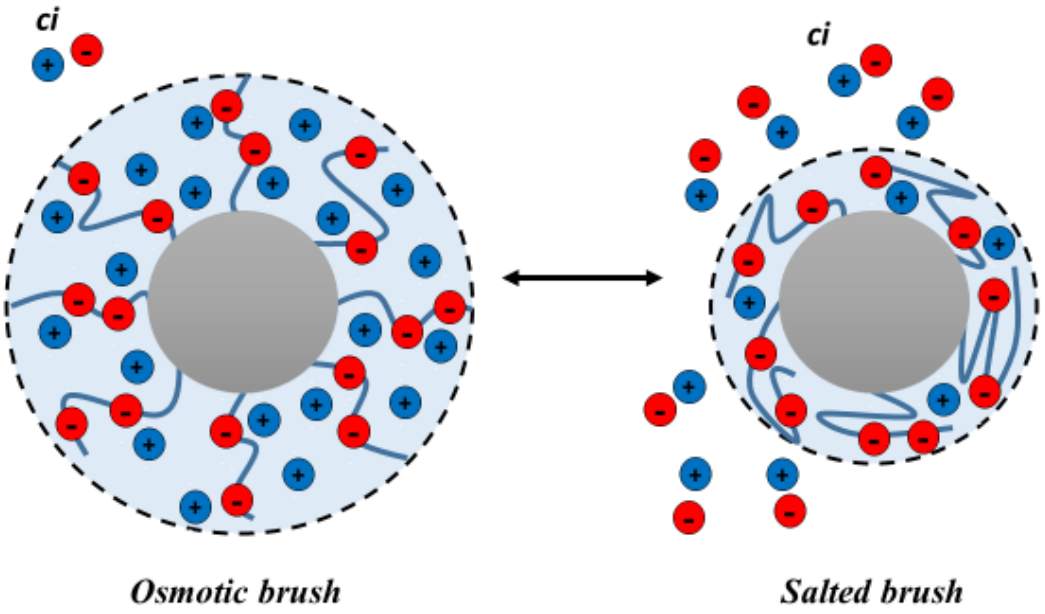

Figure 7. Schematic representation of the transition between *osmotic*- and *slated brush* on the example of anionic spherical polyelectrolyte brush. PE chains of the *osmotic brush* are stretched by the high osmotic pressure; such brush exists in a salt-free solution. In a *salted brush* the strong electrostatic interaction between PE chains are screened as consequence of increased ionic strength.

However, if the ionic strength of the solution is increased by addition of salt, the strong electrostatic interaction between PE chains will be screened and the brush will become a *salted brush*. Within this regime PE brush behaves similar to uncharged monolayer of grafted polymer chains. Therefore by regulation of the ionic strength PE brushes can switch between different states. This transition between *osmotic brush* and *salted brush* regime was demonstrated through X-ray reflectometry by monitoring the height of the brush layer.[138,139]

The swelling behavior of the PE brush cannot be understood only on the basis of electrostatic interactions alone. On the example of planar poly(*N*-methyl-pyridinium) brush it was demonstrated that ion-specific effects can lead to brush shrinking in the swollen state.[140] In this particular case the increase of iodine counterions concentration resulted in the dramatic collapse of the brush. Further increase of the iodine ions concentration however resulted in brush re-swelling. Therefore "salting-out" and "salting-in" driven by ion-specific effects at high ionic strength can overrule the electrostatic interactions.

3.1.3.1. Planar Polyelectrolyte Brushes (PPBs)

Much attention has been given to PPBs in order to immobilize proteins or enzymes. From the fact that protein molecules immobilized by PE brushes keep their conformation and (enzymatic) activity,[62] PPBs appears as promising systems to use as biosensor.[67] PPBs can by characterized by as *e.g.* water contact angle analysis, ellipsometry,[141] atomic force microscopy (AFM),[74] Fourier transform infrared (FT-IR) spectroscopy, near-edge X-ray absorption fine structure

(NEXAFS) spectroscopy[76] and quartz crystal microbalance with dissipation monitoring (QCM-D).[142] PPBs based on poly(acrylic acid) chains supported on silicon wafer were used to study the adsorption of bovine serum albumin (BSA) by fixed-angle optical reflectometry.[62] It was found that approximately 30% of the brush volume is occupied by protein molecules and that protein concentration in solution plays almost no effect on the amount of adsorbed proteins.

3.1.3.2. Spherical Polyelectrolyte Brushes (SPBs)

SPBs can be characterized by numerous experimental techniques such as dynamic light scattering (DLS),[143,144] small angle X-ray and neutron scattering (SAXS, SANS),[145,146] cryogenic transmission electron microscopy (cryo-TEM),[147] chain cleavage and conductometric titration.[133] SPBs are a class of functional colloidal particles with a wide application potential. Cationic SPBs composed of polystyrene (PS) core and poly-(2-aminoethylmethacrylate) (PAEMH) chains were used as carriers for catalytically active metal nanoparticles such as Au and Pd.[148] It was shown that the resulting composite particles exhibit excellent colloidal stability and their catalytic activity was monitored by a model reaction of the reduction of 4-nitrophenol by sodium borohydride (BH_4^-). SPBs including *quenched* and *annealed* brushes were used for immobilization of large number of proteins thus opening the possibility of substantial biomedical applications. It was shown that BSA and β-Lactoglobulin (BLG) can be separated by *cationic* and *anionic* SPBs based on protein charge anisotropy.[149]

3.2. Proteins

3.2.1. Lysozyme (Lys)

Lysozyme (Lys) is an antimicrobial enzyme that represents the class of glycoside hydrolases.[150] It catalyze the hydrolysis of the (1→4)-*β*-glycosidic linkages between N-acetylmuramic acid and N-acetyl-D-glucosamine in the peptidoglycans of bacterial cell walls.[151] Its antibacterial properties and conformational stability are the reasons of such interest and wide use of this protein. Over the years Lys has been used in biotechnological and therapeutic applications.[152,153]

Lys is a globular and relatively small protein.[150] As for one of the first proteins with revealed three-dimensional structure[154] it is widely used in experimental and theoretical studies.[150] Lys is an ellipsoidal, single-chain polypeptide with molecular weight of 14,3 kDa that consist of 129 residues organized in six *α*-helices and three *β*-sheets connected by flexible loops and groped into two domains, *α* and *β* (see **Figure 8**).[155]

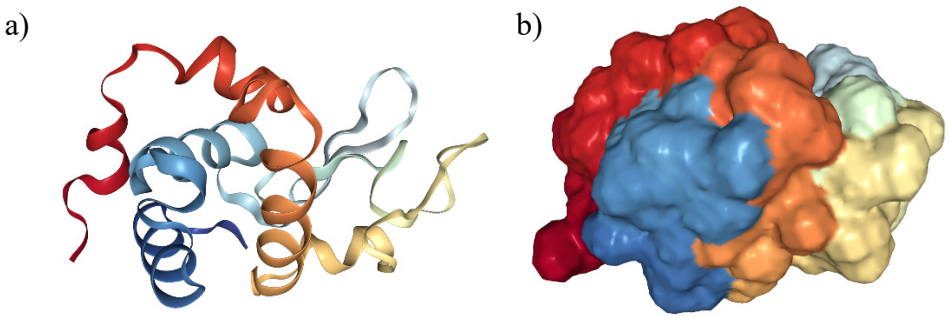

Figure 8. **(a)** Crystal structure of hen egg white lysozyme (HEWL). **(b)** Electrostatic surface view of the HEWL. (PDB: 1DPX)

α-helices contribute to about 30-40% to the secondary structure of this protein and the *β*-sheet content is less than 10%. Due to the presence of four disulfide bridges and approximate dimensions of 30 x 30 x 45 Å it is considered as a rigid molecule. Lys contain 14 acidic and 18 basic residues and it is characterized by isoelectric point of $pI = 11$. The active site of this protein is located within negatively charged crevice between domains. The negative charge is attributed to the presence of glutamic acid- and aspartate residues.

3.2.2. Human Serum Albumin (HSA)

Human Serum Albumin (HSA) represents a wide family of proteins that includes vitamin D-binding protein, human-specific component (Gc) and α-fetoprotein (AFP).[156] Unlike *Gc* and *AFP*, albumins are non-glycosylated and they are also non-active in terms of immunosuppression. Those multi-domain and relatively large proteins plays multiple physiological functions due to the fact that they are the major soluble protein component of the bloodstream. Therefore albumins are one of the main contributors to colloid osmotic pressure of the blood. Moreover, the extravascular protein stands for 60% of the total albumin.[156] HSA is best known for its significant role in supporting the transport, distribution and metabolism of numerous endo- and exogenous ligands.[156] These ligands constitute a chemically diverse group which includes amino acids, fatty acids, steroids, metals (notably calcium, copper and zinc) and many pharmaceuticals. Due to its commonness - with blood concentration of about 7 x 10^{-4} M

and its extraordinary binding capacity, HSA affects the drug efficiency and rate of delivery, thus being an important factor with regard to development of drugs and their availability.[157]

HSA is a protein with molecular weight of about 66 kDa that consist of 585 amino acids grouped into three homologous domains (I, II and III). Each of those is composed by two halical subdomains (A and B) that are connected by random coil.[157] Therminal regions of structurall domains participate in the formation of interdomain helices that are linking domain IB to IIA and IIB to IIIA, respectively. The structural organisation of HSA is presented in **Figure 9**.

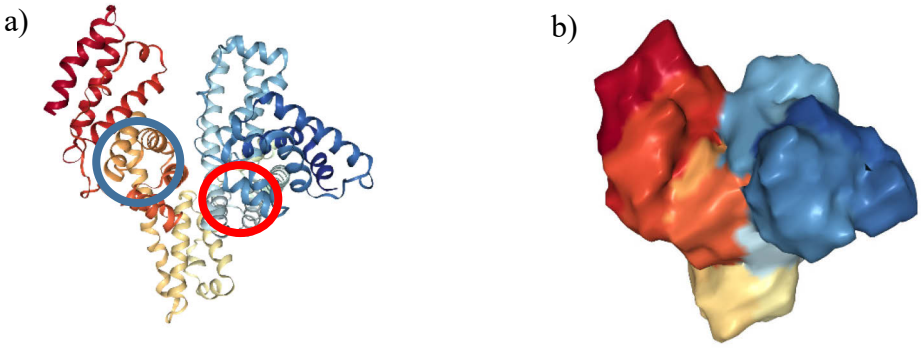

Figure 9. **(a)** Crystal structure of HSA. Sudlow site I (in subdomain IIA) is indicated by red circle; Sudlow site II (in subdomain IIIA) is indicated by blue circle. **(b)** Electrostatic surface view of the HSA. (PDB: 1AO6)

From previous binding studies it became evident that HSA can reversibly bind a multitude of different ligands.[158,159] The principal binding sites on HSA are located in subdomains IIA and IIIA, and named as Sudlow I and Sudlow II, respectively.[160,161] In both these regions a part of the hydrophobic core is surrounded by positively charged residues to form a pocket.[161] The pocket of subdomain IIA is formed by hydrophobic side chains and it is predominantly non-polar. The entrance of it, is surrounded by positively charged amino acid residues.[161] Subdomain IIIA, which is almost the same size as subdomain IIA is characterized by the pocket with large solvent accessibility and a single hydroxyl patch located at the mouth of the pocked.[162] Due to these structural features Sudlow site I accommodates most preferably bulky heterocyclic anions, whereas aromatic carboxylates bind to Sudlow site II.[157]

3.3. Proteins and Polyelectrolytes

Polyelectrolytes (PEs) and proteins in aqueous solution interact with each other as well as with their surroundings resulting in formation of polyelectrolyte-protein complexes (PE-P).[11–13,52,80,87,163] Due to its relation to the interaction of DNA with repair proteins it becomes an important problem in modern biophysics.[164,165] By considering the adsorption of proteins onto surface, two fundamental approaches, regarding this process can be distinguished. In the first approach, in order to avoid biofouling the protein adsorption must be prevent.[166] The fact that biomedical devices such as implants or nanoparticles will be immediately covered by a dense layer of adsorbed proteins upon implantation into human body is the reason of such intense research in this field. The resulting protein "corona" will completely isolate the device from its target and furthermore will cause the immune response to these materials.[167–170] In the second approach protein immobilization is desirable. This is due to many applications in which enzymes are used as catalysts. In most cases in both approaches, PE brushes are used to control the protein adsorption. Thus surfaces coated with PE brushes are frequently studied as they are related to "smart" and stimuli responsive materials often used as biosensors.[171] PE brushes are an excellent system to study protein adsorption, since protein immobilized onto them retains their conformation and (enzymatic) activity.[69,70] It has been shown that several proteins including human serum albumin (HSA) can adsorb onto a-like charge spherical polyelectrolyte brushes (SPBs).[32] It was revealed that the secondary structure of adsorbed proteins is undisturbed.[68] It was also demonstrated that adsorbed proteins are distributed evenly within the brush layer.[73,172] Moreover several studies reported a strong influence of ionic strength on the amount of adsorbed proteins.[173–175] In particular, the uptake decreases with increasing ionic strength indicating the strong influence of electrostatics in protein interaction with PE brushes. The formation of PE-P complexes is brought about by a combination of electrostatic interactions and entropy gain.[52,82,84,85,99,176] The complexation is therefore influenced by density, distribution and extent of ionization of the dissociable groups on the protein surface as well as on the PE chains.

3.3.1. Protein Structure upon Binding

Protein conformation upon binding to PEs is one of the most important aspects of this process. The analysis of the protein structure can focus on demonstrating if the protein structure is preserved or on find an evidence of changes in protein conformation.[177] This depends if the studied process is related to protein immobilization or allosteric interactions resulting in enhancement or inhibition of the protein activity. Experimental techniques such as fluorescence, circular dichroism (CD) and Fourier transform infrared (FT-IR) spectroscopy have been used to establish that the structure of adsorbed proteins is largely preserved and stabilized by PEs.[13,178] In contrast, the conformational change upon binding to heparin appears for several proteins in e.g. antithrombin.[179] FT-IR spectroscopy was used to analyze the secondary structure of native and adsorbed proteins. This technique, unlike the circular dichroism is not limited to translucent solutions.[180] It can be successfully applied to turbid samples such as latex particles.[181] Thus, it is suitable for analysis of the secondary structure of proteins adsorbed onto PEs brushes. Proteins in IR spectra show characteristic absorption bands (amide I and II) between 1500 and 1700 cm^{-1}.[182–184] The amide I band arise in approximately 80% from stretching vibration of the C=O bond, whereas the amide II band can be mainly

associated with C-N stretching vibrations and bending of N-H bond.[185] The shape, position and intensity of the amide bands depend strongly on the secondary structure of the protein. IR signals arising from the structural components of the protein that are present in the amide I band are enlisted in **Table 1**.[185]

Table 1. Elements of the protein-secondary structure present in the amide I band.

Wave number (cm^{-1})	Structure element
1620 – 1640	β – sheet
1640 – 1650	Random coil
1650 – 1658	α – helix
1660 – 1690	loops
1670 – 1680	β – sheet

The standard deviation upon determination of elements of the secondary structure of the protein by FT-IR spectroscopy does not exceed 5%.[186] Over the recent years this technique was successfully applied in several studies regarding protein immobilization on PE brushes.[81,163,181,187,188]

3.3.2. Thermodynamic Analysis of Protein Interaction with Polyelectrolytes by Isothermal Titration Calorimetry (ITC)

3.3.2.1. Thermodynamic Analysis

3.3.2.1.1. Counterion Condensation

A highly charged polyelectrolyte in solution attracts its surrounding counterions so that a certain fraction of them is condensed to the macroion.[189] This condensation of counterions on a polyelectrolyte (PE) chain can be analysed based on the Onsager-Manning-Oosawa theory.[190–193]

In that way, the charge of PE chain is balanced by condensed counterions and by a fraction of counterions that interact with PE chain *via* screened Debye-Hückel interaction.[3] Condensation occurs when the charge-density parameter, $\xi = \frac{l_B}{l}$ (for the case of monovalent charge groups and counterions) is greater than unity. Here, $\lambda = \frac{e}{l}$ is the charge density of the polymer chain and $l_B = \frac{e^2}{4\pi\varepsilon_0\varepsilon_r k_B T}$ is the Bjerrum length, where e stands for the electron charge, ε_0 for vacuum permittivity , ε_r for dielectric constant and k_BT for the thermal energy.

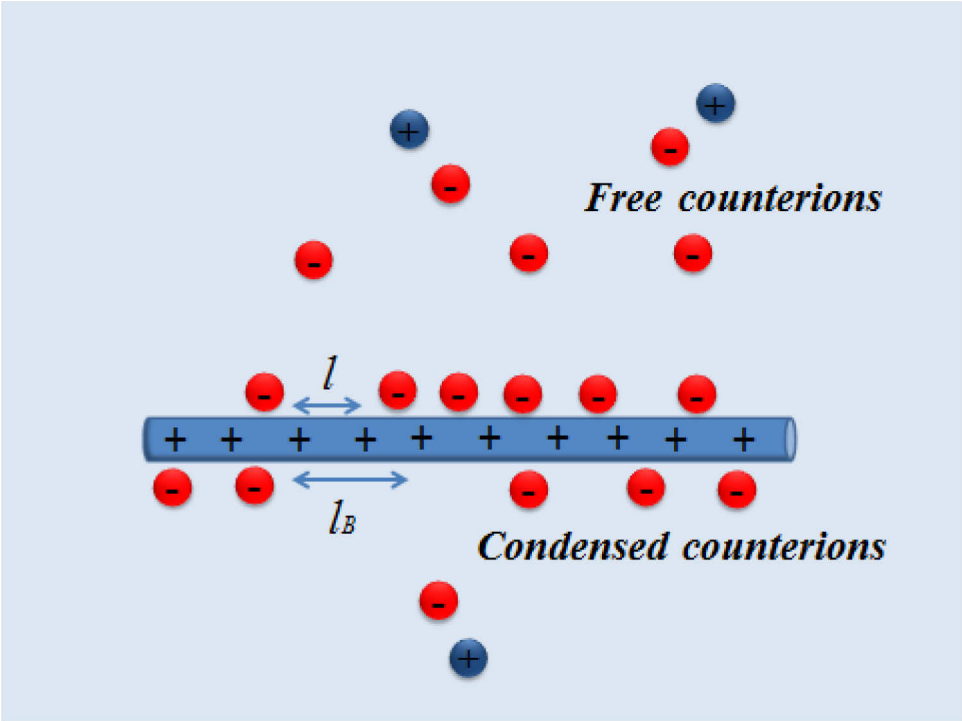

Figure 10. Schematic representation of the ion condensation. A rod-like polymer with high charge ($l_B > l$) attracts a number of oppositely charged counterions.

As shown by Manning, in dilute solutions for macroions characterized by $\xi > 1$ a fraction of 1-1/ξ of the counterions will condense on them in order to lower ξ to unity.[189] The screening effect of the ions around the PE chain is equivalent to a second fraction $(2\xi)^{-1}$ of bound counterions. Thus, a fraction of 1-1/(2ξ) is relevant for counterion release from the macroion.[165]

3.3.2.1.2. Counterion Release

Recent studies on PE-P binding demonstrated an attractive interaction of the proteins above its isoelectric point (pI) with highly charged PEs at low salt concentration.[52,194,195] Isothermal titration calorimetry (ITC) revealed that the entropy is one of the main driving forces for such interaction.[52,196] The observed entropic attraction is due to counterion release. Proteins carry patches of positive and negative charge on their surface due to the asymmetric distribution of charged residues.[197] This charge anisotropy allows PE-P interaction. Upon such interaction proteins can act as multivalent counterions in regard to charged PE chains thus releasing a number of its condensed monovalent counterions.[198] Theoretical predictions estimates that z[1-1/(2ξ)] is the number of released counterions upon binding, where z represents the number of charged sites of the PE. As a consequence the considerable overall gain in entropy can promote the adsorption of proteins, as mentioned before, even on the "wrong side" of isoelectric point.

The attractive contribution to the Gibbs free energy of binding due to counterion release, ΔG_{cr} can be estimated through:[16,196]

$$\frac{\Delta G_{cr}}{k_B T} = \Delta N_{-} \ln\left[\frac{c_s}{c_{patch}}\right] + \Delta N_{+} \ln\left[\frac{c_s}{c_{PE}}\right] \quad (1)$$

Here ΔN_{-} is the number of negative counterions released form the positive patch on the protein surface. ΔN_{+} is the number of positive counterions released from the PE chain. c_s represents the concentration of salt in solution; c_{patch} is the concentration of negative counterions that are

accumulated on the positive patch on the protein surface and c_{PE} stands for the concentration of counterions condensed on the PE chain. As discussed in previous section c_{PE} can be estimated by Onsager-Manning-Oosawa theory.[190–193]

3.3.2.1.3. Effect of the Ionic strength on the Binding Free Energy

The non-monotonic salt dependence was observed for interactions of β-Lactoglobulin (BLG),[80] ribonuclease (RNase),[175] lysozyme (Lys)[13] and human serum albumin (HSA)[52] with synthetic strong polyanion and polycations as well as for heparin and anthitrombin.[86] This particular behavior, namely the highest PE-P binding affinity occur when the Debye length is of the comparable size as the protein radius and is referred as a non-specific PE-P binding. A highly influential study was reported by Record *et al.*[199] in which a general thermodynamic analysis on the effect of ionic strength on ligand-nucleic acid interaction was developed. In the proposed approach due to the counterion release as a main driving force for PE-P complex formation (see **Figure 11**), the condensed counterions must be included in the stoichiometry of the binding.[53] Also the role of water release and hydration upon such process cannot be overlooked what has been considered by Tanford.[46]

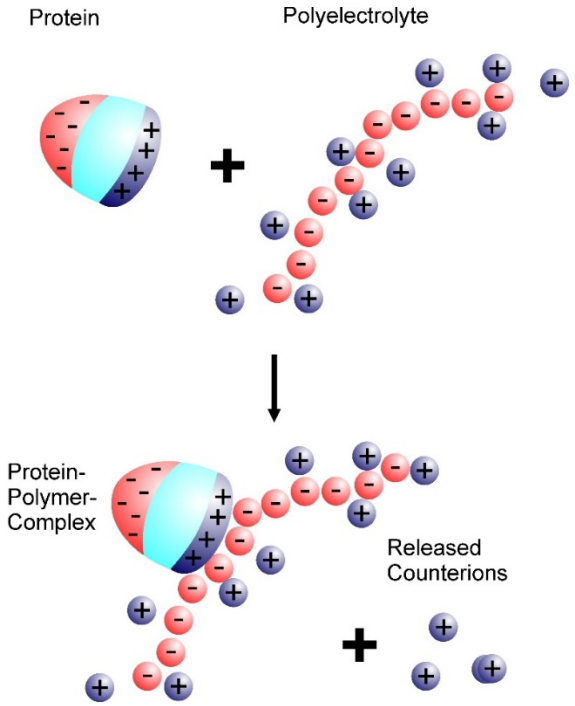

Figure 11. Schematic illustration of the counterion release upon interaction between highly charged PE and protein.

In that way, for association between charged polymer *PE* and protein *P* and formation of their non-covalent complex *PEP,* in solution containing an excess of the electrolyte $M_{p+}X_{p-}$ the following chemical equilibria can be formulated:

$$P + PE \overset{K_b}{\rightarrow} PEP + (\Delta n_M)M + (\Delta n_X)X + (\Delta n_W)W \qquad (2)$$

where

$$K_b = \frac{[PEP] a_M^{\Delta n_M} a_X^{\Delta n_X} a_W^{\Delta n_W}}{[P][PE]} \quad (3)$$

and

$$K_T = \frac{[PEP] \gamma_{PEP} a_M^{\Delta n_M} a_X^{\Delta n_X} a_W^{\Delta n_W}}{[P][PE] \gamma_P \gamma_{PE}} \quad (4)$$

and

$$K_b = \frac{K_T \gamma_P \gamma_{PE}}{\gamma_{PEP}} \quad (5)$$

However a_M, a_X and a_W are not independent variables. Following Tanford the activities of solute and solvent species can be related by the Gibbs-Duhem equation:[46]

$$dlna_W = -\frac{n_X}{n_W} dlna_X - \frac{n_M}{n_W} dlna_M \quad (6)$$

Here we assume that the concentration of the polyelectrolyte is small [PEP] ≈ 0.

Equation (6) can be further generalized as proposed by Tanford.[46]

$$dlna_W = -\frac{c_s p}{55.6} dlna_{\pm} \quad (7)$$

where c_s is the molal concentration of electrolyte, 55.6 is the molality of water and $a_{\pm} = a_{MX}^{\frac{1}{p}} = \left(a_M^{p^+} a_X^{p^-}\right)^{\frac{1}{p}}$

Here $p = p+ + p-$ and for a monovalent salt, $p = p+ = p- = 1$, thus $p = 2$

Furthermore,

$$n_M dlna_M + n_X dlna_X = (n_M + n_X) dlnc_s + n_M dln\gamma_M + n_X dln\gamma_X =$$

$$(n_M + n_X) dlna_{\pm} + \frac{1}{p}(p^- n_M - p^+ n_X) dln\left(\frac{\gamma_M}{\gamma_X}\right) \approx (n_M + n_X) dlna_{\pm} \quad (8)$$

By combining equations (3) – (8) the following relation is obtain

$$dlnK_b = -\Delta\left(n_M + n_X - \frac{c_s p}{55.6} n_W\right) dlna_{\pm} + dln\left(\frac{\gamma_P \gamma_{PE}}{\gamma_{PEP}}\right) \quad (9)$$

The effect of electrolyte ($M_{p^+}X_{p^-}$) on K_b can be analyzed more closely with consideration of binding between linear negatively-charged polymer and a protein bearing patches of positive charges on its surface (see Figure 11).

$$\frac{dlnK_b}{dlna_{\pm}} = -\Delta\left(n_M + n_X - \frac{c_s p}{55.6} n_W\right) + \frac{dln\left(\frac{\gamma_P \gamma_{PE}}{\gamma_{PEP}}\right)}{dlna_{\pm}} \quad (10)$$

Due to the release of cations condensed on the charged polymer it can be assumed that K_b is dependent only on the concentration of cations [M^+] and independent on the concentration of

anions [X^-]. If considered interaction results in uptake or release of water molecules as well as cations, the dependence of K_b on monovalent electrolyte $M_{p+}X_{p-}$ can be formulated as

$$\frac{dlnK_b}{dlnc_s} = -\Delta n_{ci} + \frac{2c_s\Delta w}{55.6} \quad (11)$$

where $\Delta n_X = 0$; $\Delta n_M = \Delta n_{ci}$ and the activity coefficient is disregarded: $a_\pm \rightarrow c_s$. Δn_{ci} represents the moles of released ($\Delta n_{ci} > 0$) counterions (in this particular case, cations) and Δw stands for the moles of water molecules released ($\Delta w > 0$) upon binding. Integrating the equation (11) in the boundaries for the concentration of electrolyte $M_{p+}X_{p-}$, c_s and 1M:

$$\int_{1M}^{c_s} dlnK_b = -\Delta n_{ci} \int_{1M}^{c_s} dlnc_s + 0.036\Delta w \int_{1M}^{c_s} c_s dlnc_s \quad (12)$$

results in

$$lnK_b - lnK_b(1M) = -\Delta n_{ci} lnc_s + 0.036 \cdot \Delta w \cdot (c_s - 1) \quad (13)$$

Special attention must be paid to the integration constant 0.036·Δw which ensures the correct limit for c_s = 1M.[200,201] Equation (13) shows that Δw must be of the order of 10^2 to produce a noticeable effect on K_b, that is, a noticeable curvature in plots of $ln\ K_b$ vs. $ln\ c_s$. This has been shown clearly in the work of Bergqvist and Ladbury.[202] Moreover, if the second term in equation (13) can be dismissed, these plots can be used to extrapolate the binding constant to high ionic strength where counterion release should no longer influence K_b (see the discussion of this point in ref.[53]). Moreover, equation (13) shows that Δw must be of the order of 10^2 to produce a noticeable effect on K_b, that is, a noticeable curvature in plots of ln K_b vs. ln c_s. If the second term in equation (13) can be dismissed, these plots should be linear and can be used to obtain the binding constant K_b *(1M).* In this the following relation can be used for data evaluation:

$$lnK_b = lnK_b(1M) - \Delta n_{ci} lnc_s \quad (13a)$$

3.3.2.1.4. Donnan Effect

The confinement of counterions compensating the charge of PE chains within the PE brush is an essential property of PE brushes. The phase boundary between the bulk solution and charged PE brush and by this an unequal ion distribution originates the electric potential across the boundary. Assuming the electroneutrality of this system the concentration of counterions within the brush can be given, due to Donnan equilibrium by:[68]

$$\frac{c_{brush}}{c_{salt}} = \left(\frac{\alpha c_p}{2c_{salt}}\right) + \sqrt{1 + \left(\frac{\alpha c_p}{2c_{salt}}\right)^2} \quad (14)$$

with the Donnan-potential expressed as follows

$$\Delta\varphi = e^{-1} k_B T ln\left[\left(\frac{\alpha c_p}{2c_{salt}}\right) + \sqrt{1 + \left(\frac{\alpha c_p}{2c_{salt}}\right)^2}\right. \quad (15)$$

where c_p denotes the concentration of monomer units within the brush and α corresponds to the fraction of charged monomer units.

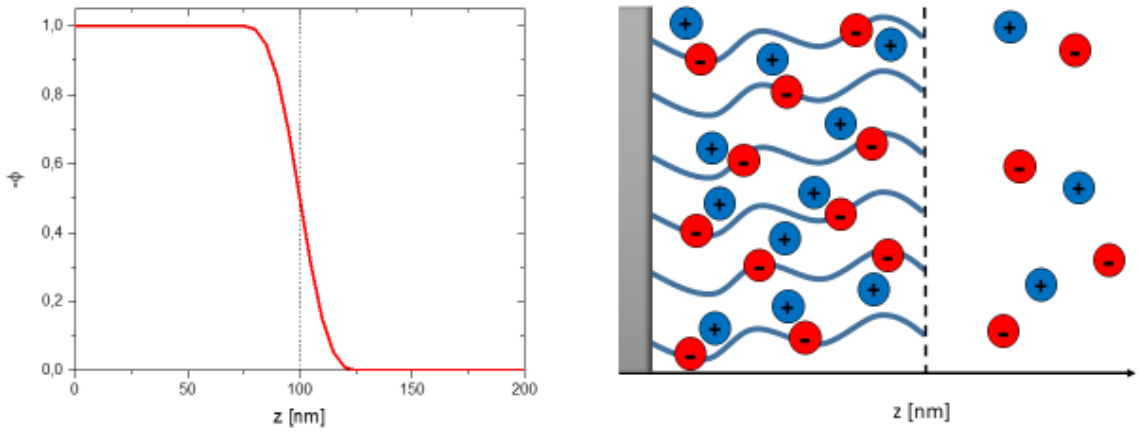

Figure 12. The phase boundary between PE brush and bulk solution. **(a)** *φ(z)* represents the Donnan – potential for anionic PE brush of 100 nm thickness as a function of distance *z* measured from the solid surface. **(b)** Schematic illustration of a surface functionalized with PE brush. The brush charge is compensated by counterions confined within its layer.

In case of a negatively charged PE chains the concentration of protons within the brush, acting as counterions, can be greater than in the solution. As a consequence, pH within the brush layer can be lower than the pI of interacting protein. This effect can even lead to a charge reversal of a given protein promoting the protein adsorption onto PE brushes.[3,203] Clearly due to the role of charge-charge interaction the protein adsorption highly depends on the overall ionic strength, which fact was proven for planar and spherical PE brushes.[173–175,204–206]

3.3.2.1.5. Counterion Release in PE Brushes

It was found that positively and negatively charged patches on the protein surface interact with PE brush with a significant asymmetry. In particular, positively charged patches are attracted whereas negatively charged patches are repelled. This pattern manifested for PE brushes on any morphology. The observed protein binding to a like-charged PE brush at low ionic strength as well as the brush resistance for such process at conditions of high ionic strength can be explained by a possible charge reversal of the adsorbed protein.[134,207] In a phenomenological approach proposed by Yigit *et al*. the total free energy of binding (w_{tot}) between protein and PE brush can be described as a sum of three major contributions: the *van der Waals* and excluded-volume interaction ($w_{exl+vdW}$), the electrostatic interaction (w_{ele}), and the counterion release contribution (w_{cr}):[82]

$$w_{tot} = w_{excl+vdW} + w_{ele} + w_{cr} \qquad (16)$$

These contributions can be in general divided into repulsive and attractive ones. Protein and PE brush should repel each other due to the electrostatic and electrosteric repulsion. Protein penetrating a PE brush causes unfavorable steric interaction with PE chains. It also raises the osmotic pressure of confined counterions. Thus binding can occur only if an attractive force is capable to overcome these repulsive contributions. In approach presented in equation (16) the

most prominent repulsive contribution is reflected by the excluded volume part which is completely dominated by osmotic contribution of the counterions. The electrostatic part takes into account the monopolar repulsion and dipolar and Born attraction. Only the latter term is strongly attractive.[208] Therefore decrease of the strength of the binding between protein and PE brush at higher salt concentration can be related to a strongly diminished counterion release effect.

3.3.2.1.6. Effect of Temperature on the Binding

With modern calorimeters, precise values of the binding constant, K_b and the free energy of binding, ΔG_b can be measured across a wide range of temperatures (errors for ΔG_b are approximately 0.4 kJ/mol for recent analysis on various protein-ligand systems).[209,210] The enthalpic and entropic contributions to the binding can be extracted from the van't Hoff analysis.

$$\frac{dlnK_b}{d(\frac{1}{T})} = -\frac{\Delta H_b}{R} \tag{17}$$

This linear relation between the logarithm of the binding constant, $ln\ K_b$ and the temperature T assumes that the heat capacity change ΔC_p of the analyzed binding process is zero.[211] Thus, the binding enthalpy ΔH_b and the binding entropy ΔS_b are temperature-independent. This assumption was often found to be too general.[212,213] Several studies on protein-macromolecule binding showed that temperature variation of ΔH_b can be quite large.[13,52] The resulting non-zero ΔC_p, can be taken within the experimental error as a constant, resulting in the following relations:[211]

$$\Delta H_b = \Delta H_{b,ref} + \Delta C_p(T - T_{ref}) \tag{18}$$

$$\Delta S_b = \Delta S_{b,ref} + \Delta C_p \ln(\frac{T}{T_{ref}}) \tag{19}$$

$$\Delta G_b = \Delta H_{b,ref} - T\Delta S_{b,ref} + \Delta C_p[T - T_{ref} - Tln\left(\frac{T}{T_{ref}}\right)] \tag{20}$$

Equation (20) is known as the nonlinear van't Hoff equation, where T_{ref} denotes a reference temperature that can be chosen and $\Delta H_{b,ref}$ and $\Delta S_{b,ref}$ represents the enthalpy and entropy of binding at that temperature, respectively. ΔH_b, ΔS_b and ΔG_b as a function of temperature are presented in **Figure 13**. T_S is defined as a characteristic temperature at which $\Delta S_b = 0$. The second characteristic temperature is T_H at which $\Delta H_b = 0$.

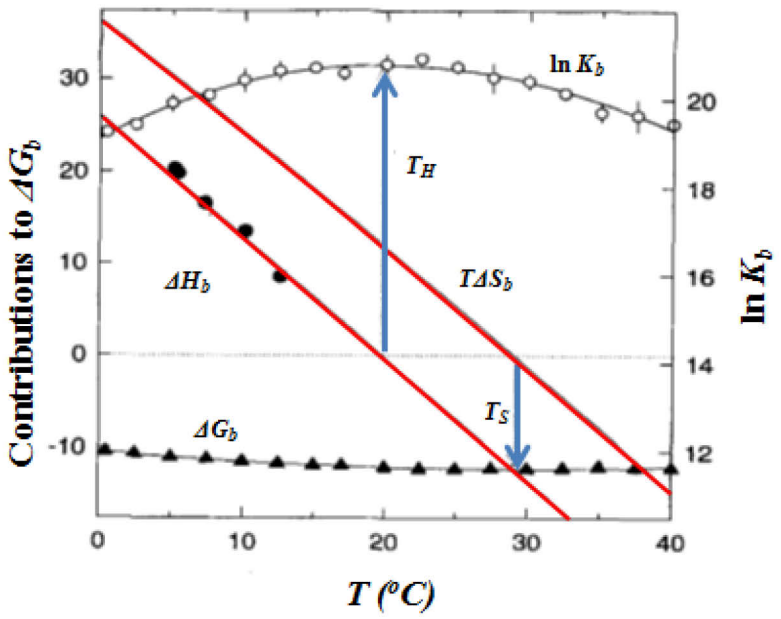

Figure 13. Thermodynamic profiles derived from studies of the site specific binding of BamHI endonuclease to DNA. Values for ΔG_b are fitted with the integrated form of the nonlinear van't Hoff equation (equation (20)). ΔH_b and ΔS_b contributions to ΔG_b are presented by solid red lines. Experimental values (●) of ΔH^{ITC} were obtained from direct calorimetric measurements. Plot is reprinted form ref.[7]

A long discussion was devoted to the questioning of the application of equation (20) to experimental data due to the observed discrepancies between binding enthalpy, ΔH_b and calorimetric enthalpy, ΔH^{ITC}.[214,215] Concerns were raised whether this discrepancies are originating from the measurement errors and methods of the analysis.[8,54,209,216] It must be stressed at this point, that ΔH^{ITC} so the directly measured heat effect upon protein-macromolecule interaction is often mistaken for the enthalpy of binding (ΔH_b). In reality ΔH^{ITC} contains several contributions of the associated effects. Following the assumption of Kozlov and Lohman, the directly measured calorimetric enthalpy can be split into:[217]

$$\Delta H^{ITC} = \Delta H_b + \Delta H_{prot} + \Delta H_{ion} \qquad (21)$$

Here ΔH_{prot} represents the enthalpy associated with the protonation of free or bound protein/macromolecule and ΔH_{ion} is the enthalpy of ionization of the buffer. In fact, equation (21) could be even expanded with ΔH_w in order to include the heat effect associated with the hydration of protein, macromolecule, protein-macromolecule complex and ions. As shown by Ran *et al.*[13] binding experiments done in two different buffer solutions allowed determination of the contribution of buffer ionization to the overall measured enthalpy. Moreover they showed that ΔH_b can be even of a different sign than ΔH^{ITC}. Nevertheless, as thoroughly discussed by Xu *et al*. the measured binding constant K_b in a properly conducted ITC experiment is a true equilibrium constant.[53] Thus, if ΔC_p can be assumed to be a constant, the equation (20) is exact. Therefore the non-linear van't Hoff analysis gives precise thermodynamic information of a given binding process.

3.3.2.1.7. Enthalpy-Entropy Cancellation

For a system characterized by a non-zero heat capacity change, ΔC_p that is much larger than the binding entropy, ΔS_b, $|\Delta C_p| \gg |\Delta S_b|$ we get the following relations:[218]

$$\Delta H_b \approx \Delta C_p (T - T_H) \tag{22}$$

$$T\Delta S_b \approx \Delta C_p (T - T_S) \tag{23}$$

$$\Delta G_b \approx \Delta C_p (T_S - T_H) \tag{24}$$

These relations clearly show that the free energy of binding, ΔG_b is approximately a constant in a range of temperatures where both the binding enthalpy, ΔH_b and the binding entropy, ΔS_b are varying linearly with T and change their sign. This is the origin of the enthalpy-entropy cancellation (EEC) meaning that enthalpic and entropic contributions to the binding compensate one another.[54,56,219,220]

Most importantly, the EEC can be related to counterion condensation. As indicated by Dragan *et al*.[28] the binding free energy can be split into:

$$\Delta G_b = \Delta G_{res} + \Delta G_{ci} \tag{25}$$

where ΔG_{res} is the residual of the Gibbs free energy of binding deriving from K_b *(1M)* (see section **3.3.2.1.3.**) and ΔG_{ci} denotes the part related to counterion release. Since counterion release is an entirely entropic effect it can be assumed that:

$$\Delta G_{ci} \approx -T\Delta S_{ci} = -\Delta n_{ci} \cdot RT \cdot \ln\left(\frac{c_{ci}}{c_s}\right) \tag{26}$$

Here ΔS_{ci} represents the change of entropy of the counterions, c_{ci} is the concentration of the condensed counterions[1,31,221] and c_s is the concentrations of counterions in the bulk.[53] Thus equation (26) demonstrates the gain of entropy related to the release of Δn_{ci} counterions from a phase with concentration c_{ci} to the bulk phase with concentration c_s. If the total binding entropy $\Delta S_b(T)$ is known for different temperatures, its residual part $\Delta S_{res}(T)$ can be obtained through:[222]

$$\Delta S_{res}(T) = \Delta S_b(T) - \Delta S_{ci}(T) \tag{27}$$

Over the years a vast number of well-controlled and precise experiments gave clear evidence that *EEC* is a general feature upon protein interaction with polyelectrolytes. Li *et al*. with an extensive set of ITC measurements of a various ligand-receptor systems show that *EEC* is a real physical phenomenon.[110] Fox *et al*. studied the possible molecular basis of *EEC* upon protein-ligand complex formation by carefully chosen model systems.[9] They showed that between similar binding processes, not intermolecular contacts but rather molecular motion and the water network rearrangement are sources of high differences in enthalpy and entropy thus leading to their compensation. Following this unexpected result Xu *at al*.[53] re-analyzed a large number of studies regarding polyelectrolyte interaction with various proteins including early work of Record and Lohman[2,164,199,201,223–226] on DNA up to most recent reports of Ran *et al*.[12,13] on charge dendrimers. They demonstrated that the observed strong *EEC* for formation of multiple PE-P complexes can be attributed to water release / uptake. As they shown the binding

or release of water molecule at 293 K gives change in ΔG_b close to zero and is accompanied by entropic contribution of approximately 6.5 kJ/mol. Thus the ΔS_b term must be compensated by concomitant ΔH_b.

3.3.2.2. Isothermal Titration Calorimetry

Isothermal Titration Calorimetry (ITC) is an experimental technique widely used in thermodynamic studies of molecular interaction in solution.[227] As it offers fast and precise measurements of the heat effect associated with biomolecular binding, ITC is an important technique in colloid and material science, drug design and biochemistry.[228–230] Due to its sensitivity ITC was used to analyze the interaction of proteins with variety of species among which synthetic and natural polyelectrolytes can be distinguish.[11–13,25,52,80,175,231]

The ITC instrument is equipped with a high precision stirring syringe (filled with one reactant in *e.g.* protein solution) and consist of two identical cells composed of a highly efficient thermal conductive material which in addition is inert to a large variety of solvents. Both cells are enclosed within an adiabatic jacket. The described setup is schematically presented in **Figure 14**. One of previously mentioned cells contains water and acts as a reference cell, while the other contains the second reactant (in *e.g.* polyelectrolyte solution). During the measurement, before each titration the microcalorimeter equilibrate these two cells at exactly the same temperature. However while injecting reactant one to the sample cell filled with reactant two (when binding occurs) the temperature difference between the sample- and the reference cell will appear. This temperature change is observed as time-dependent input that gives incremental heat change *dQ/dt(Q')* in µcal/sec. The heat sensing devices detect that temperature difference and give differential power (DP) feedback to the heaters, which compensate this difference and equilibrate the cells to the same temperature.

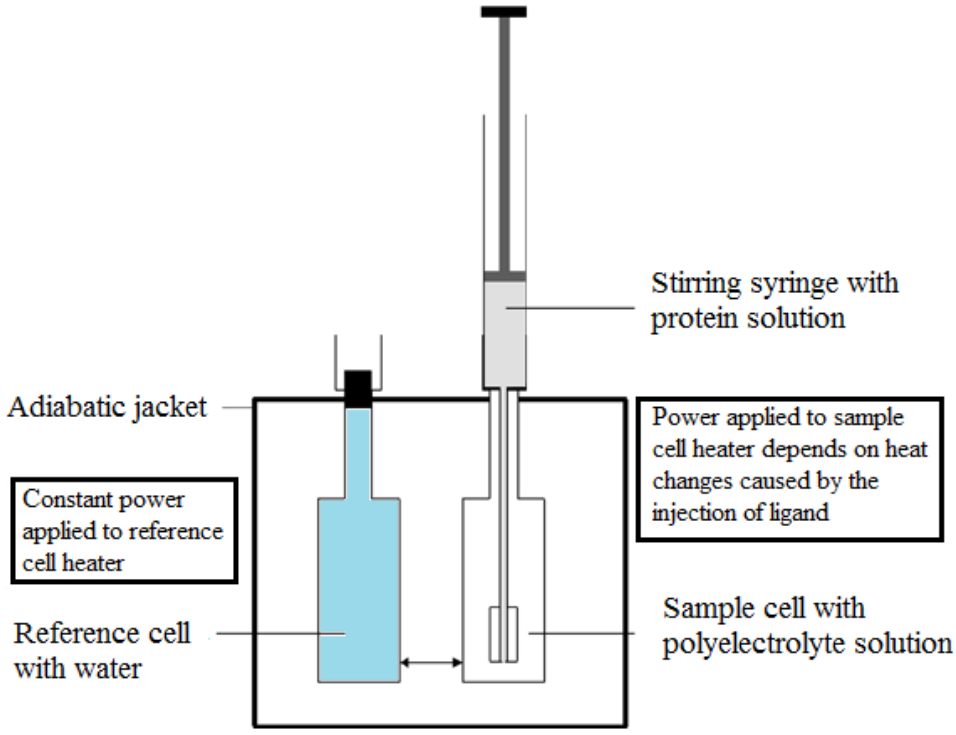

Figure 14. Schematic representation of an isothermal titration calorimeter (ITC).

During the course of experiment the reactant one placed inside of the syringe is successively titrated by several injections into the sample cell. The time-dependent evolution of heat Q upon titration compared to a reference cell is a core of the experiment. **Figure 15** presents typical ITC results of binding between protein (in this case lysozyme (Lys)) and polyelectrolyte (in this case heparin (Hep)). Integrated, with respect to the time, heats of each injection are divided by the number of moles of injectant allows to calculate the incremental heat, ΔQ as a function of molar ratio between protein and polyelectrolyte. In order to evaluate the binding data the heat of dilution of the protein has to be subtracted. Therefore a separate experiment is required. After such correction the binding signal can be fitted with an appropriate model revealing the binding constant K_b, the number of binding sites N and the calorimetric enthalpy ΔH^{ITC}.

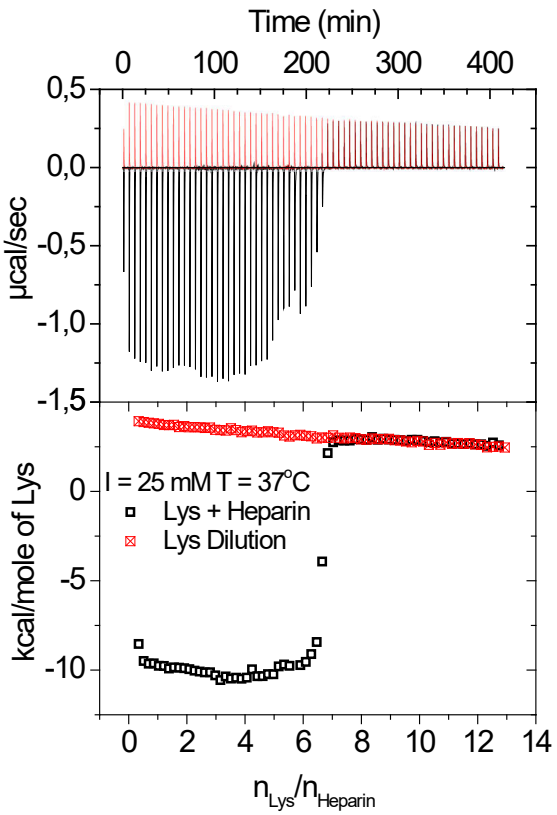

Figure 15. ITC data for the binding of Lys to Hep at pH 7.4 and temperature of 37°C in phosphate buffer solution of 10 mM ionic strength. NaCl was added in order to adjust the total ionic strength of the solution to 25 mM. The upper panel shows the raw data of the binding (black spikes) and the dilution of Lys by buffer (red spikes). The integrated heats of each injection are shown in the lower panel.

The quality of an ITC measurement depends on several different conditions. All of them can influenced the shape and therefore the quality of the ITC isotherm. The concentration of the macromolecule $[M]_t$ and protein $[P]_t$ are one of the most important issues to obtain a proper ITC measurement. Exact values of these concentrations depends on the binding mechanism and on the binding constant K_b. **Figure 16** presents a set of simulated ITC isotherms in the case when PE binds to protein with 1:1 stoichiometry.[232]

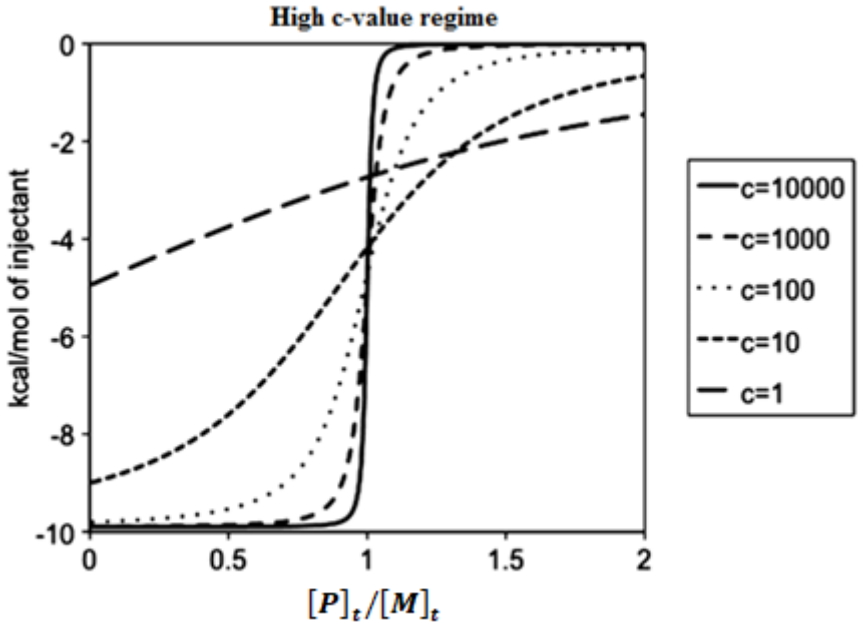

Figure 16. Simulated ITC titration curves for varying values of c-parameter and with *N* set to 1. Plot is reprinted form ref.[232]

The value of Wiseman *c*-parameter which represent the shape of the binding isotherm is determined by binding constant K_b due to the following equation:[233,234]

$$c = N \cdot K_b \cdot [M]_t \tag{28}$$

Where *N* refers to the number of binding sites of macromolecule. This simulation leads to the following conclusions: Large values of *c*-parameter leads to an accurate value of the binding enthalpy ΔH_{ITC}, but the accurate fitting of the binding constant K_b can be achieved only when $c < 500$. In the regime of very high *c*-values ($c > 500$) the shape of ITC isotherm is nearly invariant with K_b. On the other hand, at small *c* values ($c < 10$) the inflection point becomes poorly defined and the binding stoichiometry will be determined with a certain error.

3.3.2.3. Evaluation of ITC Data

3.3.2.3.1. Single Set of Identical Binding Sites (SSIS) Model

The single set of independent binding site (SSIS) model is based on the Langmuir equation.[235] It assumes equilibrium between the unoccupied binding sites within the macromolecule, the number of protein molecules in solution and the macromolecule occupied binding sites. In principal it relates the fraction of adsorption sites in macromolecule containing bound protein molecules θ to the binding constant K_b:

$$\theta = \frac{K_b[P]}{1+K_b[P]} \tag{29}$$

where *[P]* is the concentration of free protein molecules in solution. Since the total concentration of $[P]_t$ in the solution is known, *[P]* is connected to the $[P]_t$ as follows:

$$[P]_t = [P] + N\theta[M] \tag{30}$$

For macromolecule containing N adsorption sites, θ is N_b/N where N_b represents the number of protein molecules bound per macromolecule and *[M]* is the total macromolecule concentration in solution. Subtracting equation (29) into equation (30) gives

$$[P]_t = [P] + \frac{N \cdot K_b[P] \cdot [M]}{1 + K_b[P]} \tag{31}$$

Solving of equation (29) for *[P]* leads to a quadratic equation

$$\theta^2 - \theta \left[1 + \frac{[P]_t}{N[M]} + \frac{1}{NK_b[M]}\right] = 0 \tag{32}$$

The heat Q after each injection i is equal to

$$Q = [M]V_0 N \theta \Delta H^{ITC} \tag{33}$$

Solving the equation (32) for θ and then substituting this into equation (33) gives

$$Q = \frac{N[M]\Delta H^{ITC} V_0}{2}\left[1 + \frac{[P]_t}{N[M]} + \frac{1}{NK_b[M]} - \sqrt{\left(1 + \frac{[P]_t}{N[M]} + \frac{1}{NK_b[M]}\right)^2 - \frac{4[P]_t}{N[M]}}\right] \tag{34}$$

The analysis includes the effect of the increase of the volume during titration. The experimental data are fitted by calculating the heat change of the solution ΔQ_i released with each injection i and corrected for displaced volume ΔV_i

$$\Delta Q_i = Q_i + \frac{dV_i}{V_0}\left[\frac{Q_i + Q_{i-1}}{2}\right] - Q_{i-1} \tag{35}$$

The process of fitting experimental data involves initial guesses for N, K_b and ΔH^{ITC}; calculation of ΔQ_i for each injection and comparison of these values with the measured heat for the corresponding experimental injections; improvement in the initial values on the basis of the Marquardt methods. The iteration of the above procedure proceeds until the satisfactory fit is achieved.[236]

3.3.2.3.2. Two Sets of Independent Binding Sites (TSIS) Model

This model represents the binding process in which the macromolecule has two non-identical binding sites. Each set of binding sites is characterized by a binding constants K_{b1} and K_{b2} describing the binding affinity of a ligand to the corresponding site. There are six free parameters involved in this model: The binding constants K_{b1} and K_{b2}, the molar heat of binding ΔH_1^{ITC} and ΔH_2^{ITC}, and respective number of binding sites N_1 and N_2. Each type of site is therefore characterized by its own fractional saturation θ_1 and θ_2.

Hence,

$$K_{b1} = \frac{\theta_1}{(1-\theta_1)[P]} \qquad K_{b2} = \frac{\theta_2}{(1-\theta_2)[P]} \tag{36}$$

Knowing the total concentrations of protein $[P]_t$ and the macromolecule $[M]_t$ in the solution, the unknown free protein concentration *[P]* can be related by the following equation:

$$[P]_t = [P] + [M]_t(N_1\theta_1 + N_2\theta_2) \quad (37)$$

Solving equation (36) for θ_1 and θ_2 and substituting into equation (37) gives:

$$[P]_t = [P] + \frac{N_1[M]_t[P]K_{b1}}{1+[P]K_{b1}} + \frac{N_2[M]_t[P]K_{b2}}{1+[P]K_{b2}} \quad (38)$$

Solving the equation (38) for *[P]* results in a cubic equation of the form:

$$[P]^3 + p[P]^2 + q[P] + r = 0 \quad (39)$$

where:

$$p = \frac{1}{K_{b1}} + \frac{1}{K_{b2}} + (N_1 + N_2)[M]_t - [P]_t$$

$$q = \left(\frac{N_1}{K_{b2}} + \frac{N_2}{K_{b1}}\right)[M]_t - \left(\frac{1}{K_{b1}} + \frac{1}{K_{b2}}\right)[P]_t + \frac{1}{K_{b1}K_{b2}} \quad (40)$$

$$r = \frac{-[P]_t}{K_{b1}K_{b2}}$$

Equations (39) and (40) are solved numerically for *[P]* in the calorimetric software using Newton's method once the fitting parameters N_1, N_2, K_{b1}, K_{b2} and the bulk concentrations are assigned. The values for θ_1 and θ_2 are then given by substitution of *[P]* into equation (36).
After each injection, the heat Q of the solution within the volume V_0 of the calorimetric cell is equal to:[236]

$$Q = [M]_t V_0(N_1\theta_1\Delta H_1^{ITC} + N_2\theta_2\Delta H_2^{ITC}) \quad (41)$$

The experimental data are fitted by calculating the heat change of the solution ΔQ_i released with each injection i and corrected for the displaced volume ΔV_i as described in previous section.

3.3.2.3.3. Two Component Ligand Binding (TCLB) Model

The adsorption of protein to polyelectrolyte can be generalized to the binding of any ligand to a given macromolecule. TCLB model discussed here is an extension of one component ligand binding model introduced previously by Dzubiella *et al*.[31,237,238]

Upon adsorption of N^b ligand molecules to a macromolecule, the total heat exchanged per macromolecule $H(N^b)$ is related to the heat Q measured in the ITC experiment as:

$$Q(x) = c_d V \int_0^x dx' \frac{\partial H(N^b(x'))}{\partial x'} \quad (42)$$

where c^0 is the total ligand concentration, c_d is the total concentration of the macromolecule, $x = c^0/c_d$ is the molar ratio, V is the titration volume and $N^b(x)$ represents the binding isotherm.

The differential heat $Q'(x) = dQ/dx$ measured in the ITC experiment is given as:

$$\frac{1}{c_d V} Q'(x) = \frac{\partial H(N^b(x))}{\partial N^b} \frac{\partial N^b(x)}{\partial x} \quad (43)$$

Due to the complex interactions governing the binding of a ligand to a macromolecule, a linear proportion between $H(N^b)$ and N^b is assumed:

$$H(N^b) = \Delta H N^b \quad (44)$$

where ΔH represents the heat exchanged per bound ligand.

Thus, equation (43) can be rewrite to connect the differential heat exchange measured in the ITC experiment to the binding model $N^b(x)$:

$$\frac{1}{c_d V} Q'(x) = \Delta H \frac{\partial N^b(x)}{\partial x} \quad (45)$$

For the case of two ligands *A* and *B*, respectively, when ligand *A* is titrated to the solution of ligand *B* and the macromolecule, equation (45) changes as:

$$\frac{1}{c_d V} Q'(x) = \Delta H_A \frac{\partial N_A^b(x)}{\partial x} + \Delta H_B \frac{\partial N_B^b(x)}{\partial x} = (\Delta H_A + \lambda \Delta H_B) \frac{\partial N_A^b}{\partial x} \quad (46)$$

where $x = c_A/c_d$ is the molar ration of ligand *A* to that of the macromolecule and $\lambda = \frac{\partial N_B^b(x)}{\partial N_A^b(x)}$ is an exchange ratio - assumed to be constant thorough the titration.

Equation (46) can be further rewrite as:

$$\frac{1}{\eta} \frac{\Delta Q}{\Delta x} = \frac{\Delta N_A^b(x)}{\Delta x} \quad (47)$$

where $\eta = c_d V(\Delta H_A + \lambda \Delta H_B)$ is a constant. Hence, the heat exchange associated with the i^{th} injection ($i = 1, 2, 3, .. n$) ΔQ_i is proportional to the number of bound molecules of ligand *A* $\Delta N^b{}_A(x_i)$. The amount of the ligand *A* molecules adsorbed to the macromolecule during the *i* and the following injections can be obtained thorough:

$$\Delta N_A^b(x_{i+1}) = \frac{\Delta Q_{i+1}}{\Delta Q_i} \Delta N_A^b(x_i) \quad (48)$$

The further key assumption made here are that the amount of the ligand *A* in the first injection ($i = 1$) is entirely bound to the macromolecule and that the directly measured calorimetric enthalpy ΔH^{ITC} equals to that of the binding enthalpy ΔH_b.

3.3.3. Analysis of Polyelectrolyte Brush upon Interaction with Proteins by Quartz Crystal Microbalance (QCM).

3.3.3.1. Quartz Crystal Microbalance with Dissipation Monitoring (QCM-D)

Quartz Crystal Microbalance is an analytical technique that has become widely used to study soft and solvated interfaces.[239–244] It works in liquids and provides in-situ, real-time information on changes of the material organization at interface[245] It also provides information about the coupled solvent inside of the interfacial film.[246–248] A number of information can be obtained from QCM data, in terms of the characteristics of the material distribution at an interface, its connection with the surface, and the role of the liquid in which the interfacial film is immersed.[249–251]

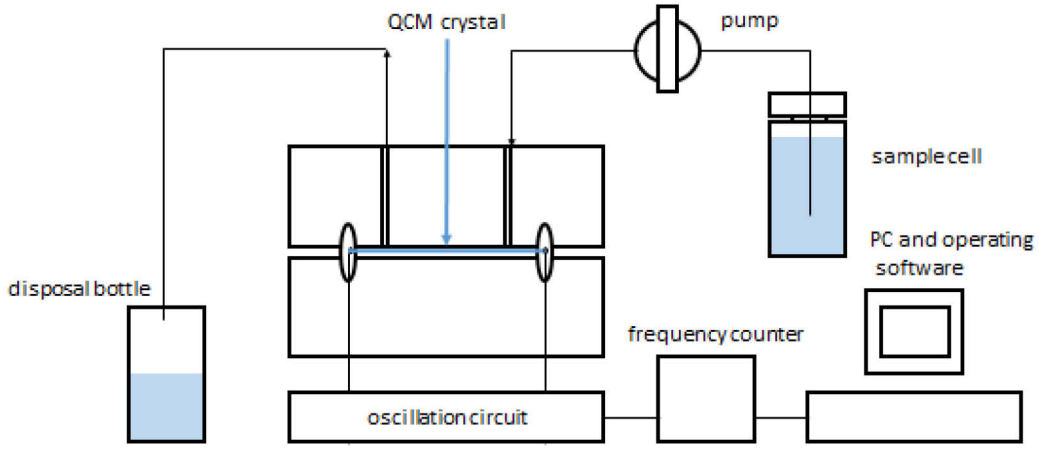

Figure 17. Schematic representation of the QCM instrumentation.

QCM is based on the inverse piezoelectric effect in which for crystalline materials characterized by a particular symmetry properties a mechanical deformation is driven by application of voltage.[252] A typical QCM sensor is composed of a thin quartz disc placed between two metal electrodes. By varying of applied voltage across the electrodes a cyclical deformation is induced, which results in an oscillatory motion of excited crystal. A standing wave arise inside the crystal if the frequency of the applied voltage matches or multiples the resonance frequency of the crystal. The kind of oscillation arising in the excited crystal depends on the cut of the crystal in regard to its crystallographic axes.[253] Sensors most commonly used in the QCM technique which are AT-cut quartz crystals vibrate in the so-called thickness-shear mode. In this type of vibration the two surfaces move relative to each other in an anti-parallel manner. When crystal is in resonance, the vibrating surfaces are located at the antinodes of a standing wave with the wavelength $2d/n$, where d is the thickness of the crystal and n represents the overtone number. This leads to the resonance frequency $f_n = nc/2d$, where c is the speed of sound in quartz. Shear-waves decay rapidly in gases and liquids, thus making QCM an interface-specific analytical technique.[244]

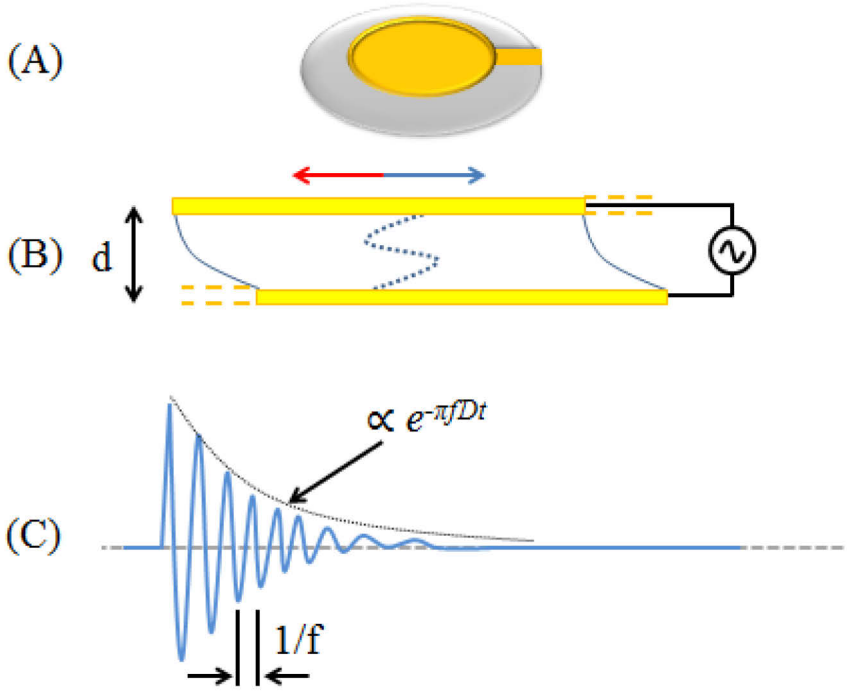

Figure 18. Schematics of QCM-D operation. **(A)** 5 MHz quartz crystal (Q-Sense). The yellow color depicts the gold electrode. **(B)** Side view of the crystal. By varying of applied voltage across the electrodes a cyclical deformation is induced, which results in an oscillatory motion of excited crystal. The third overtone (blue wave in the middle) is illustrated. **(C)** Upon QCM-D experiment the driving voltage is turned off and on, and the oscillation decay is monitored.

Upon QCM-D experiment an external voltage is turned off and on, so the oscillations are left to decay freely.[254] Due to the piezoelectric properties of quartz, these freely decaying mechanical oscillations generate a voltage. This signal is recorded and yields two parameters per overtone, the resonance frequency f_n and the dissipation D_n. The common usage of quartz crystals as oscillators results from their low energy dissipation and exceptional stability. The described basics of the QCM measurement require an electrode coating of the crystal.

The most important property of QCM technique in the context of the present work is its sensitivity in regard to the organization of the material at a given interface. As example distinction between a layer of adsorbed liposomes by optical mass-sensitive techniques such as surface plasmon resonance (SPR) or ellipsometry renders a difficult task.[244] Such distinction is facile with QCM technique. QCM is able to distinguish between layers of monomeric proteins and protein aggregates,[251] monomeric and clustered membrane-bound proteins,[249] surface-grafted DNA molecules with different organization pattern[255] *etc*.

3.3.3.2. Evaluation and Interpretation of QCM-D Data

The common use of quartz crystals as microbalances is due the linear relationship between changes in the mass per unit area of the resonator, Δm_f and the resonance frequency at the n^{th} harmonic, as defined by Sauerbrey:[256]

$$\Delta f_n = -\frac{n}{C}\Delta m_f \qquad (49)$$

The proportionality constant, C depends only on the fundamental resonance frequency and the material properties of the quartz crystal (-17,7 ng·Hz^{-1}cm^{-2} for 5 MHz crystal).[245] Kanazawa and Gordon[257] proposed how to include the role played by the liquid in which crystal is immersed. Thus, in liquids the resonance frequency of a crystal can be related with the viscosity η_l and density ρ_l of a given liquid medium:

$$\Delta f_n = -\frac{f_n}{2}\Delta D_n = -\frac{1}{C}\sqrt{\frac{n\rho_l\eta_l}{2\omega_F}} \qquad (50)$$

Here $\omega_F = 2\pi f_F$ represents the angular fundamental resonance frequency. Equation (50) presents a proportional relation between the decrease in the frequency and the increase in the dissipation to the square root of liquid viscosity and density. Due to the sensitivity of the QCM technique to the properties of the bulk liquid, it is imperative to perform a reference measurement in the same medium. In that way it is possible to separate contribution of the bulk liquid from the film properties.

In order to interpret the QCM data for a thin film in a quantitative way a several approaches have been developed over the years.[258] A common approach assumes a continuum model with sample properties parametrized by one or more elements of a certain intrinsic properties such as thickness, density and viscoelasticity as *e.g.* Voigt-Voinova model (see **Figure 19**).[259] In this model the film is characterized by four parameters: thickness, t_f, density, ρ_f, shear viscosity, η_f and shear modulus, μ_f. The bulk liquid above the film is a semi-infinite layer (η_l, ρ_l). However, a proper determination or even estimation of parameters characterizing the Vogit element can render a difficult experimental task. Moreover this approach is not applicable for films composed of discrete particles adsorbed on the surface of the crystal, where the thickness of the film is of the comparable size as the diameter of adsorbed particles.[244]

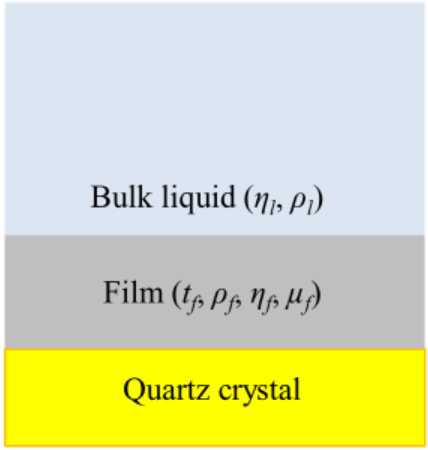

Figure 19. Schematic representation of the layered structure of Voigt-Voinova model. The QCM sensor is covered by a film modeled as a single Voigt element (grey layer). Layer above the film is a semi-infinite Newtonian liquid.

Thus, if a laterally homogenous film can be approximated as rigid the Sauerbrey equation can be used.[258] For a rigid film the changes of the normalized frequency $\Delta f_n/n$ exhibit no significant dependence on the harmonic number or more quantitatively the ratio of $\Delta D_n/(-\frac{\Delta f_n}{n}) \ll 4 \times 10^{-}$

^{7} Hz^{-1} for a 5 MHz crystal.[244] If these conditions are fulfilled the Sauerbrey equation can be used for determination of the areal mass density, Δm_f of the film. It must be kept in mind that if the film is solvated, the obtained Δm_f will include the mass of the adsorbate and of the solvent which requires a well-considered experimental approach in order to obtain the reliable data, *e.g.* reference measurements.

4. Results and Discussion

4.1. Adsorption of Mono- and Divalent Ions to dPGS

Condensed counterions are the key feature that determines the properties of PEs in solution as pointed out in section **3.3.2.1.1.** Thus, understanding the counterion condensation is crucial in order to analyse the complicate interactions of PEs in biologically-relevant systems. As a consequence of counterion condensation, the structural charge Z of PE is effectively neutralised.[260,261] Effective charge Z_{eff} of the PE is by this significantly lower in comparison to the bare structural charge Z. The difference between Z and Z_{eff} of PE therefore accounts for the amount of counterions that are condensed to it. This phenomena influences the interaction of PE with other entities,[262,263,272–274,264–271] among which the formation of PE-P complexes is the focal point in colloidal science.[16,17,19,57,58,275,276] In recent studies on dPGS-Lys interaction by Xu *et al.*[222,277] and Ran *et al.*[13] it was established that the strong binding of Lys to dPGS and formation of a protein corona around dPGS is driven by counterion release.[31] Since dPGS is a PE with promising biomedical applications[115,278,279] (see section **3.1.2.1.**), it is important to study how multivalent cations that are present in the blood serum, such as Mg^{2+} and Ca^{2+} can influence the interaction of this molecule with proteins. This justifies the suitability of studies on the competitive ion partitioning between mono and divalent counterions as it will change the Z_{eff} of dPGS influencing its interaction with proteins and other relevant components of the blood serum.

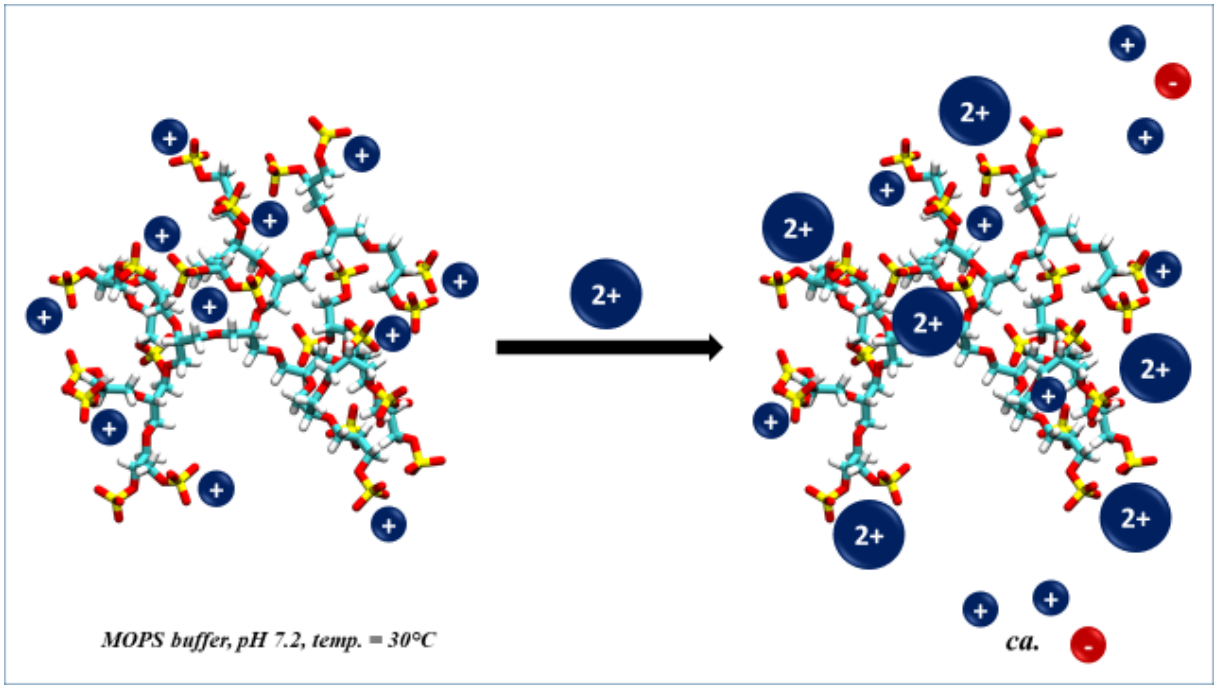

Figure 20. Schematic illustration of the competitive binding between divalent and monovalent cations to dPGS in water medium. Red and blue color indicates the negative and positive charge, respectively.

The theory discussed here was developed by Rohit Nikam in his thesis (Berlin 2020). He presented a theoretical analysis of the competition between mono- and divalent counterions upon binding to dPGS-like PEs. The author compared mean filed continuum and discrete binding models along with corse-grained computer simulations of dPGS. The presented models are fairly transferable to experimental studies thus helping in systematic analysis of the key electrostatic features of dPGS-like PEs.

In present chapter one of these models, namely the mean-field Poisson–Boltzmann (PB) model (see section **4.1.2.2.**) as it is widely used in colloidal science and electrochemistry,[280–284] is directly compared with calorimetric measurements. In order to contribute to clarification of the counterion condensation to PEs and available methods of studying this phenomena, here a 1:1 comparison of theoretical approach with experiment is presented. Firstly, the ion-specific effects upon binding to dendritic PE are analyzed by comparison of the ITC isotherms representing the Mg^{2+} and Ca^{2+} interaction with dPGS. Secondly, the competitive binding of mono- and divalent counterions to dPGS is analyzed addressing the challenges in the fitting of the binding model to the experimental data.

4.1.1. Binding Isotherms

ITC experiments were conducted on a Microcal VP-ITC instrument (Microcal, Northampton, MA). All samples used in the measurements were prepared in a buffer solution of 10 mM MOPS and such NaCl concentration to adjust a certain ionic strength after the final injection of the titrant (Mg^{2+}, Ca^{2+}). The pH of each solution was fixed to 7.2. A total of 280 µL of Mg^{2+}, Ca^{2+} buffer solution was titrated with 35 successive injections of 8 µL each into the cell containing 1.43 mL of dPGS solution. The stirring rate of 307 rpm was set with a time interval of 300 s between each injection. The concentrations of divalent ions in the injectant and the concentrations of dPGS are enlisted in the **section 6.6.** The measurements were performed at 30°C. Before each experiment all samples were degassed and thermostatted for several minutes at 1 degree below the experimental temperature.

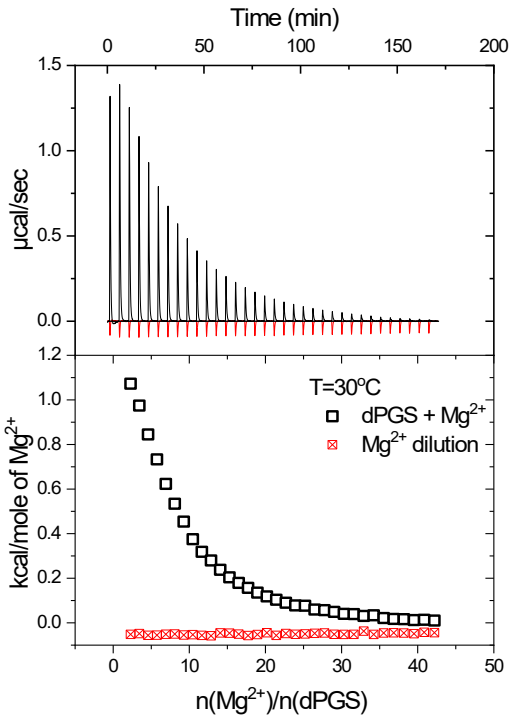

Figure 21. ITC data for the binding of Mg^{2+} ions to dPGS at pH 7.2 and temperature of 30°C in 10 mM MOPS buffer. The upper panel shows the raw data of the binding (black spikes) and the dilution of Mg^{2+} by buffer (red spikes). The integrated heats of each injection are shown in the lower panel.

The evaluation of ITC data is demonstrated in **Figure 21** which shows the raw-ITC signal of the binding (black curves and circles) and dilution of divalent-ion solution (red curves and

squares). For further analysis the heat of dilution of divalent-ions was subtracted from the heat of adsorption.

4.1.2. Analysis of the Interaction Between dPGS and Divalent Cations

4.1.2.1. Ion Specificity

After evaluation of ITC data described in section **4.1.1.** due to analyze the ion specificity upon adsorption of Mg^{2+} and Ca^{2+} to dPGS, the integrated isotherms were fitted with SSIS model (see section **3.3.2.3.1.**) as presented in semi-logarithmic plot in **Figure 22**. The thermodynamic parameters for the binding are listed in **Table 2**. All signals of the binding of divalent-ions to dPGS were endothermic in the entire range indicating that the driving force of this process is of the entropic origin.[196] Obtained thermodynamic parameters (see Table 2) show, that in the limit of error, there is no difference in binding of Mg^{2+} and Ca^{2+} to dPGS. Thus, Z_{eff} of dPGS should depend only on the valency of the condensed counterions and influence of their size (in regard to Mg^{2+} and Ca^{2+}) can be neglected. Based on that, the further analysis will be focused only on the one species of divalent-ions, namely the Mg^{2+} ions.

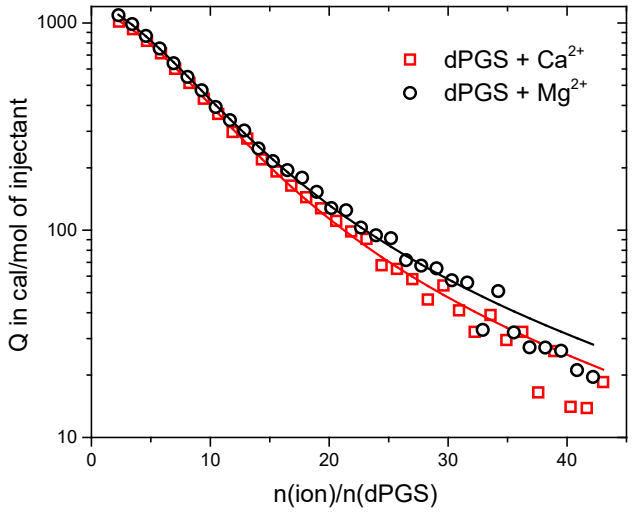

Figure 22. Binding isotherms for Ca^{2+} and Mg^{2+} interacting with dPGS. Solid lines represent the SSIS fit. Thermodynamic data resulting from the fitting are listed in Table 2.

Table 2. Thermodynamic parameters for the binding of Ca^{2+} and Mg^{2+} to dPGS as resulting from the SSIS fit.

Ion	I (mM)	N_b	ΔH^{ITC} (kJ·mol^{-1})	K_b x 10^{-3} (mol^{-1})	ΔG_b (kJ·mol^{-1})
Ca^{2+}	16,5	7,9 ± 0,2	6,8 ± 0,2	6,3 ± 0,5	-22,0 ± 0,2
Mg^{2+}	16,5	7,5 ± 0,2	8,1 ± 0,4	5,1 ± 0,4	-21,5 ± 0,2

total concentration of Mg^{2+} ions $[Mg^{2+}]^{tot}$ and Ca^{2+} ions $[Ca^{2+}]^{tot}$ is 0,8 mM.

4.1.2.2. Ion-Specific Penetrable Poisson-Boltzmann (PPB) Model

A non-linear canonical Poisson-Boltzmann penetrable sphere model is implemented to make a quantitative comparison between the number of Mg^{2+} ions bound to dPGS. In presented approach, based on recent studies,[221,285] and developed by R. Nikam dPGS is modelled as a sphere of bare radius r_d in aqueous bath of radius R and volume V.

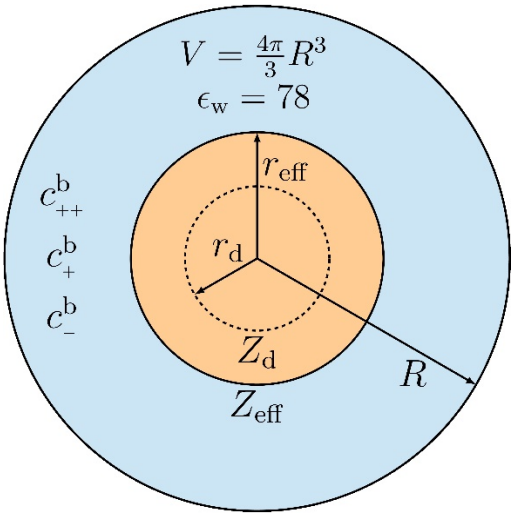

Figure 23. Schematic representation of dPGS in the PPB model. The blue area represents the computational cell domain and is assumed to be spherical with and with a uniform dielectric constant of water ε_w = 78. The volume V is the same as the titration volume in ITC experiment. Orange sphere at the center of the computational domain represents the dPGS molecule with a charge valency Z. r_{eff} is the distance that separates the electric double layer regime ($r > r_{eff}$) from the non-linear counterion condensation regime ($r < r_{eff}$). Plot is reprinted with permission from R. Nikam.

The divalent and monovalent cations as well as the monovalent anions that are present in the dPGS solution are referred to with subscripts ++, + and -, respectively. The total number of ions i (i = ++, +, -) in volume V is denoted as n_i, while the corresponding total and the bulk concentrations are denoted as $c_i^{tot} = n_i/V$ and c_i^0, respectively. c_i^0 is calculated using the conservation of mass principle as shown in the supplementary material. In order to maintain the total electroneutrality in the domain the total charge of anions is exactly balanced by the total charge of the cations. All ions and the dPGS molecule are assumed to be in an aqueous bath having a uniform dielectric constant ε_w = 78 at a temperature T = 298 K. The Bjerrum length (see section **3.3.2.1.1.**) l_B is 0.7 nm. The charge profiles are resolved in the radial distance from the macromolecular center, r. Due to the structural properties of dPGS a penetrable model is chosen instead of a standard PB model typically used in studies of colloidal charge renormalization.[286–288] dPGS is assumed to be a perfect penetrable sphere with a charge valency $Z = z_sN_s$ = -34e and radius r_{eff}. Thus, the charged monomers of dPGS have a uniform number distribution $c_s = N_s/v_{eff}$ within the volume v_{eff}. c_s is applicable only within the dPGS domain, i.e., $c_s(r) = c_s(1 - H(r - r_{eff}))$, where $H(r)$ is the heaviside-step function. As an improvement to the standard PB model, here a contribution of the intrinsic ion-specific interaction $\Delta\mu_{int,i}$ between the ion and the dPGS is considered.[289,290] $\Delta\mu_{int,i}$ represents the additional non-electrostatic effects that can drive adsorption, *e.g.,* dispersion, hydration and hydrophobic forces and can be interpreted as the ion-specific binding chemical potential of the condensed ion. The inclusion of $\Delta\mu_{int,i}$ has been considered in previous works, for example, as a term reflecting the steric ion-ion packing effects in a Donnan model for ion binding by polyelectrolytes or charged hydrogels.[291–293] Assuming the electrostatic potential far away from

dPGS, $\Phi(r \to R) = 0$, the chemical potential is balanced for each ion, between the bulk regime far from dPGS and the regime at the finite distance r from the center of dPGS:

$$lnc_i^0 = z_i\Phi(r) + lnc_i(r) + \beta\Delta\mu_{int}, i(r) \quad (51)$$

where $\beta^{-1} = k_BT$ is the thermal energy and $\Delta\mu_{int,i}$ is considered on a local level, *i.e.*, $\Delta\mu_{int,i}(r) = \Delta\mu_{int,i}(1 - H(r - r_{eff}))$. The Boltzmann ansatz then becomes:

$$c_i^0(r) = c_i^0 e^{z_i\Phi(r) - \beta\Delta\mu_{int,i}(r)} \quad (52)$$

The distance-resolved electrostatic potential can be calculated from equation (52) together with the Poisson equation as:

$$\nabla^2\Phi(r) = -4\pi l_B(\sum_i z_i c_i(r) + z_s c_s(r)) \qquad \forall\, i = ++, +, - \quad (53)$$

which establishes the PPB model including ion-specific binding effects. The boundary conditions used are $(d\Phi = dr)(r \to 0) = 0$ and $\Phi(r \to R) = 0$. The number of bound ions of species i within the dPGS radius r_{eff}, is then given by:

$$N_i^b = \int_0^{r_{eff}} c_i(r) 4\pi r^2 dr \;\forall\, i = +, ++ \quad (54)$$

4.1.2.2. Comparison of ITC Data with PPB Model

Experimental data evaluated according to the two component ligand binding (TCLB) model described in section **3.3.2.3.3.** are plotted in **Figure 24** and **Figure 25**. In both, the number of adsorbed Mg^{2+} ions per dPGS molecule is presented as a function of total moles of Mg^{2+} normalized per total moles of dPGS, n_{++}/n_{dPGS}. As shown in Figure 24, PPB model with the ion-specific intrinsic binding chemical potential $\Delta\mu_{int,i}$ set to zero, predicts that from 8 to 10 Mg^{2+} ions are bound per dPGS molecule.

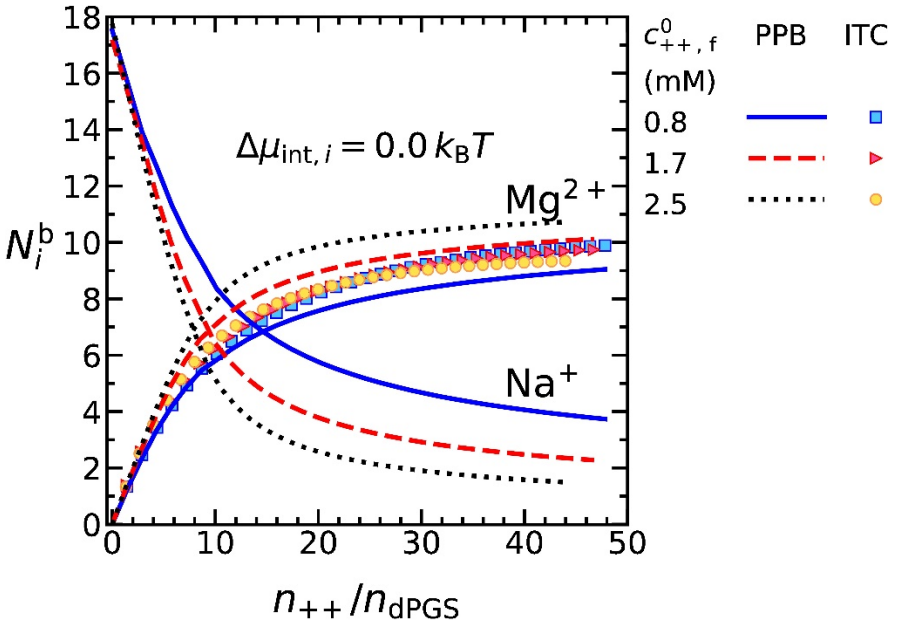

Figure 24. Number of bound counterions N_i^b ($i = Mg^{2+}, Na^+$) as a function of total amount of Mg^{2+} ions normalized per total moles of dPGS, n_{++}/n_{dPGS}. The ion-specific intrinsic binding chemical potential $\Delta\mu_{int,i}$ is set to zero.

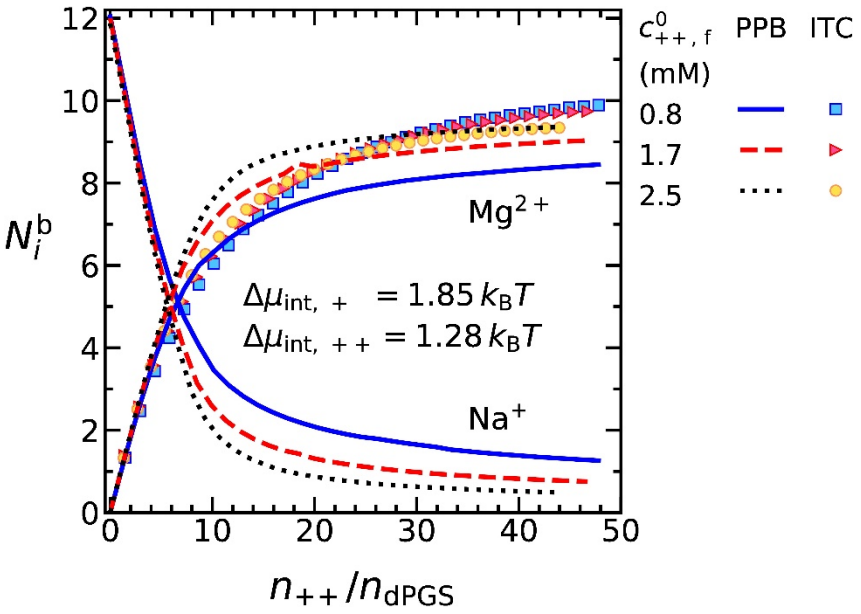

Figure 25. Fitted number of bound counterions N_i^b (i = Mg^{2+}, Na^+) from PPB model to that from TCLB model, as a function of total amount of Mg^{2+} ions normalized per total moles of dPGS, n_{++}/n_{dPGS}. The ion-specific intrinsic binding chemical potentials for both monovalent and divalent counterions are calculated as $\Delta\mu_{int,+}$ = 1.63 k_BT and $\Delta\mu_{int,++}$ = 1.18 k_BT.

When $\Delta\mu_{int,i}$ for both, monovalent and divalent counterions is calculated as $\Delta\mu_{int,++}$ = 1.28 k_BT and $\Delta\mu_{int,+}$ = 1.85 k_BT as presented in Figure 25, the obtained number of bound Mg^{2+} ions becomes slightly narrowed (from 8 to 9). On both figures a clear and systematic correlation between increasing concentration of Mg^{2+} ions and the number of bound Mg^{2+} ions per dPGS molecule is evident.

The outcome of theoretical predictions can be directly compared with experimental results displaying a similar trend and with the limit of error, the same number of bound divalent-ions. Regardless of $\Delta\mu_{int,i}$, ITC results in Figure 24 and 25 show that approximately 9 to 10 Mg^{2+} ions are bound per dPGS molecule. This number stands in a very good agreement with theoretical predictions. However, experimental results do not show a clear correlation between the number of bound Mg^{2+} and its concentration. This is caused by the limitations of the VP-ITC calorimeter on the one hand, and the assumptions involved in the TCLB model (see section **3.3.2.3.3.**) on the other. It must be kept in mind that the interaction discussed here is an example of low binding affinity. Thus, the accuracy of calorimetric measurements in this case is limited to the number of bound Mg^{2+} ions. The distinction between the solution of higher Mg^{2+} concentration in a range between 0.8 and 2.5 mM is, unfortunately, too subtle for the VP-ITC calorimeter. Most importantly, the TCLB model assumes that the calorimetric enthalpy ΔH^{ITC} is equal to the binding enthalpy ΔH_b. As pointed out in section **3.3.2.1.6.** calorimetric enthalpy contains, in addition to ΔH_b, several contributions of the associated effects. However, the observed agreement between experimental and theoretical results justify the assumption made here and suggest that the heat effects associated to the heat of adsorption in the analyzed system are marginal. Nevertheless, as discussed in section **3.3.2.1.6.** and as will be shown in the following sections, ΔH^{ITC} can significantly differ from ΔH_b. Thus, special attention must always be paid upon assumption that ΔH^{ITC} equals ΔH_b.

4.1.2.3. Conclusion

This chapter present a direct comparison between calorimetric measurements and computer simulations on the interaction of dPGS with divalent and monovalent ions in aqueous solution. The calorimetric measurements show that the ion-specific effects are marginal with regard to Mg^{2+} and Ca^{2+} ions upon binding to dPGS. The overall number of Mg^{2+} ions adsorbed per dPGS molecule obtained by ITC experiment stands in a very god agreement with theoretical predictions of the PPB model. Since PPB model gives a relatively accurate picture of the dPGS-counterion electrostatic binding affinity, the reported approach is envisioned to become applied in the future analysis of counterion condensation and interactions between various different PEs and proteins.

4.2. Protein Adsorption to Heparin

Heparin is a glycosaminoglycan (GAG) consisting of disaccharide units with different sulfation patterns, as discussed in section **3.1.1.1.** It often serves as a model for the heparan sulfate polysaccharide components of proteoglycans.[37] In general, GAG-based materials receive increasing attention for their therapeutic application in sequestering or defined delivery of cytokines and growth factors.[294] A quantitative understanding of the interaction of GAGs with proteins is a critical condition for tailoring the functionality of the related systems.

While the binding of proteins to heparin is often considered non-specific, the term "intermediate specificity" was suggested to account for the correlation of sulfation patterns to protein binding.[295] Moreover, GAG chain conformations have been discussed to result in the disposition of charged moieties and a "hidden specificity". The current view is that while certain sets of GAG sulfate groups are identified to be particularly important in protein binding, the definition of minimal binding epitopes is often lacking.[295] However, it is generally agreed that well-defined pentasaccharide structures[296,297] (mimicked in synthetic oligosaccharides such as in Fondaparinux[98,298–300]) are necessary for a specific binding of the blood coagulation enzyme antithrombin and thus for heparin's anticoagulant activity.

For the present discussion, it suffices to keep in mind that one heparin repeating unit bears, on average, three sulfate groups and one carboxyl group. Hence, heparin is among the most highly charged biopolymers. Therefore, a large fraction of counterions should be condensed on the chain which is found indeed.[301,302] In a number of recent studies the effect of counterion release was studied in detail by a combination of calorimetric investigations with molecular dynamics (MD) simulations.[12,13,31,52,53,303] The ionic strength in solution and temperature are the two decisive variables.[13,53] The binding constants K_b obtained by isothermal titration calorimetry (ITC)[26,55,304,305] were compared to the results of MD-simulations on a quantitative level. Good agreement of theory and experiment was found.[31] Plots of log K_b vs. log c_s where found to be strictly linear for synthetic polyelectrolytes (PEs)[31,53] as has been found in earlier studies on biological systems.[2,23,30,306,307] Thus, these data could be extrapolated to a salt concentration c_s of 1 M where electrostatic effects should play no role anymore.[28,30,53] In this way the measured binding constant K_b and in turn the free energy of binding ΔG_b can be decomposed into a part due to counterion release and a residual part still operative at high salt concentrations.[28,53] Here the binding of lysozyme to heparin in aqueous solution is analyzed with regard to varying ionic strength and temperature. The motivation of the present study originates from recent work on

hydrogels that are capable of sequestering proteins and in particular cytokines that may prevent wound healing.[308–310]

Since the early work of Olson *et al.*[311] and of Mascotti and Lohman[306] it is well-establish that electrostatic interaction and counterion release plays a central role for the binding of proteins to heparin.[17,195,312–317] The prevalence of electrostatic interaction for the interaction proteins with heparin has been corroborated by a considerable number of subsequent investigations.[86] A number of studies suggests that counterion release should be operative since plots of log K_b vs. log c_s were found to be linear, at least at higher ionic strength.[86,195,306,311] However, this conclusion has been criticized by Dubin and coworkers[17,86,318] and there seems to be no general consensus on the main driving forces of protein binding to heparin.

To contribute to a clarification of this point, this chapter presents a comprehensive study of the binding of lysozyme (Lys) to heparin (Hep). The choice of Lys derives from the fact that this protein is stable in solution and has been used as model compound in earlier investigations.[13,31] In particular, it turned out that Lys can be used to a certain extend as model for cytokines like the selectins (see the discussion in ref.[31]). Hence, the results of the present studies can be compared to the binding constant of Lys to other PEs and may serve for a better understanding of the interaction of proteins with GAGs in general.

The following study is based on the analysis of the binding constant K_b measured by ITC as a function of salt concentration c_s and temperature T. Firstly, the binding constant K_b is analyzed solely in terms of counterion release, as devised recently.[53] A possible release or uptake of water molecules upon binding will be considered as a second entropic factor.[37–40,319,320] The comprehensive analysis of K_b as the function of temperature and salt concentration thus allows to discuss the marked enthalpy-entropy cancellation (EEC; ref.[4–9]) that is found for the present system.

4.2.1. Binding Isotherms

ITC experiments were conducted on a Microcal iTC_{200} instrument (Microcal, Northampton, MA). All samples used in the measurements were prepared in a phosphate buffer. For that, 3.8 mM of Na_2HPO_4 and 1.2 mM of NaH_2PO_4 were dissolved in Milli-Q water. The pH of the solution was adjusted, at room temperature (20°C), to 7.4 by addition of NaOH. In order to prepare buffers with different ionic strengths, NaCl was added into the buffer individually. A total of 39 µL of Lys-buffer solution was titrated into the sample cell with 39 successive injections. The stirring rate was set at 750 rpm with a time interval of 120 and 180 s between each injection. The sample cell contained 200 µL of Hep solution in a matching buffer. In order to obtain a full matrix of ionic strength- and temperature dependence the measurements were performed at ionic strength of: 25, 35, 50, 75 and 100 mM and temperature of: 15, 20, 25, 30, 35 and 37°C. Before each experiment all samples were degassed and thermostatted for several minutes at 1 degree below the experimental temperature. The good reproducibility of data was ensured for several factors such as the type of the calorimeter, stirring rate, time interval between each injection and the concentrations of the reactants (see section **7.3.2.**).

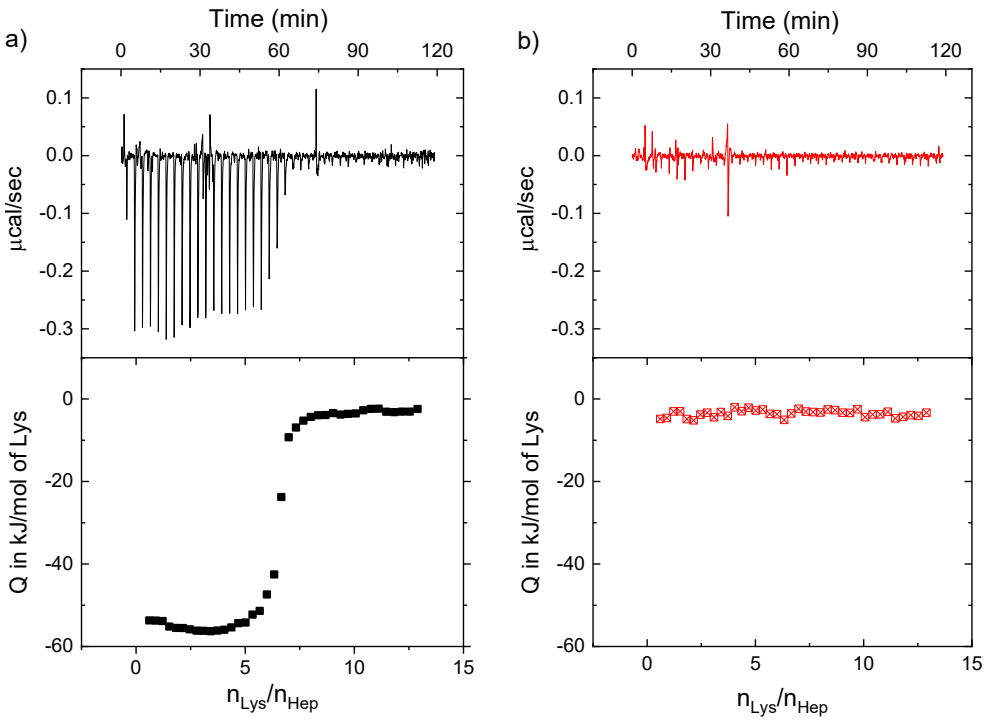

Figure 26. ITC data of the adsorption of Lys to Hep **(a)** and corresponding data of the Lys heat of dilution **(b)**. Measurements were performed at pH 7.4, I = 25 mM and T = 37°C, [Hep] = 2 x 10^{-4} mM. The upper panel shows the raw data of the adsorption and the dilution of Lys by buffer solution.

The evaluation of ITC data is demonstrated in **Figure 26 a)** which shows the raw ITC signal of binding (top panel) and Figure 26 b) presenting the dilution of protein (top panel). For further analysis the heat of dilution of the protein was subtracted from the heat of adsorption. The accuracy of the data was judged by the Wiseman parameter,[233,234] as discussed in section **3.3.2.2.** For the measurement displayed in Figure 26 (at I = 25 mM and T = 37°C) the Wiseman parameter *c* is 166.

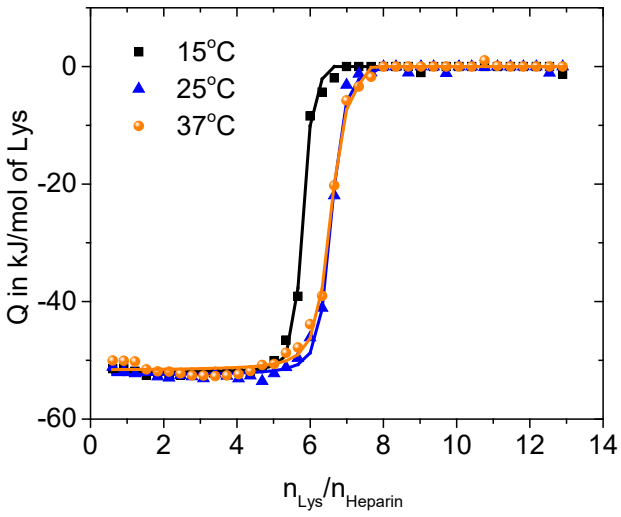

Figure 27. Effect of temperature on binding. Integrated heats of adsorption of Lys to Hep at constant ionic strength of 25 mM are displayed. Solid lines presents the single set of identical sites (SSIS) fit.

The single set of independent binding site (SSIS) model was chosen to fit all data.[235] **Figure 27** displays typical fits obtained for 3 different temperature. Additional measurements conducted at different Lys and Hep concentrations were used to ensure that the measured binding constants are independent of the concentrations of the reactants (see supplement material).

All measurements were conducted at low Hep concentrations to avoid the formation of complex coacervates.[321] Aqueous solutions of Hep of higher concentration ([Hep] = 0.01 g/L) with Lys turned turbid after 12 hours. This observation points to the onset of aggregation effected perhaps through crosslinking of complexes by Lys. The time needed for this process, however, is much larger than the time needed for the ITC-runs described here.

4.2.2. Thermodynamic Analysis of Lysozyme Binding to Heparin

4.2.2.1. Dependence of the Binding Constant K_b on Ionic Strength

All experiments were performed with a single batch of Hep purified by extensive dialysis prior to use. The molecular weight *ca.* 15.000 g/mol which amounts to *ca.* 24 repeating units per chain (average molecular weight of 580 g/mol of the heparin disaccharide unit taking into account the degree of sulfation; cf. ref[322]). The experiments were performed in a buffer solution at fixed pH of 7.4. Under these conditions both the Lys as well as the Hep carries opposite effective charges.

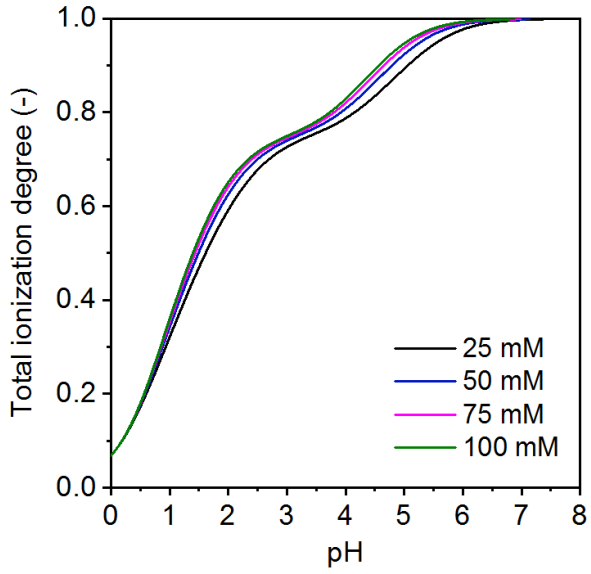

Figure 28. Total ionization degree resulting from the ionization of the sulfate and carboxyl groups of heparin as a function of the solution pH for different salt concentrations of the electrolyte. The ionization curves were calculated according to ref.[323] (for details see supplementary information) for a temperature of 37°C taking into account chain end effects on the fractional charge.[302,324]

According to theory for counterion condensation at linear polyelectrolytes developed by Manning[302,324], the fraction of charged groups (not compensated by condensed ions) of the Hep used in this study is approximately 29% to 35% (depending on the ionic strength and temperature; see the supplement) of the total number of ionizable groups. The corresponding sulfate and carboxyl groups of Hep are completely ionized at pH 7.4 (see **Figure 28**) providing the basis for electrostatic interactions with positively charged patches of Lys.

After the evaluation of the ITC data described in section **4.2.1.** the integrated isotherms were fitted with the SSIS model (see section **3.3.2.3.1.**). Figure 27 shows the ITC-diagrams for three different temperatures, the diagrams for the remaining temperatures are gathered in the supplement. **Table S2** gathers the matrix of data obtained as the function of both T and c_s.

The dependence on temperature for a given salt concentration is relatively small whereas there is a strong dependence on ionic strength. These features have been observed for a wide variety of systems where a highly charged polyelectrolyte as *e.g.* DNA is interaction with proteins.[7,28,30,218] The same behaviour was found for Lys and human serum albumin (HSA) interacting with a highly charged dendritic polyelectrolyte.[12,13,53] As discussed in previous section, this finding points to a strong EEC which phenomena will be explored further below.[53]

Table S2 shows that in average 6 Lys molecules are bound to one Hep molecule. This number is relatively constant and hardly changes with temperature or salt concentration. Thus, the complexes formed by Lys and Hep turn out to be comparable over a relatively wide range of temperature and ionic strength. Thus, Lys forms well-defined complexes with Hep which is the prerequisite for the following analysis. However, at this stage there is no further information whether the binding is taking place at random in a non-specific manner or whether there is a specific binding to well-defined pentasaccharide structures[296,297] (cf. also the discussion in ref.[86,297]).

Figure 27 shows that for I = 25 mM the calorimetric enthalpy ΔH^{ITC} is practically independent of temperature. There is a decrease of its magnitude only at the highest salt concentration under consideration here. As discussed in section **3.3.2.1.6.**,[13,53] ΔH^{ITC} can contain other contributions related to linked equilibria. Evidently, the assumption made for the two component ligand binding (TCLB) model (see section **3.3.2.3.3.**) applied in previous chapter for dPGS-Mg^{2+} interaction, is in the present case invalid. The discrepancy between ΔH^{ITC} and the binding constant ΔH_b that is observed here, shows the importance of a systematic thermodynamic analysis. The nearly vanishing dependence of ΔH^{ITC} on T and on c_s demonstrates in addition that this quantity is not directly related to the strength of binding but to a local interaction between the surface of the Lys molecules and of the Hep. Several ITC-diagrams obtained at different ionic strength are displayed in **Figure 29**. Up to a salt concentration c_s of 75 mM, very precise data can be obtained whereas the highest salt concentration leads to a Wiseman parameter of 52 (see section **3.3.2.2.**). Hence, a salt concentration of c_s = 100 mM turned out to be the highest salt concentration where data with sufficient precision can be obtained.

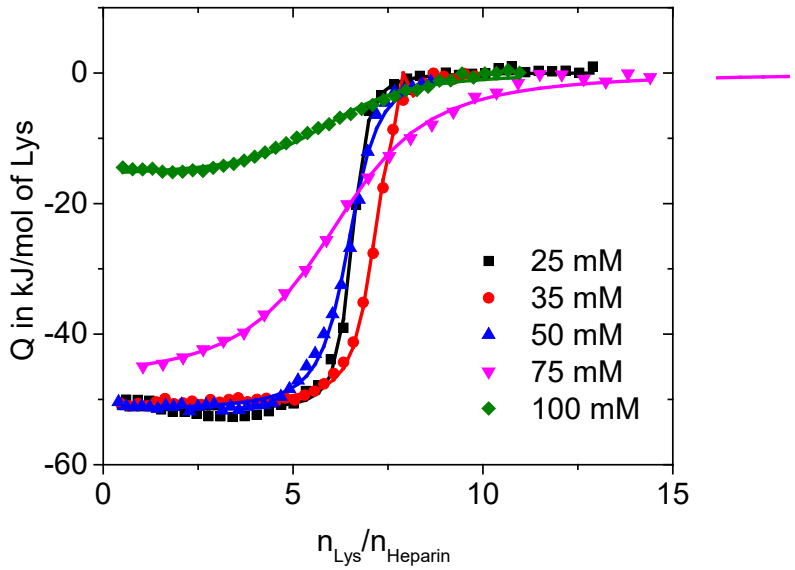

Figure 29. Effect of the ionic strength on binding. The integrated heats of adsorption at constant temperature of 37°C and four different ionic strengths are displayed. Solid lines presents the SSIS fit.

The analysis of the experimental binding constants K_b in terms of equation (13a) is shown in **Figure 30**. Here the data obtained at 25°C are shown; plots showing the data for other temperatures are given in the supplementary material. For all temperatures plots with very good linearity are obtained and fits with equation (13a) turned out to be fully sufficient. Attempts to fit these data with equation (13) indicate that these data are compatible with a number of released water molecules Δw of the order of ≤ 200. Evidently, a possible release of water molecules can have only a minor contribution to the binding free energy as it is obvious from equation (13). Hence, the present data can be evaluated by use of equation (13a) as outlined recently for the interaction of Lys with dendritic polyglycerol sulfate (dPGS).[53]

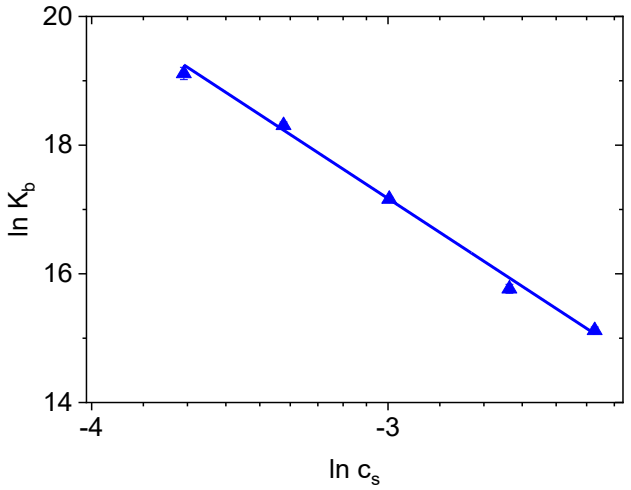

Figure 30. Dependence of the logarithm of the binding constant, *ln* K_b on the logarithm of the salt concentration, *ln* c_s at temperature of 25°C. The solid blue line represents the fit to equation (13a).

Data deriving from this analysis in terms of equation (13a) are gathered in **Table 3**. Approximately 3 ions are released per bound Lys.

Table 3. Thermodynamic parameters resulting from the fit of experimental data to equation (13a).

Temperature (°C)	Δn_{ci}	ln K_b(1M) (M^{-1})	ΔG_{res} (kJ/mol)
15	2.9 ± 0.2	9.2 ± 0.4	-22.1 ± 1.1
20	2.8 ± 0.2	9.1 ± 0.4	-22.2 ± 1.1
25	3.0 ± 0.1	8.1 ± 0.3	-20.1 ± 0.8
30	2.7 ± 0.2	8.7 ± 0.5	-22.0 ± 1.3
37	3.0 ± 0.3	7.7 ± 0.8	-19.9 ± 2.0

Δn_{ci}: net number of release counterions deriving from fits of equation (13a) to the experimental binding constants K_b; K_b (1M): Binding constant obtained by extrapolation of the experimental binding constants K_b to a salt concentration c_s of 1 M; ΔG_{res}: residual free energy as defined through equation (25), $\Delta G_{res} = -kT\ ln(K_b\ (1M))$.[53]

As indicated above, Δn_{ci} is the net release of ions and may include also the uptake of ions upon binding. As found in many previous investigations[13,30,53,303] related to counterion release, Δn_{ci} does not depend on temperature with the present limits of error. This observation is due to the fact that the release of counterions as well as the release of water molecules is a purely entropic phenomenon (cf. the discussion in ref.[320]).

The excellent linearity of plots according to equation (13a) can now be used for the extrapolation of the binding constant to the reference concentration of 1 M in order to obtain $K_b\ (1M)$. Table S2 gathers the respective results. $\Delta G_b\ (1M)$ is around -20 kJ/mol and depends hardly on temperature. A comparison with the data gathered in Table 3 shows that $\Delta G_b\ (1M)$ makes up approximately 50% of the free energy of binding.

Compared to the vast literature on the interaction of DNA with proteins (see e.g. ref. [2,7,28,30,218] and further citations given there), the number of studies considering explicitly the salt dependence of the binding of heparin to various proteins is much smaller. Olson and coworkers investigated the binding of heparin to thrombin.[311] Here straight lines in plots of log K_b versus log c_s were found and the number of released ions was found to be approximately 5.

A comprehensive investigation of the interaction of heparin with oligopeptides by Mascotti and Lohman containing basic amino acids again demonstrated that log K_b depends linearly on log c_s for the entire range of salt concentrations.[306] Two ions were released from heparin for each bound tripeptide. These authors also analysed the older literature and found that up to 6 ions are released per bound protein. In recent study of Lys binding to dPGS it was found that 3 counetrions are released per bound Lys[13,31] which compares well with the range of 2.7 – 3.0 found here. Data on the binding of fibroblast-growth-factor-2 (FGF-2) to heparin reported by Thompson *et al.*[325] similarly point at the importance of electrostatic interactions. FGF-2 is a 16 kDa sized growth factor that controls cell survival, migration and differentiation and displays an overall basic net charge with strongly positively charged patches. Thompson *et al.*[325] found that three FGF-2 molecules bind per 5 kDa heparin which would relate to nine FGF-2 bound per one 15 kDa heparin. The total binding energy of -36.4 kJ/mol per bound FGF-2 of which 30% (ΔG_{ci} = -10.9 kJ/mol) can be attributed to electrostatic effects due to the release of two to three counterions. The authors furthermore used systematic point mutations of FGF-2 which provided evidence of lysine 125 and arginine 120 contributing more than 31% of the total binding energy. Molecular modelling pointed to a distance of less than 0.3 nm of the two

charged moieties to the sulfate groups of heparin which was interpreted as a formation of two salt bridges. Thus, binding of one FGF-2 requires five to six monosaccharide units with two to three counterions released, contribute approximately -11 kJ/mol to the total binding energy. Here, the comparably sized and charged lysozyme requires eight to nine monosaccharide units for binding corresponding to the release of three counterions contributing with -20 kJ/mol to the binding energy. Thus, for both proteins the entropy gain due to counterion release effects can be concluded to contribute 30 – 50% to the total binding energy. Moreover, salt-bridge formation resulting from the release of counterions contributes to ΔG_{res}. In consequence, electrostatic interaction seems to dominate protein binding to heparin in both cases.

4.2.2.2. Dependence of the Binding Free Energy ΔG_b on Temperature

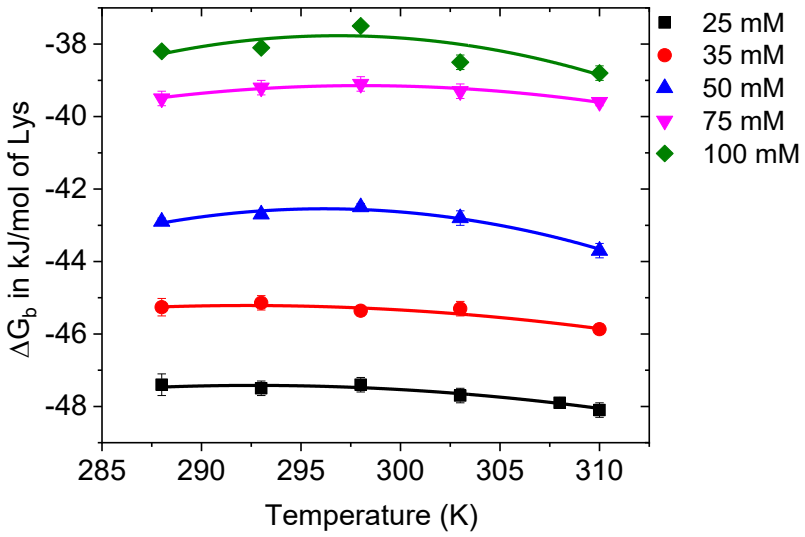

Figure 31. Dependence of the free Gibbs energy of binding ΔG_b on temperature for all ionic strengths. Solid lines represents the fits obtained from the nonlinear van't Hoff relation equation (20).

As discussed in section **3.3.2.1.6.** the dependence of ΔG_b on temperature T can be modeled by the nonlinear van't Hoff equation (20).[23,326,327] **Figure 31** displays the fits for all salt concentrations under consideration here. The respective enthalpies ΔH_b and entropies ΔS_b with the specific heats ΔC_p are gathered in Table S1. These fits are relatively robust and the resulting parameters are hardly changed by small errors of K_b. **Figure 32** displays the comparison for all thermodynamic data obtained for all salt concentrations.

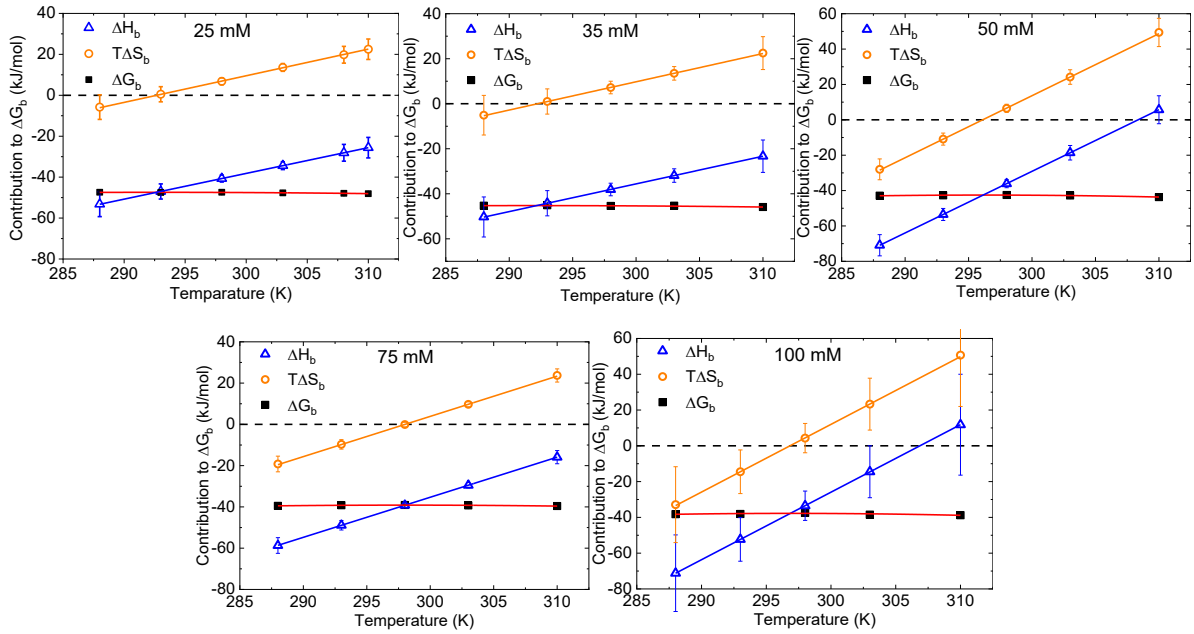

Figure 32. The thermodynamic parameters *(ΔG_b, ΔH_b and $T\Delta S_b$)* obtained for all salt concentrations as a function of temperature. All thermodynamic data deriving from these fits are gathered in Table S2.

The dependence of ΔG_b on T is hard to see whereas respective enthalpies ΔH_b and entropies ΔS_b vary strongly with temperature as predicted by equations (22) – (24). Figure 32 also demonstrates that the temperatures where ΔH_b and ΔS_b vanish, vary with salt concentration. Similar features have been found for many other systems in which PEs interact with proteins.[28,53,303]

4.2.2.3. Enthalpy-Entropy Cancellation

The present data will be analyzed as lined out in section **3.3.2.1.7.** The plot of ΔH_b against $T\Delta S_b$ for all ionic strengths under consideration here is displayed in **Figure 33 a)**. There is a marked cancellation of enthalpy and entropy which becomes much clearer when ΔH_b to $T\Delta S_{res}$ are compared: Application of equations (25) and (26) leads to $T\Delta S_{ci}$ which may be subtracted from $T\Delta S_b$ in turn to obtain $T\Delta S_{res}$ according to equation (27).[28,53] Figure 33 b) shows the resulting plot and demonstrates that all data lie on a common master curve. The resulting best fit to the data presented in Figure 33 b) is given by:

$$\Delta H_b = -20.9\ kJ/mol + 1.02 \cdot T\Delta S_{res} \qquad (55)$$

The intercept of -20.9 kJ/mol represents the average value of ΔG_{res} for all temperatures and reflects the fact that this part of the free energy of binding is independent of temperature within the present limits of error (see Table 3). The slope is 1.02 which is unity within the limits of error indicates a full compensation of enthalpy and entropy.

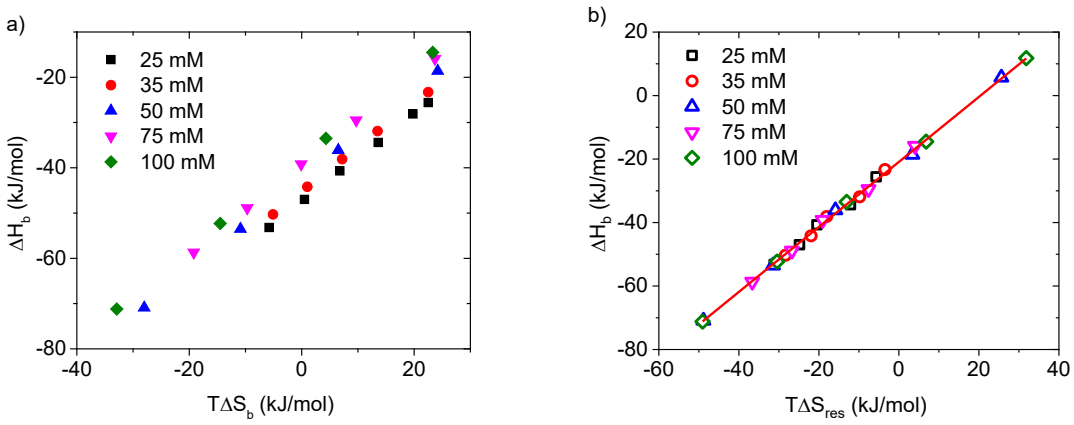

Figure 33. Enthalpy-entropy cancellation for the binding between Hep and Lys. **(a)** Enthalpy, ΔH_b is plotted against $T\Delta S_b$ for all ionic strengths. **(b)** Enthalpy, ΔH_b is plotted against $T\Delta S_{res}$ for all ionic strengths. The solid red line represents the fit by equation (55).

The same behavior was found for Lys interacting with dPGS recently[53] and for DNA interacting with various proteins.[28] Evidently, the EEC found here presents a far more general phenomenon, most probably related to changes in the water structure upon complex formation.[28] Moreover, the dissection of ΔG_b into ΔG_{ci} and ΔG_{res} is applicable to quite a number of systems.

As discussed in section **3.3.2.1.7.**, ΔG_{res} presents the part of the binding free energy ΔG_b related to factors not related to counterion release. Thus, ΔG_{res} comprise factors such as hydrogen bonding and salt bridges and reflects in many respects the specific part of ΔG_b. ΔG_{res} obtained for the binding of Lys to dPGS was analyzed by MD-simulation in detail. For this system ΔG_{res} could be rationalized mainly in terms of ion-bridging.[53] For heparin this point is in need of further studies, preferably by MD-simulations.

The foregoing discussion has pointed to the intimate relation between counterion release and the enthalpy-entropy cancellation. This connection now lead to an important conclusion regarding the driving forces of binding: Figure 32 conveys the idea that complexation between lysozyme and heparin at 25 mM and low temperature is mainly enthalpy-driven. However, data taken at higher salt concentration demonstrate that the entropic term becomes larger and larger. Thus, at $T = T_H$ (which is around 57°C for c_s = 25 mM) the binding enthalpy is zero and complexation is entirely driven by entropy. For higher c_s this temperature is even lower. Hence, the data compared in Figure 32 present only another way of showing the EEC. The thermodynamic data obtained by equation (20) should therefore be interpreted with caution.[326]

The findings presented in this section can now be compared to structural data of heparin discussed in section **4.2.2.1.**: It was found that all charged groups are ionized and that between 29 and 35% of the charges are not balanced. Minsky *et al.*[302] found for a degree of polymerization of 24 an effective charge of 37% of the structural charge (see Table 2 of ref.[302]) which fully agrees with obtained value. With 1 nm being the length of the disaccharide unit (see Figure 3) and four structural charges, b = 0.25 nm and the charge parameter ξ = 2.84 (see section **3.3.2.1.1.**). The estimate 1-1/ξ would lead to 65% of the counterions being condensed. Hence, *ca.* 2.7 of 4 counterions are condensed to the main chain and are expected to be released upon binding of lysozyme. Here, an ion release Δn_{ci} of 2.7 to 3 was found which is in fully agreement given the various approximations.

Moreover, equation (1) allows to estimate the surface concentration c_{ci} of the condensed counterions which amounts to 0.91 – 0.92 M. This concentration compares well with the one found recently for dPGS which are of the order of 1 M or of double-stranded DNA[1] which is similar magnitude. It reflects the fact that Hep is among the biopolymers with the highest charge density. It is evident that Hep interacts with proteins much in the way DNA is binding proteins. As presented in chapter **4.1.** of dPGS interaction with mono- and divalent ions, the effective charge, Z_{eff} of heparin should depend only on the valency of counterions and should not be influenced by the ion-specific effects. Evidently, the investigation of interactions between less charged, structurally differing GAGs with proteins[295,328] will certainly expand the scope and the power of engineered GAG-based materials and systems, including GAG-based antiviral therapeutics.[329]

4.2.2.4. Conclusion

Upon ITC measurements of Hep-Lys interaction two decisive variables have been changed systematically: The dependence on salt concentration c_s that leads to the net number of released counterions Δn_{ci} and $K_b(1M)$, the binding constant at a reference salt concentration of 1 M (see the discussion of eq.(13a) in section **3.3.2.1.3.**). The dependence on temperature that allows to dissect the binding free energy ΔG_b by use of eq.(20) into the respective enthalpies ΔH_b and entropies ΔS_b together with the specific heat ΔC_p. A strong enthalpy-entropy cancellation was found similar to the results for many other systems.[28,53] The binding free energy ΔG_b could be dissected into a part ΔG_{ci} due to counterion release and a residual part ΔG_{res}. The latter quantity reflects specific contributions as *e.g.* salt bridges or hydrogen bonds.[28,53] Thus, the binding of lysozyme to heparin may directly be compared to the well-studied binding of proteins to DNA. The reported approach is envisioned to become applied in the future analysis of interactions between various different GAGs and signaling proteins (cytokines, chemokines, growth factors), paving the way for the fabrication of GAG-based polymer hydrogel networks with rationally designed protein binding characteristics.

4.3. Protein Adsorption to β-CD-S

As solubilizing agents, cyclodextrins (CDs) are used in pharmaceutical industry to process liquid drugs into microcrystalline or amorphous powder, to reduce gastrointestinal drug irritation and to prevent from drug–drug and drug–excipient interactions.[102,103,330,331] The native CDs in aqueous solution undergo self-association[332,333] with the lowest solubility for β-CDs. Szejtli[334] have attributed this phenomena to the formation of the intramolecular hydrogen bonds of the β-CD rim. It was found that partial substitution of the hydroxyl groups (even by hydrophobic moieties such as methoxy-functional groups), resulted in significant increase in the aqueous solubility of β-CDs.[331] Enhanced solubility thus became the main reason for further chemical modifications of β-CDs.[335]

In recent studies, isothermal titration calorimetry (ITC) was used to investigate the complexation of β-CDs with several drugs such as: paenol,[336] acetovanillone,[336] sertaconazole[337] and ozinide anitimalarials.[338] In all cases the high binding constant ($K_b \geq 10^6$ M^{-1}) indicate a formation of strong complexes, proving high solubilizing activity of β-CDs. This studies focused on low-molecular drugs for which inclusion in the internal cavity of CDs is possible. Interaction of CDs with bigger entity was reported by Merkus *et al*.[339] The authors showed, that dimethyl-beta-cyclodextrin (DM-β-CD) can inhibit or reduce the efflux function

of P-glycoprotein (P-gp) – an efflux transporter present in the apical region of epithelial cells in the brain, liver, kidney and gastrointestinal tract.[339] However, investigation on β-CDs enhancing bioavailability and stability of high-molecular drugs as well as the detailed study on interaction between CDs and proteins have still a low recognition.

Here in order to contribute to the analysis of the interactions between β-CDs with proteins the binding of lysozyme (Lys) to highly sulfated β-CD (β-CD-S) in aqueous solution is analysed with respect to varying ionic strength. β-CD-S is a sulfated, cyclic oligosaccharide shaped of a truncated cone or torus (see section **3.1.1.2.**) and the choice of Lys as a model protein was discussed in chapter **4.2.**

The following study is based on the analysis of the binding constant K_b measured by ITC as a function of salt concentration c_s. The binding constant K_b is analyzed solely in terms of counterion release, in the same way as discussed with regard to heparin in section **4.2.2.1**.[53]

4.3.1. Binding Isotherms

ITC experiments were conducted on a Microcal VP-ITC instrument (Microcal, Northampton, MA). All samples used in the measurements were prepared in a phosphate buffer. For that, 3.8 mM of Na_2HPO_4 and 1.2 mM of NaH_2PO_4 were dissolved in Milli-Q water. The pH of the solution was adjusted, at room temperature (20°C), to 7.4 by addition of NaOH. In order to prepare buffers with different ionic strengths, additional NaCl was added into the buffer individually. A total of 280 µL of Lys-buffer solution was titrated into the sample cell with 70 successive injections of 4 µL each. The stirring rate was set at 307 rpm with a time interval of 300 and 360 s between each injection. The cell was containing 1.43 mL of β-CD-S solution in a matching buffer. The measurements were performed at 37°C. Before each experiment all samples were degassed and thermostatted for several minutes at 1 degree below the experimental temperature.

The evaluation of ITC data is demonstrated in **Figure 34** which shows the raw-ITC signal of binding (black curves and squares) and dilution of protein (red curves and squares). For further analysis the heat of dilution of the protein was subtracted from the heat of adsorption.

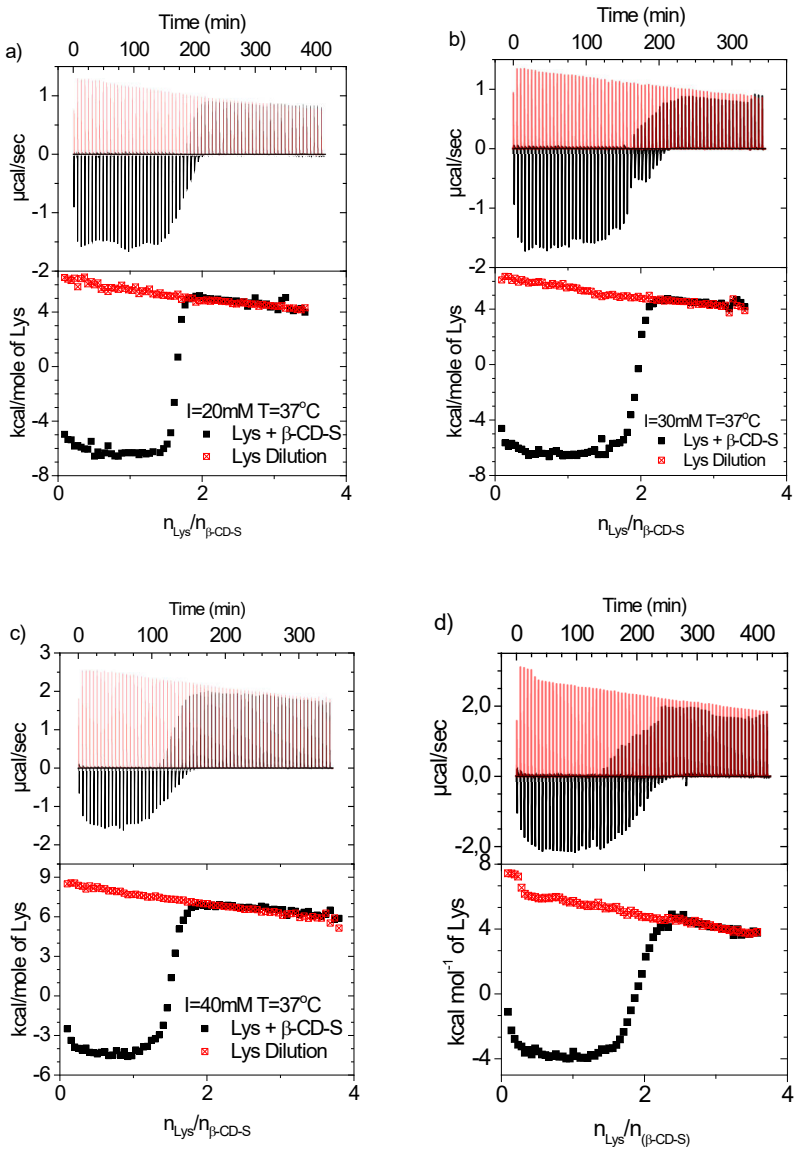

Figure 34. ITC data for the adsorption of Lys to β-CD-S at pH 7.4, **(a)** I = 20 mM, **(b)** I = 30 mM, **(c)** I = 40 mM and **(d)** I = 60 mM at T = 37°C. The upper panel shows the raw data of the adsorption (black curves) and dilution of Lys by buffer (red curves). The integrated heats of each injection are shown in the lower panel.

4.3.2. Thermodynamic Analysis of Lysozyme Binding to β-CD-S

4.3.2.1. Dependence of the Binding Constant K_b on Ionic Strength

A series of ITC experiments was performed at four different ionic strengths: 20, 30, 40 and 60 mM. The experiments were performed in a buffer solution at constant temperature of 37°C and fixed pH of 7.4. Under these conditions Lys and β-CD-S carries opposite effective charges (positive for Lys and negative for β-CD-S). The integrated isotherms were fitted with the single set of identical binding sites (SSIS) model. **Figure 35** demonstrates the SSIS data fit.

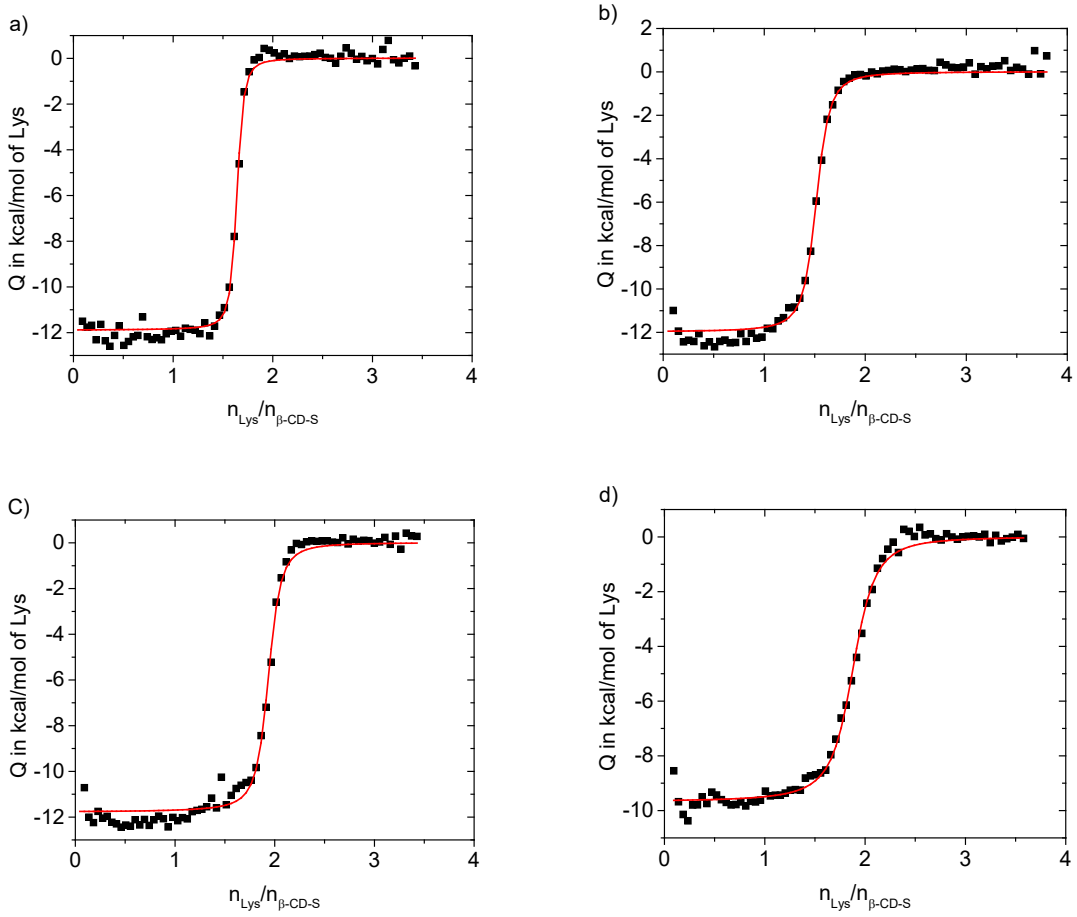

Figure 35. Integrated heats of each injection after subtraction (corrected for protein heat of dilution), **(a)** I = 20 mM, **(b)** I = 30 mM, **(c)** I = 40 mM and **(d)** I = 60 mM at T = 37°C. Red line presents the single set of identical sites (SSIS) fit.

As shown in Figure 35 at low salt concentrations (20 – 40 mM), the measured heat effect (ΔH^{ITC}) did not change significantly. The free energy of binding, ΔG_b in this case presents only small dependence on the ionic strength (see **Table 4**).

Table 4. Thermodynamic parameters resulting from the SSIS model.

I (mM)	N	K_b x 10^{-6} (M^{-1})	ΔH^{ITC} (kJ/mol)	ΔG_b (kJ/mol)
20	1.6	19.2 ± 10	-49.8 ± 0.5	-43.2 ± 1.9
30	1.9	6.6 ± 2.9	-49.3 ± 0.5	-40.5 ± 1.5
40	1.5	3.6 ± 1.7	-50.2 ± 0.7	-38.9 ± 1.8
60	1.8	0.81 ± 0.09	-40.5 ± 1.2	-35.1 ± 0.3

However, at high ionic strength of 100 mM the measured heat effect changes dramatically. Two adsorption sites are present upon binding between Lys and β-CD-S at high salt concentration, thus the binding mechanism changes with increasing ionic strength (see **Figure 36**).

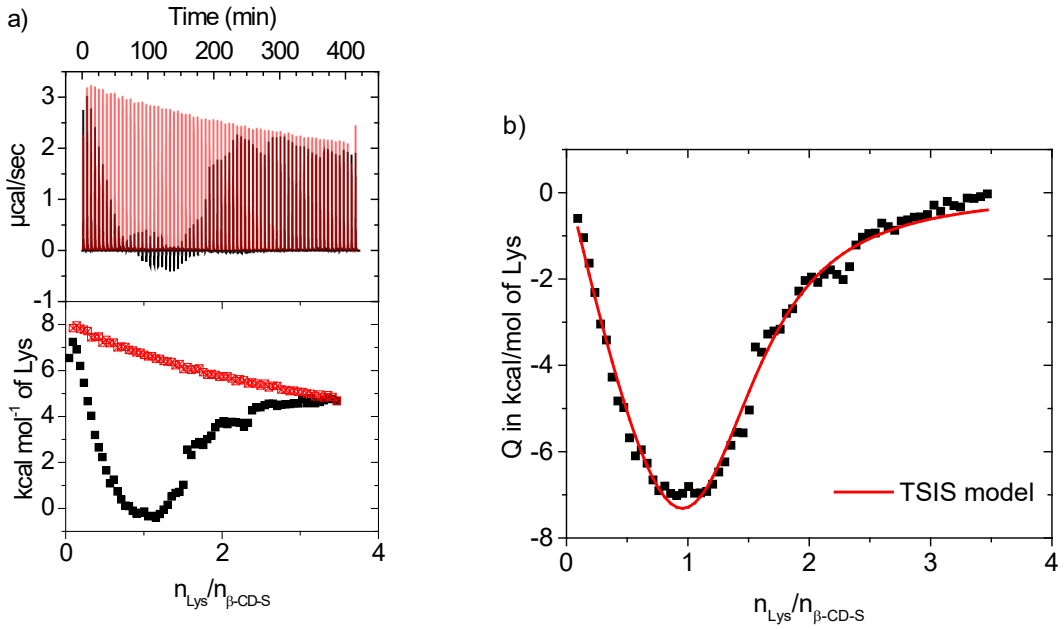

Figure 36. (a) ITC data for the adsorption of Lys to β-CD-S at pH 7.4, I = 100 mM and T = 37°C. The upper panel shows the raw data of the adsorption (black curves) and dilution of Lys by buffer (red curves). The integrated heats of each injection are shown in the lower panel. **(b)** Integrated heats of each injection after subtraction (corrected for protein heat of dilution). Red line presents the two sets of independent binding sites (TSIS) fit.

Table 5. Thermodynamic parameters resulting from the TSIS model.

I (mM)	N_1	K_{b1} x 10^{-4} (M^{-1})	ΔH_1 ^{ITC} (kJ/mol)	ΔG_{b1} (kJ/mol)
100	0.5 ± 0.2	5.6 ± 1.4	-7.8 ± 3.5	-28.2 ± 0.6
	N_2	**K_{b2} x 10^{-4} (M^{-1})**	**ΔH_2 ^{ITC} (kJ/mol)**	**ΔG_{b2} (kJ/mol)**
	0.8 ± 0.4	5.9 ± 1.1	6.2 ± 3.2	-28.3 ± 0.5

Following the analysis presented in section **4.2.2.1.**, the linear relation between *ln* K_b and *ln* c_s (see **Figure 37**) yields $\Delta n_{ion} \approx 3{,}0 \pm 0{,}2$ which means that approximately 3 ions are released upon binding of two Lys molecules to a β-CD-S.

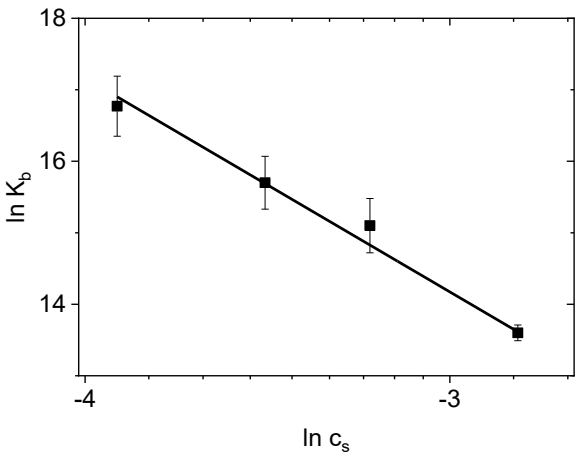

Figure 37. Dependence of the logarithm of the binding constant, *ln* K_b on the logarithm of the salt concentration, *ln* c_s at temperature of 37°C. Solid black line represents the fit to equation (13a).

4.3.2.2. Conclusion

In this chapter the dependence on salt concentration c_s on β-CD-S interaction with Lys lead to the net number of released counterions Δn_{ci} and $K_b(1M)$, (see the discussion of eq.(13a) in section **3.3.2.1.3.**). However, the investigation on β-CD-S interaction with Lys should be extended in order to verify the dependence on temperature in the same manner as discussed for Hep-Lys in sections **4.2.2.2.** and **4.2.2.3.** Such expanded analysis may lead to direct comparison to well-studied binding of proteins to DNA. The reported approach may become applied in the future analysis of interactions between CDs and various different proteins, thus enabling the fabrication of polymer drugs with enhanced solubility and rationally designed protein binding characteristics.

4.4. Protein Adsorption onto SPBs

Here, the analysis of the polyelectrolyte-protein (PE-P) interaction presented in previous chapters is extend in order to obtain the full thermodynamic information on the binding of protein to spherical polyelectrolyte brushes (SPBs). The SPB, shown schematically in **Figure 38**, consist of a solid core particle of approximately 115 nm diameter to which long PE chains are densely grafted.[16,340,341] Isothermal titration calorimetry (ITC) was used to determine the binding constants at different ionic strengths and for a range of temperatures. To ensure that the heat signal is not due to a partial unfolding upon binding, the complex was studied by Fourier transform infrared (FT-IR) spectroscopy, where changes in protein secondary structure upon adsorption to the brush layer would show up in the spectra immediately.[181,342] The analysis of all data obtained here allow to present a comprehensive discussion of the driving forces for adsorption, including the role of water in the process.

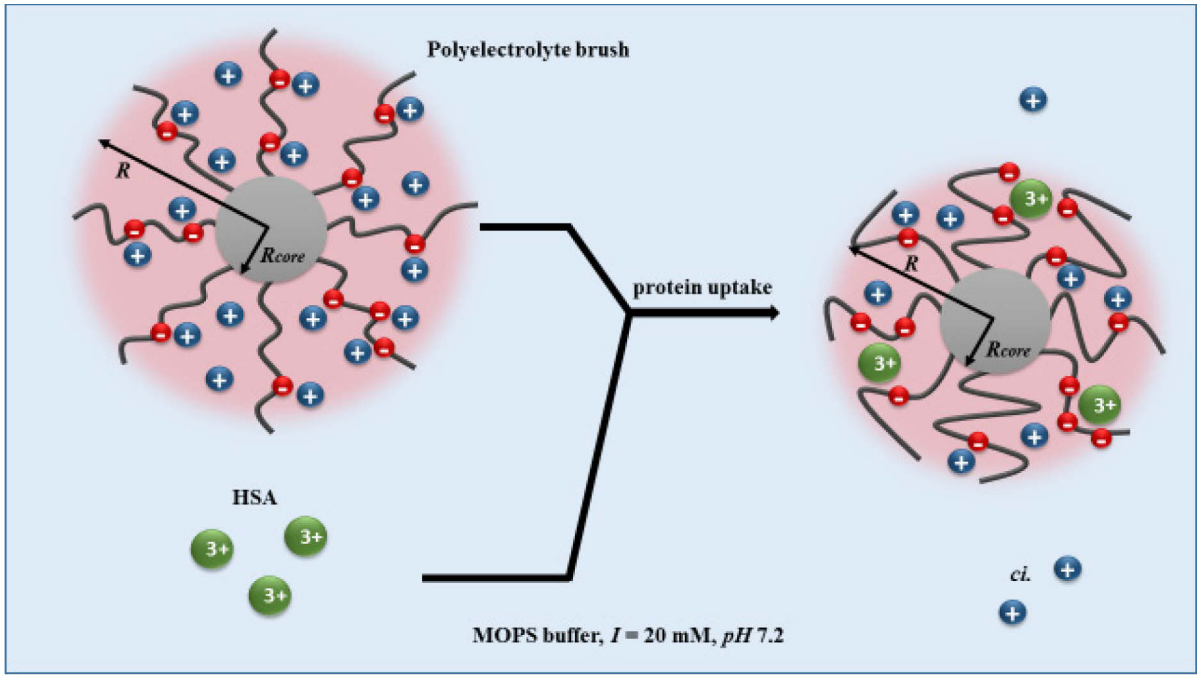

Figure 38. Schematic illustration of a spherical polyelectrolyte brush in the process of protein adsorption. The polyelectrolyte brush consist of a solid polystyrene core (grey sphere) with radius $R_{h,core} = 57\ nm$ and surface grafted poly(acrylic acid) chains. Red spheres on the PAA chains represent the negative charge of the acidic residues, while blue spheres represent the positive counterions; note the presence of condensed and free counterions within the brush layer. The HSA molecules are represented by green spheres. The radius of the brush $R = 288\ nm$ decreased after protein adsorption to *196 nm*.

4.4.1. Analysis of the Secondary Structure of Adsorbed Proteins by FT-IR Spectroscopy

The spectra of human serum albumin (HSA) before and after adsorption onto SPBs are plotted in **Figure 39**. Following the analysis discussed in section **3.3.1.** (ref.[81,181]) it is possible to identify characteristic amide I (mainly the C=O stretch) and amide II (a C-N stretching coupled with N-H bending) band maxima at 1652 and 1546 cm^{-1}, respectively

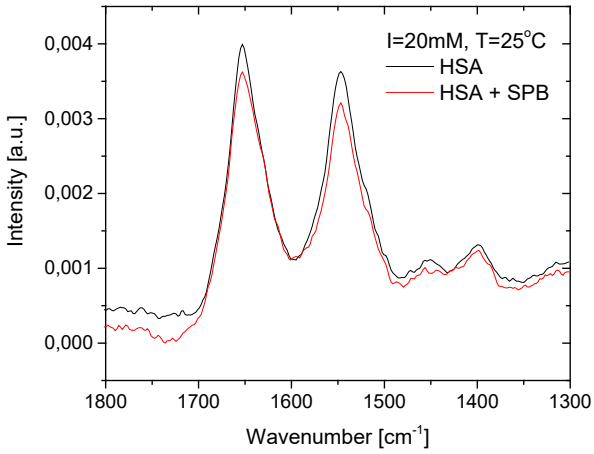

Figure 39. FT-IR spectra of free HSA (solid black line) and HSA immobilized on SPB particles (solid red line).

After adsorption onto SPBs, the peak position, peak shape and the intensity of the bands remain unchanged within the limits of error. This analysis showed no significant disturbance in the secondary structure of the protein adsorbed onto these particles. Thus the ITC-signal arises exclusively from the adsorption process and is not due to partial unfolding of the protein (see the discussion of this point in references[13,68]).

4.4.2. Binding Isotherms

ITC experiments were conducted using a Microcal VP-ITC instrument (Microcal, Northampton, MA). All samples used in the measurements were prepared in a buffer solution of 10 mM MOPS and 10 mM NaCl to adjust the ionic strength. The pH of each solution was fixed to 7.2. A total of 280 µL of HSA-buffer solution was titrated into the cell containing 1.4 mL of SPB solution in 94 successive injections of 3 µL each. The stirring rate of 307 rpm was set with a time interval of 360 s between each injection. The concentrations of HSA were as follows: 24.0 g/L; 35.0 g/L; 45.0 g/L and the concentrations of SPB varied from 1.38 to 1.84 g/L. These concentrations were chosen to obtain more data points at lower molar ratios while increasing the temperature. The measurements were performed at 25, 27, 29, 31, 33, 35, 36 and 37°C and at an ionic strength of 20 mM and 50 mM. All samples were degassed and thermostated for several minutes at 1 degree below the experimental temperature before the ITC-measurements.

The evaluation of ITC data is demonstrated for the adsorption of HSA onto SPBs at T = 27°C. Special emphasis was given to the subtraction of the heat of dilution. **Figure 40 a)** shows the raw-ITC signal of adsorption (black curves and circles) and dilution of HSA (green curves and points). The heat of dilution of HSA was subtracted from the heat of adsorption. For some cases the subtraction of the heat of dilution of HSA was insufficient.

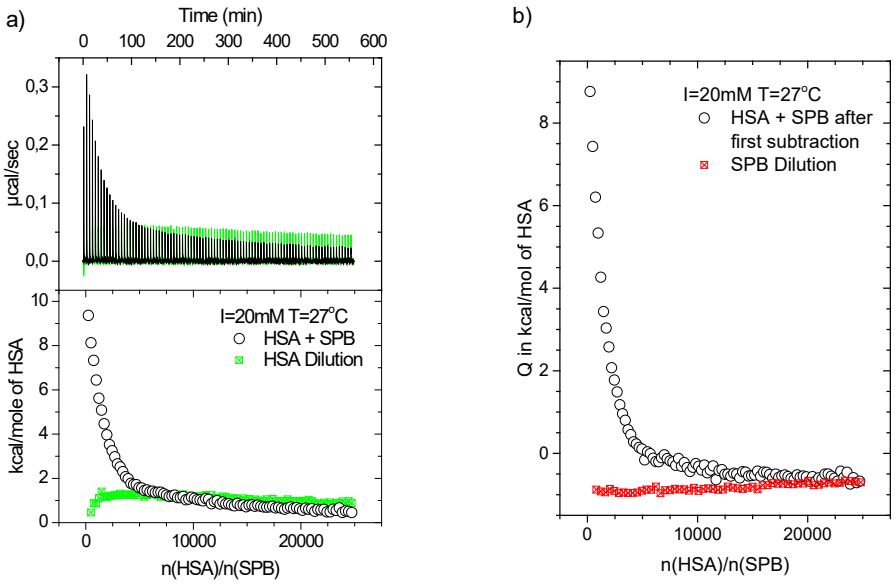

Figure 40. **(a)** ITC data for the adsorption of HSA onto SPBs at pH 7.2, I = 20 mM, T = 27°C. The upper panel shows the raw data of the adsorption of HSA onto SPBs (black curves) and the dilution of HSA by buffer (green curves). The integrated heats of each injection are shown in the lower panel. **(b)** Integrated heats of each injection after first subtraction (corrected for protein heat of dilution) (black circles) and the dilution of SPBs by buffer (red points).

At low protein concentration (*24 g/L*) a considerable heat effect caused by the heat of dilution of SPB was observed. Therefore a double subtraction for measurements performed at low protein concentration was performed. Hence, after subtracting the heat of dilution of HSA from the heat of adsorption (see Figure 40 b), black circles) the heat of dilution of SPB was subsequently subtracted (see Figure 40 b), red points). In this way ITC-measurements can be performed also under conditions in which the signal from the binding process has become rather weak.

4.4.3. Thermodynamic Analysis of HSA Interaction with SPBs

The following study is based on the analysis of the binding constant K_b measured by ITC as a function of salt concentration c_s and temperature T. Firstly, the binding constant K_b is analyzed solely in terms of counterion release, in the same way as discussed for heparin (section **4.2.2.1.**) and β-CD-S (section **4.3.2.1.**).

Under the conditions of performed ITC experiments (see section **4.4.2.**) both the HSA as well as the SPB carry a net negative effective charge. After the evaluation of ITC data described in section **4.4.2.**, the integrated isotherms were fitted with the two set of independent sites (TSIS) model and the results were compared to fit results from the single set of identical sites (SSIS) model. A semi-logarithmic plot was used to determine the best fit .[11] **Figure 41** shows that the present data are better described by the TSIS model, which assumes the presence of two different binding sites of the SPB for HSA.

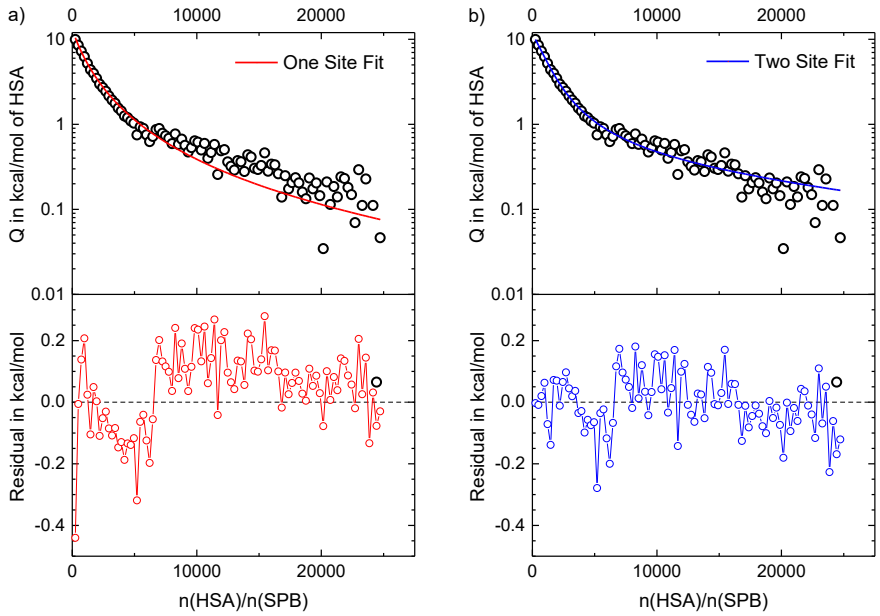

Figure 41. Binding isotherm after double subtraction (corrected for HSA-, and SPB heat of dilution) for the adsorption of HSA onto SPB at pH 7.2 (I = 20 mM, T = 27°C). The fit quality for: **(a)** SSIS model and **(b)** TSIS model are demonstrated in a semi-logarithmic plot (top panels). Lower panels depicts the residual errors for respective fits.

This finding, observed previously in the case of SPB interacting with proteins,[196] may be explained as follows: From the spherical geometry of the SPB particles two regions in the polyelectrolyte brush can be distinguished. The inner region with the higher chain density in which proteins can interact with more than one chain, and the outer region with the lower chain density in which proteins can interact with only one polyelectrolyte chain. In the present case the first binding site can be considered as the adsorption of HSA to unoccupied poly(acrylic acid) (PAA) chains of the brush. The second binding site may represent the second adsorption step when HSA binds to a PAA chain already occupied by a previously adsorbed protein. Evidently, the first binding step can be investigated with higher accuracy than the second one and the following discussion will be focused on these data. All data obtained with the TSIS model are given in Table S3 of the supplement.

4.4.3.1. Dependence of the Binding Constant K_b on Ionic Strength

To elucidate the effect of ionic strength on binding, ITC measurement at 37°C and I = 50 mM was performed. As shown in **Figure 42**, the measured heat effect decreased dramatically with increasing salt concentration. Therefore, the binding constant K_b at I = 50 mM could not be determined with sufficient accuracy.

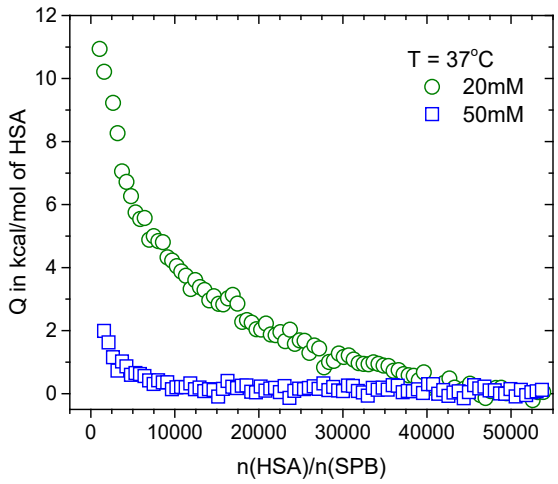

Figure 42. Effect of ionic strength on binding. The integrated heats Q of adsorption of HSA onto SPB at constant temperature of 37°C for I = 20 and 50 mM are displayed.

Such results was not observed in presented studies of heparin and β-CD-S but a similar, strong decrease of binding was reported for short linear PAA binding to HSA.[52] For higher ionic strengths, the repulsive forces between the SPB and the protein prevail and no adsorption takes place. This can be explained by the theoretical consideration presented in section **3.3.2.1.5**.[82] Since approximately the same free energy of binding ΔG_b as derived previously[52] for the interaction of free PAA with HSA was found, it can be conclude that the terms related to the brush layer cancel each other out to a good approximation. This comparison suggests that the first step of HSA binding onto SPB reflects most likely the interaction of PAA chains with the Sudlow II site of a given protein, as previously found in the analysis of HSA binding to single PAA-chains.[52]

The effect of pH on binding has been studied by Wittemann *et al*.[343] in detail. The pH was found to be an important but not decisive parameter for the protein adsorption onto SPBs. The decisive parameter is the ionic strength whereas the pH only modifies the strength of adsorption. For single polyelectrolyte chains, this problem has been studied by Dubin *et al*.[176,194] who came to comparable results. Therefore all experiments reported here were done at the optimal pH of 7.2.

4.4.3.2. Temperature Dependence of the Binding Free Energy ΔG_b

Analysis presented in section **4.2.2.2.** as well as the previous studies clearly showed that the temperature dependence of polyelectrolyte binding to protein yields the full thermodynamic information on the binding process.[3,12,13,31] **Figure 43** displays 3 ITC-isotherms, the remaining data for other temperatures are shown in Figure S15.

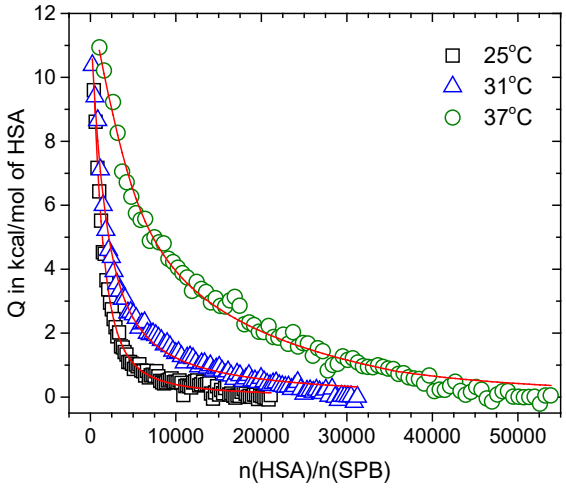

Figure 43. Effect of temperature on binding. The integrated heats, *Q*, of adsorption of HSA onto SPB at temperatures between 25°C and 37°C at I = 20 mM and the respective fits are shown. To improve clarity, data for only 3 temperatures are displayed.

Figure 43 shows that the overall calorimetric enthalpy becomes stronger with increasing temperature. The heat ΔH_i^{ITC} measured directly by ITC increases approximately linearly with increasing temperature (Figure S17) and reveals a significant positive heat capacity change $\Delta C_{p1ITC} = 13.7 \pm 1.6\ kJ{\cdot}mol^{-1}{\cdot}K^{-1}$ for the first step of binding and $\Delta C_{p2ITC} = 6.9 \pm 1.7\ kJ{\cdot}mol^{-1}{\cdot}K^{-1}$ for the second step of binding. The results of the fits are listed in the Table S4.

Figure 44 a) displays the measured binding free energy ΔG_b for the first and the second (Figure S18) adsorption step, and clearly shows the nonlinear temperature dependence of ΔG_b. The solid lines represents the best fits to equation (20). The thermodynamic parameters involved in HSA binding onto SPB were derived by analysis with the nonlinear van't Hoff equation (equation (20)) and the resulting values of ΔS_b, ΔH_b and ΔC_{pvH} are listed in Table S3. These data indicate a large positive heat capacity change $\Delta C_{p1vH} = 12.1 \pm 2.7\ kJ{\cdot}mol^{-1}{\cdot}K^{-1}$ for the first step of binding while a much lower $\Delta C_{p2vH} = 1.7 \pm 1.1\ kJ{\cdot}mol^{-1}{\cdot}K^{-1}$ is found for the second step of binding. From the well-studied phenomenon of protein binding to nucleic acids it is known that even nonspecific protein-ligand binding can lead to a positive heat capacity change due to proton uptake or dissociation and conformational change of the protein.[24] For the present system, however, a significant change of the secondary structure of an adsorbed protein can be ruled out as shown in section **4.4.1**.

Figure 44 a) presents also the temperature dependence of ΔG_b for the binding of HSA to dendritic polyglycerol sulfate (dPGS) studied by Ran *et al.* [12] and to short PAA chains as studied by Yu *et al*.[52] In all cases, a small dependence of ΔG_b is evident and arises from strong enthalpy-entropy cancellation (EEC), as will be further discussed. The same observation has been made in case of heparin and β-CD-S as well as for a large number of other biochemical systems.[23–25,28,307] Studies on the interaction of charged dendrimers with proteins are also consistent in this regard.[12,13] Figure 44 b**)** displays all thermodynamic parameters obtained for the first step of binding of HSA to the SPBs. The characteristic temperatures found for this system are, T_{1S} ~ 304 K and T_{1H} ~ 306 K.

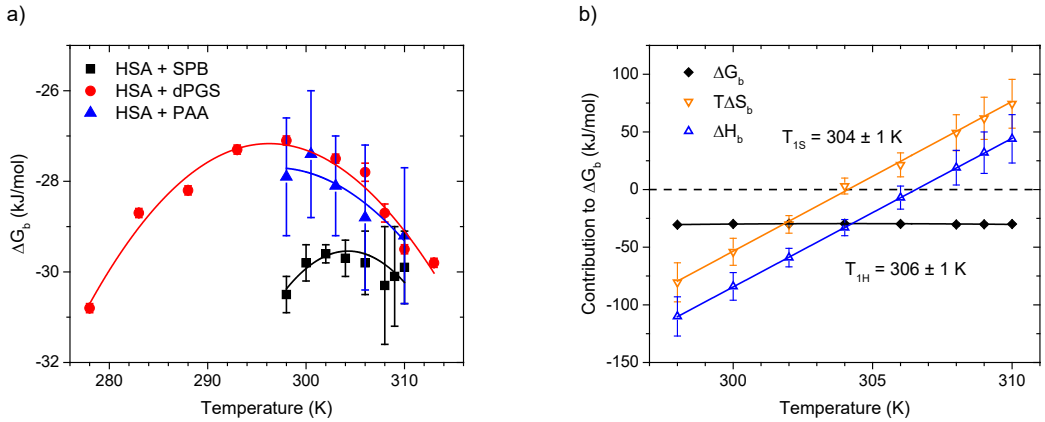

Figure 44. (**a**) Temperature dependence of the ΔG_b for the first step of binding of HSA onto SPB (black dots). Red points and blue triangles represents the temperature dependence of the ΔG_b for the binding of HSA to charged dendrimers (dPGS)[12] and short PAA chains[52], respectively. Solid lines represent the fitting obtained from the integrated form of the nonlinear van't Hoff equation (equation (20)). **(b)** Changes in the thermodynamic parameters (ΔG_b, ΔH_b, $T\Delta S_b$) that accompany the first step of binding of HSA onto SPB as a function of temperature. Black squares show the binding free energy. The solid black line shows the theoretical fit of ΔG_b (equation (20)); $T\Delta S_b$ is shown as the orange line and ΔH_b is shown as the blue line.

The discrepancies between ΔH^{ITC} and ΔH_b (see Table S4) are significant for both steps and the calorimetric values ΔH^{ITC} are greater than values resulting from the van't Hoff analysis. Similar findings were observed in the case of protein interacting with heparin (see section **4.2.2.1.**), microgels, [163] short polyelectrolytes [52] and charged dendrimers.[13] It was shown that the van't Hoff enthalpy ΔH_b can significantly deviate from the calorimetric enthalpy ΔH^{ITC} and may even change sign.[13] This discrepancy can be traced back to linked equilibria as discussed in section **3.3.2.1.6**. Expanding the analyzed system, form PEs interacting with multivalent ions (dPGS-Mg^{2+} in chapter **4.1.**), through PEs interacting with relatively small proteins (heparin-lysozyme in chapter **4.2.**) to PE brushes interacting with bulky proteins as discussed in the present chapter, the discrepancy between ΔH^{ITC} and ΔH_b from marginal becomes dramatic. Evidently, the additional contribution to ΔH_b that is related to the linked equilibria as discussed in section **3.3.2.1.6.** cannot be overlooked while considering the binding between proteins and PEs.

4.4.3.3. Contribution of Counterion-Release Entropy to the Binding of HSA

In the same way as for the binding between heparin and lysozyme, the present data will be analyzed as lined out in section **3.3.2.1.7.** The enthalpy and the entropy obtained are displayed in **Figure 45 a)**. The linearity of the data in Figure 43 a) indicates a strong EEC. The resulting fit is given by the following equations:

$$\Delta H_{b1} = -30.4\ kJ/mol + 1.0 \cdot T\Delta S_{b1} \quad (56)$$

and

$$\Delta H_{b2} = -18.3\ kJ/mol + 0.9 \cdot T\Delta S_{b2} \quad (57)$$

for the first and the second step (see Figure S20) of binding, respectively. The value of the intercept at zero $T\Delta S_{bi}$ represents the average binding free energy.

The slope close to unity indicates that the entropy factor compensates the enthalpy nearly fully over a range of ~170 kJ/mol in the first step of binding and over a range of ~20 kJ/mol in the second step of binding. Figure 45 a) also shows the comparison with the binding of HSA to

dPGS and short PAA chains, and shows that the EEC found in these systems is directly comparable to that in the present study of HSA interacting with SPBs.

In summary, it was conclude that the small dependence of ΔG_b on temperature and the concomitant EEC is indeed a general phenomenon that occurs also in more complicated systems such as the HSA binding to SPBs, as shown here. All data evaluated so far point to the fact that the binding of a protein to a PE is always accompanied by EEC.

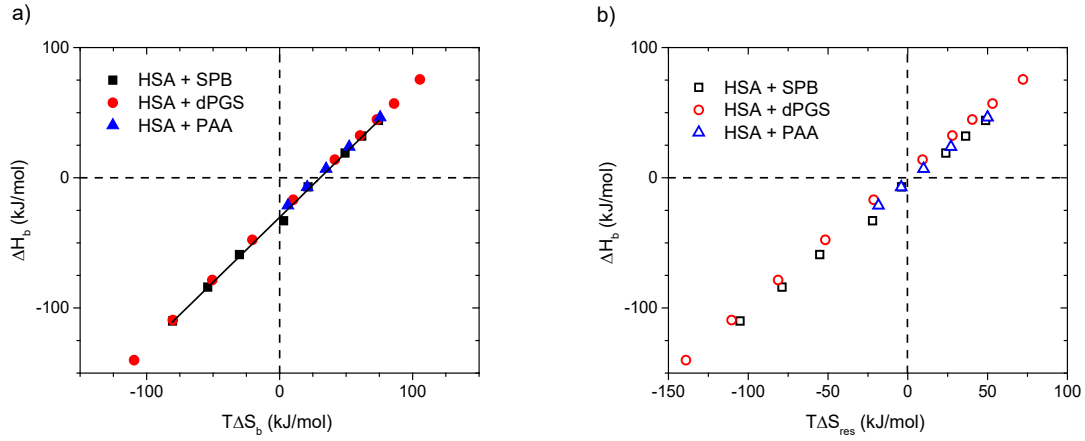

Figure 45. (a) Energetics of HSA binding to SPB. Dependence of the enthalpy, ΔH_b, on the entropy factor, $T\Delta S_b$, in the first step of binding presented as black dots. The solid black line shows the linear fit resulting from equation 50. Red points and blue triangles represent the energetics of interaction of HSA with dPGS and short PAA chains, respectively. **(b)** Enthalpy – entropy cancellation. The binding enthalpy, ΔH_b, is plotted against $T\Delta S_{res}$ according to equation (27).

Thus, the full set of thermodynamic data can be analyzed in an entirely quantitative manner as presented in section **4.2.2.4.**

As discussed above, the first step of binding observed here is related to the adsorption of one HSA molecule per PAA chain. Therefore, in further analysis the value of $\Delta n_{ci} = 3.0 \pm 0.5$, previously furnished by Yu *et al.*[52] was used. The concentration of condensed counterions on a linear PAA-chain may be estimated at ambient temperature (see section **3.3.2.1.1.**) according to Manning by:[1]

$$c_{si} = 24.3 \cdot (\xi \cdot b^3)^{-1}, \qquad (58)$$

For a PAA chain $b = 0.25$ nm. For water at 25°C, $\xi = (7.1 \cdot b^{-1})$.[1] For PAA chains under these conditions the $c_{si} \sim 0.55$ mol/L. Note, this concentration is independent of c_s.[1]

Figure 45 b) plots ΔH_b as a function of $T\Delta S_{res}$ obtained from equation (27) (see Table S5). The plot leads to comparable data for these systems. The intercept located near zero represents the average value of ΔG_{res}. Its small value demonstrates that the counterion release is the only decisive contribution that leads to the binding of HSA to short polyelectrolyte chains, charged dendrimers and SPBs.

4.4.3.4. Conclusion

Presented experiments show that HSA adsorption onto SPBs is a two-step process. Moreover, the thermodynamic analysis based on the variation of c_s and T revealed that the counterion release entropy is the main contribution to the binding free energy (ΔG_b). ITC measurements, performed over a range of temperatures between 25 and 37°C show a strong temperature dependence of the calorimetric enthalpy (ΔH^{ITC}) along with a nearly temperature-invariant ΔG_b.

A nonlinear van't Hoff analysis (according to eq. (20)) demonstrated that this system exhibits a marked enthalpy-entropy cancellation. The performed analysis thus allows a systematic comparison of the present results with heparin-lysozyme interaction discussed above (see chapter **4.2.**) as well as with a large set of data from other systems.[7,12,13,22,28,52,303] Such comparison demonstrates that a strong EEC is a general feature occurring in systems in which the binding is dominated by counterion release.

4.5. Protein Adsorption onto PPBs

In this section a quartz crystal microbalance with dissipation monitoring (QCM-D) study of human serum albumin (HSA) adsorption onto a planar poly(acrylic acid) (PAA) brush is presented. This study allows a quantitative comparison with calorimetric studies of the same problem, presented in chapter **4.4.** In that way precise structural information can be combined with thermodynamic information. The brush layer was synthesized through atom transfer radical polymerization (ATRP).[344–346] By analysis of QCM-D data based on thermodynamic study of a well-controlled model system[52] a comprehensive study on brush synthesis and its interaction with proteins is discussed. A combination of established protocols[79,347] based on varying ionic strength and changing pH was used to probe the brush response.

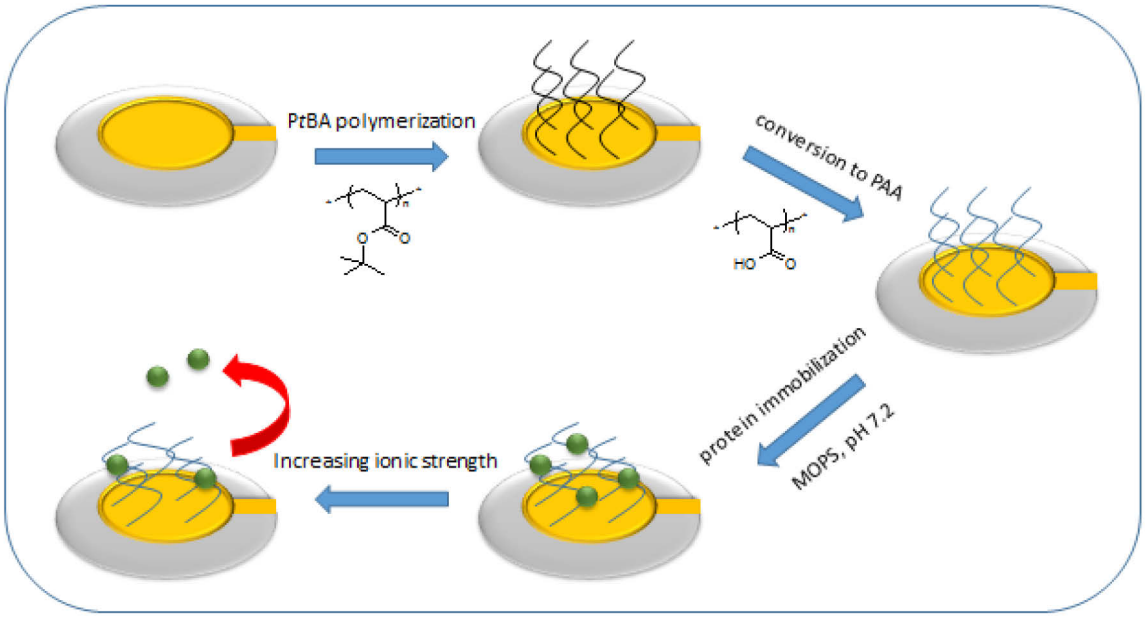

Figure 46. Schematic illustration of the gold QCM sensor functionalized with PAA chains. Green spheres represent the human serum albumin (HSA). The red arrow corresponds to the HSA desorption determined by increasing ionic strength (see section **4.5.2.**).

4.5.1. Course of Experiment

4.5.1.1. Protein Adsorption to PPBs

The QCM crystals were calibrated at constant pH of 7.2 in the buffer solution containing 10 mM MOPS buffer and 10 mM NaCl. From this point forward such buffer solutions characterized by pH = 7.2 and I = 20 mM will be called the starting buffer. The calibrated crystals were then subjected to a 5 g/L HSA suspension in the matching buffer solution (10 mM

MOPS and 10 mM NaCl) at controlled temperature of 25°C and a flow rate of 50 µL/min. Conditions of temperature and flow rate are unified for all solution used in this study. Afterwards QCM crystals were rinsed with the starting buffer.

The influence of the salt concentration was studied by a step-wise increase of ionic strength to I = 50, 75, 100 and 120 mM adjusted by NaCl added to the buffer. Afterwards QCM crystals were rinsed with the starting buffer. After the step-wise increase of the ionic strength the QCM crystals were immersed in the buffer solution of the same pH and ionic strength conditions as at the beginning of the experiment.

In the studies regarding the influence of pH the QCM crystals were then rinsed by buffer solution of constant ionic strength (20 mM) but different pH (pH = 6.5 and 7.6, respectively). In the final step the QCM crystals were rinsed with the starting buffer. After pH change, the QCM crystals were immersed in the buffer solution of the same pH and ionic strength conditions (pH 7.2 and I = 20 mM) as at the beginning of the experiment.

4.5.1.2. Response of Protein-Free Brush to pH

The QCM crystals were at first calibrated in buffer solution with ionic strength of 120 mM and pH of 7.2. After calibration, crystals were rinsed with buffer solution of I = 20 mM and pH of 7.2. In the following steps QCM crystals were rinsed with buffer solutions with pH of 6.5 and 7.6 at constant ionic strength (I = 20 mM). In the final step crystals were rinsed with buffer solution of I = 20 mM and pH 7.2.

4.5.2. Effect of Ionic Strength and pH on Protein Adsorption

The conformational response of a PAA brush with a pre-adsorbed HSA layer was studied as a function of increasing salt concentration and changing pH. The course of experiment is described in section **4.5.1.1.**

Protein adsorbed strongly onto a-like charged PAA brush as indicated by the large Δf shift in step I (see **Figure 47**). Correspondingly, ΔD increased sharply at first but then, after reaching a maximum, dissipation started to decrease. This likely suggests that HSA at first accumulated on the top of the brush and then started to "migrate" toward the inside of the brush, making the brush more packed and stiffer.[172] This was conclude from a slowly decreasing ΔD which suggests the formation of an increasingly organized structure of the PAA brush as it is complexed by HSA. According to Bittrich *et al*. the observed long equilibration time in this step arises form constant incorporation of protein into the brush-protein layer.[347] The rinse of HSA suspension with starting buffer in step II resulted in a Δf increase (decreasing mass) and a ΔD decrease. This suggests the removal of the bulky HSA molecules that have accumulated on the surface of the PAA brush. As a result the brush should become more dissipative. However, the loss of the viscous layer of proteins seems to be decisive in the overall ΔD decrease. In steps III to VI, the ionic strength was increased from 20 to 50, 75, 100 and 120 mM in a step-wise fashion, at constant pH. The observed systematic Δf increase was attributed to protein desorption and commensurate brush collapse. Furthermore, the small ΔD increase arises from the additional loss of HSA from the brush due to the increase of the ion concentration in the bulk solution.[74,347] Compression of the brush, driven by increasing ionic strength, can help to expel any weakly bound HSA, as shown by Wong *et al*.[348] As a result the PAA brush becomes more dissipative. Rinsing of the brush with starting buffer in step VII decreased the ionic strength from 120 to 20 mM. The resulting Δf decrease and concomitant increase in ΔD can be

attributed to brush swelling due to the lower ion concentration in the bulk solution.[74,347] These results are in good agreement with similar studies of brush conformation in aqueous solution.[78,79,349] A predominant role of counterions in protein adsorption onto PAA brush upon increasing salt concentration was discussed in section **4.4.3.1.** Importantly, the difference in *Δf* values between steps II and VII clearly suggests that even after increasing the NaCl concentration to the highest value analyzed here, there is still a significant amount of HSA bound within the PAA brush.

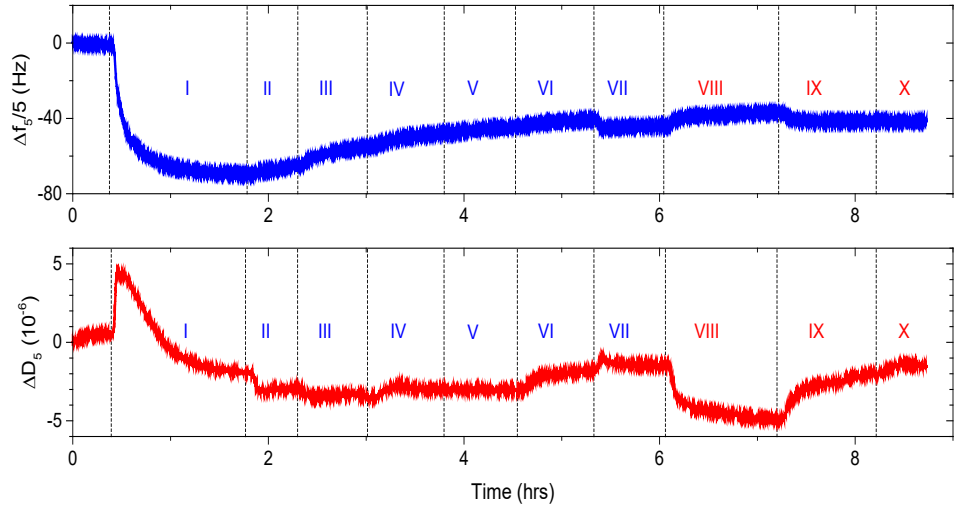

Figure 47. Ionic strength and pH induced response of a PAA brush with pre-adsorbed HSA layer monitored by QCM-D. Top panel: QCM-D normalized frequency shift. Lower panel: QCM-D dissipation shift. Swelling and deswelling events are indicated by Roman numerals. Corresponding pH and ionic strengths are indicated by red and blue color, respectively as the following: (I) 7.2; 20 mM with 5 g/L HSA suspension (II) 7.2; 20 mM (III) 7.2; 50 mM (IV) 7.2; 75 mM (V) 7.2; 100 mM (VI) 7.2; 120 mM (VII) 7.2; 20 mM (VIII) 6.5; 20 mM (IX) 7.6; 20 mM (X) 7.2; 20 mM. Steps I to VII: constant pH = 7.2. Steps: VIII to X: constant I = 20 mM. The 5th overtone is displayed.

At step VIII experiments with changing pH start. Upon changing the pH from 7.2. to 6.5 at constant NaCl concentration, *Δf* increases and *ΔD* decreases. These changes were attributed to brush collapse due to the less pronounced protonation of the carboxyl groups which allows them to form more O-H bonds.[350] As shown by Welsch,[351] the pK_a of the carboxyl groups of acrylic acid polymers within the brush can increase by two units compared to the one in solution (pK_a = 4.25).[352] This phenomenon, known as the polyelectrolyte effect, arises from the mutual interactions of the neighboring charged residues within the polyelectrolyte brush.[353] Therefore, even a small decrease in pH can result in marked protonation of the brush functional groups. *Δf* and *ΔD* shifts upon subsequent increase of pH in step IX (from 6.5 to 7.6) indicate the exact opposite effect to the one described above. Finally, upon rinsing the QCM crystals with starting buffer in step X no *Δf* change and only a small *ΔD* increase was observed which indicates brush swelling. Importantly, there is no significant difference in the *Δf* value between the initial and final states of the pH-affected experiments (steps VII and X, respectively). It suggests that upon changing the pH the brush swelling/deswelling was observed, rather than protein desorption.

4.5.3. Influence of pH on the Swelling of the PAA Brush

To verify whether the brush response during the pH-change arises from the additional HSA desorption or mainly from the brush swelling / deswelling, the response of a protein-free PAA brush as a function of pH was examined. The outcome of this experiment is presented in **Figure 48**. The time course of the experiment is described in section **4.5.1.**, and was designed to enable direct comparison with steps: VII, VIII, IX and X of the protein-adsorption experiment.

Step A shows the response of the PAA brush to decreasing ionic strength (from 120 to 20 mM) at constant pH of 7.2. The observed *Δf* decrease and corresponding increase in *ΔD* were attributed to brush swelling due to a decreased ion concentration in the bulk solution.[74,347] Upon changing the pH from 7.2 to 6.5 at constant ionic strength of 20 mM in step B, the expected collapse of the brush due to the more pronounced protonation of the carboxyl groups was observed.[350] Decreasing *Δf* and increasing *ΔD* in step C (upon pH change from 6.5 to 7.6) indicate brush swelling. The carboxyl groups in this step are balanced by counterions to a greater extent than at pH 7.2 due to their increased dissociation driven by slightly alkaline conditions. As a consequence the brush is not fully stretched which was conclude by comparison to the *Δf* and *ΔD* shifts in steps A and C. Preset results compare well with those reported by Liu *et al.*[349]

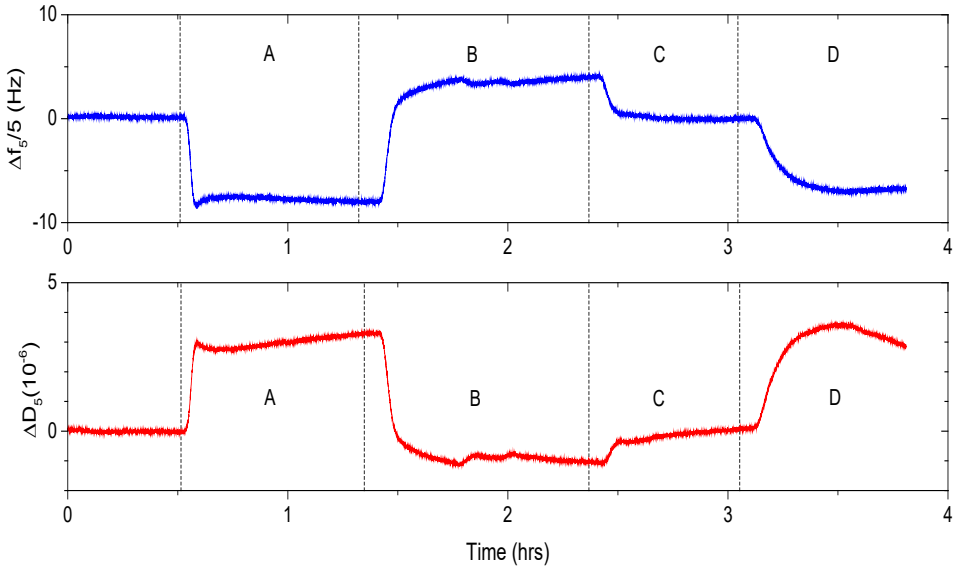

Figure 48. pH induced response of a protein-free PAA brush monitored by QCM-D. Top panel: QCM-D normalized frequency shift. Lower panel: QCM-D dissipation shift. The QCM crystals were calibrated in buffer solution with ionic strength of 120 mM and pH of 7.2. Swelling and deswelling events are indicated by capital letters. pH and ionic strengths corresponding to each step are highlighted by red and blue color, respectively. (A) 7.2; 20 mM (B) 6.5; 20 mM (C) 7.6; 20 mM (D) 7.2; 20 mM. Step A: constant pH = 7.2. Steps B, C and D: constant I = 20 mM. The 5th overtone is displayed.

In step D (upon changing the pH from 7.6 to 7.2) a strong *Δf* decrease along with increasing *ΔD* was observed indicating brush swelling. Such behavior was not observed between steps IX and X of the protein-adsorption experiment due to the presence of bound protein molecules within the PAA brush. The internal friction of a swellable polymer brush can be considerably increased by protein incorporation as shown by Bittrich *et al.*[347] The following analysis confirms that in the case of the pH changes in the studies of protein adsorption (see section **4.5.2.**) the swelling of protein-complexed PAA brush was mainly observed, rather than the protein desorption.

4.5.4. The Amount of Adsorbed Protein Determined by the Ionic Strength

The Sauerbrey equation (see section **3.3.4.2.**) was used to extract the changes of the mass density (Δm) of the brush at each step of the experiments described above (see **Figure 49**) to estimate the amount of HSA adsorbed per PAA chain. The observed brush response in steps VIII, IX and X corresponds to the swelling/deswelling of the PAA brush induced by changing pH. The calculated values of Δm upon ionic strength- and pH- changes as well as the Δm values upon pH induced swelling of a protein-free brush are presented in **Tables 6**, **7** and **8**, respectively.

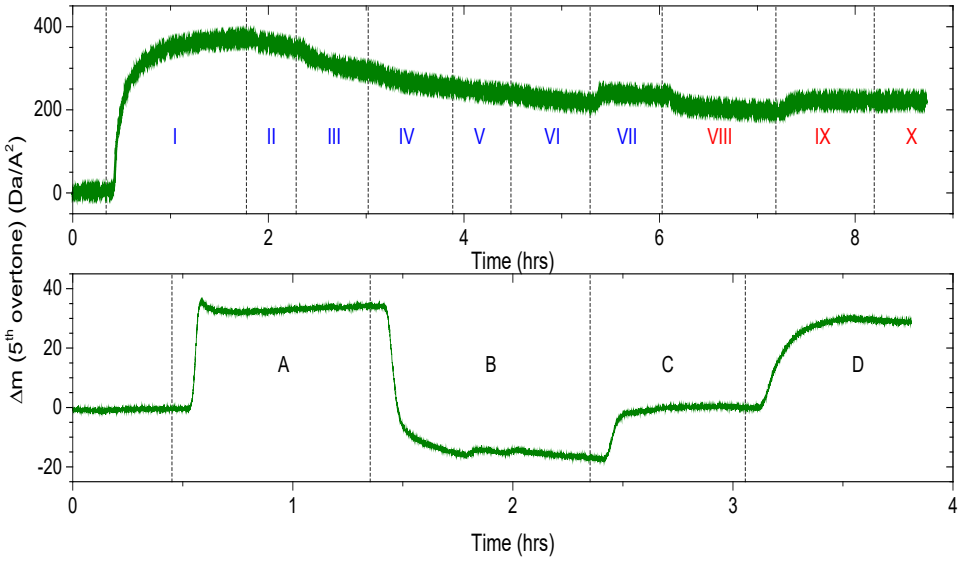

Figure 49. Top panel: calculated changes of the mass density upon ionic strength and pH induced response of protein-complexed PAA brush derived from the Sauerbrey equation. Analyzed steps are indicated by Roman numerals. pH and ionic strengths corresponding to each step are highlighted by red and blue color, respectively. (I) 7.2; 20 mM with 5 g/L HSA suspension (II) 7.2; 20 mM (III) 7.2; 50 mM (IV) 7.2; 75 mM (V) 7.2; 100 mM (VI) 7.2; 120 mM (VII) 7.2; 20 mM (VIII) 6.5; 20 mM (IX) 7.6; 20 mM (X) 7.2; 20 mM. Steps I to VII: constant pH = 7.2. Steps: VIII to X: constant I = 20 mM. Lower panel: calculated mass density upon pH induced response of protein-free PAA brush derived from the Sauerbrey equation. Analyzed steps are indicated by capital letters. The QCM crystals were calibrated in buffer solution with ionic strength of 120 mM and pH of 7.2. pH and ionic strengths corresponding to each step are highlighted by red and blue color, respectively. (A) 7.2; 20 mM (B) 6.5; 20 mM (C) 7.6; 20 mM (D) 7.2; 20 mM. Step A: constant pH = 7.2. Steps B, C and D: constant I = 20 mM.

Table 6. Calculated values of changes of the mass density (Δm) upon increasing ionic strength (IS). Roman numerals refer to the steps described in the paragraph.

Ionic strength increase	pH	I (mM)	Mass density (Da/A^2)
Step I	7.2	20	372
Step II – initial state of the IS-increase	7.2	20	353
Step III	7.2	50	297
Step IV	7.2	75	256
Step V	7.2	100	239
Step VI	7.2	120	217
Step VII – final state of the IS-increase	7.2	20	235

Table 7. Calculated values of changes of the mass density (Δm) upon changing pH. Roman numerals refer to the steps described in the paragraph.

pH change	pH	I (mM)	Mass density (Da/A^2)
Step VII – initial state of the pH-change	7.2	20	235
Step VIII	6.5	20	196
Step IX	7.6	20	220
Step X – final state of the pH-change	7.2	20	220

Table 8. Calculated values of changes of the mass density (Δm) upon pH induced swelling of a protein-free PAA brush. Capital letters refer to the steps described in the paragraph.

pH-induced protein free PAA brush swelling	pH	I (mM)	Mass density (Da/A^2)
Step A	7.2	20	33
Step B	6.6	20	-16
Step C	7.6	20	1
Step D	7.2	20	30

The changes of the mass density between each step of the pH-influence experiment (see Figure 49: Top panel) compared well to the changes of the mass density between analogous steps of the pH induced swelling of the protein-free PAA brush (see Figure 43: Lower panel), indicating that protein desorption during the pH-change is marginal. Consequently, during the pH-change only the swelling of the protein-complexed brush was observed. From the difference in the changes of the mass density recorded upon swelling of the protein-free brush (**Table 6**) the effect of the coupled solvent in the experiments can be estimate. The largest Δf shift can be observed between steps A and B thus the coupled solvent can be expressed as ± 49 Da/A^2. In

this way the obtained results can be corrected to determine with greater accuracy the amount of HSA adsorbed per PAA chain and lost during increase of the ionic strength.

The difference in Δm between the initial and the final steps of increasing ionic strength (steps II and VII in Table 6) is of about 118 ± 49 Da/A^2. This reflects the amount of desorbed HSA, and thus highlights the major influence of counterions in the process of polyelectrolyte mediated protein adsorption / desorption.[175,354,355] The remaining 220 ± 49 Da/A^2 can therefore be attributed to the HSA molecules that are attached to the PAA brush with higher affinity than the proteins desorbed during the increase of the ionic strength. This might indicate the existence of two fractions of HSA molecules within the PAA brush: those with high- and low binding affinity (see **Figure 50**).

The presence of high- and low binding affinity sites for proteins within a PE brush was previously observed for β-Lactoglobulin (BLG) binding onto SPBs and discussed in section **4.4.3.**[80] Here, due to the planar geometry of the PE brush, the presence of high- and low binding affinity sites can be attributed to polydispersity of brush chains. While, high grafting density occurs close to the surface, the chain segment density decreases towards the distal end of the brush as presented in Figure 50.

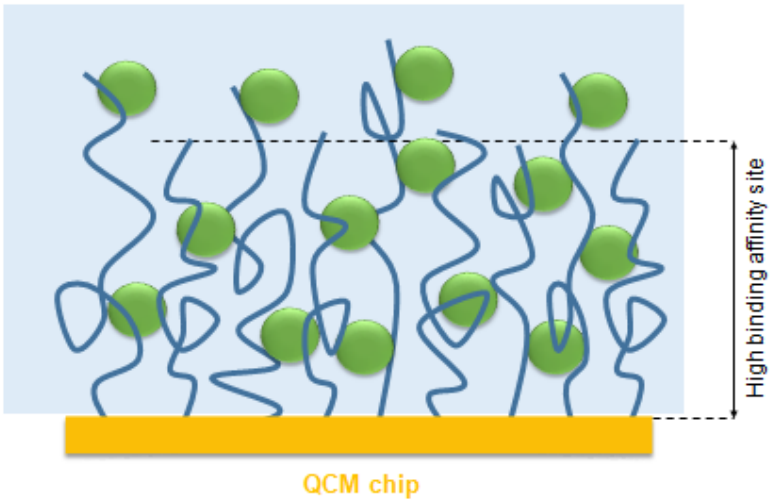

Figure 50. Schematic illustration of HSA molecules adsorbed onto PAA brush with the high- and low binding affinity.

The presence of a HSA fraction with low binding affinity indicates that this phenomenon is an example of a negative cooperativity. Therefore high- and low binding affinity may reflect the difference in protein adsorption onto free- and already preoccupied polyelectrolyte chains. A similar result was observed in the case of HSA adsorption onto PAA-based SPBs (see section **4.4.3.**).

4.5.4.1. Number of HSA Molecules per PAA Chain

From the change of the mass density at Step II (the initial state of the increasing ionic strength) with correction for the effect of coupled solvent and from the molecular weight of HSA (see section **3.2.2.**) the number of HSA molecules per nm^2 can be determine (see **Table 9**). Comparing this number to the inverse grafting density σ^{-1} = 2.9 ± 0.5 nm^2 of PAA brush allows to estimate the amount of HSA initially adsorbed per PAA chain.

Table 9. The calculated number of HSA molecules adsorbed per polyelectrolyte chain.

Considered step	Δm (Da/A^2)	HSA/nm^2 [a]	$N_{p/c}$ [b]
Step II	353 ± 49	0.53 ± 0.07	1.5 ± 0.2
Step X	220 ± 49	0.33 ± 0.07	0.9 ± 0.2

a) Number of protein molecules per nm^2.
b) Number of protein molecules per polyelectrolyte chain.

In the same way it can be verify that at Step X (the final state of pH-change) approximately one HSA molecule is adsorbed per one PAA chain (see Table 9) – the evaluation of these data are presented in the supporting material. Therefore approximately 40% of initially adsorbed HSA molecules are desorbed during the increase of the ionic strength.

These numbers are consistent with results reported by Yu *et al*.[52] and agree also with work of Wittemann *et al.* in which bovine serum albumin (BSA) molecules were released from PAA-based SPBs by washing them off with solution of higher ionic strength.[32] They reduced the number of attached BSA molecules from two per PAA chain to about one per two PAA chains. In work of HSA adsorption onto SPBs (see section **4.4.3.1.**) the influence of ionic strength on the binding was also verified. With increasing salt concentration the repulsion between investigated protein and PE brush become operative thus suppressing the adsorption process.

4.5.5. Conclusion

Present study demonstrates a successful ARGET ATRP polymerization of PAA brushes grafted from a planar gold surface of QCM crystals. The adsorption of HSA onto and the desorption from PAA brush as a function of ionic strength and pH was investigated by QCM-D. Conformational changes of the PAA brush were observed and used to correct the values measured for HSA adsorption. By releasing a part of initially adsorbed protein molecules upon increasing salt concentration we demonstrated the dominant role of counterions in the process of polyelectrolyte mediated protein adsorption / desorption. By comparison with the results of recent calorimetric studies on the protein interaction with polyelectrolytes[52] along with the results of SPB-HSA interaction discussed in section **4.4.**,this study present a new approach in which QCM data are analyzed based on the results of thermodynamic studies.

Finally, it can be conclude that QCM crystals modified through presented method based on ARGET ATRP reaction are fully functional. A comparison with large number of other brush systems interacting with proteins [32,52,73,173] lead to a full agreement in the number of adsorbed protein molecules per polyelectrolyte chain at low and high ionic strength. Thus, the present findings extend the understanding of interaction between protein and polyelectrolyte brush by comparison of systematic studies of protein adsorption / desorption driven by increased salt concentration with calorimetric studies of the same problem.

5. Summary and Outlook

The studies presented in this thesis are focused at the understanding of the mechanism and the underlying driving forces upon polyelectrolyte-protein (PE-P) interaction. The combination of experimental techniques and theoretical approach enables insight into the binding process by combining thermodynamics with structural information. PEs employed in this work such as linear-, low molecular weight-, dendritic-, and brush-like PEs offers a matrix that includes different structural features *e.g.* flexibility and surface area for binding with proteins. The adsorption studies were systematically performed using salt concentration c_s, temperature T, and pH as the main variables allowing a detailed thermodynamic analysis.

- The first investigated PE is a highly charged, dendritic polyglycerol sulphate (dPGS). To explore counterion condensation to dPGS, the ion specific effects and the competitive adsorption between mono- and divalent counterions, the isothermal titration calorimetry (ITC) and theoretical approach based on the non-linear penetrable Poisson-Boltzmann (PPB) model are employed. The calorimetric measurements show that the ion-specific effects upon binding of Mg^{2+} and Ca^{2+} ions to dPGS are marginal. The overall number of Mg^{2+} ions adsorbed per dPGS molecule obtained by ITC experiment stands in a very god agreement with theoretical predictions of the PPB model. Since PPB model gives a relatively accurate picture of the dPGS-counterion electrostatic binding affinity, the reported approach is envisioned to become applied in the future analysis of counterion condensation and interactions between various different PEs and proteins.
- In the second part, ITC is used to investigate interaction of lysozyme (Lys) with linear and low molecular weight PEs: heparin (Hep) and β-CD-S, respectively. The dependence on temperature in case of Lys-Hep interaction allows to dissect the binding free energy ΔG_b into the respective enthalpies ΔH_b and entropies ΔS_b together with the specific heat capacity ΔC_p. A strong enthalpy-entropy cancellation (EEC) was observed. The binding free energy ΔG_b could be dissected into a part ΔG_{ci} due to counterion release and a residual part ΔG_{res}. The dependence on salt concentration c_s in β-CD-S interaction with Lys lead to the net number of released counterions Δn_{ci} and $K_b(1M)$. The interaction between Lys and β-CD-S should be extended in order to verify the dependence on temperature in the same manner as in the case of Lys-Hep binding. The interaction of Lys with β-CD-S may be then directly compared to the Lys-Hep binding as well as to the well-studied binding of proteins to DNA. The reported approach is envisioned to become applied in the future analysis of interactions between various different GAGs and signaling proteins (cytokines, chemokines, growth factors), paving the way for the fabrication of GAG-based polymer hydrogel networks with rationally designed protein binding characteristics. It may also become applied in the future fabrication of polymer drugs with enhanced solubility.
- In the third part, ITC and quartz crystal microbalance with dissipation monitoring (QCM-D) are used to investigate adsorption of human serum albumin (HSA) to poly(acrylic acid) (PAA)-based PE brushes. Calorimetric measurements show that HSA adsorption onto spherical polyelectrolyte brushes (SPBs) is a two-step process. The thermodynamic analysis reveal that the counterion release entropy is the main contribution to the binding free energy (ΔG_b). ITC measurements, performed over a range of temperatures between 25 and 37°C show a strong temperature dependence of the calorimetric enthalpy (ΔH^{ITC}) along with a nearly temperature-invariant ΔG_b. As

well as for the interaction between Lys and Hep, this system exhibits a marked EEC. The performed analysis thus allows a systematic comparison of the present results with Hep-Lys interaction along with a large set of data from other systems. Such comparison demonstrates that a strong EEC is a general feature occurring in systems in which the binding is dominated by counterion release.

- Prior to investigate HSA adsorption to planar PE brush an ARGET ATRP polymerization of PAA brushes grafted from a planar gold surface of QCM crystals was employed. The adsorption of HSA onto and the desorption from PAA brush as a function of ionic strength and pH was then investigated by QCM-D. Conformational changes of the PAA brush were observed and used to correct the values measured for HSA adsorption. By releasing a part of initially adsorbed protein molecules upon increasing salt concentration, the dominant role of counterions in the process of polyelectrolyte mediated protein adsorption / desorption is demonstarte. By comparison with the results of calorimetric studies on the HSA-SPB interaction, this study present a new approach in which QCM data are analyzed based on the results of thermodynamic studies. Thus, the present findings extend the understanding of interaction between protein and PE brush by comparison of systematic studies of protein adsorption / desorption driven by increased salt concentration with calorimetric studies of the same problem.

In conclusion, this thesis provides a deeper insight into the PE-P interaction. In particular, a combination of experimental methods with theory have been applied to identify the mechanism and the thermodynamic driving forces of protein binding. Moreover, an important contribution to a more complete understanding of PE structure along with counterion- condensation and release upon binding with proteins is made which is essential for many biomedical application. It demonstrates that EEC is a general feature occurring in systems in which the binding is driven by counterion release.

6. Materials and Methods

6.1. Materials

For the synthesis of spherical polyelectrolyte brushes (SPBs); the monomers: styrene, acrylic acid (AAc) and the initiator potassium peroxodisulfate (KPS) as well as the emulsifier sodium dodecyl sulfate (SDS) were purchased form Sigma-Aldrich. Styrene contains a small amount of 4-tert-butylcatechol as stabilizer to prevent from autopolimerisation. Therefore for the purpose of polymerization reaction styrene was destabilized by flushing over a column filled with inhibitor remover (Sigma-Aldrich). AAc was distilled under reduced pressure (1 mbar, 40-45°C) in a rotary evaporator to remove the stabilizer hydroquinone monomethylether. The cleaned monomers were stored at -4°C. KPS and SDS as well as photoiniciator *2-[p-(2-hydroxy-2-methylpropiophenone)]-ethylene glycol-methacrylate* (HMEM) for the synthesis of core-shell particles were used as received.

For the synthesis of planar polyelectrolyte brushes (PPBs); the *tert*-butyl acrylate (*t*BA) monomer as well as the catalyst: $CuBr_2$; the complexing ligand: N,N,N',N',N''-Pentamethyldiethylenetriamine (PMDETA); reducing agent: L-ascorbic acid; acetone; sodium dodecyl sulfate (SDS); and trifuoroacetic acid were purchased from Sigma-Aldrich. Anhydrous dichloromethane was purchased from Merck. The surface bond initiator Bis[2-(2-bromoisobutyryloxy)undecyl]disulfide (DTBU) was synthesized according to the published procedure.[77] *t*BA contains a small amount of monomethyl ether hydroquinone as inhibitor to prevent from autopolimerisation. Therefore for the purpose of polymerization reaction *t*BA was destabilized by flushing over a column filled with activated basic aluminum oxide (Al_2O_3 from Sigma-Aldrich). All other substrates were used as received. Gold QCM sensors were purchased from QSense and clean prior to use (see section **4.5.1.1.**).

The buffer components: 3-(N-morpholino)propane sulfonic acid (MOPS) was received from Sigma-Aldrich and used directly. Sodium phosphate dibasic (Na_2HPO_4) and sodium phosphate monobasic (NaH_2PO_4) were purchased from Fluka and used without further purification.

6.2. Proteins and Buffers

Human serum albumin (HSA) and lysozyme (Lys) were used in this work to study the interactions with heparin, β-CD-S, SPBs and PPBs. Essential details about used proteins are listed in **Table 10**.

Table 10. Overview of proteins used in this study.

Protein	Origin	Supplier	Cat.-No.	LOT.-No.	Purity
Human Serum Albumin	Human serum	Sigma-Aldrich	A3782	SLBT8667	≥ 99%
Lysozyme	Chicken egg-white	Sigma-Aldrich	L6876	SLBZ2146	≥ 90%

The proteins listed above were received as lyophilized powders containing low amount of additional impurities. These proteins were used in binding studies with SPBs and dendritic polyglycerol sulfate (dPGS) without further purification. Two buffer systems were used in presented studies: 10 mM MOPS buffer pH 7.2 and 10 mM phosphate buffer pH 7.4. The

MOPS buffer was prepared by dissolving 10 mM 3-(N-morpholino) propane sulfonic acid (MOPS) in water (Millipore Milli-Q). For the phosphate buffer; sodium phosphate dibasic (8 mM; Na_2HPO_4) and sodium phosphate monobasic (2.8 mM; NaH_2PO_4) were dissolved in water (Millipore Milli-Q). The ionic strength of the buffers was adjusted by addition of a proper amount of sodium chloride (NaCl). The pH was very carefully adjusted by dropwise addition of 1 M sodium hydroxide (NaOH) with consideration of temperature-dependent acid dissociation of MOPS.

6.3. Synthesis and Characterization of SPBs

6.3.1. Synthesis of Polystyrene (PS) Core Latex

The synthesis of PS core particles with a thin layer of photoinitiator (HMEM) on their surface was accomplished by conventional emulsion polymerization using a 2 L three-necked glass reactor which was heated through a thermostat and equipped with thermometer, stirrer and reflux condenser. The synthesis was carried out as follows, 208.3 g (2.0 mol) of freshly purified styrene was added to a continuously stirred (at 320 rpm) solution consisting of 2.1 g (0.0073 mol) of SDS emulsifier in 700 ml of water. By several vacuum/nitrogen purge cycles the whole mixture was deoxygenated and gradually brought to the temperature of 80°C under nitrogen atmosphere. The polymerization process was initiated by addition of 0.44 g (0.0016 mol) of KPS initiator dissolved in 125 ml of water. After 1h of stirring at 80°C the turbid suspension was cooled to 70°C. To cover the PS core particles with a thin layer of photoinitiator a solution of 5.34 g (0.0144 mol) of HMEM dissolved in 6.0 ml (0.0816 mol) of acetone was added dropwise (0.19 ml/min) to the suspension. HMEM was added under starved conditions to achieve a well-defined core-brush morphology. The reactor was shielded from light and the reaction was continued for a further 1h. Prior to the grafting of the brushes all PS-co-HMEM latex was filtrated (after cooling to 40°C) by dialysis against water.

Table 11. Weight portions of the educts used for synthesis of PS cores.

	PS-co-HMEM
m(styrene) [g]	208.30
m(SDS) [g]	2.10
m(KPS) [g]	0.44
m(H_2O) [g]	825
m(HMEM) [g]	5.34
weight percentage (in % w/w)	18.55
hydrodynamic radius [a] $R_{h,core}$ [nm]	57.5

[a] *Before modifying the PS core latex by HMEM photoinitiator a small sample of PS core latex was taken for the purpose of $R_{h,core}$ measurements.*

6.3.2. Synthesis of Core-Brush Particles

The brush of the SPB-PAA was polymerized onto PS-co-HMEM latex as follows: Given amounts of a PS core latex modified with a thin layer of HMEM (see **Table 12**) were diluted with water to ~2.5 wt% and charged in a UV reactor (TQ 150; Heraeus, 650 cm^3 volume, range of wavelength 200-600 nm). After addition of destabilized monomer the whole reactor was degassed by repeated evacuation and subsequent addition of nitrogen. The amounts of used monomers were chosen to obtain a well-defined brush as well as to avoid aggregation of particles during polymerization process. Photopolymerization was done by use of UV/vis radiation at a temperature of 25ºC. Vigorous stirring (at 400 rpm) ensured homogeneous conditions during the photopolymerization. Small samples were drawn repeatedly to follow the extent of reaction. After 1h of irradiation the UV/vis lap was switched off and the photopolymerization ended. The latex was purified exhaustively by serum replacement using pure water until the conductance of the eluate did not change anymore.

Table 12. Weight portions of the educts used for synthesis of SPBs.

	SPB-PAA
m(PS-co-HMEM) [a] [g]	106.0
m(PS-co-HMEM) [b] [g]	19.6
m(H_2O) [g]	600.0
m(AAc) [g]	5.8

[a] latex, [b] solid

6.3.3. Purification of SPB Particles

SPB particles were purified by ultrafiltration in order to remove unreacted monomers, dissolved polymers and surfactant molecules from particles dispersion. Ultrafiltration was carried out in serum replacement cells which contain cellulose nitrate membrane. For the purpose of SPBs purification membranes with pore size of 100 nm were chosen. The serum was replaced against water (Milli-Q) under overpressure of nitrogen (1.2 bar) until the conductivity of eluate had reached the conductivity of pure water ($\kappa < 1$ μS).

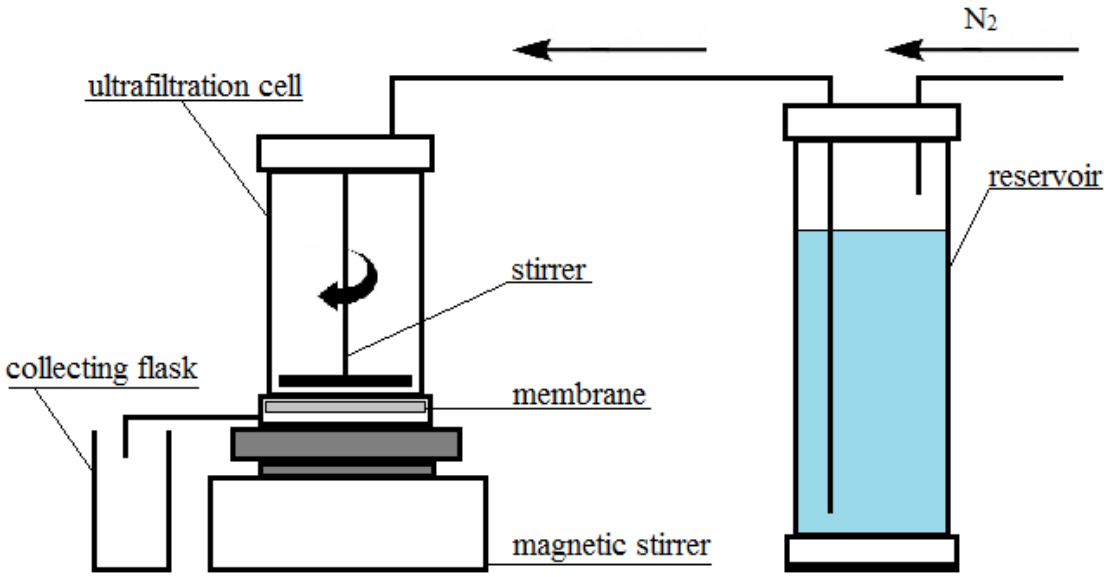

Figure 51. Schematic representation of an ultrafiltration cell.

After purification the molecular weight of SPB particles $M_{w,\,SPB}$ was calculated by the use of the following formula:

$$M_{w,SPB} = (m_{core} + m_{brush})N_A = \frac{\rho_{core}\frac{4}{3}\pi R_{h,core}^3}{w_{core}} N_A \qquad (56)$$

Because of the mass balance of SPBs dispersion before and after ultrafiltration the mass of monomers unpolymerized into the brush can be determined and so the mass fraction of the core can be calculated via $w_{core} = m_{core}/(m_{brush} + m_{core})$. The ρ_{core} and $R_{h,core}$ denotes, respectively, the density of the PS core (ρ_{core} = 1.055 x 10^{-21} g nm^{-3}) and the hydrodynamic radius of the PS core determined by DLS.

Table 13. The respective values of molecular weight and size of SPB particles.

	AAc[a] [%]	w_{core}	Mw [g mol^{-1}]	$R_{h,core}$ [nm]	L_c [nm]
SPB-PAA	40	0.909	5.56 x 10^8	57.5	231

[a] *amount of AAc added for polymerization (molar percent of styrene)*

6.3.4. Dynamic Light Scattering (DLS)

Particle size can be determined by the measurement of time-dependent fluctuations in the intensity of the scattered light from a suspension or solution. This technique is known as Dynamic Light Scattering (DLS), a.k.a. Quasi-Elastic Light Scattering (QELS). Brownian motions of the macromolecules in solution imparts a randomness to the phase of scattered light, as light scatters from the moving macromolecules. Therefore when the scattered light from two or more particles is added together, there will occur a constructive or destructive interference leading to the random changes in the intensity of scattered light. Those random changes in the intensity are directly related with the rate of the molecule diffusion through the solvent, which in turn is related to the hydrodynamic radii of the particles.

The DLS measurements were performed by using a compact ALV/CGS-3 instrument, which is equipped with a He-Ne laser (wavelength of λ = 632.8 nm). This instrument allows to perform

simultaneously, dynamic and static light scattering experiments. Pseudo cross correlation function are received by using an ALV 5000/E multiple-τ correlator. The setup permits to measure at angle ranging from 17° to 150°, therefore covering a scattering vector range of 0.0039 – 0.0256 nm^{-1}. The temperature of the samples was controlled using a tempered bath containing toluene as index matching substance. All measurements performed on this instrument were done at a scattering angle of 90° and at temperature of 298 K. For the purpose of those measurements SPBs as well as PS-cores were dispersed in buffer solution (see section 1.2), therefore there were diluted to a concentration of 0.01 g/L. All samples were filtered through a syringe filter (polyethersulfone (PES) membrane with 1.2 µm pore width) in order to avoid the presence of dust. To obtain thermal equilibrium, before the measurement, all samples were incubated at the desired temperature for 5 minutes. For each experiment a set of 3 measurements was performed and each one of it consists of 10 single runs. The DLS data were analyzed with the software AfterALV to obtain the hydrodynamic radius of measured particles.

The fluctuations in the scattered light are quantified via second order correlation function:

$$g^{(2)}(\tau) = \frac{<I(t)I(t+\tau)>}{<I(t)>^2} \tag{57}$$

where *I(t)* refers to the intensity of the scattered light at time *t*, and the brackets denotes averaging over all *t*. The correlation function depends on the delay *τ*, which is the amount that a duplicate intensity trace is shifted from the original one before the averaging is performed. The correlation function for a monodisperse sample can be analyzed by the equation:

$$g^{(2)}(\tau) = B + \beta \exp(-2\Gamma\tau) \tag{58}$$

where *B* refers to the baseline of the correlation function at infinite delay, *β* represents the correlation function at zero delay and *Γ* denotes the decay rate. In order to obtain the correlation function decay rate *Γ*, the measured correlation function is fitted to equation (58) by a nonlinear squares fitting algorithm. From this point, *Γ* can be converted to the diffusion constant *D* for the particle via the relation:

$$D = \frac{\Gamma}{q^2} \tag{59}$$

Here, *q* is the magnitude of the scattering vector, and is given by:

$$q = \frac{4\pi n_o}{\lambda_o} \sin(\frac{\theta}{2}) \tag{60}$$

where n_o is the solvent index of refraction, λ_o is the vacuum wavelength of the incident light and θ is the scattering angle. Finally, the diffusion constant can be interpreted as the hydrodynamic radius R_h of a diffusing sphere via Stokes-Einstein equation:

$$R_h = \frac{k_B T}{6\pi\eta D} \tag{61}$$

Where, k_B is Boltzman's constant, *T* is the temperature in K and η is the solvent viscosity.

6.3.5. Conductometric and Potentiometric Titration

Conductometric and Potentiometric titration measurements were performed simultaneously by using Mettler Toledo SevenCompactTM pH/Ionnmeter S220 and a conductometer WTW Cond 197i. For this titration experiment, the SPB dispersion was diluted with water to a total concentration of 0.5 wt %. Then, 30 mL of the SPB suspension were titrated with 0.01 M NaOH. The titration were run in a thoroughly cleaned 50 mL beaker fitted with the *pH* and the conductivity electrode. The NaOH solution was slowly added to the SPB dispersion with a rate of 0.1 mL/min.

The conductometric and potentiometric titration curves of SPB are shown in **Figure 52.** The amount of acrylic acid polymerized into the brush of SPB particles was determined from the equivalent point of both titration curves.

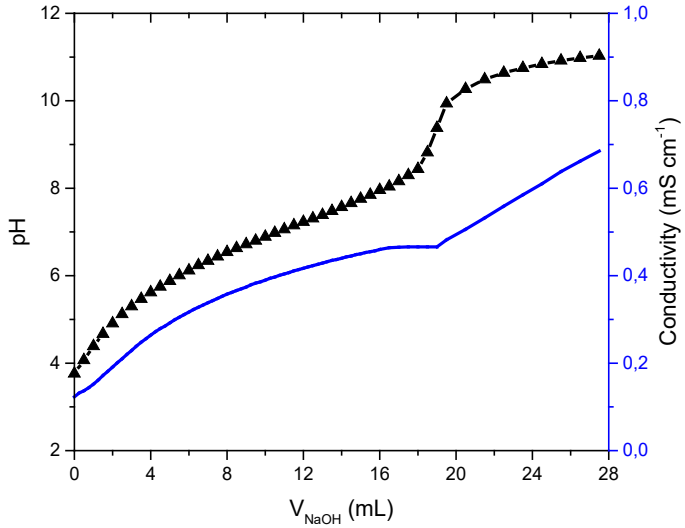

Figure 52. Conductometric and potentiometric titration curves of SPB in millipore water.

In addition, the dissociation degree α_{diss} of the carboxylic acid functional groups was calculated as a function of the amount of added NaOH and thus, as a function of the *pH* according to:

$$\alpha_{diss} = \frac{[V]_{pH}}{[V]_{eq}} \tag{62}$$

Where $[V]_{pH}$ and $[V]_{eq}$ are the volume of added NaOH at a given *pH* value and at the equivalent point, respectively. To calculate the apparent pK_a value of the carboxylic acid functional groups as a function of dissociation degree, the following equation was used:

$$pK_a = pH - log(\frac{\alpha_{diss}}{1-\alpha_{diss}}) \tag{63}$$

6.3.6. Determination of the Molecular Weight of the Tethered Polyelectrolyte Chains

The grafted PAA chains were cleaved off from the PS core particles due to the fact that the ester bond of the photoinitiator can be hydrolyzed in alkaline conditions. In order to do so, a sample of purified SPB latex was heated to 97°C in 2.0 M aqueous NaOH for 17 days. Such a treatment is necessary since negative coions such as the hydroxide ions are repelled from anionic brushes.[356]

Due to the loss of the steric stabilization by PAA chains the latex coagulated. The amount of the PAA chains in the supernatant serum was calculated due to the informations obtained from the conductometric and potentiometric titration experiment (see section **6.3.5.**). The kinematic viscosity [u] of PAA chains was measured by using a Lauda iVisc Viscosimeter Version 1.01 with Mikro-Ubblohde capillary in 2.0 M NaOH at 25°C.

Table 14. The kinematic viscosity [u] and the density [d] of PAA chains solution and 2.0 M aqueous NaOH (solute).

	u [nm^2/s]	**d [g/cm^3]**
PAA in 2.0M NaOH[a]	1.34982	1.07870
2.0 M NaOH[b]	1.24401	1.07253

[a, b] *measurements were performed at 25°C*

Together with the kinematic viscosity of the solvent and with the measured densities of both solute and solvent the intrinsic viscosity [η] was determined. The viscosity average molecular weight ($M\eta$) of the PAA chains was calculated according to the Mark-Houwink relation (K = 4.22 x 10^{-2} mL/g, α = 0,64)[357]

$$[\eta] = KM^{\alpha} \tag{64}$$

The determination of the molecular weight $M\eta$ together with the known amount of PAA on the surface allows the calculation of the grafting density (σ) via:

$$\sigma = \frac{\frac{wt\%\ brush}{wt\%\ core}\rho_{core}\frac{4}{3}\pi R_{h,core}^3}{M_\eta 4\pi R_{h,core}^2} N_A \tag{65}$$

In order to prove a brush structure, the average distance (D) between neighboring grafted points of polymer chains should be smaller than two times of the gyration radius (R_g) of a free polymer chain ($D < 2R_g$), which can be calculated via through:

$$R_g = \left(\frac{3M_\eta[\eta]}{10\pi N_A}\right)^{\frac{1}{3}} \tag{66}$$

Table 15. The respective values of the structural parameters of synthesized spherical PAA brush.

	initiator	I[a](%)	AAc[b] [%]	Mη [g mol^{-1}]	σ [nm^{-2}]	R_g [nm]	D [nm]
SPB-PAA	HMEM	0.8	14	96000	0.013	9.97	8.77

[a] *amount of photoinitiator (molar percent of styrene).* [b] *amount of AAc monomer polymerized into brush (molar percent of styrene)*

6.3.7. Cryogenic Transmission Electron Microscopy (Cryo-TEM)

Cryogenic Transmission Electron Microscopy was performed on a JEOL JEM-2100 transmission electron microscope (JEOL GmbH, Eching, Germany). The Cryo-TEM samples were prepared by placing a 4 μL drop of SPB dispersion on a lacey carbon-coated copper TEM grid (200 mesh, Electron Microscopy Sciences, Hatfield, PA), and frozen in liquid ethane at its freezing point with an FEI vitrobot Mark IV with setting condition of: 4 °C and 95% humidity. All grids before experiment were pretreated by glow-discharged and inserted into the microscope holder (Gatan 914, Gatan, Munich, Germany). Examination of samples was carried out at temperature of 90 K. The TEM was operated at an acceleration voltage of 200 kV. The Cryo-TEM micrographs were recorded at a number of magnifications with a bottom-mounted 4*4k CMOS camera (TemCam-F416, TVIPS, Gauting, Germany).
The Cryo-TEM image of SPB's is shown in **Figure 53**.

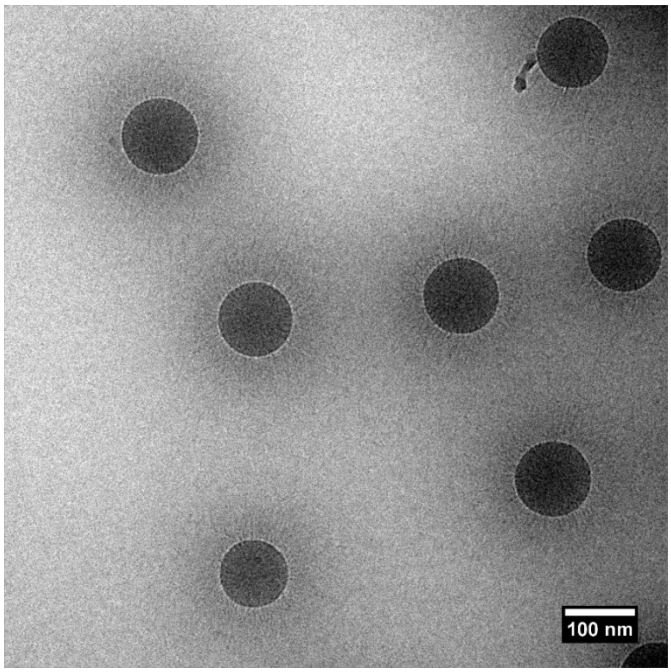

Figure 53. Cryo-TEM image of a 0.1 wt% of SPB particles suspension in MOPS buffer solution.

6.4. Synthesis and Characterization of PPBs

6.4.1. Immobilization of DTBU Initiator on the Surface of QCM Crystals

The functionalization of the surface of QCM crystals with DTBU initiator was carried out as follows; QCM crystals were thoroughly cleaned by rinsing them with 1% SDS solution, DI water, and ethanol and by sonicating them for 5 minutes in each of the substrates mentioned above. Each sonication was performed at constant temperature of 50°C. In the final step of the cleaning procedure the QCM crystals were dried under nitrogen and exposed to air plasma (Harric Plasma Cleaner) for 2 minutes to activate their surface. Right after cleaning the QCM crystals were immersed for 24 h at room temperature in solution containing 35 mL of ethanol and 80 μL of DTBU initiator.

6.4.2. ARGET ATRP Polymerization of poly(*tert*-butyl acrylate) (P*t*BA)

The polymerization of P*t*BA brush on the surface of gold QCM crystals bearing a thin layer of DTBU initiator was accomplished towards surface initiated "grafting from" method with activator regenerated by electron transfer (ARGET) atom transfer radical polymerization (ARGET ATRP). The reaction was performed according to the following procedure: 12.0 mL (82.7 mmol) of freshly purified *tert*-butyl acrylate monomer was added to a 100 mL glass flask that contained the solution of acetone (35.0 mL; 0.48 mol), $CuBr_2$ (67.1 mg; 0.30 mmol) and PMDETA (64.7 μL; 0.31 mmol). The flask was sealed with rubber septum and purged with nitrogen for 1 h. Then 0.7 g of ascorbic acid (4.0 mmol) was add to the monomer solution in a glovebox under the argon atmosphere and the whole mixture was stirred for 5 minutes until color changed. The QCM crystals functionalized with DTBU initiator were dried under nitrogen and transferred to the flask containing the polymerization solution. The polymerization proceeded for 22 h at room temperature. Afterwards the QCM crystals were removed and rinsed with DI water, ethanol and dried under nitrogen.

Table 16. Overview of the amount of the educts used for synthesis of P*t*BA.

	P*t*BA
V(*tert*-butyl acrylate) [mL]	12.0
V(acetone) [mL]	35.0
V(PMDETA) [μL]	64.7
m($CuBr_2$) [mg]	67.1
m(ascorbic acid) [g]	0.7

6.4.3. Conversion of poly(*tert*-butyl acrylate) Brush into poly(acrylic acid) Brush

The conversion of P*t*BA- into PAA brush was accomplished by acid hydrolysis that was carried out as follows; the QCM crystals modified with P*t*BA brush were exposed to trifluoroacetic acid (3.0 mL; 39.2 mmol) in the presence of dichloromethane (35 ml; 0.55 mol). The deprotection procedure was allowed to proceed for 18 h at temperature of 0°C. Afterwards QCM crystals were cleaned with ethanol, DI water and dried under nitrogen.

Scheme 1. Synthetic route for polymerization of poly(acrylic acid) brush from a gold substrate.

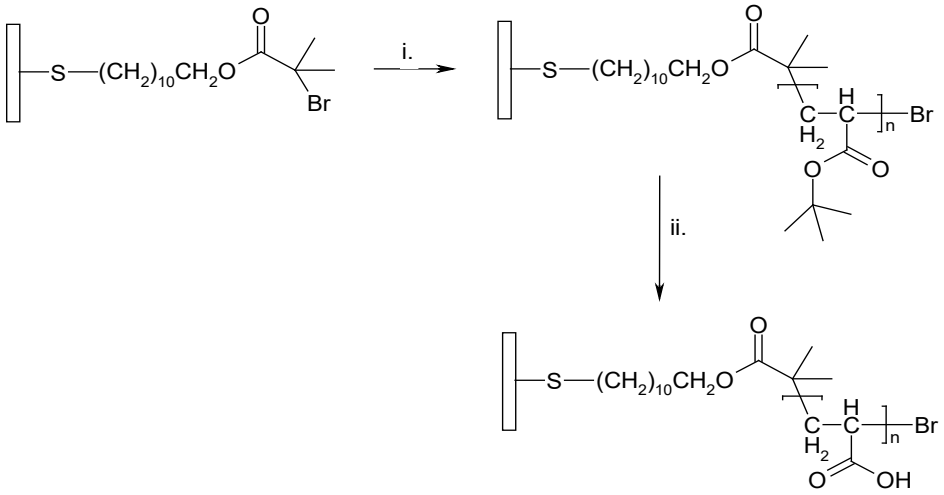

i) *tert*-butyl acrylate, acetone, $CuBr_2$, PMDETA, ascorbid acid, room temp., 22 h.

ii) trifluoroacetic acid, dichlorometane, 0°C, 18 h.

6.4.4. Static Water Contact Angle (SWCA)

Contact angles were determined using a Rame Hart NRL-100 contact angle goniometer equipped with fiber optic illuminator, 3-axis specimen stage with leveling, U1 Series SuperSpeed digital camera which operates at 100 fps and microsyringe for manual dispensing. The contact angle measurements were supported by DROPimage Advanced software that allows the static contact angle measurement in a range of 0-180° with accuracy of ±0.1° and resolution of ±0.01°. The measurements were performed by manual dispensing of 3 µL of DI water on the investigated surface and followed by DROPimage analysis. The measured contact angle (85°) correlates well with the literature values for PtBA layer assembled at the surface of poly(styrene) substrate.[358] After hydrolysis the measured static contact angle decreased to 16°. This proves the increased hydrophilicity due to the presence of the PAA layer.

Table 17. Static water contact angle data for the samples studied in this work.

Sample	Static water contact angle[a] (deg)
poly(*tert*-butyl acrylate)	85
poly(acrylic acid)	16

[a)] The standard deviation of contact angles was < 3°.

6.4.5. Ellipsometry

Ellipsometric measurements were performed an a J. A. Wollam M-88 Variable Angle Spectroscopic Ellipsometer with Hg-Xe laser with a wavelength in a range of 300-800 nm and a fixed angle of incidence of 70°.

Thickness of a film applied to the surface of a given substrate can be determined by ellipsometry which measures the change in polarization of the light reflected from a material structure. The

measurables in this technique are Ψ, the amplitude ratio and Δ, the phase difference between the p- and s- components of the polarized light. Those parameters are related by the complex reflection coefficient ρ:

$$\rho = \tan(\Psi)\, e^{i\Delta} \tag{67}$$

In the case of a multi-film layers at a given substrate the equations derived for a single reflection can be directly inverted to provide a pseudo dielectric function $< \varepsilon >$:

$$< \varepsilon >= \sin^2 \varphi \tan^2 \varphi \left(\frac{1-\rho}{1+\rho}\right)^2 \tag{68}$$

Where φ is the angle of incidence.

The thickness of the layer underlying the P*t*BA/PAA films was determined experimentally based on the optical constants of the materials provided in the instrument software, and were then used to build a model.

After a measurement a model is constructed to describe the measured sample. That model is then used to calculate the predicted response from Fresnel's equations which describe each material in regard of the optical constants and the thickness. The quality of the data fit to the model is evaluate by the mean square error (MSE):

$$MSE = \frac{1}{2N-M} \sum_{i=1}^{N} \left[\left(\frac{\Psi_i^{mod} - \Psi_i^{exp}}{\sigma_\Psi^{exp}}\right)^2 + \left(\frac{\Delta_i^{mod} - \Delta_i^{exp}}{\sigma_{\Delta i}^{exp}}\right)^2 \right. \tag{69}$$

Where N represents the number of used pairs of Ψ and Δ, M represents the number of variable parameters in the regression analysis and σ represents the standard deviation of the experimental data points. The minimum MSE indicates the satisfying correspondence of calculated results with the measured ones.

The P*t*BA/PAA film thickness were then determined using a Cauchy layer logarithm.

Measured thickness depends on the optical constants of the measured material, therefore to obtain the correct results from an ellipsometry the refractive index n and the extinction coefficient k of a given material must be known or determined as well. In the case of a transparent film (where k is negligible) a Cauchy relationship for n can be used to analyze the ellipsometry data:

$$n(\lambda) = A + \frac{B}{\lambda^2} + \frac{C}{\lambda^3} \tag{70}$$

Where λ is the wavelength and the three parameters A, B and C are adjusted to fit the refractive index of a given material. From ellipsometry the dry thickness of the polymer film was found to be 18 nm. After hydrolysis the polymer brush thickness in a dry state decreased to 8 nm. The drop in the brush thickness can be attributed to the removal of the bulky *tert*-butyl groups. A similar observation was reported recently.[359]

Table 18. Ellipsometry data for the samples of planar polymer brush studied in this work.

Sample	Thickness[a] (nm)
poly(*tert*-butyl acrylate)	18
poly(acrylic acid)	8

[a)] *Thickness was determined by ellipsometry as an average of three samples, typical error for the thickness measurement is ± 1 nm.*

6.4.6. Determination of the Grafting Density

The grafting density σ of the PAA brush was determined from the following equation:

$$\sigma = h\rho N_A/M_n \quad (71)$$

Here h is the dry polymer thickness, ρ the density of PAA (= 1.1 g/cm^3)[360], N_A Avogadro's number, and M_n the polymer molecular weight. To estimate M_n we used a systematic comparison by Wu *et al.* on PAA brushes anchored to a flat silicon wafer with variation of the grafting densities at several ionic strengths.[76] As a result we can predict the thickness of the wet PAA brush H as it should present the dry thickness multiplied by the factor of 6.5 ± 0.5 (see **Table 19**).

Table 19. Parameters used for determination of the molecular weight of grafted PAA chains M_n.

Parameter	Value
h (nm)	8 ± 1
H (nm)	52 ± 11
$N_{m.u.}$	208 ± 44
$M_{m.u.}$ (g/mol)	72.07
M_n (g/mol)	15000 ± 3171

Assuming that each monomer unit is a bead with diameter of 0.25 nm we can determine the number of monomer units $N_{m.u.}$ within a single PAA chain. Multiplying the molecular weight of a monomer unit $M_{m.u.}$ by $N_{m.u.}$ we can estimate the molecular weight M_n of a single grafted PAA chain. The grafting density was estimated to be σ = 0.35 ± 0.13 nm^{-2}. Such high grafting densities were also reported for PAA brushes achieved by a similar polymerization procedure on a flat silicon surface[76] where PAA brushes with grafting density up to 0.85 nm^{-2} have been achieved. However, in the present case the molecular weight of the single grafted PAA chain as well as the grafting density is only estimated. The wet thickness H of the PAA brush does not represent the total length of the polyelectrolyte chain. Therefore the estimated σ refers to the maximal grafting density of the analyzed brush.

6.5. Fourier Transform Infrared (FT-IR) Spectroscopy

The analysis of the P*t*BA and PAA brushes as well as the secondary structure of free and immobilized HSA onto SPBs were performed by using a Fourier Transform Infrared – Attenuated Total Reflection (FTIR-ATR) spectroscopy setup including an ABB FTLA2000

spectrometer equipped with the PIKE MIRacle ATR sampling accessory in set with a diamond crystal plate. In **Figure 54** the MIRacle ATR setup is schematically presented.

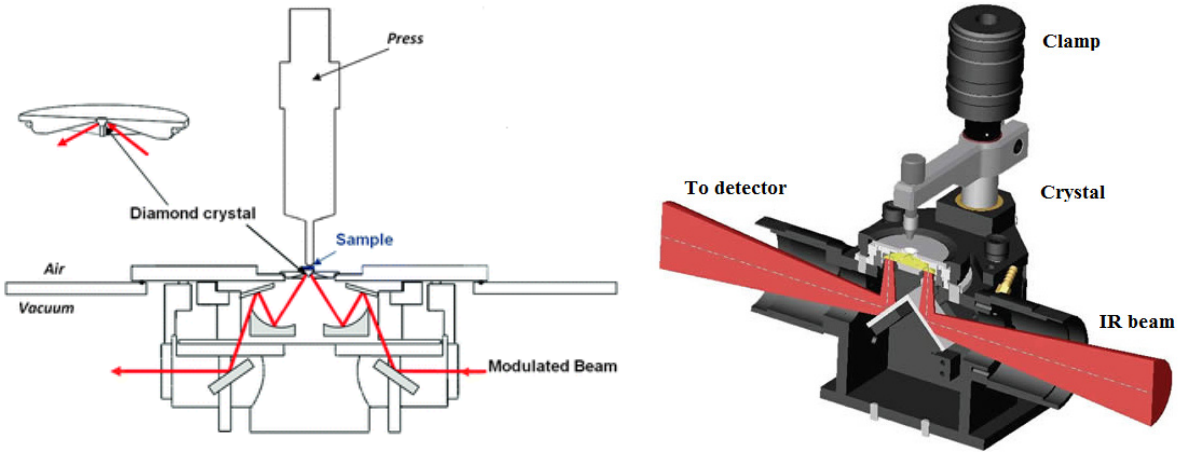

Figure 54. MIRacle-ATR sampling accesories.

6.5.1. FT-IR of HSA Adsorbed onto SPBs

The measurements of the secondary structure of HSA were conducted in 10 mM MOPS buffer *pH* 7.2 at 298 K. To study the structure of the free protein, HSA was dissolved in 10 mM MOPS buffer *pH* 7.2 to a concentration of 5.0 g/L. The effect of immobilization on the secondary structure was analyzed using protein-loaded SPB samples adjusted with 10 mM MOPS buffer to a concentration of 0.5 wt%. In order to avoid any free HSA in SPB-HSA sample the molar ratio between protein and SPB-particles was adjust based on the ITC results obtained at 298 K. Measurements of the pure SPB particles were accomplished at concentration of 0.5 wt% of the SPB suspension.

All samples were filtered through a membrane syringe filter (0.8 µm pore width, PALL, Acrodisc) in order to remove any dust contamination. Then the sample solution was injected onto the crystal plate fully covering the crystal. The buffer solution was measured as well and used as reference spectrum. The results are discussed in section **4.3.1.**

6.5.2. FT-IR of PPBs

Spectra were recorded at 2 cm^{-1} resolution and 22680 scans were collected. A representative samples of surface functionalized with P*t*BA/PAA brush were thoroughly cleaned with 1% SDS solution, DI water and ethanol and then dried under nitrogen. The samples were placed at the sample slot of FTIR instrument and pressed with a swivel pressure tower. A gold surface that was afterwards functionalized with P*t*BA/PAA brush was measured as well and used as background for further measurements.

The FT-IR spectrum (see **Figure 55**) contains the expected peaks at 1731 cm^{-1} (C=O stretch)[141] and 2973 cm^{-1} (asymmetric CH3 stretching vibration)[141] and a doublet at 1370/1395 cm^{-1} (symmetric methyl deformation mode), showing the presence of the tBA moiety.[141] The PtBA chains were converted to PAA *via* acidic hydrolysis. This was achieved by immersing the

samples in a solution containing 35 mL of dichloromethane and 3 mL of trifluoroacetic acid for 18 h in an ice bath (~0 °C).

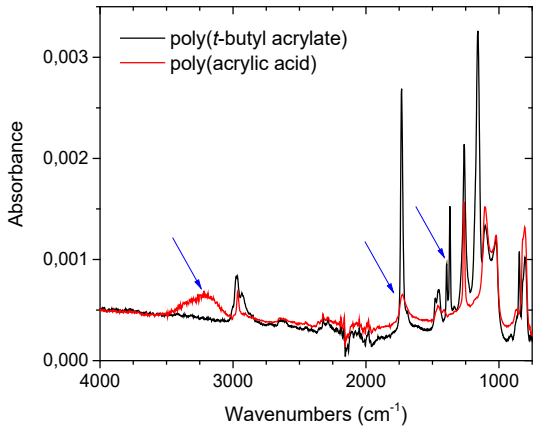

Figure 55. FT-IR spectra of poly(tert-butyl acrylate) (PtBA) and poly(acrylic acid) (PAA).

The FT-IR spectrum after hydrolysis showed a broad peak at 3000 – 3500 cm $^{-1}$, a broadening of the peak at 1731 cm $^{-1}$ and the loss of the peaks associated with the pendant methyl groups (see Figure 1), thereby documenting the successful cleavage of the *t*BA moiety.[141] A similar procedure was used recently in synthesis of poly(methacrylic acid) brush from silica nanoparticles.[361]

6.6. ITC Measurements

The ITC measurements were conducted on a VP-ITC instrument (MicroCal, GE Healthcare, Freiburg, Germany) and on a Microcal iTC$_{200}$ instrument (MicroCal, Northampton, MA), booth controlled by the VPViewer software (MicroCal).

The reference- and the sample cell of the ITC machines are composed of Hastelloy® Alloy C-276. The working volume of the sample cell is 1.43 mL (VP-ITC) and 200 µL (iTC$_{200}$) while string syringe allows to inject 280 µL (VP-ITC) or 39 µL (iTC$_{200}$) of reactant in total. For the experiments conducted on a VP-ITC instrument the reference power was set to 15 µcall/sec with the stirring speed in the sample cell of 307 rpm. For the experiments conducted on a iTC$_{200}$ instrument the reference power was set to 10 µcall/sec with the stirring speed in the sample cell of 750 rpm. After thermal equilibration the protein solution was titrated dropwise into the sample cell and Q was evaluated for each injection step (see section **3.3.2.3.**). During the experiment the injection volume as well as the time interval between the injections were kept constant. The same experimental procedure was applied in order to determine the heat of dilution. After each measurement both sample cells as well as the syringe were very thoroughly cleaned using 2% of Decon90 solution and ultrapure Milli-Q water.

Table 20. Experimental parameters for dPGS-divalent ion measurements, conducted on a VP-ITC instrument.

System	Buffer/Ionic strength	T [K]	c (++) [mM][a)]	c (dPGS) [mM]
Ca^{2+}/dPGS	MOPS/16.5 mM	303	5.1	0.032
Mg^{2+}/dPGS	MOPS/16.5 mM	303	5.0	0.032
	MOPS/19.1 mM	303	5.0	0.020
	MOPS/16.4 mM	303	10.0	0.039
	MOPS/14.0 mM	303	15.2	0.064

[a)] *concentration of divalent ions in the injectant.*

Table 21. Experimental parameters for Hep-Lys measurements, conducted on a VP-ITC instrument.

System	Buffer/Ionic strength	T [K]	c (protein) [mM]	c (Hep) [mM]
Lys/Hep	Phosphate buffer/25 mM	288, 293, 298, 303, 308, 310	1.4×10^{-2}	2.0×10^{-4}
	Phosphate buffer/35 mM	288, 293, 298, 303, 310	1.2×10^{-2}	2.4×10^{-4}
	Phosphate buffer/50 mM	288, 293, 298, 303, 310	1.4×10^{-2}	2.9×10^{-4}
	Phosphate buffer/75 mM	288, 293, 298, 303, 310	7.8×10^{-2}	6.6×10^{-4}
	Phosphate buffer/100 mM	288, 293, 298, 303, 310	15.6×10^{-2}	22.7×10^{-4}

Table 22. Experimental parameters for β-CD-S-Lys measurements, conducted on a VP-ITC instrument.

System	Buffer/Ionic strength	T [K]	c (protein) [mM]	c (β-CD-S) [mM]
Lys/β-CD-S	Phosphate buffer/20 mM	310	1.3	0.08
	Phosphate buffer/30 mM	310	1.3	0.08
	Phosphate buffer/40 mM	310	1.8	0.10
	Phosphate buffer/60 mM	310	3.0	0.18
	Phosphate buffer/100 mM	310	3.0	0.18

Table 23. Experimental parameters for SPB-HSA measurements, conducted on a VP-ITC instrument.

System	Buffer/Ionic strength	T [K]	c (protein) [mM]	c (SPB) [mM]
HSA/SPB-PAA	MOPS/20 mM	298	0.359	3.64×10^{-6}
		300	0.363	3.13×10^{-6}
		302	0.362	2.91×10^{-6}
		304	0.525	3.50×10^{-6}
		306	0.519	2.91×10^{-6}
		308	0.686	3.43×10^{-6}
		309	0.682	3.05×10^{-6}
		310	0.681	2.70×10^{-6}
	MOPS/50 mM	310	0.680	2.70×10^{-6}

6.7. QCM-D Measurements

HSA adsorption onto planar PAA brush as a function of ionic strength and pH was studied using the quartz crystal microbalance with dissipation (QCM-D) from QSense which measures *f* and *D* for the first four odd harmonic of the crystals. The crystals used in the experiments were gold coated and had a nominal center frequency of 5 MHz.

Thoroughly cleaned and dried under nitrogen QCM sensors functionalized with PAA brush were placed inside of the QCM removable flow modules. Then the available 40 µL volume above the sensors was filled with starting buffer and the sensors were allowed to equilibrate within for 10 minutes. Afterwards at constant temperature of 25°C and at constant pump rate of 5 µL/min the frequency and dissipation were measured in order to establish the baseline.

6.7.1. Determination of the Number of HSA Molecules per PAA Chain

For an arbitrary area of $S = 20\ nm$ with grafting density of $\sigma = 0{,}35 \pm 0{,}13\ nm^{-2}$ we have approximately $N_c = 7 \pm 3$ PAA chains.
Mass density at Step II of ionic strength cycle is $353\ Da/Å^2$ (see Table 7 in section **4.5.4.**), which for an arbitrary area *S* give *706000 Da*. By taking into account the molecular weight of a single HSA molecule ($M_{w,\ HSA} = 66{,}5\ kDa$) we get $N_p = 11$ HSA molecules per area *S*. Keeping in mind that area *S* is occupied by approximately *7* PAA chains brings us to the number of HSA molecules per PAA chain ($N_{p/c}$) which in this case is *1,5*. It means that approximately three HSA molecules are adsorb per two PAA chains.

In the same fashion we can evaluate that at Step X of the pH cycle $N_{p/c} = 1$, meaning that one HSA molecule is adsorb per one PAA chain.

7. Supplement

7.1. Calculation of the Bulk Concentration c_i^0 for the Ion-Specific PPB Model

The bulk concentration of divalent and monovalent counterions c_i^0 (see section **3.3.4.2.**) is updated during each injection in the following way.:

A. Solve PB equation (Eq. (49)) (Unknown parameter c_i^0 is guessed from the outcome of previous injection.)

B. Find $c^0{}_{++}$ and iterate

Total known molar concentration of Mg^{2+} per molar concentration of dPGS: $c^{tot}{}_{++}$

The total amount of Mg^{2+} is conserved within the titration volume V (spherical cell of radius R).

$$\int_0^R c_{++}(r)4\pi r^2 dr = c_{++}^0 \int_0^R e^{-2\Phi(r)-\beta\Delta\mu_{int,++}(r)}4\pi r^2 dr = c_{++}^{tot}\left(\frac{4\pi}{3}R^3\right) \Rightarrow c_{++}^0 = \frac{c_{++}^{tot}\left(\frac{4\pi}{3}R^3\right)}{\int_0^R e^{-2\Phi(r)-\beta\Delta\mu_{int,++}(r)}4\pi r^2 dr}$$

Substitute $c^0{}_{++}$ back in Eq. (49) and repeat steps A and B till $c^0{}_{++}$ is converged.

C. Calculate bound Mg^{2+} ions after convergence of $c^0{}_{++}$ using Eq. (48), and use $c^0{}_{++}$ as initial guess for next injection.

Follow the same steps for the convergence of the bulk Na^+ concentration $c^0{}_+$.

7.2. Materials and the ITC Isotherms for dPGS-Divalent Ion Interaction Described in Sections 4.1.2.1. and 4.1.2.2.

7.2.1. Materials

Sodium phosphate dibasic (Na_2HPO_4) and sodium phosphate monobasic (NaH_2PO_4) were purchased from Fluka and used directly. Sodium chloride (NaCl), magnesium chloride hexahydrate ($MgCl_2 \cdot 6H_2O$) and Lysozyme from chicken egg-white (M_{Lys} =14,3 kDa) were received from Sigma-Aldrich and used without further purification.

dPGS was obtained by sulfation of a fractionated hyperbranched polyglycerol.[362] **Table S1** gives the molecular weight $M_{n,dPGS}$ and the degree of sulfation (DS) of dPGS as determined from the weight percentage of sulfur.[278]

Table S1. Structural properties of dPGS.

	dPGS
$M_{n,dPG}$ (kDa)	2.6
DS (%)	97
N_{ter}	34
$M_{n,dPGS}$ (kDa)	6.5

DS: the degree of sulfation determined from elemental analysis. N_{ter}: the number of terminal sulfate groups. The number-average molecular weight M_n of the dPG core as well as for dPGS was determined by gel permetation chromatography.

7.2.2. ITC Isotherms

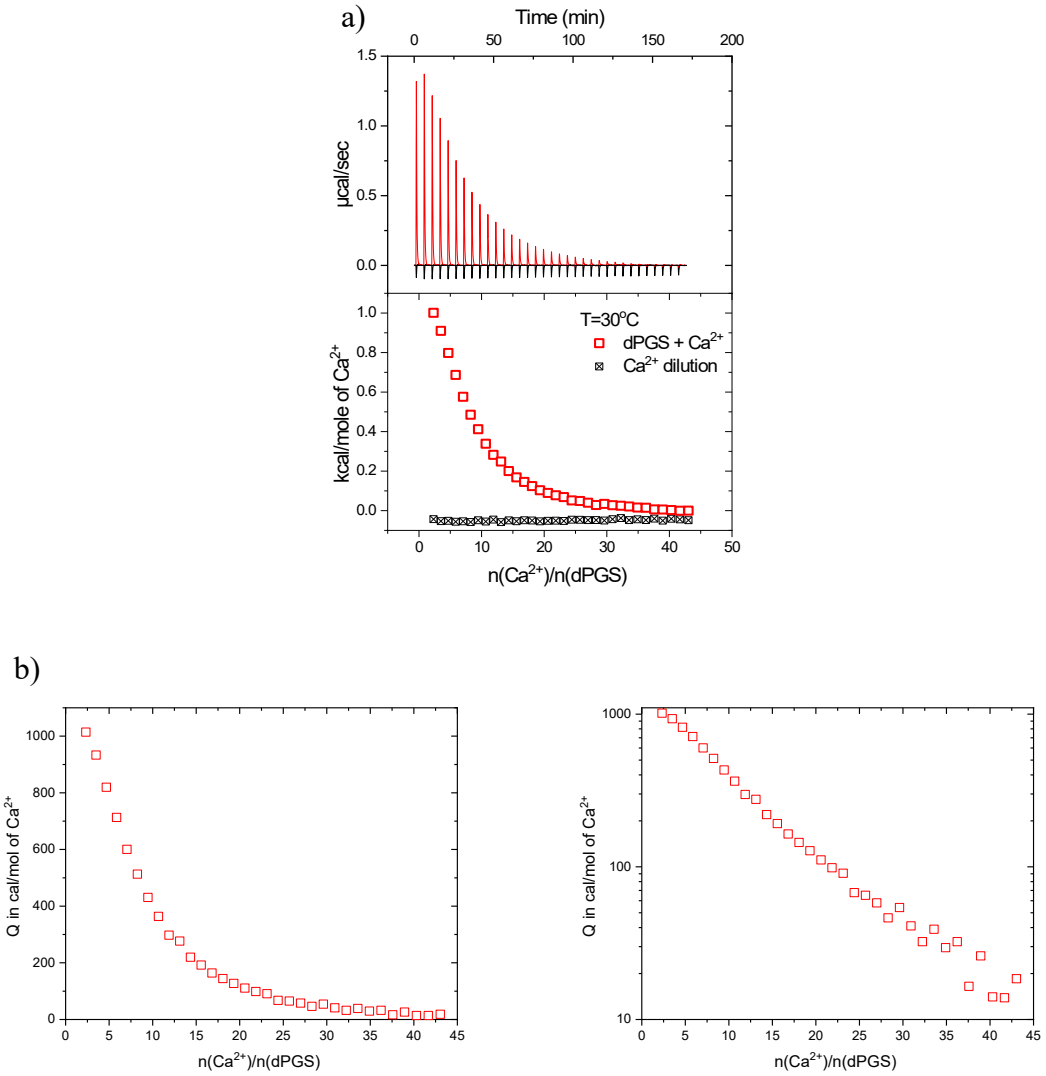

Figure S1. **(a)** ITC data for the binding of Ca^{2+} ions to dPGS at pH 7.2 and temperature of 30°C in 10 mM MOPS buffer. The upper panel shows the raw data of the binding (red spikes) and the dilution of Mg^{2+} by buffer (black spikes). The integrated heats of each injection are shown in the lower panel. **(b)** Binding isotherms for Ca^{2+} - dPGS interaction, presented on a typical ITC plot (left-handed) and semi-logarithmic plot (right-handed). Resulting $[Ca^{2+}]^{tot}$: 0,8 mM. Plots refer to section **4.1.2.1.**

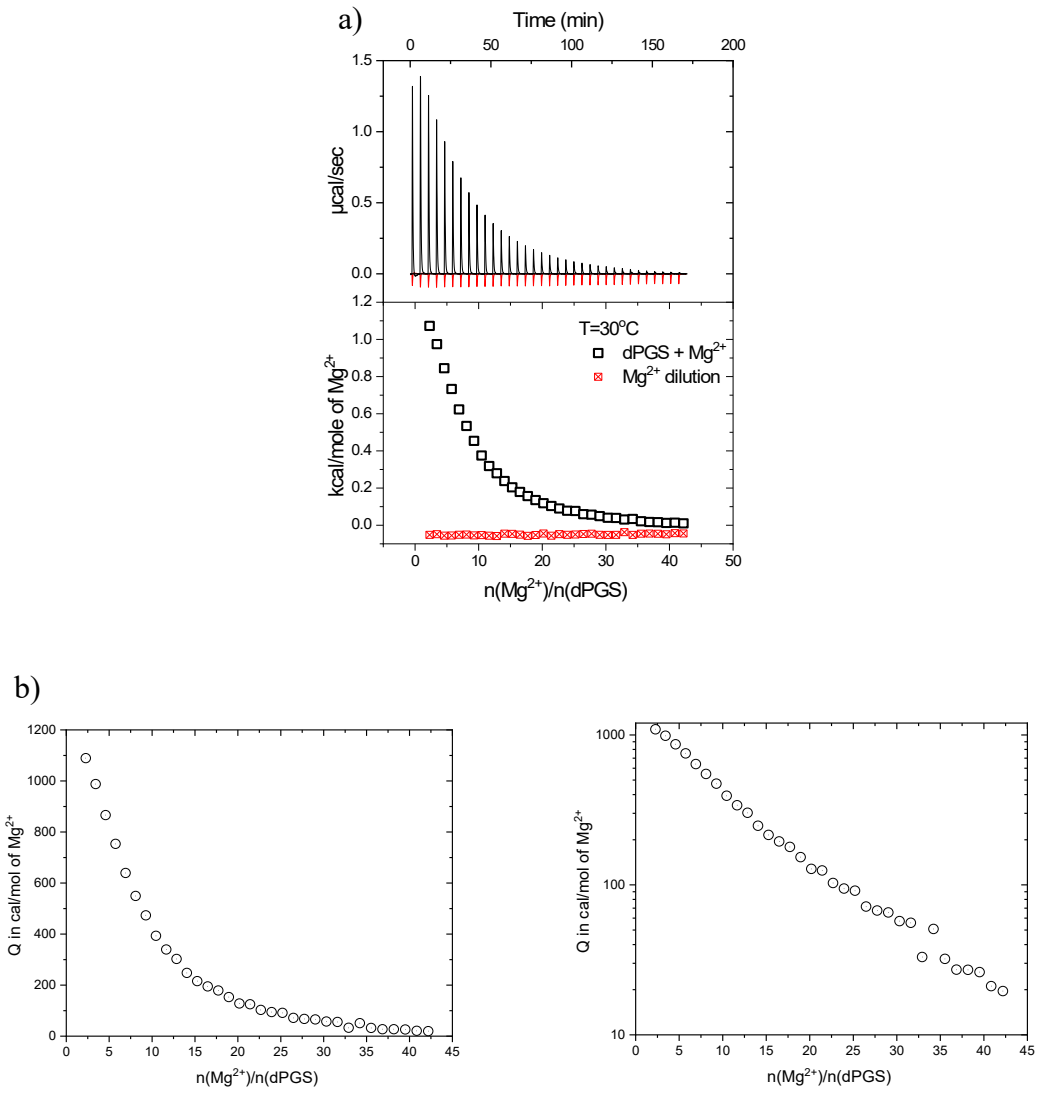

Figure S2. **(a)** ITC data for the binding of Mg^{2+} ions to dPGS at pH 7.2 and temperature of 30°C in 10 mM MOPS buffer. The upper panel shows the raw data of the binding (black spikes) and the dilution of Mg^{2+} by buffer (red spikes). The integrated heats of each injection are shown in the lower panel. **(b)** Binding isotherms for Mg^{2+} - dPGS interaction, presented on a typical ITC plot (left-handed) and semi-logarithmic plot (right-handed). Resulting $[Mg^{2+}]^{tot}$: 0,8 mM. Plots refer to section **4.1.2.1.**

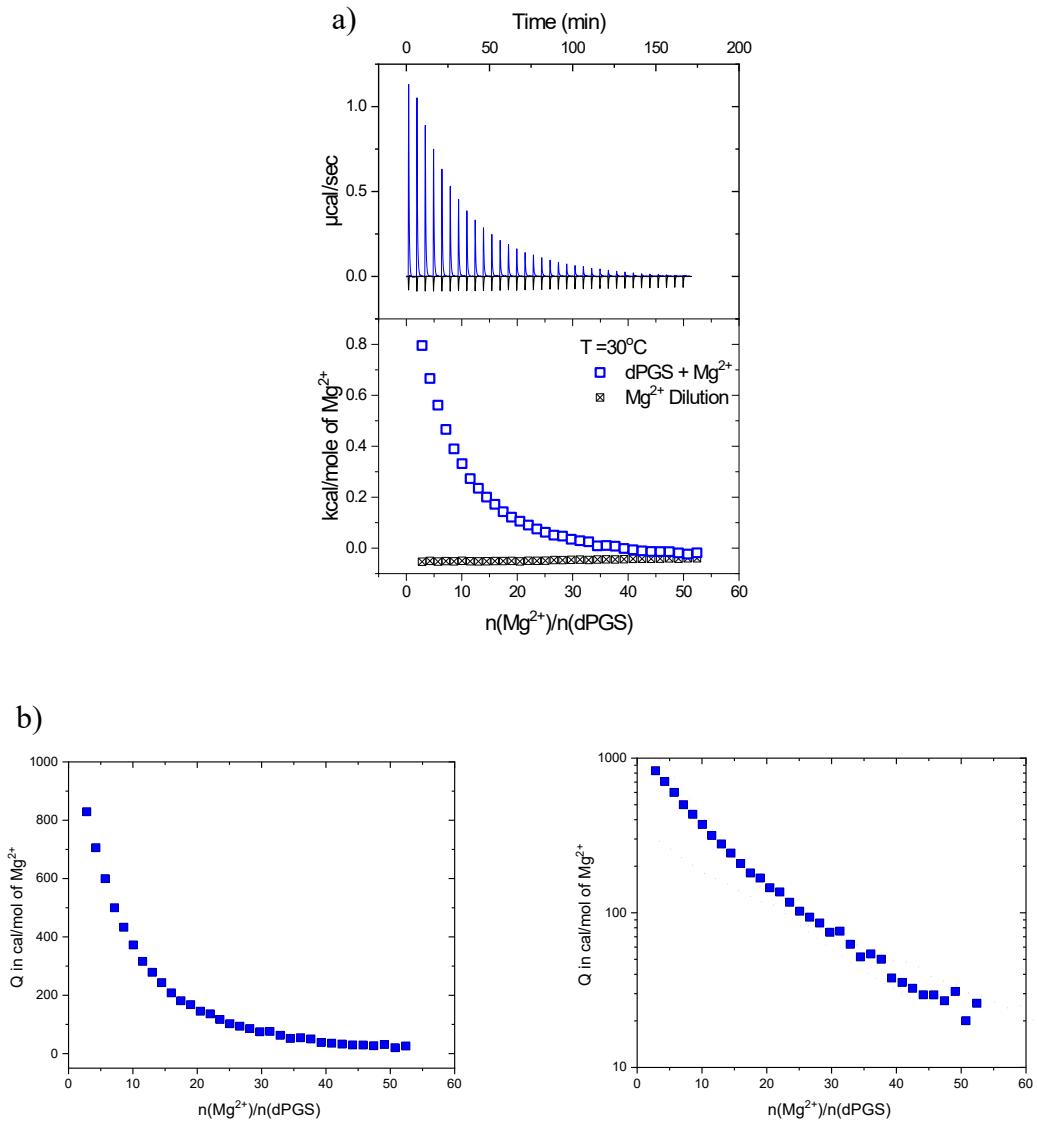

Figure S3. **(a)** ITC data for the binding of Mg^{2+} ions to dPGS at pH 7.2 and temperature of 30°C in 10 mM MOPS buffer. The upper panel shows the raw data of the binding (blue spikes) and the dilution of Mg^{2+} by buffer (black spikes). The integrated heats of each injection are shown in the lower panel. **(b)** Binding isotherms for Mg^{2+} - dPGS interaction, presented on a typical ITC plot (left-handed) and semi-logarithmic plot (right-handed). Resulting $[Mg^{2+}]^{tot}$: 0,8 mM. Plots refer to section **4.1.2.2.**

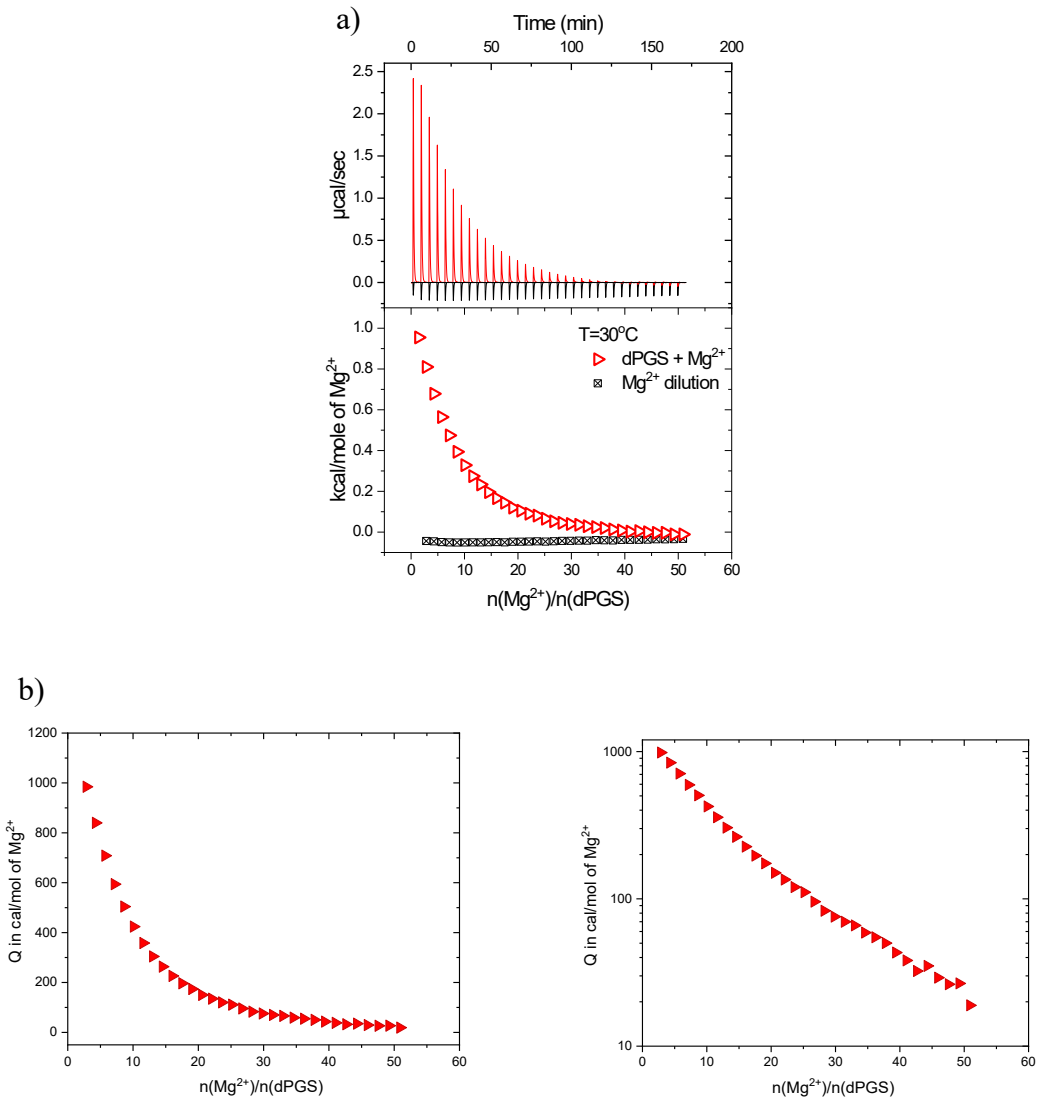

Figure S4. **(a)** ITC data for the binding of Mg^{2+} ions to dPGS at pH 7.2 and temperature of 30°C in 10 mM MOPS buffer. The upper panel shows the raw data of the binding (red spikes) and the dilution of Mg^{2+} by buffer (black spikes). The integrated heats of each injection are shown in the lower panel. **(b)** Binding isotherms for Mg^{2+} - dPGS interaction, presented on a typical ITC plot (left-handed) and semi-logarithmic plot (right-handed). Resulting $[Mg^{2+}]^{tot}$: 1,6 mM. Plots refer to section **4.1.2.2.**

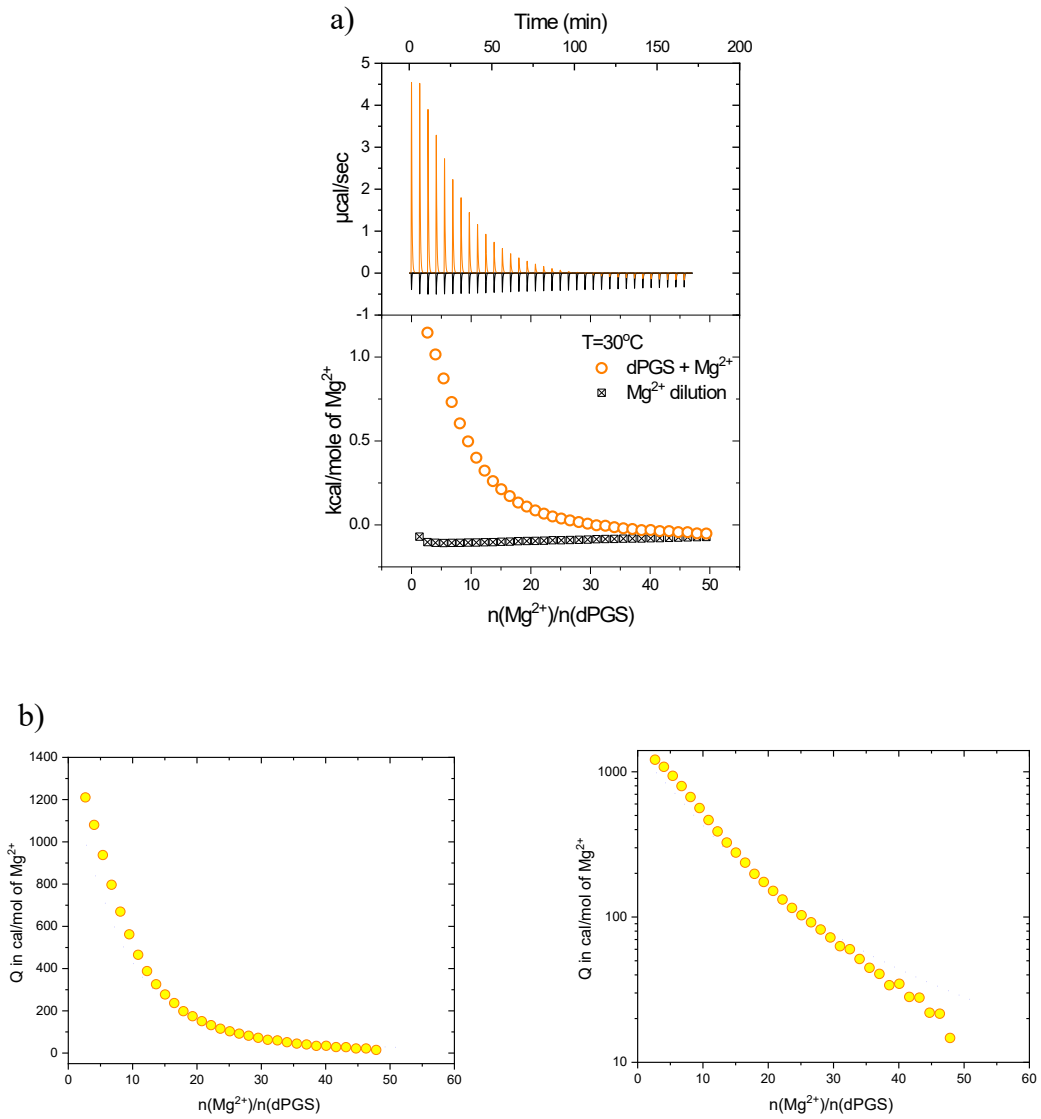

Figure S5. **(a)** ITC data for the binding of Mg^{2+} ions to dPGS at pH 7.2 and temperature of 30°C in 10 mM MOPS buffer. The upper panel shows the raw data of the binding (yellow spikes) and the dilution of Mg^{2+} by buffer (black spikes). The integrated heats of each injection are shown in the lower panel. **(b)** Binding isotherms for Mg^{2+} - dPGS interaction, presented in a typical ITC plot (left-handed) and semi-logarithmic plot (right-handed). Resulting $[Mg^{2+}]^{tot}$: 2,5 mM. Plots refer to section **4.1.2.2.**

7.3. Details on Hep-Lys Interaction Described in Chapter 4.2.

7.3.1. ITC Data

Measurements for ionic strength of 25 mM:

Temperature: 15°C

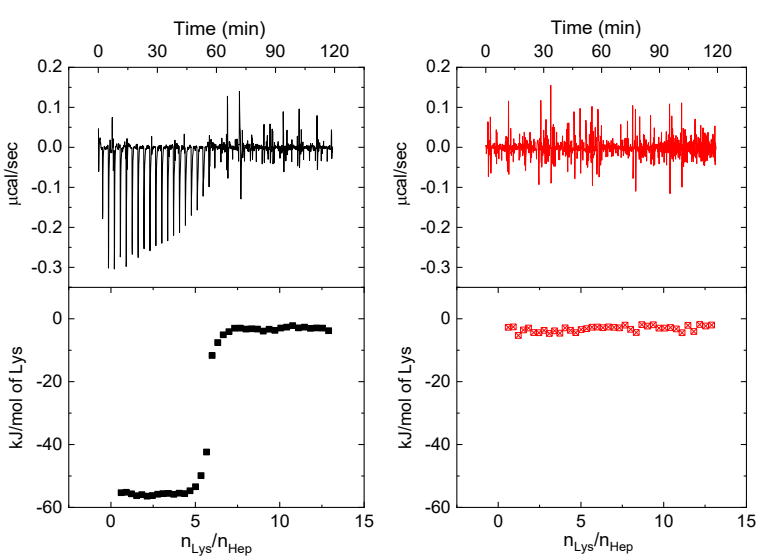

Temperature: 20°C

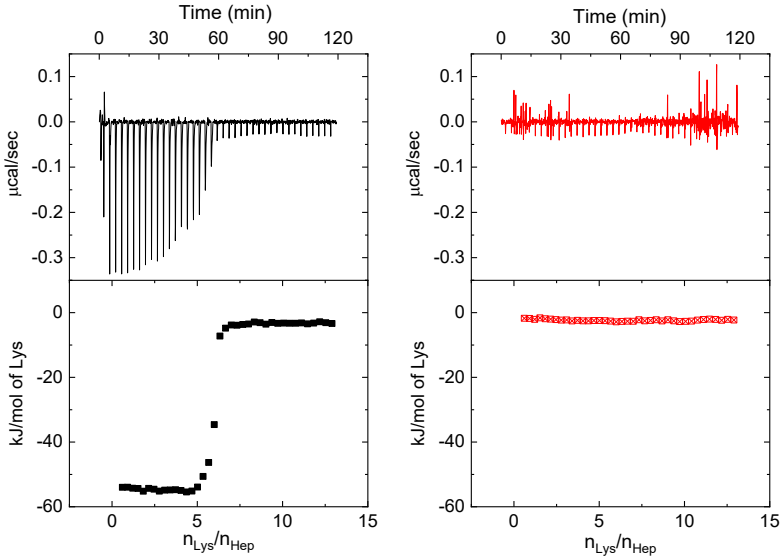

Temperature: 25°C

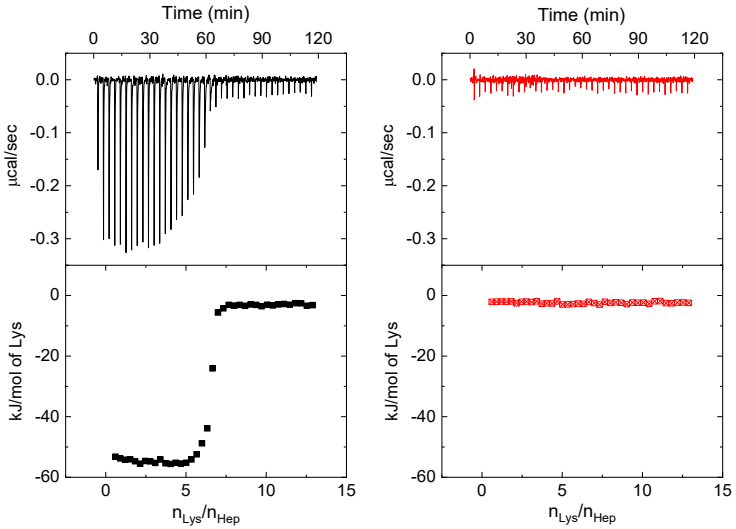

Temperature: 30°C

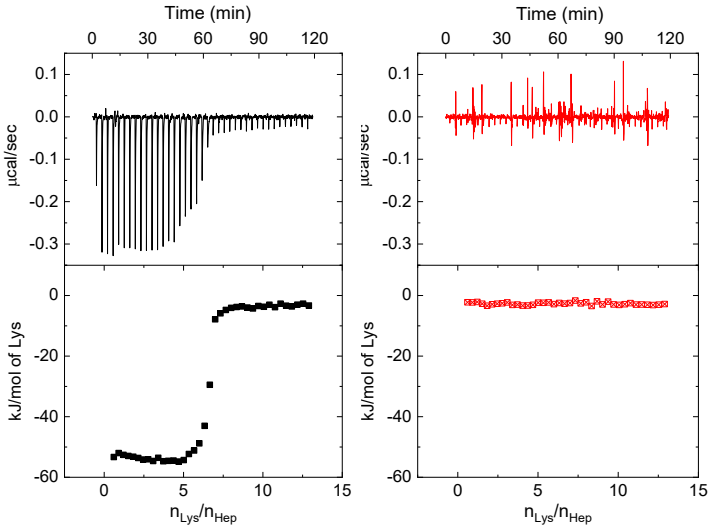

Temperature: 35°C

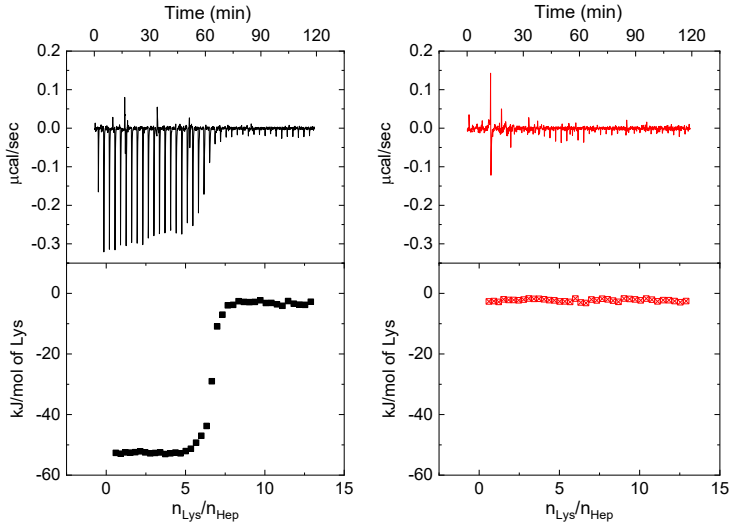

Measurements for ionic strength of 35 mM:

Temperature: 15°C

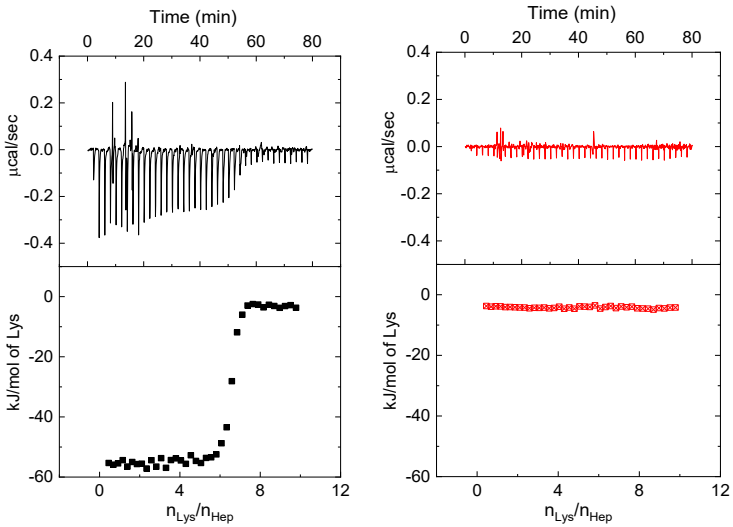

Temperature: 20°C

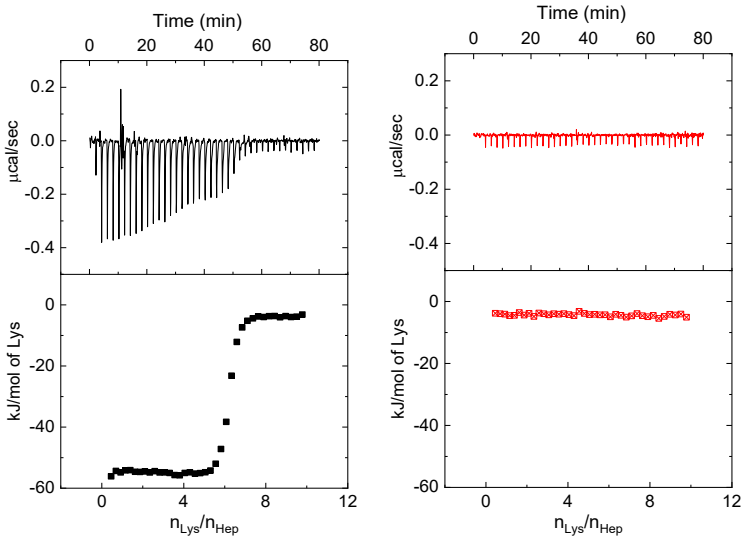

Temperature: 25°C

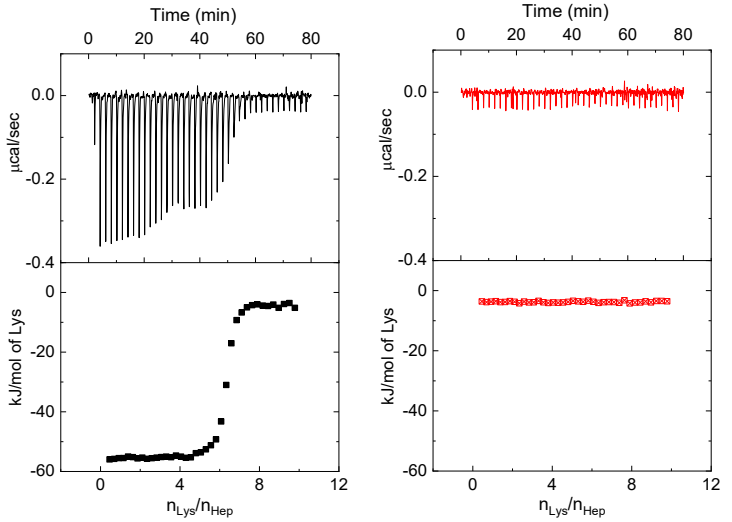

Temperature: 30°C

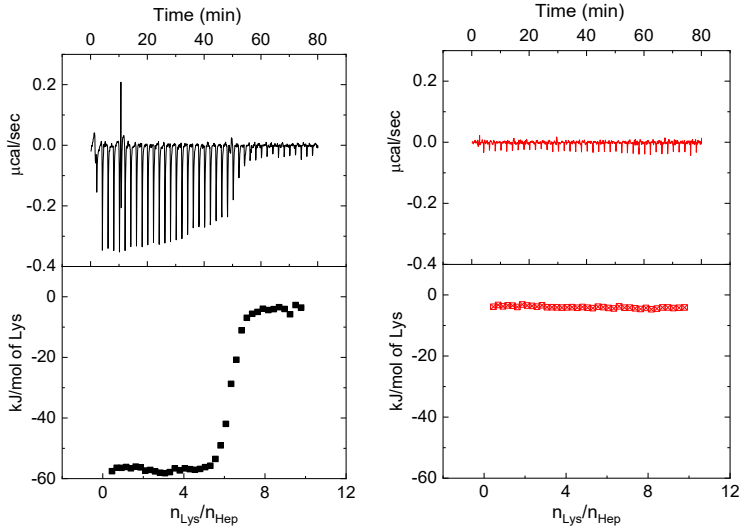

Temperature: 37ºC

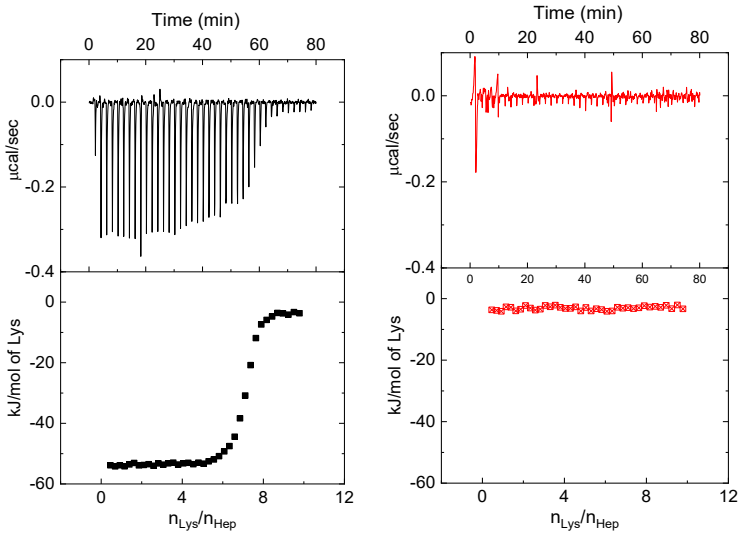

Measurements for ionic strength of 50 mM:

Temperature: 15ºC

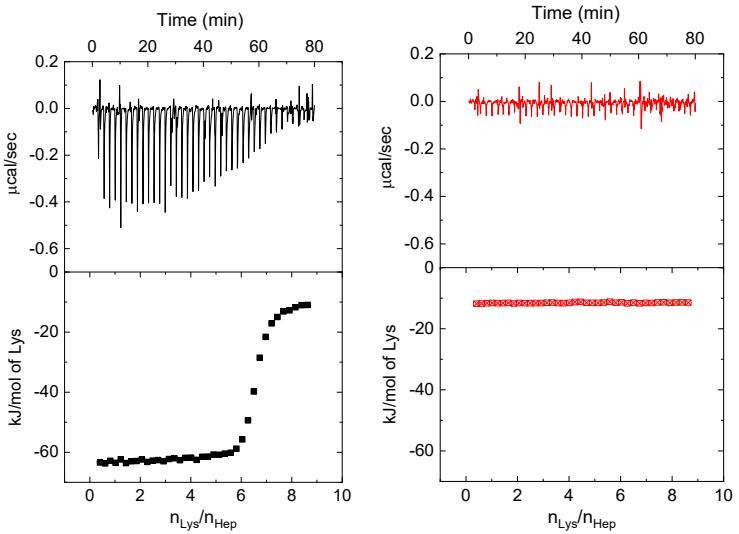

Temperature: 20ºC

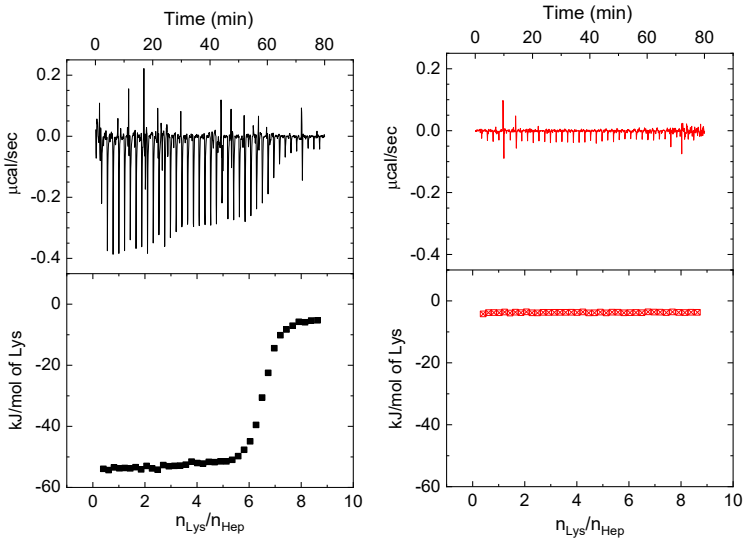

Temperature: 25ºC

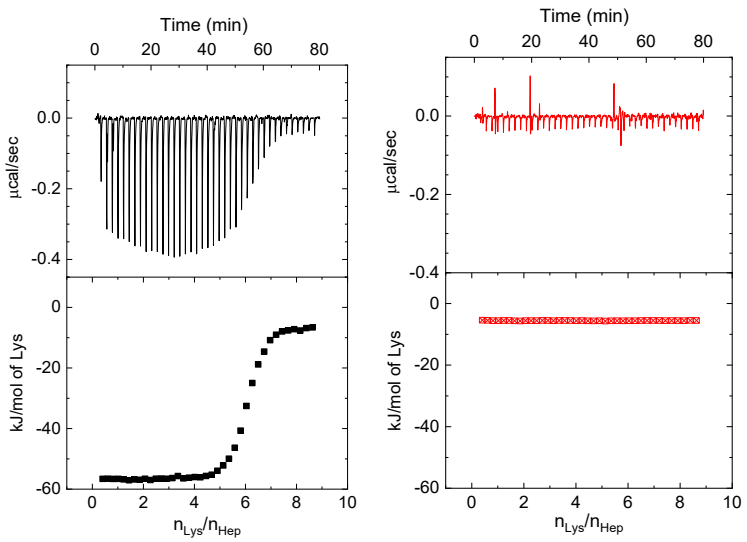

Temperature: 30ºC

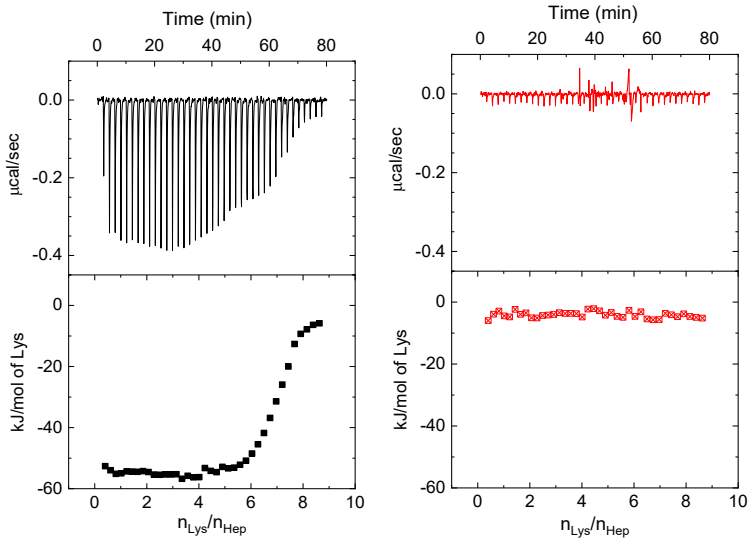

Temperature: 37ºC

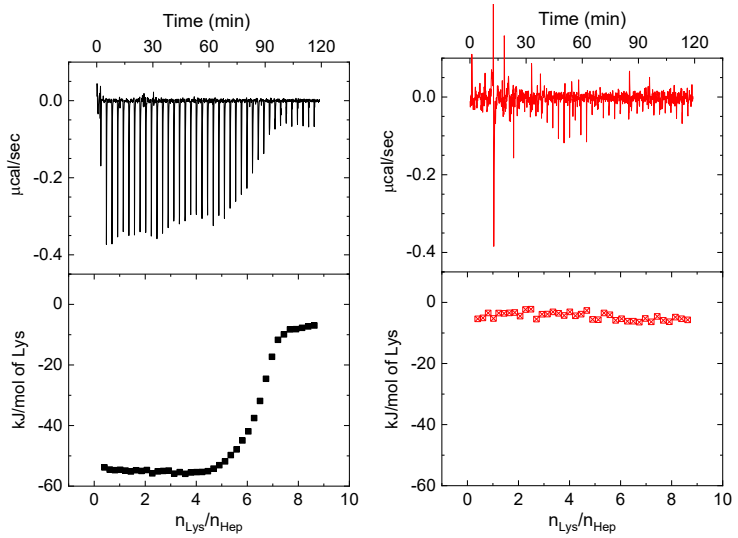

Measurements for ionic strength of 75 mM:

Temperature: 15°C

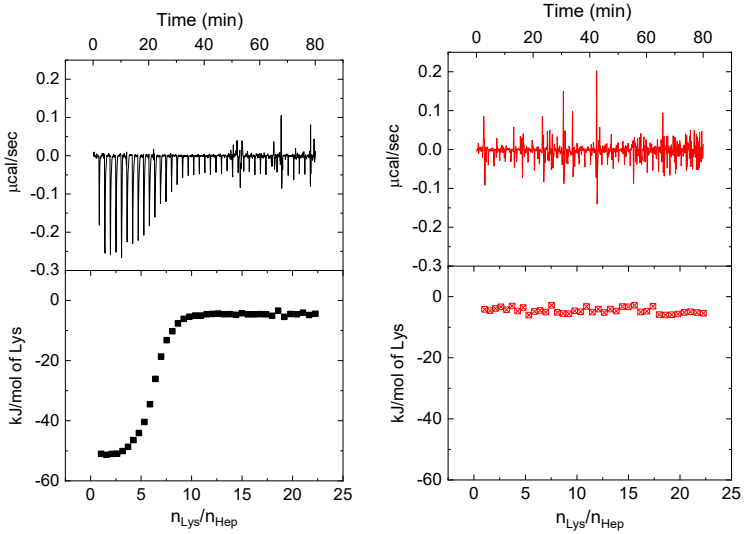

Temperature: 20°C

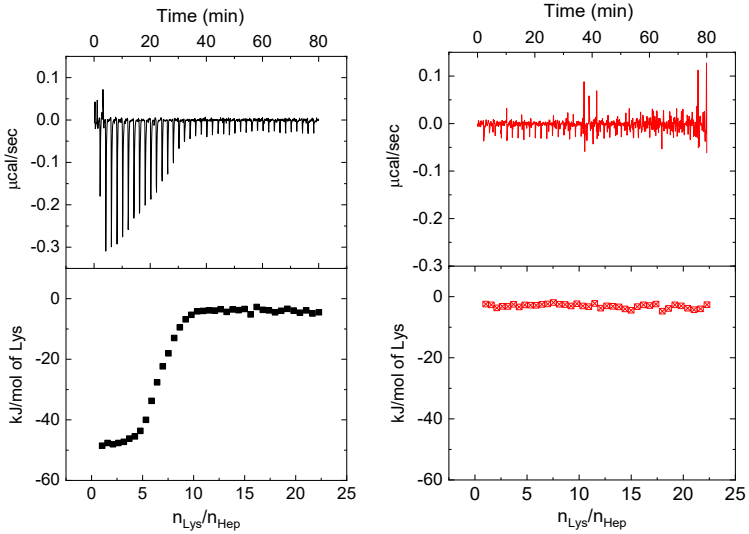

Temperature: 25°C

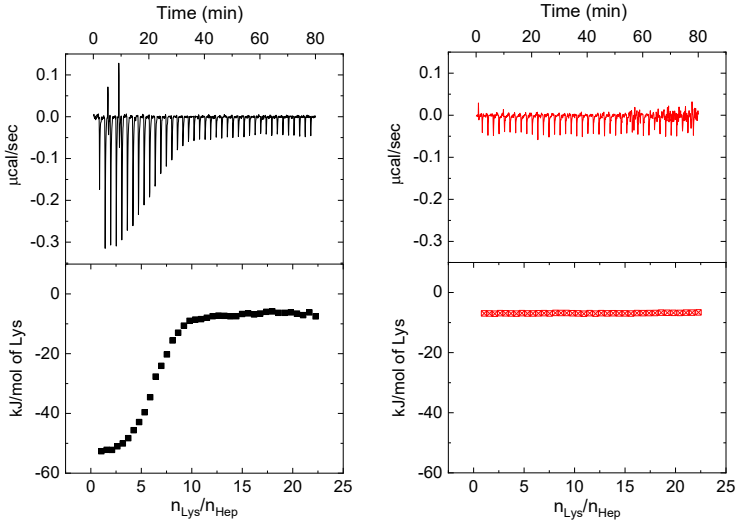

Temperature: 30°C

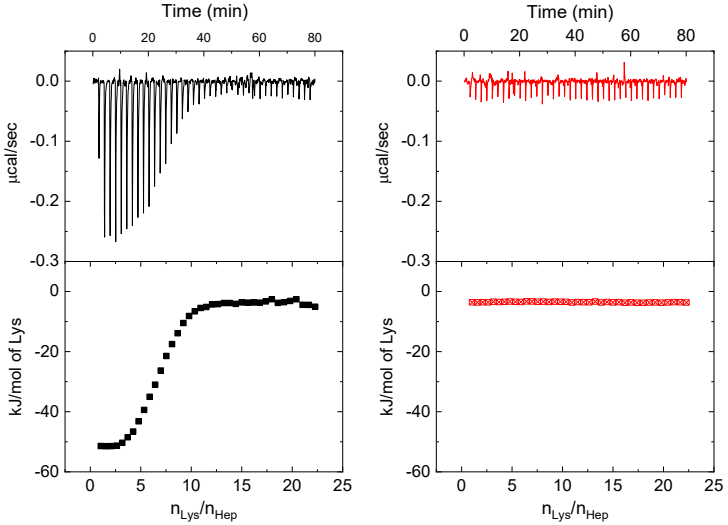

Temperature: 37ºC

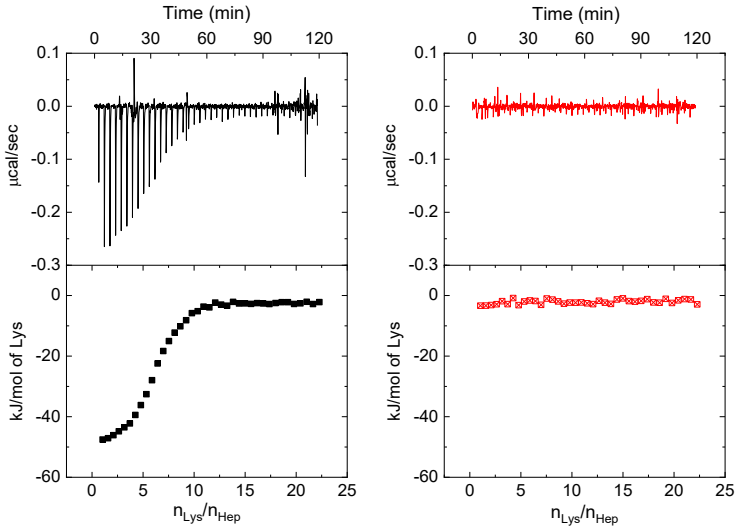

Measurements for ionic strength of 100 mM:

Temperature: 15ºC

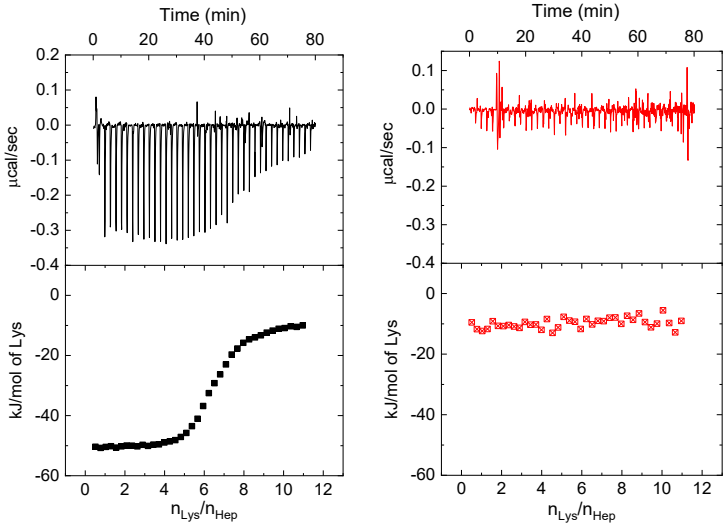

Temperature: 20ºC

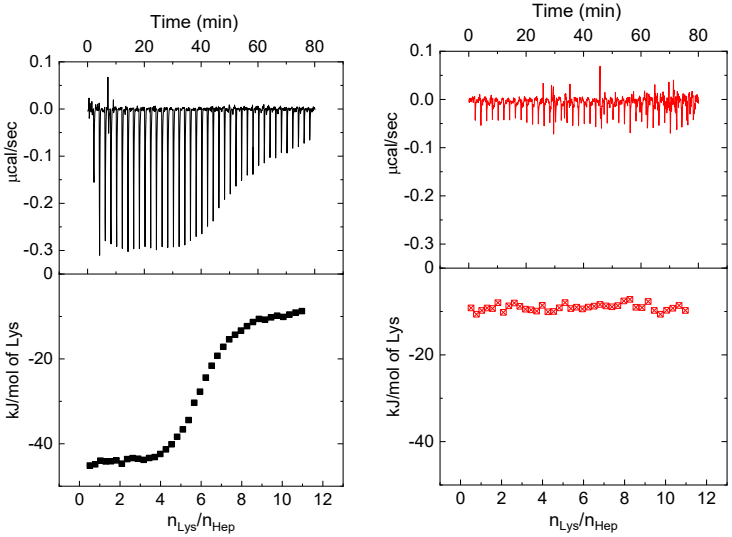

Temperature: 25ºC

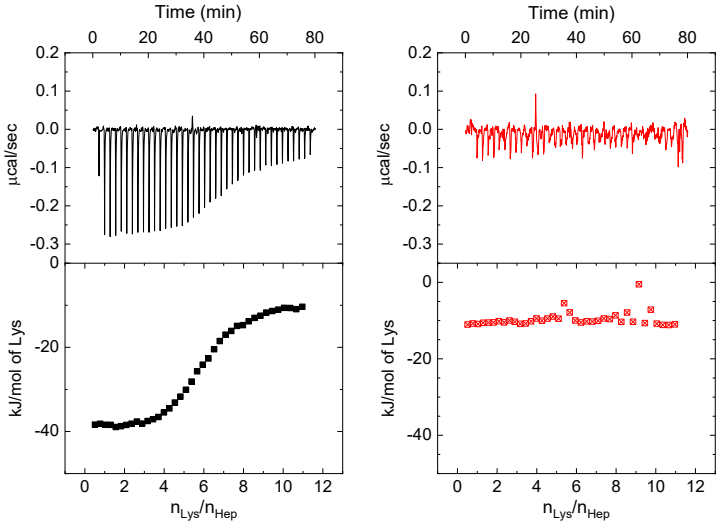

Temperature: 30ºC

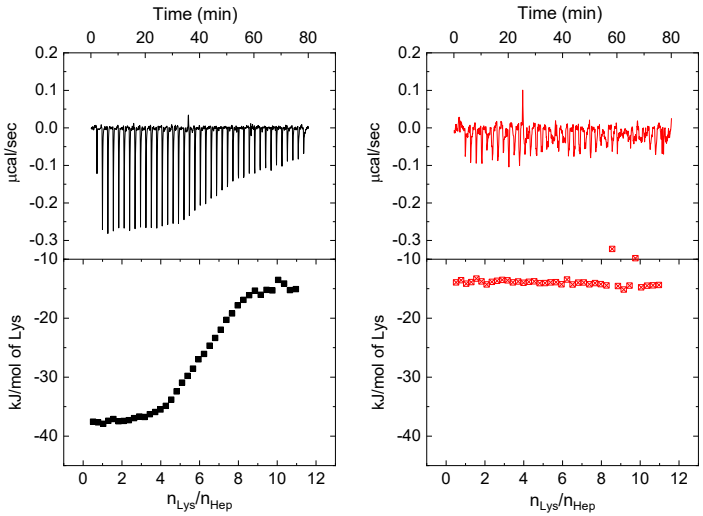

Temperature: 37ºC

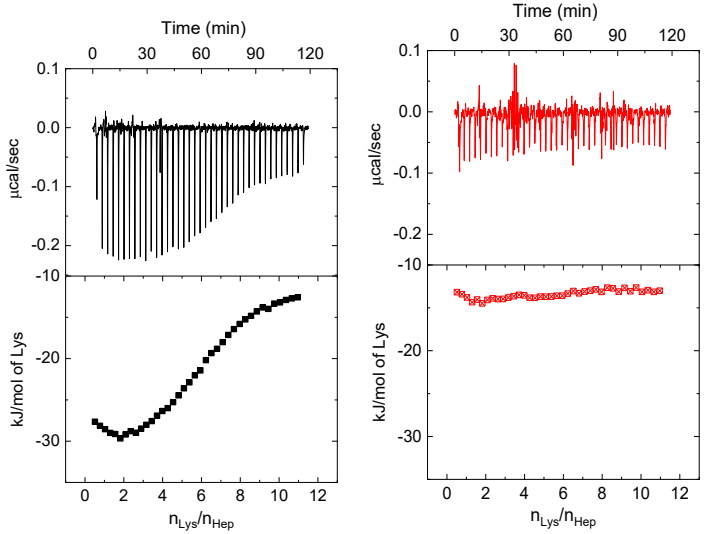

Figure S6. ITC data for the adsorption of Lys to Hep (black color) and corresponding data for the heat of dilution of Lys by buffer (red color). The upper panels show the raw data of adsorption (black curves) and dilution (red curves). The integrated heats of injection are shown in the lower panels. Measurements were conducted in phosphate buffer pH 7.4 with ionic strengths: 25, 35, 50, 75 and 100 mM at different temperatures as indicated above each plot.

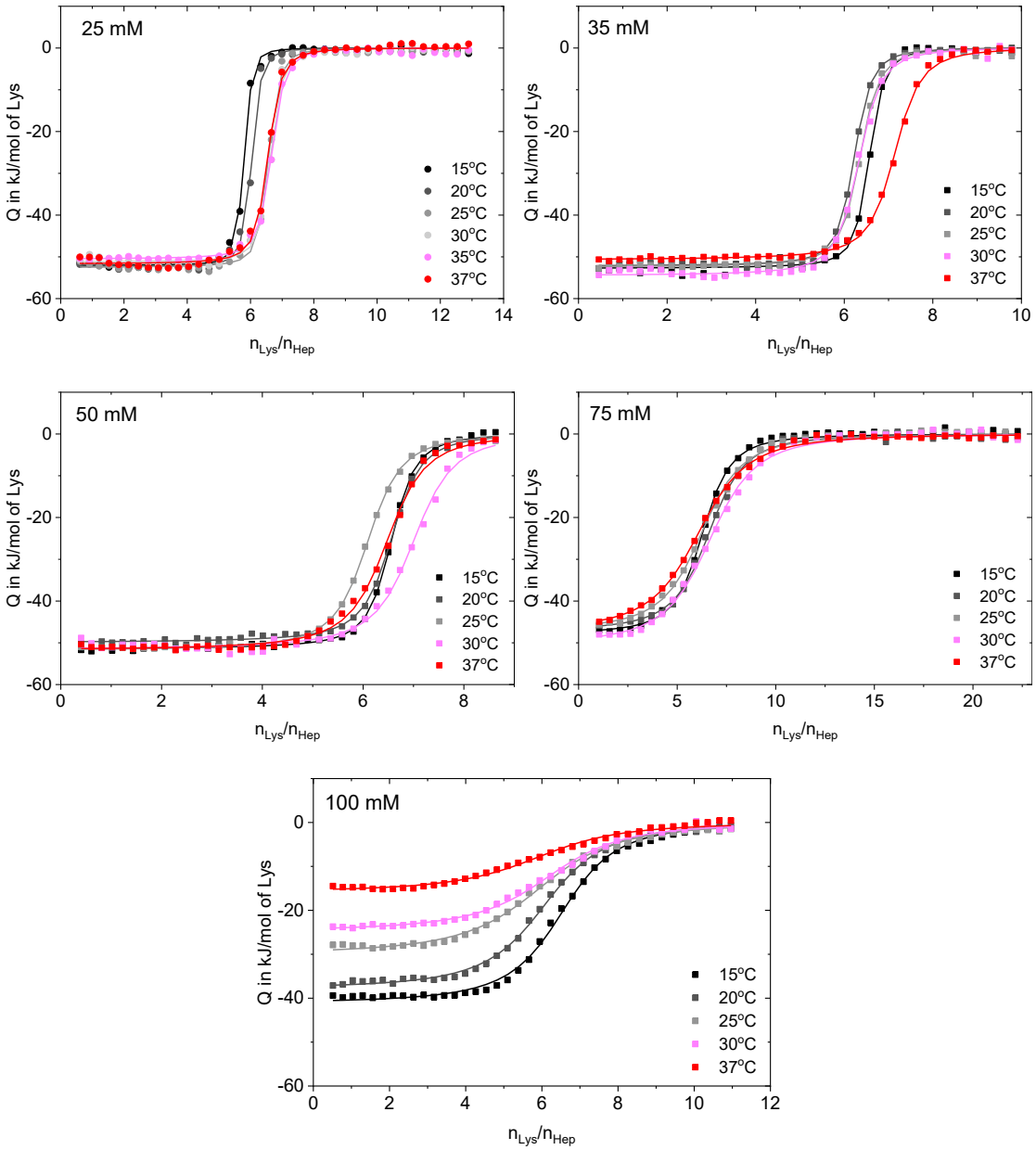

Figure S7. ITC isotherms for the adsorption of Lys to Hep in phosphate buffer pH 7.4 with ionic strengths: 25, 35, 50, 75 and 100 mM at different temperatures. The solid lines presents the fits by the SSIS model.

Table S2. Thermodynamic properties of lysozyme binding to heparin under different conditions of temperature and ionic strength.

I (mM)	Temperature (ºC)	N_b	K_b x 10^{-7} (M^{-1})	ΔH^{ITC} (kJ/mol)	ΔG_b (kJ/mol)	ΔH_b (kJ/mol)	ΔS_b (kJ/mol K)	$T\Delta S_b$ (kJ/mol)	ΔCp_{vH} (kJ/mol·K)[a)]
25	15	5.7	39 ± 6	-52.0 ± 1.3	-47.4 ± 0.3	-53.2 ± 6.1	-0.0200 ± 0.0208	-5.8 ± 6.0	1.3 ± 0.5
	20	5.9	28 ± 4	-52.4 ± 1.3	-47.5 ± 0.2	-47.0 ± 3.7	0.0016 ± 0.0127	0.5 ± 3.7	
	25	6.4	20 ± 2	-52.5 ± 1.3	-47.4 ± 0.2	-40.7 ± 1.7	0.0229 ± 0.0057	6.8 ± 1.7	
	30	6.5	17 ± 2	-51.2 ± 1.3	-47.7 ± 0.2	-34.4 ± 1.9	0.0438 ± 0.0063	13.6 ± 1.9	
	35	6.5	13 ± 1	-50.5 ± 1.2	-47.9 ± 0.1	-28.1 ± 4.1	0.0643 ± 0.0132	19.8 ± 4.1	
	37	6.4	13 ± 2	-51.6 ± 1.3	-48.1 ± 0.2	-25.6 ± 5.0	0.0725 ± 0.0163	22.5 ± 5.0	
35	15	6.4	16.18 ± 1.68	-52.7 ± 1.2	-45.3 ± 0.2	-50.3 ± 8.9	-0.0177 ± 0.0305	-5.1 ± 8.8	1.2 ± 0.7
	20	6.1	11.16 ± 0.71	-52.1 ± 1.1	-45.1 ± 0.2	-44.2 ± 5.6	0.0034 ± 0.0191	1.0 ± 5.6	
	25	6.2	8.93 ± 0.49	-52.4 ± 1.1	-45.4 ± 0.1	-38.1 ± 2.8	0.0242 ± 0.0095	7.2 ± 2.8	
	30	6.2	6.45 ± 0.51	-54.4 ± 1.2	-45.3 ± 0.2	-31.9 ± 3.0	0.0446 ± 0.0099	13.5 ± 3.0	
	37	7.0	5.34 ± 0.30	-50.6 ± 1.1	-45.9 ± 0.1	-23.3 ± 7.2	0.0727 ± 0.0235	22.5 ± 7.3	
50	15	6.5	6.06 ± 0.35	-51.4 ± 1.2	-42.9 ± 0.1	-70.9 ± 6.0	-0.0971 ± 0.0206	-28.0 ± 5.9	3.5 ± 0.6
	20	6.5	6.06 ± 0.35	-49.8 ± 1.1	-42.7 ± 0.1	-53.5 ± 3.4	-0.0371 ± 0.0117	-10.9 ± 3.4	
	25	6.0	4.08 ± 0.16	-51.7 ± 1.1	-42.5 ± 0.1	-36.1 ± 2.3	0.0218 ± 0.0077	6.5 ± 2.3	
	30	6.9	2.84 ± 0.10	-51.4 ± 1.3	-42.8 ± 0.2	-18.6 ± 4.1	0.0797 ± 0.0135	24.2 ± 4.1	
	37	6.4	2.36 ± 0.19	-51.8 ± 1.4	-43.7 ± 0.2	5.7 ± 7.9	0.1593 ± 0.0259	49.4 ± 8.0	
75	15	6.1	1.46 ± 0.10	-47.9 ± 1.3	-39.5 ± 0.2	-58.7 ± 3.8	-0.0666 ± 0.0131	-19.2 ± 3.8	1.9 ± 0.3
	20	6.5	0.97 ± 0.07	-47.2 ± 1.4	-39.2 ± 0.2	-48.9 ± 2.3	-0.0331 ± 0.0080	-9.7 ± 2.3	
	25	6.2	0.70 ± 0.06	-47.1 ± 1.5	-39.1 ± 0.2	-39.2 ± 1.1	0.0002 ± 0.0037	-0.1 ± 1.1	
	30	6.6	0.59 ± 0.04	-50.5 ± 1.6	-39.3 ± 0.2	-29.5 ± 1.3	0.0321 ± 0.0041	9.7 ± 1.2	
	37	6.2	0.47 ± 0.03	-46.5 ± 1.6	-39.6 ± 0.1	-15.9 ± 3.2	0.0766 ± 0.0103	23.7 ± 3.2	
100	15	6.5	0.83 ± 0.05	-41.1 ± 1.1	-38.2 ± 0.1	-71.2 ± 21.4	-0.1143 ± 0.0736	-32.9 ± 21.2	3.8 ± 2.1
	20	6.1	0.62 ± 0.03	-37.8 ± 1.2	-38.1 ± 0.1	-52.3 ± 12.2	-0.0494 ± 0.0418	-14.5 ± 12.2	
	25	6.0	0.37 ± 0.02	-29.9 ± 1.2	-37.5 ± 0.1	-33.5 ± 8.2	0.0145 ± 0.0276	4.3 ± 8.2	
	30	6.2	0.41 ± 0.03	-24.7 ± 1.2	-38.5 ± 0.2	-14.5 ± 14.5	0.0770 ± 0.0480	23.3 ± 14.5	
	37	6.0	0.31 ± 0.03	-15.8 ± 1.3	-38.8 ± 0.2	11.8 ± 28.2	0.1635 ± 0.0926	50.7 ± 28.7	

N_b is the number of adsorbed Lys molecules as determined by ITC. K_b, ΔH^{ITC}, ΔG_b are the experimental values of the binding constant, calorimetric enthalpy and binding free energy, respectively as determined by ITC. ΔH_b, ΔS_b and ΔCp_{vH} are the binding enthalpy, binding entropy and the heat capacity change, respectively as fitted by eq. (20).

With respect to ionic strength only

7.3.2. Effect of Different Concentrations of Lys and Hep on the Binding Constant K_b

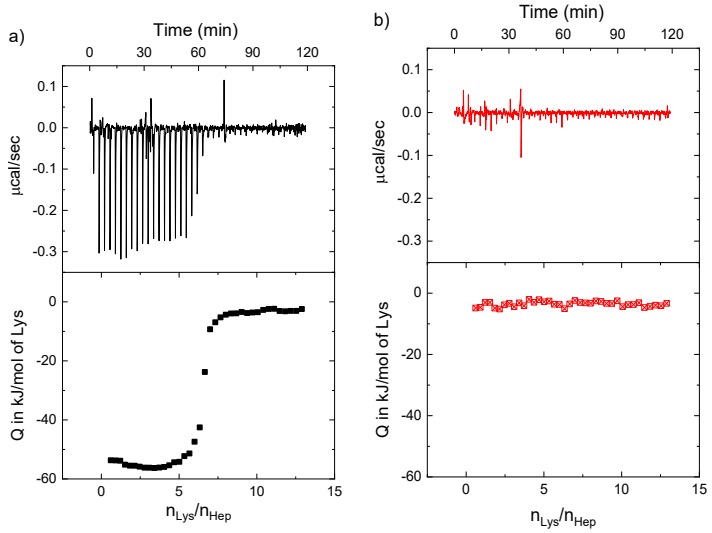

Figure S8. ITC data of the adsorption of Lys to Hep **(a)** and corresponding data of the Lys heat of dilution **(b)**. Measurements were performed at pH 7.4, I = 25 mM and T = 37°C, [Hep] = 2 x 10^{-4} mM. The upper panel shows the raw data of the adsorption and the dilution of Lys by buffer. Presented measurements were performed with iTC 200 calorimeter.

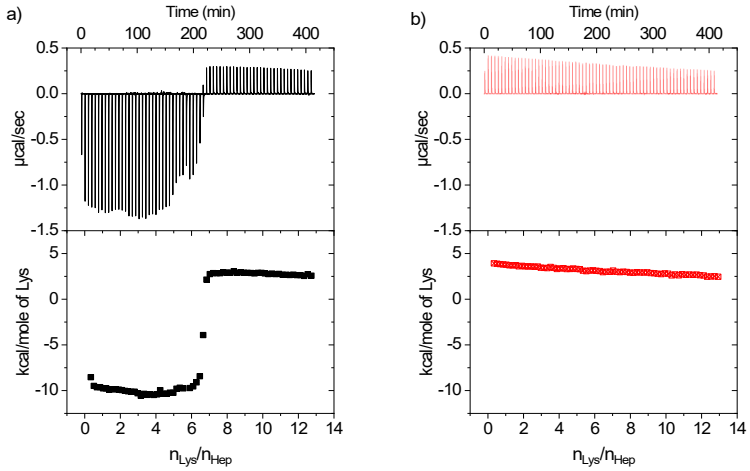

Figure S9. ITC data of the adsorption of Lys to Hep **(a)** and corresponding data of the Lys heat of dilution **(b)**. Measurements were performed at pH 7.4, I = 25 mM and T = 37°C, [Hep] = 7 x 10^{-4} mM. The upper panel shows the raw data of the adsorption and the dilution of Lys by buffer. Presented measurements were performed with VP-ITC calorimeter.

For measurement with iTC 200 calorimeter:

A total of 39 µL of Lys – buffer solution was titrated into the sample cell with 39 successive injections, with stirring rate at 750 rpm and a time interval of 180 s between each injection. The sample cell contained 200 µL of Hep solution in the matching buffer.

For measurement with VP-ITC calorimeter:

A total of 280 µL of Lys – buffer solution was titrated into the sample cell with 70 successive injections, with stirring rate at 307 rpm and a time interval of 360 s between each injection. The sample cell contained 1.43 mL of Hep solution in a matching buffer.

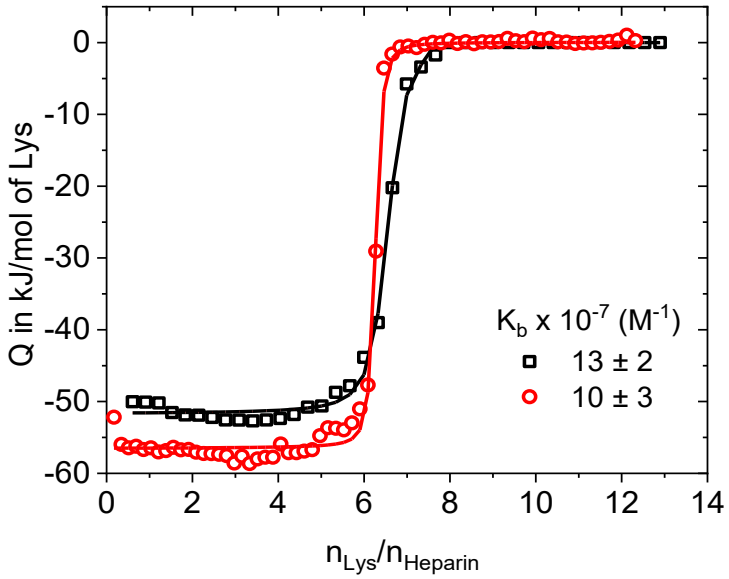

Figure S10. Integrated heats of adsorption of Lys to Hep at constant ionic strength of 25 mM and temperature of 37°C. Red data points represent the binding measured by VP-ITC calorimeter with Hep concentration of 7 x 10^{-4} mM. Black data points represent the binding measured by iTC200 calorimeter with Hep concentration of 2 x 10^{-4} mM. Solid lines presents the single set of identical sites (SSIS) fit.

Table S3. Thermodynamic data of the Lys-Hep binding. Effect of different concentrations and comparison between two types of calorimeters, VP-ITC and iTC200.

[Hep] (mM)	[Lys] (mM)	K_b x 10^{-7} (M^{-1})	ΔH^{ITC} (kJ/mol)	N_b	c*	Calorimeter type
0.0002	0.0115	13 ± 2	-51.6 ± 1.3	6.4	167	iTC200
0.0007	0.0437	10 ± 3	-56.6 ± 1.2	6.2	442	VP-ITC

**Wizeman parameter c = [Hep]*K_b*N_b*

Figure S10 and the thermodynamic data gathered in **Table S3** shows that at the same condition of ionic strength and temperature, the measured binding constant, K_b is independent of the concentration of reagents. Moreover, measured binding is not affected by the difference in the technical conditions of experiments run by different types of calorimeters.

7.3.3. Fractional Charge of Heparin

According to Manning [302,324], the fraction of charge along a linear polyelectrolyte with monovalent counter ions is given by:

$$f(s) = \frac{1}{2\xi}\left(1 - \frac{ln(\kappa b)}{ln(s/b)}\right), \quad \text{(S1)}$$

where ξ is the dimensionless charge density parameter, κ^{-1} is the Debye length, s the distance from the end, and b the spacing between neighboring charged groups. The parameter ξ is given by [302,324]:

$$\xi = \frac{e^2}{4\pi\varepsilon k_B T b} = \frac{l_B}{b}, \quad \text{(S2)}$$

where e is the elementary charge, ε the permittivity of the solvent, k_B the Boltzmann constant, T the temperature, and l_B the Bjerrum length. Chain end effects on the charge of heparins of different molecular weights (number of structural charges) were calculated on the basis of Eqs. (S1) and (S2) assuming 3 sulfate and 1 carboxyl groups per disaccharide unit (**Figure S11**).

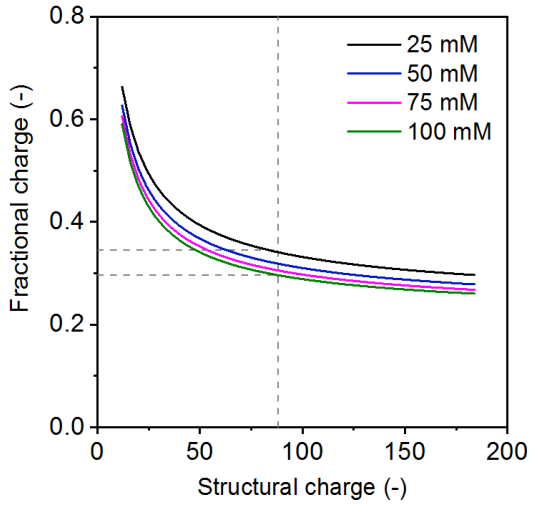

Figure S11. Fractional charge vs. structural charge calculated for heparin according to Eqs. (1) and (2) using the following parameters: c_s = 25 mM, 50 mM, 75 mM, and 100 mM (indicated), b = 0.25 nm, and T = 310.15 K (37°C). The horizontal and vertical dashed lines indicate the structural charge and the range of the resulting fractional charge of the heparin used in this study (22 disaccharide units with, in average, 3 sulfate groups and 1 carboxyl group) for salt concentrations in the range 25 mM to 100 mM.

7.3.4. Ionization of Heparin

The ionization of the heparin was calculated as a function of the pH and salt concentration in the electrolyte applying the theoretical framework developed by Paoletti *et al*. [323,363–365]. According to this approach, the apparent pK_a of a monoprotic polyacid is given by:

$$pK_{\mathrm{a}}(\alpha) = p\mathrm{K_o} + \Delta\mathrm{p}K_{\mathrm{a}}(\alpha), \tag{S3}$$

where the pK_o represents the intrinsic pK of the isolated ionisable repeat unit. The change in the apparent pK_a, ΔpK_a, is determined by the change in the ionic Gibbs free energy with the variation of the degree of dissociation α of the polymer:

$$\Delta\mathrm{p}K_{\mathrm{a}}(\alpha) = \frac{1}{2.303 n_{\mathrm{p}} RT}\frac{\partial G^{ion}}{\partial \alpha} = f\left(\alpha, \xi, C_{\mathrm{p}}, C_{\mathrm{s}}, \epsilon, T\right) \tag{S4}$$

where ξ is a dimensionless parameter characterizing the polyelectrolyte charge density, C_p the concentration of ionisable units, C_s the salt concentration (1:1 electrolyte), ε the dielectric constant, and T the temperature [323,363,365]. Full expressions for Δp$K_a(\alpha)$ under conditions without ion condensation ($\xi \leq \xi_{crit} = 1$) and with ion condensation ($\xi > \xi_{crit} = 1$) can be found in Ref. [323].

Paoletti *et al*. have further shown that for heterogeneous polyelectrolytes consisting of N different monoprotic acids with the molar fraction X_i and the intrinsic pK_o^i the overall intrinsic pK_o is a function of the overall degree of ionization α according to [364,365]:

$$\Delta\mathrm{p}K_{\mathrm{o}}(\alpha) = pK_{\mathrm{o}}^{i} + log\left[\frac{\beta_i}{1-\beta_i}\frac{1-\alpha}{a}\right] \tag{S5}$$

where β_i is the ionization degree of the i-th functional group and α is given by:

$$\alpha = \sum_{i=1}^{N} X_i \beta_i \tag{S6}$$

with

$$X_i = \frac{C_i}{\sum_{i=1}^{N} C_i} \tag{S7}$$

For the ionisation of i-th functional group, the Henderson-Hasselbalch equation can be written in the form:

$$\mathrm{p}K_i(\beta_i) = pH + \log\left[\frac{1-\beta_i}{\beta_i}\right] \quad \text{for } i = 1,\ldots,N \tag{S8}$$

Defining

$$\Delta\mathrm{p}K_i = \mathrm{p}K_1 - pK_i = log\left[\frac{\beta_i(1-\beta_1)}{\beta_1(1-\beta_i)}\right] \text{ for } i = 2,\ldots,N \tag{S9}$$

and

$$q_i = 10^{\Delta pK_i} \quad \text{for } i = 2,\ldots,N \tag{S10}$$

it is possible to obtain β_i as a function of β_1 [365]:

$$\beta_i = \frac{q_i \beta_1}{1+(q_i-1)\beta_1} \qquad \text{for } i = 2,\ldots,N \tag{S11}$$

This set of equations was used to calculate the ionization of the sulphate and carboxyl groups of the heparin and the solution pH as a function of α for the conditions in the ITC experiments taking into account chain end effects on the fractional charge of the heparin used in this study (**Figure S12**).

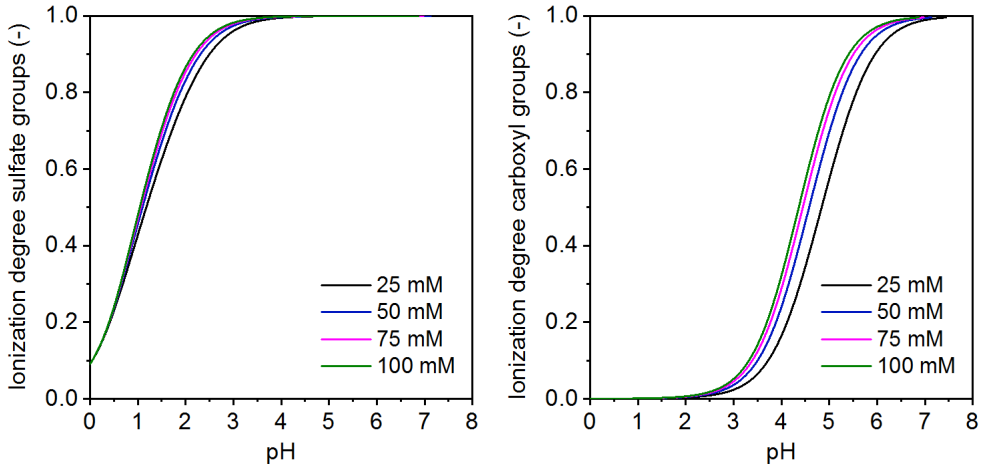

Figure S12. Ionization degree of the sulfate groups (left) and carboxyl groups (right) of heparin as a function of the solution pH for different salt concentrations of the electrolyte. The ionization curves were calculated for a temperature of 37°C taking into account chain end effects on the fractional charge.

7.4. Details on SPB-HSA Interaction Described in Chapter 4.4.

7.4.1. ITC Data

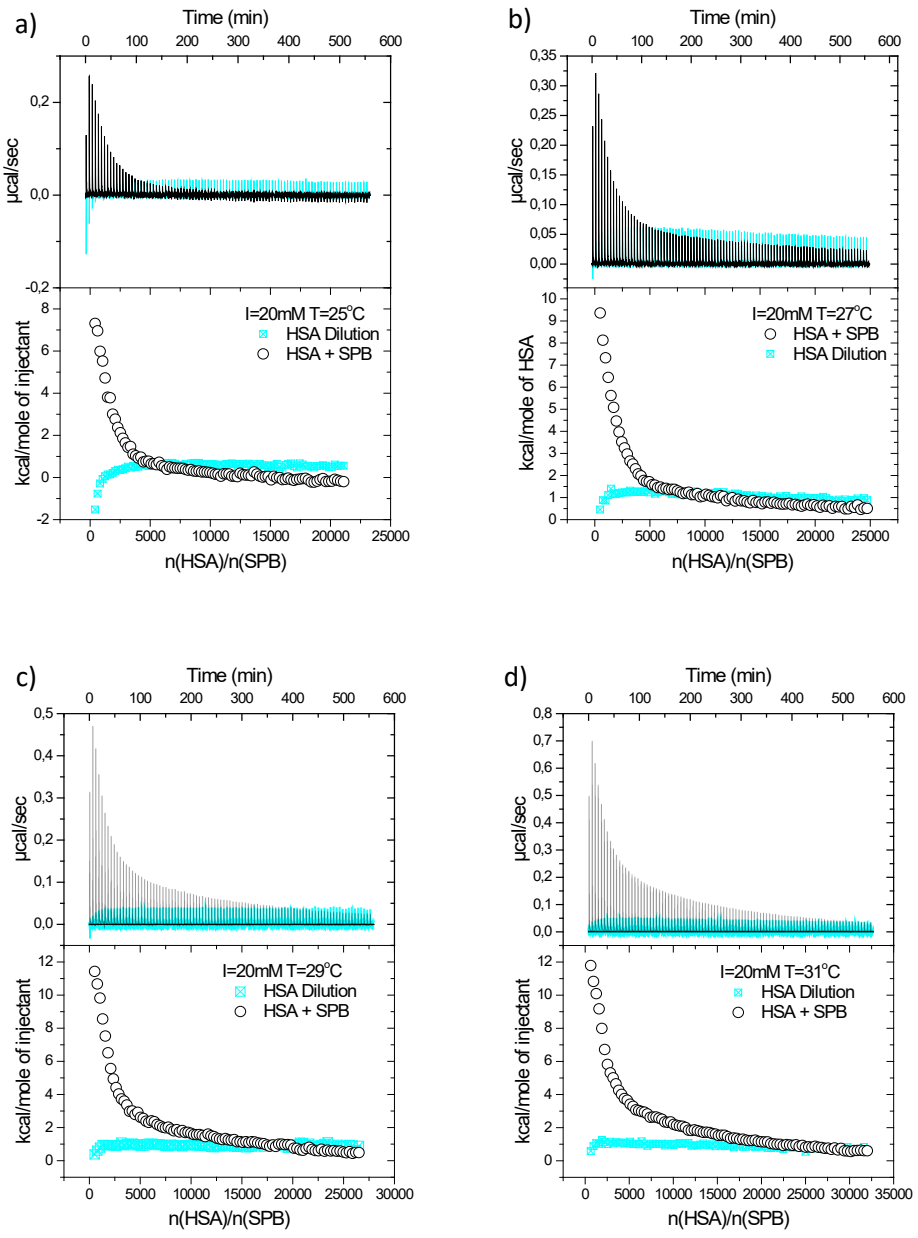

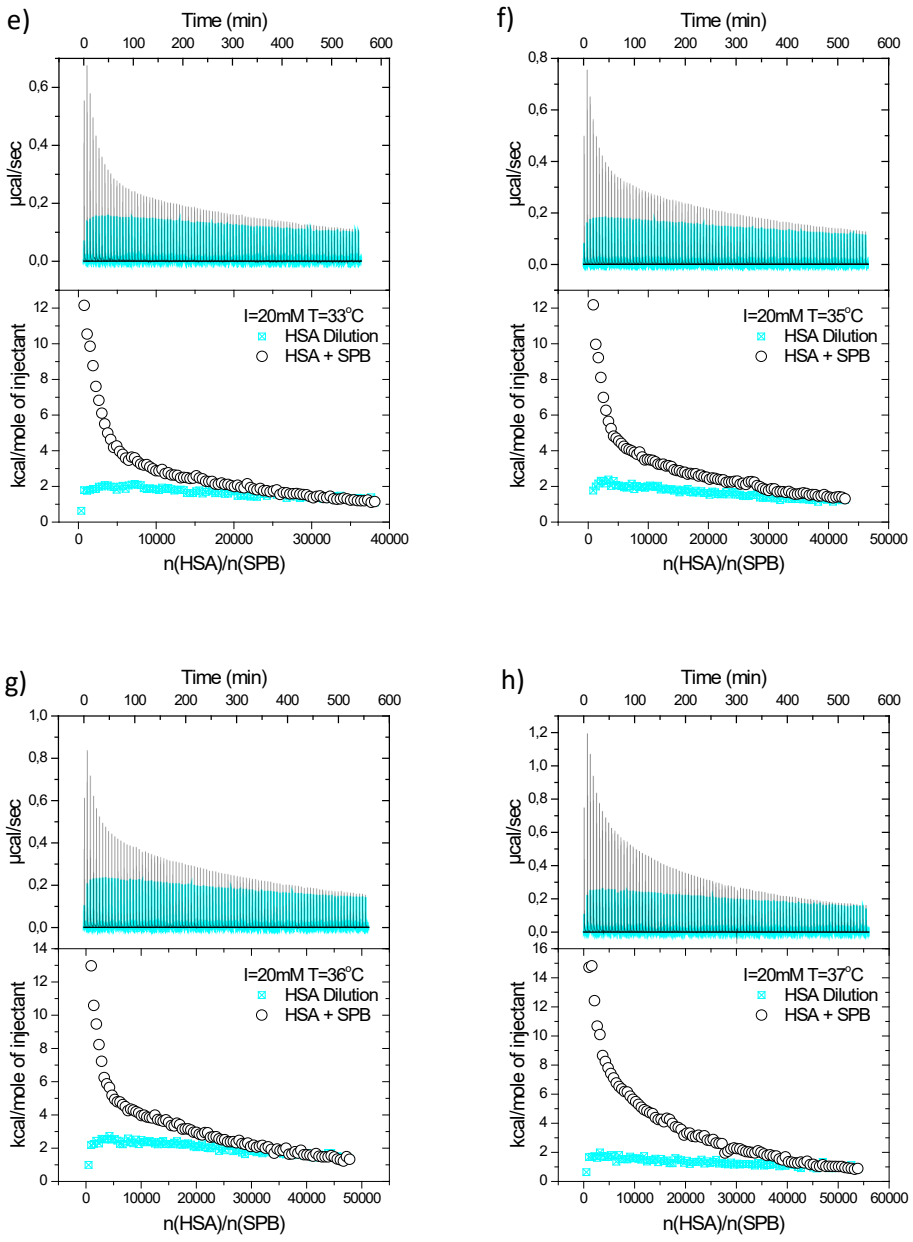

Figure S13. ITC data for the adsorption of HSA onto SPB at pH 7.2, I = 20 mM, and temperatures: (a) 25°C, (b) 27°C, (c) 29°C, (d) 31°C, (e) 33°C, (f) 35°C, (g) 36°C, (h) 37°C, respectively. The upper panel shows the raw data of the adsorption of HSA onto SPB (black curves) and dilution of HSA by buffer (cyan curves). The integrated heats of each injection are shown in the lower panel.

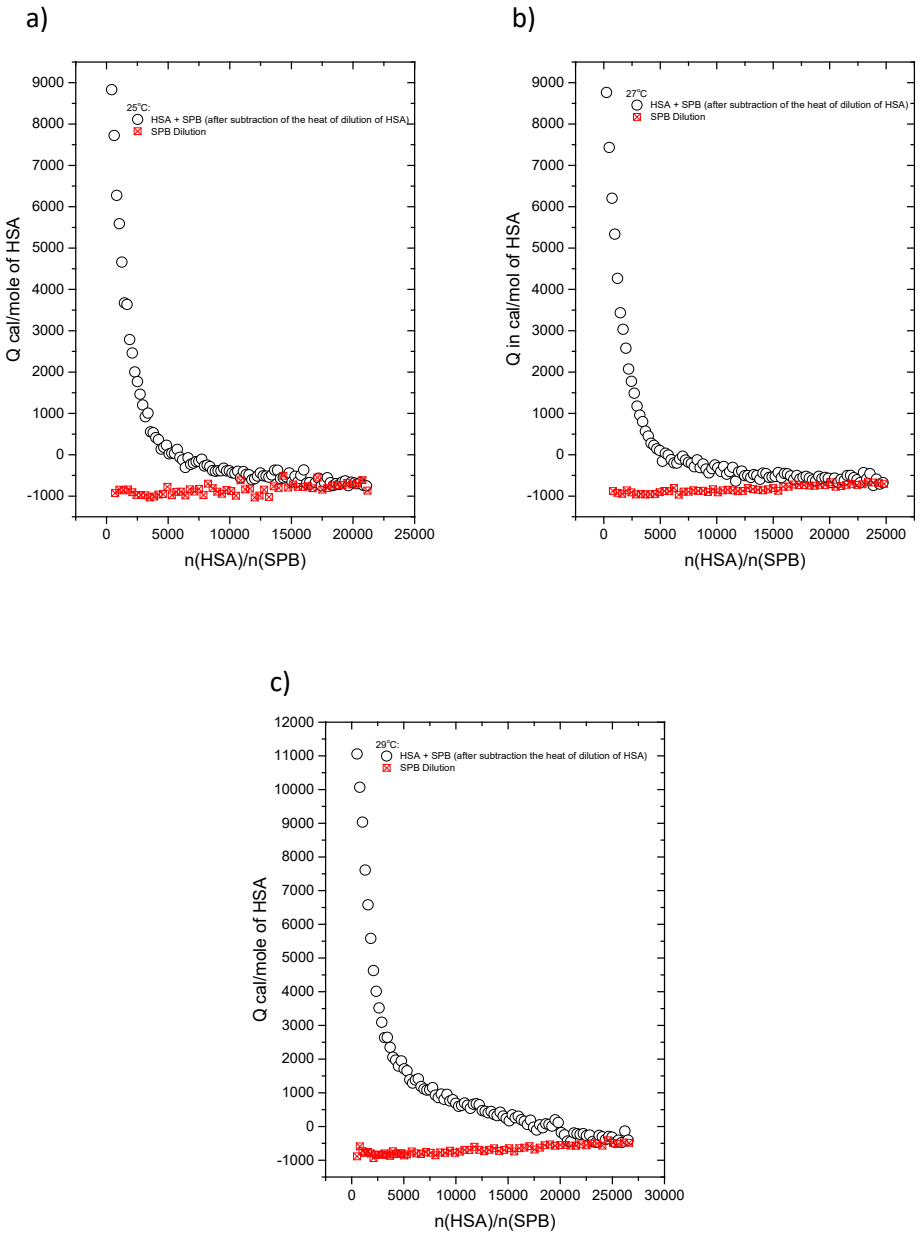

Figure S14. Integrated heats of each injection after first subtraction (corrected for protein heat of dilution) (black circles) and the heat of dilution of SPB by buffer (red squares) in the case of low protein concentration (24 g/L).

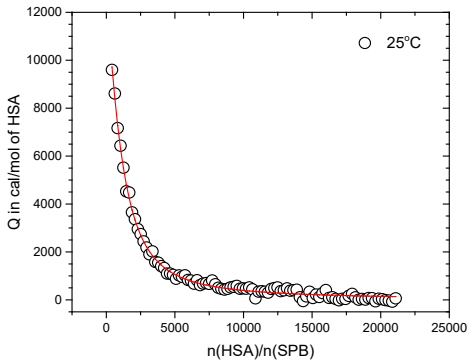
25°C
Q in cal/mol of HSA
n(HSA)/n(SPB)

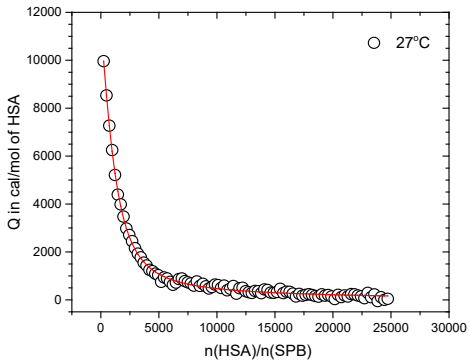
27°C
Q in cal/mol of HSA
n(HSA)/n(SPB)

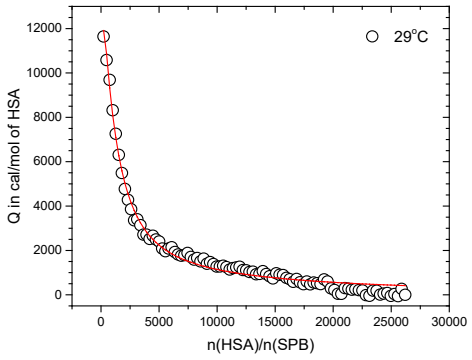
29°C
Q in cal/mol of HSA
n(HSA)/n(SPB)

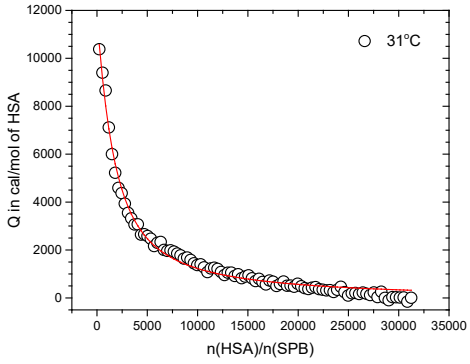
31°C
Q in cal/mol of HSA
n(HSA)/n(SPB)

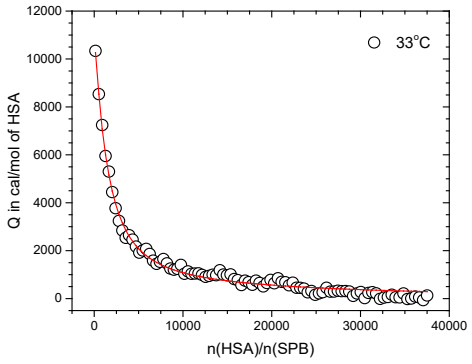
33°C
Q in cal/mol of HSA
n(HSA)/n(SPB)

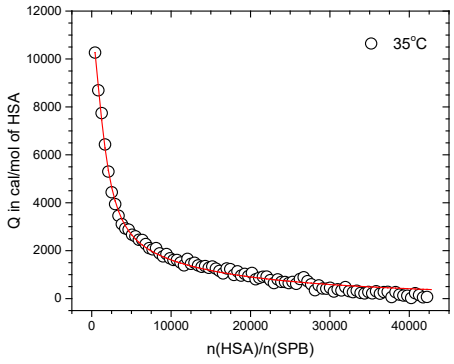
35°C
Q in cal/mol of HSA
n(HSA)/n(SPB)

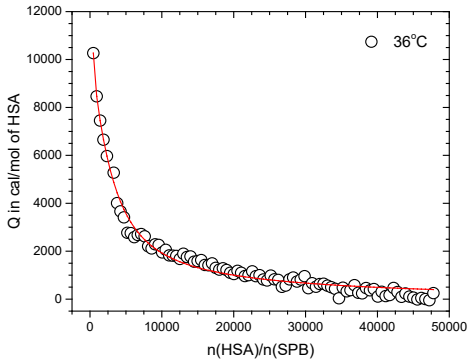
36°C
Q in cal/mol of HSA
n(HSA)/n(SPB)

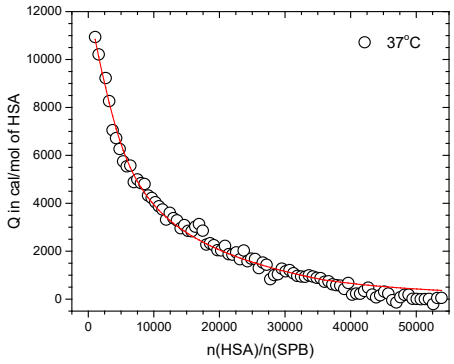
37°C
Q in cal/mol of HSA
n(HSA)/n(SPB)

Figure S15. The integrated heats Q of adsorption of HSA onto SPB at temperatures between 25°C and 37°C for I = 20 mM. The respective fits (TSIS model) are displayed as solid red line. The HSA concentrations were as follows: 24.0 g/L (for measurements at temp. 25 – 29°C); 35.0 g/L (for measurement at temp. 31°C) and 45.0 g/L (for measurement at temp. 33 – 37°C). The concentration of SPB varied from 1.38 to 1.84 g/L.

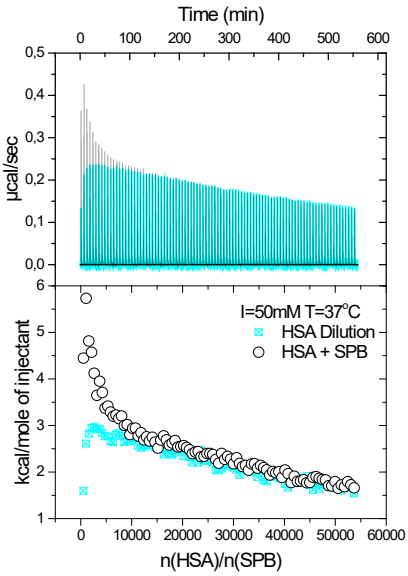

Figure S16. ITC data for the adsorption of HSA onto SPB at pH 7.2, I = 50 mM, and temperature of 37°C. The upper panel shows the raw data of the adsorption of HSA onto SPB (black curves) and dilution of HSA by buffer (cyan curves). The integrated heats of each injection are shown in the lower panel. Plot refer to section **4.4.3.1.**

7.4.2. Thermodynamic Data

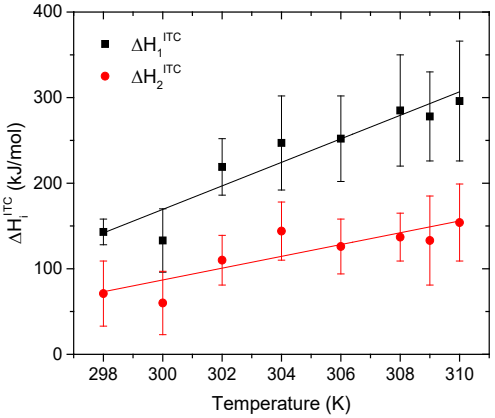

Figure S17. Total calorimetric enthalpies (ΔH_i^{ITC}) for HSA adsorption onto SPBs at different temperatures at I = 20 mM and pH 7.2. Plot refer to section **4.4.3.2.**

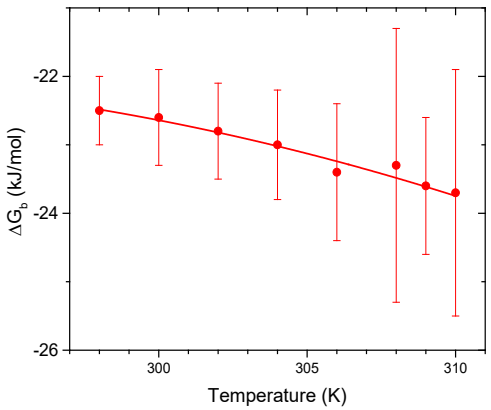

Figure S18. Temperature dependence of the ΔG_b in the second step of binding of HSA onto SPB. Solid red line represents the fitting obtained from the integrated form of the nonlinear van't Hoff equation (eq. 20). Plot refer to section **4.4.3.2.**

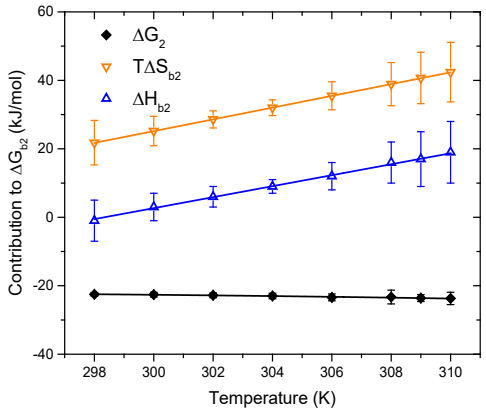

Figure S19. Changes in the thermodynamic parameters (ΔG_b, ΔH_b, $T\Delta S_b$) that accompanies the second step of binding of HSA onto SPB as a function of temperature. Black squares shows the binding free energy. Solid black line shows the theoretical fit of ΔG_b (eq. 20). $T\Delta S_b$ is shown as dashed orange line. ΔH_b is shown as dashed blue line. Characteristic temperatures for the second step of binding ($T_{2S} = 284 \pm 7\ K$ and $T_{2H} = 298 \pm 7\ K$) are not displayed in the plot in order to maintain the better clarity. Plot refer to section **4.4.3.2.**

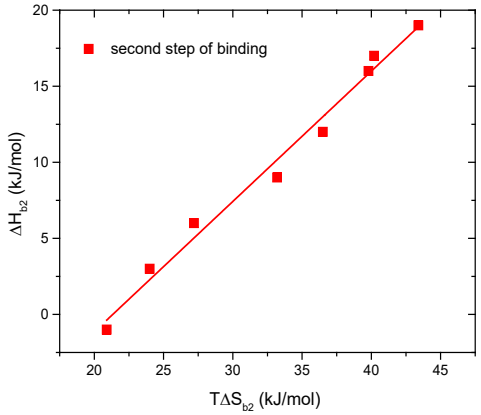

Figure S20. Energetics of HSA binding to SPB: dependence of the enthalpy, ΔH_b on the entropy factor, $T\Delta S_b$ in the second step of binding. Solid black line shows the linear fit resulting in equation 51. Plot refer to section **4.4.3.3.**

Table S4. Thermodynamics parameters for the first and second binding of HSA onto SPB.

T (K)	N_1	ΔH_1^{ITC} (kJ / mol)	$K_{b1} \cdot 10^{-5}$ (mol^{-1})	ΔG_{b1} (kJ / mol)	ΔH_{b1} (kJ / mol)	ΔS_{b1} (kJ / mol / K)	N_2	ΔH_2^{ITC} (kJ / mol)	$K_{b2} \cdot 10^{-4}$ (mol^{-1})	ΔG_{b2} (kJ / mol)	ΔH_{b2} (kJ / mol)	ΔS_{b2} (kJ / mol / K)
298	663 ± 58	143 ± 15	2,24 ± 0.38	-30.5 ± 0,4	-110 ± 17	-0.27 ± 0.06	493 ± 260	71 ± 38	0.9 ± 0.2	-22.5 ± 0.5	-1 ± 6	0.07 ± 0.02
300	787 ± 240	133 ± 37	1,55 ± 0.26	-29.8 ± 0,4	-84 ± 12	-0.18 ± 0.04	600 ± 290	60 ± 37	0.9 ± 0.3	-22.6 ± 0.7	3 ± 4	0.08 ± 0.01
302	944 ± 120	219 ± 33	1,34 ± 0.12	-29.6 ± 0,2	-59 ± 8	-0.10 ± 0.03	627 ± 330	110 ± 29	0.9 ± 0.3	-22.8 ± 0.7	6 ± 3	0.09 ± 0.01
304	689 ± 130	247 ± 55	1,25 ± 0.20	-29.7 ± 0,4	-33 ± 7	0.01 ± 0.02	558 ± 470	144 ± 34	0.9 ± 0.3	-23.0 ± 0.8	9 ± 2	0.11 ± 0.01
306	650 ± 280	252 ± 50	1,20 ± 0.34	-29.8 ± 0,7	-7 ± 10	0.07 ± 0.03	450 ± 260	126 ± 32	1.0 ± 0,4	-23.4 ± 1.0	12 ± 4	0.12 ± 0.01
308	760 ± 320	285 ± 65	1,36 ± 0.62	-30.3 ± 1,3	19 ± 15	0.16 ± 0.05	633 ± 390	137 ± 28	0.9 ± 0.6	-23.3 ± 2.0	16 ± 6	0.13 ± 0.02
309	612 ± 300	278 ± 52	1,23 ± 0.50	-30.1 ± 1,1	32 ± 18	0.20 ± 0.06	433 ± 270	133 ± 52	1.0 ± 0.4	-23.6 ± 1.0	17 ± 8	0.13 ± 0.02
310	541 ± 160	296 ± 70	1,08 ± 0.32	-29.9 ± 0,8	44 ± 21	0.24 ± 0.07	470 ± 240	154 ± 45	1.0 ± 0.6	-23.7 ± 1.8	19 ± 9	0.14 ± 0.03

N_i - number of adsorbed proteins determined from titrations at each temperature. K_{bi}, ΔH_i^{ITC} and ΔG_{bi} values are the experimental values determined from titrations at each temperature. ΔH_{bi}, ΔS_{bi}, $\Delta C_{p1vH} = 12.1 \pm 2.7\ kJ \cdot mol^{-1} \cdot K^{-1}$ and $\Delta C_{p2vH} = 1.7 \pm 1.1\ kJ \cdot mol^{-1} \cdot K^{-1}$- binding enthalpy, entropy and heat capacity change, respectively as obtaing through application of equation (20). $\Delta C_{p1ITC} = 13.7 \pm 1.6\ kJ \cdot mol^{-1} \cdot K^{-1}$ and $\Delta C_{p2ITC} = 6.9 \pm 1.7\ kJ \cdot mol^{-1} \cdot K^{-1}$ - obtained from linear temperature dependence of ΔH_i^{ITC}.

Table S5. The calculated gain of entropy ΔG_{ci} and the residual part ($T\Delta S_{res}$) of the total binding entropy $T\Delta S_b$.

T (K)	ΔG_{ci} (kJ / mol)	$T\Delta S_{res}$ (kJ / mol)
298	-24.6	-105.1
300	-24.8	-78.8
302	-25.0	-55.2
304	-25.1	-22.1
306	-25.3	-3.9
308	-25.5	23.8
309	-25.5	36.3
310	-25.6	48.8

Average error on ΔG_{ci} and $T\Delta S_{res}$ is 4 and 14 kJ·mol^{-1}, respectively.

7.5. Details on PPB-HSA Interaction Described in Chapter 4.5.

7.5.1. QCM-D Data for I- and pH Cycle upon HSA Adsorption

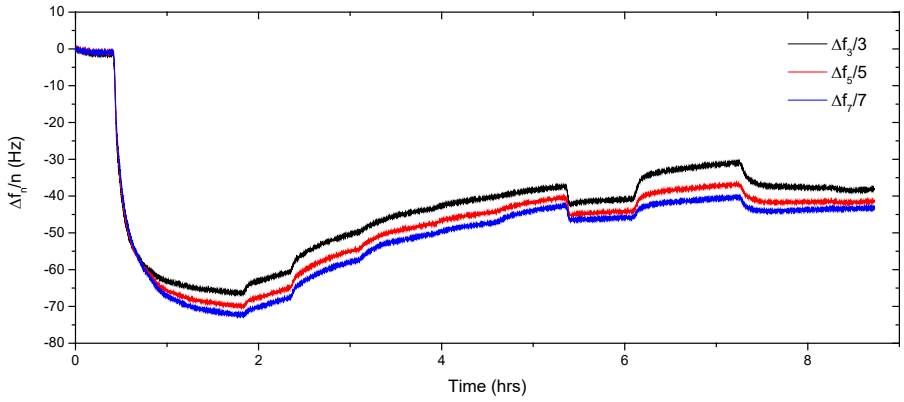

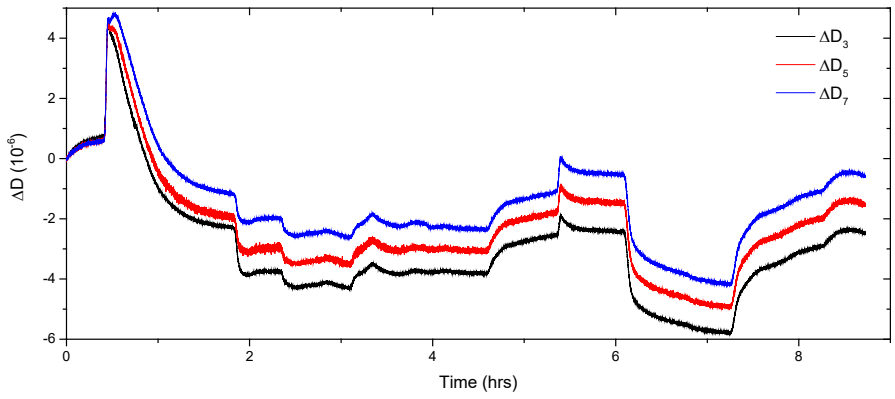

Figure S21. I- and pH induced response of protein pre-complexed PAA brush monitored by QCM-D. Top panel: QCM-D normalized frequency signal. Lower panel: QCM-D dissipation signal. Results for the third, the fifth, and the seventh overtone are displayed. Plots refer to section **4.5.2.**

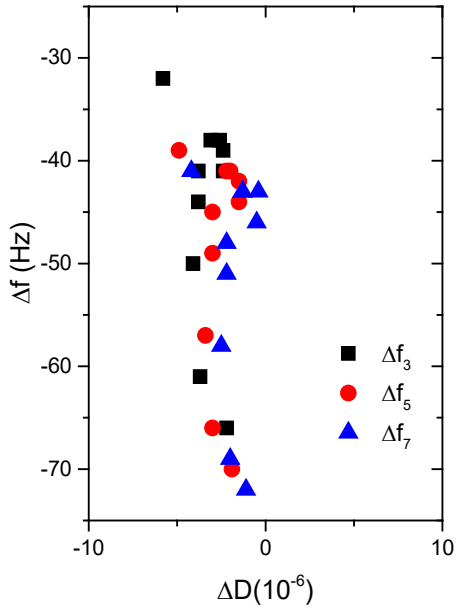

Figure S22. Distribution of Δ*f* as a function of the corresponding Δ*D*. Results for the third, the fifth, and the seventh overtone are displayed. Plot refer to section **4.5.2.**

7.5.2. QCM-D Data for pH Induced Swelling/Deswelling of a Protein-Free PAA Brush

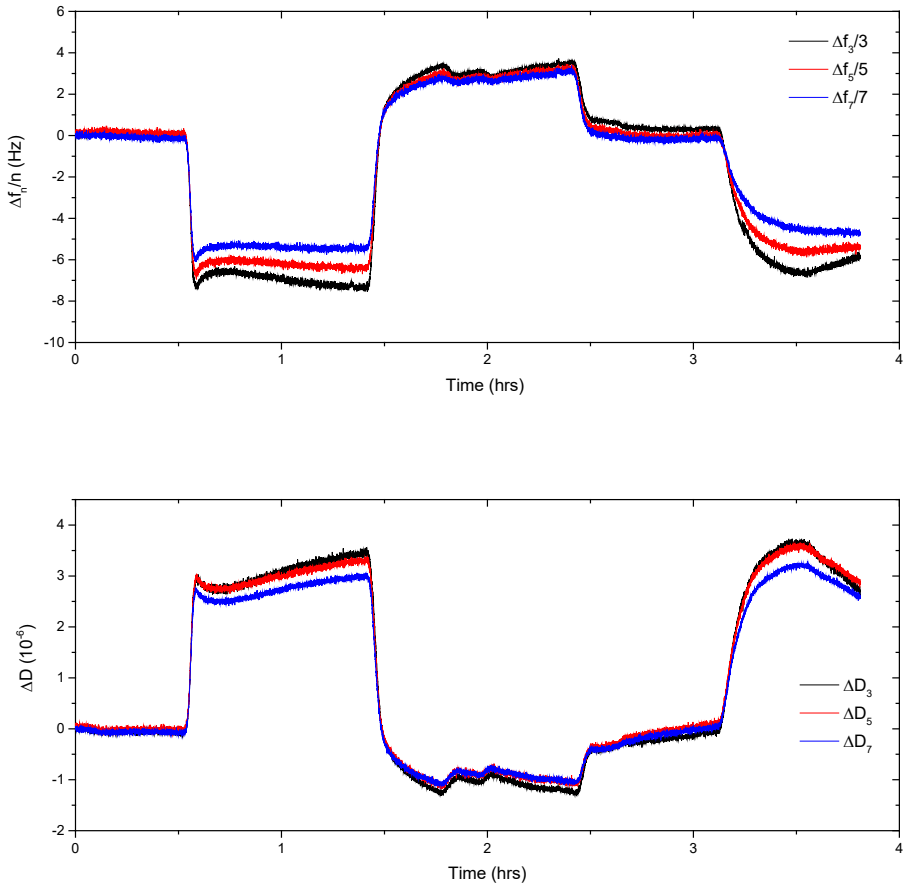

Figure S23. pH induced response of protein-free PAA brush monitored by QCM-D. Top panel: QCM-D normalized frequency signal. Lower panel: QCM-D dissipation signal. Results for the third, the fifth, and the seventh overtone are displayed. Plots refer to section **4.5.3.**

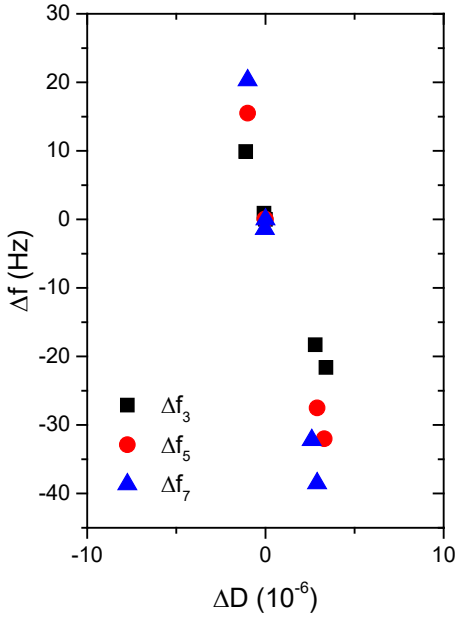

Figure S24. Distribution of Δ*f* as a function of the corresponding Δ*D*. Results for the third, the fifth, and the seventh overtone are displayed. Plot refer to section **4.5.3.**

BIBLIOGRAPHY

(1) Manning, G. S. The Molecular Theory of Polyelectrolyte Solutions with Applications to the Electrostatic Properties of Polynucleotides. *Q. Rev. Biophys.* **1978**, *11* (02), 179. https://doi.org/10.1017/S0033583500002031.

(2) Record, M. T.; Anderson, C. F.; Lohman, T. M. Thermodynamic Analysis of Ion Effects on the Binding and Conformational Equilibria of Proteins and Nucleic Acids: The Roles of Ion Association or Release, Screening, and Ion Effects on Water Activity. *Q. Rev. Biophys.* **1978**, *11* (2), 103–178.

(3) Xu, X.; Angioletti-Uberti, S.; Lu, Y.; Dzubiella, J.; Ballauff, M. Interaction of Proteins with Polyelectrolytes: Comparison of Theory to Experiment. *Langmuir*. American Chemical Society August 2019, pp 5373–5391. https://doi.org/10.1021/acs.langmuir.8b01802.

(4) Lumry, R.; Rajender, S. Enthalpy-Entropy Compensation Phenomena in Water Solutions of Proteins and Small Molecules: A Ubiquitous Properly of Water. *Biopolymers* **1970**, *9* (10), 1125–1227. https://doi.org/10.1002/bip.1970.360091002.

(5) Spolar, R. S.; Ha, J. H.; Record, M. T. Hydrophobic Effect in Protein Folding and Other Noncovalent Processes Involving Proteins. *Proc. Natl. Acad. Sci.* **1989**, *86* (21), 8382–8385. https://doi.org/10.1073/pnas.86.21.8382.

(6) Jen-Jacobson, L.; Engler, L. E.; Jacobson, L. A. Structural and Thermodynamic Strategies for Site-Specific DNA Binding Proteins. *Structure* **2000**, *8* (10), 1015–1023. https://doi.org/10.1016/S0969-2126(00)00501-3.

(7) Jen-Jacobson, L.; Engler, L. E.; Ames, J. T.; Kurpiewski, M. R.; Grigorescu, A. Thermodynamic Parameters of Specific and Nonspecific Protein-DNA Binding. *Supramol. Chem.* **2000**, *12* (2), 143–160. https://doi.org/10.1080/10610270008027446.

(8) Chodera, J. D.; Mobley, D. L. Entropy-Enthalpy Compensation: Role and Ramifications in Biomolecular Ligand Recognition and Design. *Annu. Rev. Biophys.* **2013**, *42* (1), 121–142. https://doi.org/10.1146/annurev-biophys-083012-130318.

(9) Fox, J. M.; Zhao, M.; Fink, M. J.; Kang, K.; Whitesides, G. M. The Molecular Origin of Enthalpy/Entropy Compensation in Biomolecular Recognition. *Annu. Rev. Biophys.* **2018**, *47* (1), 223–250. https://doi.org/10.1146/annurev-biophys-070816-033743.

(10) Yu, S.; Xu, X.; Yigit, C.; van der Giet, M.; Zidek, W.; Jankowski, J.; Dzubiella, J.; Ballauff, M. Interaction of Human Serum Albumin with Short Polyelectrolytes: A Study by Calorimetry and Computer Simulations. *Soft Matter* **2015**, *11* (23), 4630–4639. https://doi.org/10.1039/C5SM00687B.

(11) Yu, S.; Schuchardt, M.; Tölle, M.; Van Der Giet, M.; Zidek, W.; Dzubiella, J.; Ballauff, M. Interaction of Human Serum Albumin with Uremic Toxins: A Thermodynamic Study. *RSC Adv.* **2017**, *7* (45), 27913–27922. https://doi.org/10.1039/c7ra02838e.

(12) Ran, Q.; Xu, X.; Dey, P.; Yu, S.; Lu, Y.; Dzubiella, J.; Haag, R.; Ballauff, M. Interaction of Human Serum Albumin with Dendritic Polyglycerol Sulfate: Rationalizing the Thermodynamics of Binding. *J. Chem. Phys.* **2018**, *149* (16), 163324. https://doi.org/10.1063/1.5030601.

(13) Ran, Q.; Xu, X.; Dzubiella, J.; Haag, R.; Ballauff, M. Thermodynamics of the Binding of Lysozyme to a Dendritic Polyelectrolyte: Electrostatics Versus Hydration. *ACS Omega* **2018**, *3* (8), 9086–9095. https://doi.org/10.1021/acsomega.8b01493.

(14) De Kruif, C. G.; Weinbreck, F.; De Vries, R. Complex Coacervation of Proteins and Anionic Polysaccharides. *Curr. Opin. Colloid Interface Sci.* **2004**, *9*, 340–349. https://doi.org/10.1016/j.cocis.2004.09.006.

(15) Wittemann, A.; Ballauff, M. Interaction of Proteins with Linear Polyelectrolytes and Spherical Polyelectrolyte Brushes in Aqueous Solution. *Physical Chemistry Chemical Physics*. 2006, pp 5269–5275. https://doi.org/10.1039/b609879g.

(16) Becker, A. L.; Henzler, K.; Welsch, N.; Ballauff, M.; Borisov, O. Proteins and Polyelectrolytes: A Charged Relationship. *Curr. Opin. Colloid Interface Sci.* **2012**, *17* (2), 90–96.

https://doi.org/10.1016/j.cocis.2011.10.001.

(17) Kayitmazer, A. B.; Seeman, D.; Minsky, B. B.; Dubin, P. L.; Xu, Y. Protein–Polyelectrolyte Interactions. *Soft Matter* **2013**, *9* (9), 2553. https://doi.org/10.1039/c2sm27002a.

(18) Du, X.; Dubin, P. L.; Hoagland, D. a.; Sun, L. Protein-Selective Coacervation with Hyaluronic Acid. *Biomacromolecules* **2014**, *15* (3), 726–734. https://doi.org/10.1021/bm500041a.

(19) Kizilay, E.; Kayitmazer, A. B.; Dubin, P. L. Complexation and Coacervation of Polyelectrolytes with Oppositely Charged Colloids. *Adv. Colloid Interface Sci.* **2011**, *167* (1–2), 24–37. https://doi.org/10.1016/j.cis.2011.06.006.

(20) Lohman, T. M.; Bujalowski, W. Effects of Base Composition on the Negative Cooperativity and Binding Mode Transitions of Escherichia Coli SSB-Single-Stranded DNA Complexes. *Biochemistry* **1994**, *33* (20), 6167–6176. https://doi.org/10.1021/bi00186a016.

(21) Sasaki, T.; Kanke, Y.; Nagahashi, M.; Toyokawa, M.; Matsuda, M.; Shimizu, J.; Misawa, Y.; Takita, T. Dietary Docosahexaenoic Acid Can Alter the Surface Expression of CD4 and CD8 on T Cells in Peripheral Blood. *J. Agric. Food Chem.* **2000**, *48* (4), 1047–1049. https://doi.org/10.1016/j.bpc.2011.05.005.

(22) Datta, K.; Wowor, A. J.; Richard, A. J.; LiCata, V. J. Temperature Dependence and Thermodynamics of Klenow Polymerase Binding to Primed-Template DNA. *Biophys. J.* **2006**, *90* (5), 1739–1751. https://doi.org/10.1529/biophysj.105.071837.

(23) Datta, K.; LiCata, V. J. Thermodynamics of the Binding of Thermus Aquaticus DNA Polymerase to Primed-Template DNA. *Nucleic Acids Res.* **2003**, *31* (19), 5590–5597. https://doi.org/10.1093/nar/gkg774.

(24) Niedzwiecka, A.; Stepinski, J.; Darzynkiewicz, E.; Sonenberg, N.; Stolarski, R. Positive Heat Capacity Change upon Specific Binding of Translation Initiation Factor EIF4E to MRNA 5‘ Cap †. *Biochemistry* **2002**, *41* (40), 12140–12148. https://doi.org/10.1021/bi0258142.

(25) Niedzwiecka, A.; Darzynkiewicz, E.; Stolarski, R. Thermodynamics of MRNA 5‘ Cap Binding by Eukaryotic Translation Initiation Factor EIF4E †. *Biochemistry* **2004**, *43* (42), 13305–13317. https://doi.org/10.1021/bi0491651.

(26) Privalov, P. L. Microcalorimetry of Macromolecules: The Physical Basis of Biological Structures. In *Journal of Solution Chemistry*; 2015; Vol. 44, pp 1141–1161. https://doi.org/10.1007/s10953-015-0337-x.

(27) Janin, J.; Bonvin, A. M. Protein–Protein Interactions. *Curr. Opin. Struct. Biol.* **2013**, *23* (6), 859–861. https://doi.org/10.1016/j.sbi.2013.10.003.

(28) Dragan, A. I.; Read, C. M.; Crane-Robinson, C. Enthalpy–Entropy Compensation: The Role of Solvation. *European Biophysics Journal*. May 2017, pp 301–308. https://doi.org/10.1007/s00249-016-1182-6.

(29) Yu, Y. B.; Lavigne, P.; Kay, C. M.; Hodges, R. S.; Privalov, P. L. Contribution of Translational and Rotational Entropy to the Unfolding of a Dimeric Coiled-Coil. *J. Phys. Chem. B* **1999**, *103* (12), 2270–2278. https://doi.org/10.1021/jp983533r.

(30) Privalov, P. L.; Dragan, A. I.; Crane-Robinson, C. Interpreting Protein/DNA Interactions: Distinguishing Specific from Non-Specific and Electrostatic from Non-Electrostatic Components. *Nucleic Acids Research*. April 2011, pp 2483–2491. https://doi.org/10.1093/nar/gkq984.

(31) Xu, X.; Ran, Q.; Dey, P.; Nikam, R.; Haag, R.; Ballauff, M.; Dzubiella, J. Counterion-Release Entropy Governs the Inhibition of Serum Proteins by Polyelectrolyte Drugs. *Biomacromolecules* **2018**, *19* (2), 409–416. https://doi.org/10.1021/acs.biomac.7b01499.

(32) Wittemann, A.; Haupt, B.; Ballauff, M. Adsorption of Proteins on Spherical Polyelectrolyte Brushes in Aqueous Solution. *Physical Chemistry Chemical Physics*. 2003, pp 1671–1677. https://doi.org/10.1039/b300607g.

(33) Wittemann, A.; Haupt, B.; Ballauff, M. Polyelectrolyte-Mediated Protein Adsorption. *Progress in Colloid and Polymer Science*. 2006, pp 58–64. https://doi.org/10.1007/2882_064.

(34) Fogarty, A. C.; Laage, D. Water Dynamics in Protein Hydration Shells: The Molecular Origins of the Dynamical Perturbation. *J. Phys. Chem. B* **2014**, *118* (28), 7715–7729. https://doi.org/10.1021/jp409805p.

(35) Duboué-Dijon, E.; Fogarty, A. C.; Hynes, J. T.; Laage, D. Dynamical Disorder in the DNA Hydration Shell. *J. Am. Chem. Soc.* **2016**, *138* (24), 7610–7620. https://doi.org/10.1021/jacs.6b02715.

(36) Abel, S.; Galamba, N.; Karakas, E.; Marchi, M.; Thompson, W. H.; Laage, D. On the Structural and Dynamical Properties of DOPC Reverse Micelles. *Langmuir* **2016**, *32* (41), 10610–10620. https://doi.org/10.1021/acs.langmuir.6b02566.

(37) Parsegian, V. A.; Rand, R. P.; Rau, D. C. Macromolecules and Water: Probing with Osmotic Stress. *Methods Enzymol.* **1995**, *259* (C), 43–94. https://doi.org/10.1016/0076-6879(95)59039-0.

(38) Parsegian, V. A.; Rand, R. P.; Rau, D. C. Osmotic Stress, Crowding, Preferential Hydration, and Binding: A Comparison of Perspectives. *Proc. Natl. Acad. Sci. U. S. A.* **2000**, *97* (8), 3987–3992. https://doi.org/10.1073/pnas.97.8.3987.

(39) Ben-Yaakov, D.; Burak, Y.; Andelman, D.; Safran, S. A. Electrostatic Interactions of Asymmetrically Charged Membranes. *EPL* **2007**, *79* (4), 48002. https://doi.org/10.1209/0295-5075/79/48002.

(40) Sidorova, N. Y.; Rau, D. C. The Osmotic Sensitivity of Netropsin Analogue Binding to DNA. *Biopolymers* **1995**, *35* (4), 377–384. https://doi.org/10.1002/bip.360350405.

(41) DeRouchey, J.; Parsegian, V. A.; Rau, D. C. Cation Charge Dependence of the Forces Driving DNA Assembly. *Biophys. J.* **2010**, *99* (8), 2608–2615. https://doi.org/10.1016/j.bpj.2010.08.028.

(42) Stanley, C.; Krueger, S.; Parsegian, V. A.; Rau, D. C. Protein Structure and Hydration Probed by SANS and Osmotic Stress. *Biophys. J.* **2008**, *94* (7), 2777–2789. https://doi.org/10.1529/biophysj.107.122697.

(43) Deredge, D. J.; Baker, J. T.; Datta, K.; LiCata, V. J. The Glutamate Effect on DNA Binding by Pol I DNA Polymerases: Osmotic Stress and the Effective Reversal of Salt Linkage. *J. Mol. Biol.* **2010**, *401* (2), 223–238. https://doi.org/10.1016/j.jmb.2010.06.009.

(44) Bergqvist, S.; O'Brien, R.; Ladbury, J. E. Site-Specific Cation Binding Mediates TATA Binding Protein - DNA Interaction from a Hyperthermophilic Archaeon. *Biochemistry* **2001**, *40* (8), 2419–2425. https://doi.org/10.1021/bi002488m.

(45) Suryawanshi, H.; Sabharwal, H.; Maiti, S. Thermodynamics of Peptide−RNA Recognition: The Binding of a Tat Peptide to TAR RNA. *J. Phys. Chem. B* **2010**, *114* (34), 11155–11163. https://doi.org/10.1021/jp1000545.

(46) Tanford, C. Extension of the Theory of Linked Functions to Incorporate the Effects of Protein Hydration. *J. Mol. Biol.* **1969**, *39* (3), 539–544. https://doi.org/10.1016/0022-2836(69)90143-0.

(47) Ha, J.-H.; Capp, M. W.; Hohenwalter, M. D.; Baskerville, M.; Record, M. T. Thermodynamic Stoichiometries of Participation of Water, Cations and Anions in Specific and Non-Specific Binding of Lac Repressor to DNA. *J. Mol. Biol.* **1992**, *228* (1), 252–264. https://doi.org/10.1016/0022-2836(92)90504-D.

(48) Mascotti, D. P.; Lohman, T. M. Thermodynamics of Single-Stranded RNA and DNA Interactions with Oligolysines Containing Tryptophan. Effects of Base Composition. *Biochemistry* **1993**, *32* (40), 10568–10579. https://doi.org/10.1021/bi00091a006.

(49) Bergqvist, S.; Williams, M. A.; O'Brien, R.; Ladbury, J. E. Reversal of Halophilicity in a Protein-DNA Interaction by Limited Mutation Strategy. *Structure* **2002**, *10* (5), 629–637. https://doi.org/10.1016/S0969-2126(02)00749-9.

(50) Bergqvist, S.; Williams, M. A.; O'Brien, R.; Ladbury, J. E. Halophilic Adaptation of Protein-DNA Interactions. In *Biochemical Society Transactions*; 2003; Vol. 31, pp 677–680. https://doi.org/10.1042/BST0310677.

(51) Bergqvist, S.; Williams, M. A.; O'Brien, R.; Ladbury, J. E. Heat Capacity Effects of Water Molecules and Ions at a Protein-DNA Interface. *J. Mol. Biol.* **2004**, *336* (4), 829–842. https://doi.org/10.1016/j.jmb.2003.12.061.

(52) Yu, S.; Xu, X.; Yigit, C.; van der Giet, M.; Zidek, W.; Jankowski, J.; Dzubiella, J.; Ballauff, M. Interaction of Human Serum Albumin with Short Polyelectrolytes: A Study by Calorimetry and Computer Simulations. *Soft Matter* **2015**, *11* (23), 4630–4639. https://doi.org/10.1039/C5SM00687B.

(53) Xu, X.; Ballauff, M. Interaction of Lysozyme with a Dendritic Polyelectrolyte: Quantitative Analysis of the Free Energy of Binding and Comparison to Molecular Dynamics Simulations. *J. Phys. Chem. B* **2019**, *123* (39), 8222–8231. https://doi.org/10.1021/acs.jpcb.9b07448.

(54) Lumry, R.; Rajender, S. Enthalpy-Entropy Compensation Phenomena in Water Solutions of Proteins and Small Molecules: A Ubiquitous Properly of Water. *Biopolymers* **1970**, *9* (10), 1125–1227. https://doi.org/10.1002/bip.1970.360091002.

(55) Vega, S.; Abian, O.; Velazquez-Campoy, A. On the Link between Conformational Changes, Ligand Binding and Heat Capacity. *Biochim. Biophys. Acta - Gen. Subj.* **2016**, *1860* (5), 868–878. https://doi.org/10.1016/j.bbagen.2015.10.010.

(56) Geschwindner, S.; Ulander, J.; Johansson, P. Ligand Binding Thermodynamics in Drug Discovery: Still a Hot Tip? *Journal of Medicinal Chemistry*. 2015, pp 6321–6335. https://doi.org/10.1021/jm501511f.

(57) Halperin, A.; Tirrell, M.; Lodge, T. P. Tethered Chains in Polymer Microstructures. In *Macromolecules: Synthesis, Order and Advanced Properties*; Springer-Verlag: Berlin/Heidelberg, 2006; pp 31–71. https://doi.org/10.1007/BFb0051635.

(58) MILNER, S. T. Polymer Brushes. *Science (80-.).* **1991**, *251* (4996), 905–914. https://doi.org/10.1126/science.251.4996.905.

(59) Currie, E. P. K.; Norde, W.; Cohen Stuart, M. A. Tethered Polymer Chains: Surface Chemistry and Their Impact on Colloidal and Surface Properties. *Adv. Colloid Interface Sci.* **2003**, *100–102*, 205–265. https://doi.org/10.1016/S0001-8686(02)00061-1.

(60) Szleifer, I.; Carignano, M. A. Tethered Polymer Layers: Phase Transitions and Reduction of Protein Adsorption. *Macromol. Rapid Commun.* **2000**, *21* (8), 423–448. https://doi.org/10.1002/(SICI)1521-3927(20000501)21:8<423::AID-MARC423>3.0.CO;2-J.

(61) Erol, M.; Du, H.; Sukhishvili, S. Control of Specific Attachment of Proteins by Adsorption of Polymer Layers. *Langmuir* **2006**, *22* (26), 11329–11336. https://doi.org/10.1021/la061790e.

(62) de Vos, W. M.; Biesheuvel, P. M.; de Keizer, A.; Kleijn, J. M.; Cohen Stuart, M. A. Adsorption of the Protein Bovine Serum Albumin in a Planar Poly(Acrylic Acid) Brush Layer As Measured by Optical Reflectometry. *Langmuir* **2008**, *24* (13), 6575–6584. https://doi.org/10.1021/la8006469.

(63) Reichhart, C.; Czeslik, C. Native-like Structure of Proteins at a Planar Poly(Acrylic Acid) Brush. *Langmuir* **2009**, *25* (2), 1047–1053. https://doi.org/10.1021/la802905s.

(64) Hollmann, O.; Steitz, R.; Czeslik, C. Structure and Dynamics of α-Lactalbumin Adsorbed at a Charged Brush Interface. *Phys. Chem. Chem. Phys.* **2008**, *10* (10), 1448. https://doi.org/10.1039/b716264b.

(65) Tjipto, E.; Quinn, J. F.; Caruso, F. Layer-by-Layer Assembly of Weak-Strong Copolymer Polyelectrolytes: A Route to Morphological Control of Thin Films. *J. Polym. Sci. Part A Polym. Chem.* **2007**, *45* (18), 4341–4351. https://doi.org/10.1002/pola.22179.

(66) Sergio, E. M.; Andrew, A. B.; Omar, A.; Wilhelm, T. S. H. Following Polymer Brush Growth Using the Quartz Crystal Microbalance Technique. *Macromol. Rapid Commun.* **2005**.

(67) Hamley, I. W.; Ansari, I. A.; Castelletto, V.; Nuhn, H.; Rösler, A.; Klok, H.-A. Solution Self-Assembly of Hybrid Block Copolymers Containing Poly(Ethylene Glycol) and Amphiphilic β-Strand Peptide Sequences. *Biomacromolecules* **2005**, *6* (3), 1310–1315. https://doi.org/10.1021/bm049286g.

(68) Welsch, N.; Lu, Y.; Dzubiella, J.; Ballauff, M. Adsorption of Proteins to Functional Polymeric Nanoparticles. *Polymer (Guildf).* **2013**, *54* (12), 2835–2849. https://doi.org/10.1016/j.polymer.2013.03.027.

(69) Xia, J.; Mattison, K.; Romano, V.; Dubin, P. L.; Muhoberac, B. B. Complexation of Trypsin and Alcohol Dehydrogenase with Poly(Diallyldimethylammonium Chloride). *Biopolymers* **1997**, *41* (4), 359–365. https://doi.org/10.1002/(SICI)1097-0282(19970405)41:4<359::AID-BIP1>3.0.CO;2-L.

(70) Caruso, F.; Schüler, C. Enzyme Multilayers on Colloid Particles: Assembly, Stability, and Enzymatic Activity. *Langmuir* **2000**, *16* (24), 9595–9603. https://doi.org/10.1021/la000942h.

(71) Khandare, J.; Calderón, M.; Dagia, N. M.; Haag, R. Multifunctional Dendritic Polymers in Nanomedicine: Opportunities and Challenges. *Chem. Soc. Rev.* **2012**, *41* (7), 2824–2848. https://doi.org/10.1039/C1CS15242D.

(72) Martínez Rivas, C. J.; Tarhini, M.; Badri, W.; Miladi, K.; Greige-Gerges, H.; Nazari, Q. A.; Galindo Rodríguez, S. A.; Román, R. Á.; Fessi, H.; Elaissari, A. Nanoprecipitation Process: From Encapsulation to Drug Delivery. *Int. J. Pharm.* **2017**, *532* (1), 66–81. https://doi.org/10.1016/j.ijpharm.2017.08.064.

(73) Henzler, K.; Haupt, B.; Rosenfeldt, S.; Harnau, L.; Narayanan, T.; Ballauff, M. Interaction Strength between Proteins and Polyelectrolyte Brushes: A Small Angle X-Ray Scattering Study. *Phys. Chem. Chem. Phys.* **2011**, *13* (39), 17599–17605. https://doi.org/10.1039/c1cp20663j.

(74) Yadav, V.; Harkin, A. V.; Robertson, M. L.; Conrad, J. C. Hysteretic Memory in PH-Response of Water Contact Angle on Poly(Acrylic Acid) Brushes. *Soft Matter* **2016**, *12* (15), 3589–3599. https://doi.org/10.1039/C5SM03134F.

(75) Reinhardt, M.; Kreuzer, M.; Geue, T.; Dahint, R.; Ballauff, M.; Steitz, R. Poly-Acrylic Acid Brushes and Adsorbed Proteins. *Zeitschrift für Phys. Chemie* **2015**, *229* (7–8). https://doi.org/10.1515/zpch-2014-0540.

(76) Wu, T.; Gong, P.; Szleifer, I.; Vlček, P.; Šubr, V.; Genzer, J. Behavior of Surface-Anchored Poly(Acrylic Acid) Brushes with Grafting Density Gradients on Solid Substrates: 1. Experiment. *Macromolecules* **2007**, *40* (24), 8756–8764. https://doi.org/10.1021/ma0710176.

(77) Tan, J. F.; Blencowe, A.; Goh, T. K.; Dela Cruz, I. T. M.; Qiao, G. G. A General Method for the Synthesis and Isolation of Well-Defined Core Cross-Linked Multistar Assemblies: A Route toward Enhanced PH-Responsive Polymers. *Macromolecules* **2009**, *42* (13), 4622–4631. https://doi.org/10.1021/ma802834x.

(78) Delcroix, M. F.; Huet, G. L.; Conard, T.; Demoustier-Champagne, S.; Du Prez, F. E.; Landoulsi, J.; Dupont-Gillain, C. C. Design of Mixed PEO/PAA Brushes with Switchable Properties Toward Protein Adsorption. *Biomacromolecules* **2013**, *14* (1), 215–225. https://doi.org/10.1021/bm301637h.

(79) Delcroix, M. F.; Demoustier-Champagne, S.; Dupont-Gillain, C. C. Quartz Crystal Microbalance Study of Ionic Strength and PH-Dependent Polymer Conformation and Protein Adsorption/Desorption on PAA, PEO, and Mixed PEO/PAA Brushes. *Langmuir* **2014**, *30* (1), 268–277. https://doi.org/10.1021/la403891k.

(80) Henzler, K.; Haupt, B.; Lauterbach, K.; Wittemann, A.; Borisov, O.; Ballauff, M. Adsorption of β-Lactoglobulin on Spherical Polyelectrolyte Brushes: Direct Proof of Counterion Release by Isothermal Titration Calorimetry. *J. Am. Chem. Soc.* **2010**, *132* (9), 3159–3163. https://doi.org/10.1021/ja909938c.

(81) Henzler, K.; Wittemann, A.; Breininger, E.; Ballauff, M.; Rosenfeldt, S. Adsorption of Bovine Hemoglobin onto Spherical Polyelectrolyte Brushes Monitored by Small-Angle X-Ray Scattering and Fourier Transform Infrared Spectroscopy. *Biomacromolecules* **2007**, *8* (11), 3674–3681. https://doi.org/10.1021/bm700953e.

(82) Yigit, C.; Kanduč, M.; Ballauff, M.; Dzubiella, J. Interaction of Charged Patchy Protein Models with Like-Charged Polyelectrolyte Brushes. **2017**, *33* (1), 417–427. https://doi.org/10.1021/acs.langmuir.6b03797.

(83) Claesson, P. M.; Poptoshev, E.; Blomberg, E.; Dedinaite, A. Polyelectrolyte-Mediated Surface Interactions. *Adv. Colloid Interface Sci.* **2005**, *114–115*, 173–187. https://doi.org/10.1016/j.cis.2004.09.008.

(84) de Vries, R.; Cohen Stuart, M. Theory and Simulations of Macroion Complexation. *Curr. Opin. Colloid Interface Sci.* **2006**, *11* (5), 295–301. https://doi.org/10.1016/j.cocis.2006.09.004.

(85) Ulrich, S.; Seijo, M.; Stoll, S. The Many Facets of Polyelectrolytes and Oppositely Charged Macroions Complex Formation. *Curr. Opin. Colloid Interface Sci.* **2006**, *11* (5), 268–272. https://doi.org/10.1016/j.cocis.2006.08.002.

(86) Seyrek, E.; Dubin, P. Glycosaminoglycans as Polyelectrolytes. *Adv. Colloid Interface Sci.* **2010**, *158* (1–2), 119–129. https://doi.org/10.1016/j.cis.2010.03.001.

(87) Capila, I.; Linhardt, R. J. Heparin-Protein Interactions. *Angew. Chemie Int. Ed.* **2002**, *41* (3), 390–412.

https://doi.org/10.1002/1521-3773(20020201)41:3<390::AID-ANIE390>3.0.CO;2-B.

(88) Mulloy, B.; Linhardt, R. J. Order out of Complexity – Protein Structures That Interact with Heparin. *Curr. Opin. Struct. Biol.* **2001**, *11* (5), 623–628. https://doi.org/10.1016/S0959-440X(00)00257-8.

(89) Lindahl, U.; Li, J. Chapter 3 Interactions Between Heparan Sulfate and Proteins—Design and Functional Implications. In *International Review of Cell and Molecular Biology*; 2009; pp 105–159. https://doi.org/10.1016/S1937-6448(09)76003-4.

(90) Powell, A. K. Interactions of Heparin/Heparan Sulfate with Proteins: Appraisal of Structural Factors and Experimental Approaches. *Glycobiology* **2004**, *14* (4), 17R-30R. https://doi.org/10.1093/glycob/cwh051.

(91) Whitelock, J. M.; Iozzo, R. V. Heparan Sulfate: A Complex Polymer Charged with Biological Activity. *Chem. Rev.* **2005**, *105* (7), 2745–2764. https://doi.org/10.1021/cr010213m.

(92) Weitz, J. I.; Harenberg, J. New Developments in Anticoagulants: Past, Present and Future. *Thromb. Haemost.* **2017**, *117* (07), 1283–1288. https://doi.org/10.1160/TH16-10-0807.

(93) Young, E. The Anti-Inflammatory Effects of Heparin and Related Compounds. *Thromb. Res.* **2008**, *122* (6), 743–752. https://doi.org/10.1016/j.thromres.2006.10.026.

(94) Ricciuti, B.; Foglietta, J.; Chiari, R.; Sahebkar, A.; Banach, M.; Bianconi, V.; Pirro, M. Emerging Enzymatic Targets Controlling Angiogenesis in Cancer: Preclinical Evidence and Potential Clinical Applications. *Med. Oncol.* **2018**, *35* (1), 4. https://doi.org/10.1007/s12032-017-1064-5.

(95) Tieken, C.; Versteeg, H. H. Anticoagulants versus Cancer. *Thromb. Res.* **2016**, *140*, S148–S153. https://doi.org/10.1016/S0049-3848(16)30114-1.

(96) Lander, A. D. Proteoglycans: Master Regulators of Molecular Encounter? *Matrix Biol.* **1998**, *17* (7), 465–472. https://doi.org/10.1016/S0945-053X(98)90093-2.

(97) Boer, C.; Meesters, M. I.; Veerhoek, D.; Vonk, A. B. A. Anticoagulant and Side-Effects of Protamine in Cardiac Surgery: A Narrative Review. *Br. J. Anaesth.* **2018**, *120* (5), 914–927. https://doi.org/10.1016/j.bja.2018.01.023.

(98) Gandhi, N. S.; Mancera, R. L. Heparin/Heparan Sulphate-Based Drugs. *Drug Discov. Today* **2010**, *15* (23–24), 1058–1069. https://doi.org/10.1016/j.drudis.2010.10.009.

(99) Minsky, B. B.; Dubin, P. L.; Kaltashov, I. A. Electrostatic Forces as Dominant Interactions Between Proteins and Polyanions: An ESI MS Study of Fibroblast Growth Factor Binding to Heparin Oligomers. *J. Am. Soc. Mass Spectrom.* **2017**, *28* (4), 758–767. https://doi.org/10.1007/s13361-017-1596-0.

(100) Minsky, B. B.; Zheng, B.; Dubin, P. L. Inhibition of Antithrombin and Bovine Serum Albumin Native State Aggregation by Heparin. *Langmuir* **2014**, *30* (1), 278–287. https://doi.org/10.1021/la4039232.

(101) Kumar, A.; Sahoo, S. K.; Padhee, K.; Pal, P.; Kochar, S.; Satapathy, A.; Pathak, N. Reveiw on Solubility Enhancement Techniques for Hydrophobic Drugs. *Int. J. Compr. Pharm.* **2011**.

(102) Kurkov, S. V.; Loftsson, T. Cyclodextrins. *Int. J. Pharm.* **2013**, *453* (1), 167–180. https://doi.org/10.1016/j.ijpharm.2012.06.055.

(103) Sayani, A. P.; Chien, Y. W. Systemic Delivery of Peptides and Proteins across Absorptive Mucosae. *Critical Reviews in Therapeutic Drug Carrier Systems*. 1996.

(104) Davis, M. E.; Brewster, M. E. Cyclodextrin-Based Pharmaceutics: Past, Present and Future. *Nat. Rev. Drug Discov.* **2004**, *3* (12), 1023–1035. https://doi.org/10.1038/nrd1576.

(105) Liu, L.; Guo, Q. X. The Driving Forces in the Inclusion Complexation of Cyclodextrins. *Journal of Inclusion Phenomena*. 2002. https://doi.org/10.1023/A:1014520830813.

(106) Chou, Y.-W.; Huang, W.-S.; Ko, C.-C.; Chen, S.-H. Enantioseparation of Cetirizine by Sulfated-β-Cyclodextrin-Mediated Capillary Electrophoresis. *J. Sep. Sci.* **2008**, *31* (5), 845–852. https://doi.org/10.1002/jssc.200700487.

(107) Maynard, D. K.; Vigh, G. Heptakis(2-O-Methyl-3,6-Di-O-Sulfo)- β-Cyclodextrin: A Single-Isomer, 14-

Sulfated β-Cyclodextrin for Use as a Chiral Resolving Agent in Capillary Electrophoresis. *Electrophoresis* **2001**, *22* (15), 3152–3162. https://doi.org/10.1002/1522-2683(200109)22:15<3152::AID-ELPS3152>3.0.CO;2-I.

(108) Süß, F.; Sänger-van de Griend, C. E.; Scriba, G. K. E. Migration Order of Dipeptide and Tripeptide Enantiomers in the Presence of Single Isomer and Randomly Sulfated Cyclodextrins as a Function of PH. *Electrophoresis* **2003**, *24* (6), 1069–1076. https://doi.org/10.1002/elps.200390124.

(109) Bilensoy, E. *Cyclodextrins in Pharmaceutics, Cosmetics, and Biomedicine*; Bilensoy, E., Ed.; John Wiley & Sons, Inc.: Hoboken, NJ, USA, 2011. https://doi.org/10.1002/9780470926819.

(110) Li, L.; Dantzer, J. J.; Nowacki, J.; O'Callaghan, B. J.; Meroueh, S. O. PDBcal: A Comprehensive Dataset for Receptor–Ligand Interactions with Three-Dimensional Structures and Binding Thermodynamics from Isothermal Titration Calorimetry. *Chem. Biol. Drug Des.* **2008**, *71* (6), 529–532. https://doi.org/10.1111/j.1747-0285.2008.00661.x.

(111) Irie, T. Cyclodextrins in Peptide and Protein Delivery. *Adv. Drug Deliv. Rev.* **1999**, *36* (1), 101–123. https://doi.org/10.1016/S0169-409X(98)00057-X.

(112) Macarak, E. J.; Kumor, K.; Weisz, P. B. Sulfation and Hemolytic Activity of Cyclodextrin. *Biochem. Pharmacol.* **1991**, *42* (7), 1502–1503. https://doi.org/10.1016/0006-2952(91)90467-J.

(113) Sunder, A.; Hanselmann, R.; Frey, H.; Mülhaupt, R. Controlled Synthesis of Hyperbranched Polyglycerols by Ring-Opening Multibranching Polymerization. *Macromolecules* **1999**, *32* (13), 4240–4246. https://doi.org/10.1021/ma990090w.

(114) Rades, N.; Licha, K.; Haag, R. Dendritic Polyglycerol Sulfate for Therapy and Diagnostics. *Polymers (Basel).* **2018**, *10* (6), 595. https://doi.org/10.3390/polym10060595.

(115) Dernedde, J.; Rausch, A.; Weinhart, M.; Enders, S.; Tauber, R.; Licha, K.; Schirner, M.; Zugel, U.; von Bonin, A.; Haag, R. Dendritic Polyglycerol Sulfates as Multivalent Inhibitors of Inflammation. *Proc. Natl. Acad. Sci.* **2010**, *107* (46), 19679–19684. https://doi.org/10.1073/pnas.1003103107.

(116) Gröger, D.; Kerschnitzki, M.; Weinhart, M.; Reimann, S.; Schneider, T.; Kohl, B.; Wagermaier, W.; Schulze-Tanzil, G.; Fratzl, P.; Haag, R. Selectivity in Bone Targeting with Multivalent Dendritic Polyanion Dye Conjugates. *Adv. Healthc. Mater.* **2014**, *3* (3), 375–385. https://doi.org/10.1002/adhm.201300205.

(117) Reimann, S.; Schneider, T.; Welker, P.; Neumann, F.; Licha, K.; Schulze-Tanzil, G.; Wagermaier, W.; Fratzl, P.; Haag, R. Dendritic Polyglycerol Anions for the Selective Targeting of Native and Inflamed Articular Cartilage. *J. Mater. Chem. B* **2017**, *5* (24), 4754–4767. https://doi.org/10.1039/C7TB00618G.

(118) Schneider, T.; Welker, P.; Licha, K.; Haag, R.; Schulze-Tanzil, G. Influence of Dendritic Polyglycerol Sulfates on Knee Osteoarthritis: An Experimental Study in the Rat Osteoarthritis Model. *BMC Musculoskelet. Disord.* **2015**, *16* (1), 387. https://doi.org/10.1186/s12891-015-0844-3.

(119) Dey, P.; Hemmati-Sadeghi, S.; Haag, R. Hydrolytically Degradable, Dendritic Polyglycerol Sulfate Based Injectable Hydrogels Using Strain Promoted Azide–Alkyne Cycloaddition Reaction. *Polym. Chem.* **2016**, *7* (2), 375–383. https://doi.org/10.1039/C5PY01326G.

(120) von Lospichl, B.; Hemmati-Sadeghi, S.; Dey, P.; Dehne, T.; Haag, R.; Sittinger, M.; Ringe, J.; Gradzielski, M. Injectable Hydrogels for Treatment of Osteoarthritis – A Rheological Study. *Colloids Surfaces B Biointerfaces* **2017**, *159*, 477–483. https://doi.org/10.1016/j.colsurfb.2017.07.073.

(121) Maysinger, D.; Gröger, D.; Lake, A.; Licha, K.; Weinhart, M.; Chang, P. K. Y.; Mulvey, R.; Haag, R.; McKinney, R. A. Dendritic Polyglycerol Sulfate Inhibits Microglial Activation and Reduces Hippocampal CA1 Dendritic Spine Morphology Deficits. *Biomacromolecules* **2015**, *16* (9), 3073–3082. https://doi.org/10.1021/acs.biomac.5b00999.

(122) Maysinger, D.; Ji, J.; Moquin, A.; Hossain, S.; Hancock, M. A.; Zhang, I.; Chang, P. K. Y.; Rigby, M.; Anthonisen, M.; Grütter, P.; et al. Dendritic Polyglycerol Sulfates in the Prevention of Synaptic Loss and Mechanism of Action on Glia. *ACS Chem. Neurosci.* **2018**, *9* (2), 260–271. https://doi.org/10.1021/acschemneuro.7b00301.

(123) Borisov, O. V.; Birshtein, T. M.; Zhulina, E. B. Polyelectrolyte Brushes. *Makromol. Chemie. Macromol. Symp.* **1993**, *65* (1), 199–204. https://doi.org/10.1002/masy.19930650122.

(124) Biesalski, M.; Rühe, J. Preparation and Characterization of a Polyelectrolyte Monolayer Covalently Attached to a Planar Solid Surface. *Macromolecules* **1999**, *32* (7), 2309–2316. https://doi.org/10.1021/ma980628i.

(125) Ahrens, H.; Förster, S.; Helm, C. A. Polyelectrolyte Brushes Grafted at the Air/Water Interface. *Macromolecules* **1997**, *30* (26), 8447–8452. https://doi.org/10.1021/ma970949e.

(126) Muller, F.; Delsanti, M.; Auvray, L.; Yang, J.; Chen, Y. J.; Mays, J. W.; Demé, B.; Tirrell, M.; Guenoun, P. Ordering of Urchin-like Charged Copolymer Micelles: Electrostatic, Packing and Polyelectrolyte Correlations. *Eur. Phys. J. E* **2000**, *3* (1), 45–53. https://doi.org/10.1007/s101890070040.

(127) Zhang, L.; Yu, K.; Eisenberg, A. Ion-Induced Morphological Changes in ``Crew-Cut'' Aggregates of Amphiphilic Block Copolymers. *Science (80-.).* **1996**, *272* (5269), 1777–1779. https://doi.org/10.1126/science.272.5269.1777.

(128) Biver, C.; Hariharan, R.; Mays, J.; Russel, W. B. Neutral and Charged Polymer Brushes: A Model Unifying Curvature Effects from Micelles to Flat Surfaces. *Macromolecules* **1997**, *30* (6), 1787–1792. https://doi.org/10.1021/ma9610065.

(129) Guo, X.; Weiss, A.; Ballauff, M. Synthesis of Spherical Polyelectrolyte Brushes by Photoemulsion Polymerization. *Macromolecules* **1999**, *32* (19), 6043–6046. https://doi.org/10.1021/ma990609o.

(130) Muller, F.; Fontaine, P.; Delsanti, M.; Belloni, L.; Yang, J.; Chen, Y. J.; Mays, J. W.; Lesieur, P.; Tirrell, M.; Guenoun, P. Counterion Distribution in a Spherical Charged Sparse Brush. *Eur. Phys. J. E* **2001**, *6* (2), 109–115. https://doi.org/10.1007/s101890170010.

(131) Lee, A. S.; Bütün, V.; Vamvakaki, M.; Armes, S. P.; Pople, J. A.; Gast, A. P. Structure of PH-Dependent Block Copolymer Micelles: Charge and Ionic Strength Dependence. *Macromolecules* **2002**, *35* (22), 8540–8551. https://doi.org/10.1021/ma0114842.

(132) Förster, S.; Hermsdorf, N.; Böttcher, C.; Lindner, P. Structure of Polyelectrolyte Block Copolymer Micelles. *Macromolecules* **2002**, *35* (10), 4096–4105. https://doi.org/10.1021/ma011565y.

(133) Wang, X.; Wu, S.; Li, L.; Zhang, R.; Zhu, Y.; Ballauff, M.; Lu, Y.; Guo, X. Synthesis of Spherical Polyelectrolyte Brushes by Photoemulsion Polymerization with Different Photoinitiators. *Ind. Eng. Chem. Res.* **2011**, *50* (6), 3564–3569. https://doi.org/10.1021/ie101764s.

(134) Ballauff, M. Spherical Polyelectrolyte Brushes. *Prog. Polym. Sci.* **2007**, *32* (10), 1135–1151. https://doi.org/10.1016/j.progpolymsci.2007.05.002.

(135) Zhou, F.; Huck, W. T. S. Surface Grafted Polymer Brushes as Ideal Building Blocks for "Smart" Surfaces. *Phys. Chem. Chem. Phys.* **2006**, *8* (33), 3815–3823. https://doi.org/10.1039/B606415A.

(136) Pincus, P. Colloid Stabilization with Grafted Polyelectrolytes. *Macromolecules* **1991**, *24* (10), 2912–2919. https://doi.org/10.1021/ma00010a043.

(137) Borisov, O. V.; Birshtein, T. M.; Zhulina, E. B. Collapse of Grafted Polyelectrolyte Layer. *J. Phys. II* **1991**, *1* (5), 521–526. https://doi.org/10.1051/jp2:1991186.

(138) Ahrens, H.; Förster, S.; Helm, C. A. Charged Polymer Brushes: Counterion Incorporation and Scaling Relations. *Phys. Rev. Lett.* **1998**, *81* (19), 4172–4175. https://doi.org/10.1103/PhysRevLett.81.4172.

(139) Biesalski, M.; Rühe, J. Scaling Laws for the Swelling of Neutral and Charged Polymer Brushes in Good Solvents. *Macromolecules* **2002**, *35* (2), 499–507. https://doi.org/10.1021/ma001776n.

(140) Biesalski, M.; Johannsmann, D.; Rühe, J. Electrolyte-Induced Collapse of a Polyelectrolyte Brush. *J. Chem. Phys.* **2004**, *120* (18), 8807–8814. https://doi.org/10.1063/1.1690242.

(141) Treat, N. D.; Ayres, N.; Boyes, S. G.; Brittain, W. J. A Facile Route to Poly(Acrylic Acid) Brushes Using Atom Transfer Radical Polymerization. *Macromolecules* **2006**, *39* (1), 26–29. https://doi.org/10.1021/ma052001n.

(142) Chu, X.; Yang, J.; Liu, G.; Zhao, J. Swelling Enhancement of Polyelectrolyte Brushes Induced by External Ions. *Soft Matter* **2014**, *10* (30), 5568–5578. https://doi.org/10.1039/C4SM00860J.

(143) Guo, X.; Ballauff, M. Spatial Dimensions of Colloidal Polyelectrolyte Brushes As Determined by Dynamic Light Scattering †. *Langmuir* **2000**, *16* (23), 8719–8726. https://doi.org/10.1021/la000319x.

(144) Guo, X.; Ballauff, M. Spherical Polyelectrolyte Brushes: Comparison between Annealed and Quenched Brushes. *Phys. Rev. E* **2001**, *64* (5), 051406. https://doi.org/10.1103/PhysRevE.64.051406.

(145) Dingenonts, N.; Patel, M.; Rosenfeldt, S.; Pontoni, D.; Narayanan, T.; Ballauff, M.; Dingenouts, N.; Patel, M.; Rosenfeldt, S.; Pontoni, D.; et al. Counterion Distribution around a Spherical Polyelectrolyte Brush Probed by Anomalous Small-Angle X-Ray Scattering. *Macromolecules* **2004**, *37* (21), 8152–8159. https://doi.org/10.1021/ma048828j.

(146) Groenewegen, W.; Lapp, A.; Egelhaaf, S. U.; van der Maarel, J. R. C. Counterion Distribution in the Coronal Layer of Polyelectrolyte Diblock Copolymer Micelles. *Macromolecules* **2000**, *33* (11), 4080–4086. https://doi.org/10.1021/ma000096h.

(147) Wittemann, A.; Drechsler, M.; Talmon, Y.; Ballauff, M. High Elongation of Polyelectrolyte Chains in the Osmotic Limit of Spherical Polyelectrolyte Brushes: A Study by Cryogenic Transmission Electron Microscopy. *J. Am. Chem. Soc.* **2005**, *127* (27), 9688–9689. https://doi.org/10.1021/ja0513234.

(148) Gu, S.; Lu, Y.; Kaiser, J.; Albrecht, M.; Ballauff, M. Kinetic Analysis of the Reduction of 4-Nitrophenol Catalyzed by Au/Pd Nanoalloys Immobilized in Spherical Polyelectrolyte Brushes. *Phys. Chem. Chem. Phys.* **2015**, *17* (42), 28137–28143. https://doi.org/10.1039/C5CP00519A.

(149) Wang, S.; Chen, K.; Xu, Y.; Yu, X.; Wang, W.; Li, L.; Guo, X. Protein Immobilization and Separation Using Anionic/Cationic Spherical Polyelectrolyte Brushes Based on Charge Anisotropy. *Soft Matter* **2013**, *9* (47), 11276. https://doi.org/10.1039/c3sm51482j.

(150) Kubiak-Ossowska, K.; Mulheran, P. A. Mechanism of Hen Egg White Lysozyme Adsorption on a Charged Solid Surface. *Langmuir* **2010**, *26* (20), 15954–15965. https://doi.org/10.1021/la102960m.

(151) Hanke, N.; Prager, E. M.; Wilson, A. C. Quantitative Immunological and Electrophoretic Comparison of Primate Lysozymes. *J. Biol. Chem.* **1973**.

(152) Callewaert, L.; Walmagh, M.; Michiels, C. W.; Lavigne, R. Food Applications of Bacterial Cell Wall Hydrolases. *Curr. Opin. Biotechnol.* **2011**, *22* (2), 164–171. https://doi.org/10.1016/j.copbio.2010.10.012.

(153) Sava, G. Pharmacological Aspects and Therapeutic Applications of Lysozymes. *EXS* **1996**, *75*, 433–449. https://doi.org/10.1007/978-3-0348-9225-4_22.

(154) BLAKE, C. C. F.; KOENIG, D. F.; MAIR, G. A.; NORTH, A. C. T.; PHILLIPS, D. C.; SARMA, V. R. Structure of Hen Egg-White Lysozyme: A Three-Dimensional Fourier Synthesis at 2 Å Resolution. *Nature* **1965**, *206* (4986), 757–761. https://doi.org/10.1038/206757a0.

(155) CANFIELD, R. E. THE AMINO ACID SEQUENCE OF EGG WHITE LYSOZYME. *J. Biol. Chem.* **1963**, *238*, 2698–2707.

(156) He, X. M.; Carter, D. C. Atomic Structure and Chemistry of Human Serum Albumin. *Nature* **1992**, *358* (6383), 209–215. https://doi.org/10.1038/358209a0.

(157) Fasano, M.; Curry, S.; Terreno, E.; Galliano, M.; Fanali, G.; Narciso, P.; Notari, S.; Ascenzi, P. The Extraordinary Ligand Binding Properties of Human Serum Albumin. *IUBMB Life (International Union Biochem. Mol. Biol. Life)* **2005**, *57* (12), 787–796. https://doi.org/10.1080/15216540500404093.

(158) Curry, S. Beyond Expansion: Structural Studies on the Transport Roles of Human Serum Albumin. *Vox Sang.* **2002**, *83*, 315–319. https://doi.org/10.1111/j.1423-0410.2002.tb05326.x.

(159) Ascenzi, P.; Fasano, M. Allostery in a Monomeric Protein: The Case of Human Serum Albumin. *Biophys. Chem.* **2010**, *148* (1–3), 16–22. https://doi.org/10.1016/j.bpc.2010.03.001.

(160) Sudlow, G.; Birkett, D. J.; Wade, D. N. The Characterization of Two Specific Drug Binding Sites on Human Serum. *Mol. Pharmacol.* **1975**.

(161) Sudlow, G.; Birkett, D. J.; Wade, D. N. The Characterization of Two Specific Drug Binding Sites on Human Serum Albumin. *Mol. Pharmacol.* **1975**, *11* (6), 824–832.

(162) Sugio, S.; Kashima, A.; Mochizuki, S.; Noda, M.; Kobayashi, K. Crystal Structure of Human Serum Albumin at 2.5 Å Resolution. *Protein Eng. Des. Sel.* **1999**, *12* (6), 439–446. https://doi.org/10.1093/protein/12.6.439.

(163) Welsch, N.; Becker, A. L.; Dzubiella, J.; Ballauff, M. Core–Shell Microgels as "Smart" Carriers for Enzymes. *Soft Matter* **2012**, *8* (5), 1428–1436. https://doi.org/10.1039/C1SM06894F.

(164) DeHaseth, P. L.; Lohman, T. M.; Record, M. T. Nonspecific Interaction of Lac Repressor with DNA: An Association Reaction Driven by Counterion Release. *Biochemistry* **1977**, *16* (22), 4783–4790. https://doi.org/10.1021/bi00641a004.

(165) Record, M. T.; Anderson, C. F.; Lohman, T. M. Thermodynamic Analysis of Ion Effects on the Binding and Conformational Equilibria of Proteins and Nucleic Acids: The Roles of Ion Association or Release, Screening, and Ion Effects on Water Activity. *Q. Rev. Biophys.* **1978**, *11* (2), 103–178. https://doi.org/10.1017/S003358350000202X.

(166) Dobrovolskaia, M. A.; Germolec, D. R.; Weaver, J. L. Evaluation of Nanoparticle Immunotoxicity. *Nat. Nanotechnol.* **2009**, *4* (7), 411–414. https://doi.org/10.1038/nnano.2009.175.

(167) Lynch, I.; Salvati, A.; Dawson, K. A. What Does the Cell See? *Nat. Nanotechnol.* **2009**, *4* (9), 546–547. https://doi.org/10.1038/nnano.2009.248.

(168) Klein, J. Probing the Interactions of Proteins and Nanoparticles. *Proc. Natl. Acad. Sci.* **2007**, *104* (7), 2029–2030. https://doi.org/10.1073/pnas.0611610104.

(169) Walczyk, D.; Bombelli, F. B.; Monopoli, M. P.; Lynch, I.; Dawson, K. A. What the Cell "Sees" in Bionanoscience. *J. Am. Chem. Soc.* **2010**, *132* (16), 5761–5768. https://doi.org/10.1021/ja910675v.

(170) Caracciolo, G.; Pozzi, D.; Capriotti, A. L.; Cavaliere, C.; Foglia, P.; Amenitsch, H.; Laganà, A. Evolution of the Protein Corona of Lipid Gene Vectors as a Function of Plasma Concentration. *Langmuir* **2011**, *27* (24), 15048–15053. https://doi.org/10.1021/la202912f.

(171) Xu, A.; Lenhoff, A. M. A Predictive Approach to Correlating Protein Adsorption Isotherms on Ion-Exchange Media. *J. Phys. Chem. B* **2008**. https://doi.org/10.1021/jp0754233.

(172) Henzler, K.; Rosenfeldt, S.; Wittemann, A.; Harnau, L.; Finet, S.; Narayanan, T.; Ballauff, M. Directed Motion of Proteins along Tethered Polyelectrolytes. *Phys. Rev. Lett.* **2008**, *100* (15), 158301. https://doi.org/10.1103/PhysRevLett.100.158301.

(173) Rosenfeldt, S.; Wittemann, A.; Ballauff, M.; Breininger, E.; Bolze, J.; Dingenouts, N. Interaction of Proteins with Spherical Polyelectrolyte Brushes in Solution as Studied by Small-Angle x-Ray Scattering. *Phys. Rev. E* **2004**, *70* (6), 061403. https://doi.org/10.1103/PhysRevE.70.061403.

(174) Wang, S.; Chen, K.; Li, L.; Guo, X. Binding between Proteins and Cationic Spherical Polyelectrolyte Brushes: Effect of PH, Ionic Strength, and Stoichiometry. *Biomacromolecules* **2013**, *14* (3), 818–827. https://doi.org/10.1021/bm301865g.

(175) Becker, A. L.; Welsch, N.; Schneider, C.; Ballauff, M. Adsorption of RNase A on Cationic Polyelectrolyte Brushes: A Study by Isothermal Titration Calorimetry. *Biomacromolecules* **2011**, *12* (11), 3936–3944. https://doi.org/10.1021/bm200954j.

(176) Cooper, C. L.; Goulding, A.; Kayitmazer, A. B.; Ulrich, S.; Stoll, S.; Turksen, S.; Yusa, S.; Kumar, A.; Dubin, P. L. Effects of Polyelectrolyte Chain Stiffness, Charge Mobility, and Charge Sequences on Binding to Proteins and Micelles. *Biomacromolecules* **2006**, *7* (4), 1025–1035. https://doi.org/10.1021/bm050592j.

(177) Johnson, D. J. D.; Langdown, J.; Li, W.; Luis, S. A.; Baglin, T. P.; Huntington, J. A. Crystal Structure of Monomeric Native Antithrombin Reveals a Novel Reactive Center Loop Conformation. *J. Biol. Chem.* **2006**, *281* (46), 35478–35486. https://doi.org/10.1074/jbc.M607204200.

(178) Boeris, V.; Romanini, D.; Farruggia, B.; Picó, G. Interaction and Complex Formation between Catalase and Cationic Polyelectrolytes: Chitosan and Eudragit E100. *Int. J. Biol. Macromol.* **2009**, *45* (2), 103–108.

https://doi.org/10.1016/j.ijbiomac.2009.04.009.

(179) Schedin-Weiss, S.; Richard, B.; Hjelm, R.; Olson, S. T. Antiangiogenic Forms of Antithrombin Specifically Bind to the Anticoagulant Heparin Sequence †. *Biochemistry* **2008**, *47* (51), 13610–13619. https://doi.org/10.1021/bi801656u.

(180) Pelton, J. T.; McLean, L. R. Spectroscopic Methods for Analysis of Protein Secondary Structure. *Anal. Biochem.* **2000**, *277* (2), 167–176. https://doi.org/10.1006/abio.1999.4320.

(181) Wittemann, A.; Ballauff, M. Secondary Structure Analysis of Proteins Embedded in Spherical Polyelectrolyte Brushes by FT-IR Spectroscopy. *Anal. Chem.* **2004**, *76* (10), 2813–2819. https://doi.org/10.1021/ac0354692.

(182) Barrera, F. N.; Garzón, M. T.; Gómez, J.; Neira, J. L. Equilibrium Unfolding of the C-Terminal SAM Domain of P73 †. *Biochemistry* **2002**, *41* (18), 5743–5753. https://doi.org/10.1021/bi0159478.

(183) Butler, B. C.; Hanchett, R. H.; Rafailov, H.; MacDonald, G. Investigating Structural Changes Induced By Nucleotide Binding to RecA Using Difference FTIR. *Biophys. J.* **2002**, *82* (4), 2198–2210. https://doi.org/10.1016/S0006-3495(02)75566-5.

(184) Castellanos, I. J.; Cruz, G.; Crespo, R.; Griebenow, K. Encapsulation-Induced Aggregation and Loss in Activity of γ-Chymotrypsin and Their Prevention. *J. Control. Release* **2002**, *81* (3), 307–319. https://doi.org/10.1016/S0168-3659(02)00073-1.

(185) Winter, R.; Noll, F.; Czeslik, C. *Methoden Der Biophysikalischen Chemie*; Vieweg+Teubner: Wiesbaden, 2011. https://doi.org/10.1007/978-3-8348-8143-4.

(186) Dousseau, F.; Pezolet, M. Determination of the Secondary Structure Content of Proteins in Aqueous Solutions from Their Amide I and Amide II Infrared Bands. Comparison between Classical and Partial Least-Squares Methods. *Biochemistry* **1990**, *29* (37), 8771–8779. https://doi.org/10.1021/bi00489a038.

(187) Jackler, G.; Wittemann, A.; Ballauff, M.; Czeslik, C. Spherical Polyelectrolyte Brushes as Carrier Particles for Proteins: An Investigation of the Structure of Adsorbed and Desorbed Bovine Serum Albumin. *Spectroscopy* **2004**, *18* (2), 289–299. https://doi.org/10.1155/2004/526159.

(188) Welsch, N.; Wittemann, A.; Ballauff, M. Enhanced Activity of Enzymes Immobilized in Thermoresponsive Core−Shell Microgels. *J. Phys. Chem. B* **2009**, *113* (49), 16039–16045. https://doi.org/10.1021/jp907508w.

(189) Manning, G. S. Limiting Laws and Counterion Condensation in Polyelectrolyte Solutions I. Colligative Properties. *J. Chem. Phys.* **1969**, *51* (3), 924–933. https://doi.org/10.1063/1.1672157.

(190) Manning, G. S.; Ray, J. Counterion Condensation Revisited. *J. Biomol. Struct. Dyn.* **1998**, *16* (2), 461–476. https://doi.org/10.1080/07391102.1998.10508261.

(191) Zhang, H.; Dubin, P. L.; Ray, J.; Manning, G. S.; Moorefield, C. N.; Newkome, G. R. Interaction of a Polycation with Small Oppositely Charged Dendrimers. *J. Phys. Chem. B* **1999**, *103* (13), 2347–2354. https://doi.org/10.1021/jp983436y.

(192) Deserno, M.; Holm, C.; May, S. Fraction of Condensed Counterions around a Charged Rod: Comparison of Poisson−Boltzmann Theory and Computer Simulations. *Macromolecules* **2000**, *33* (1), 199–206. https://doi.org/10.1021/ma990897o.

(193) Naji, A.; Jungblut, S.; Moreira, A. G.; Netz, R. R. Electrostatic Interactions in Strongly Coupled Soft Matter. *Phys. A Stat. Mech. its Appl.* **2005**, *352* (1), 131–170. https://doi.org/10.1016/j.physa.2004.12.029.

(194) Kayitmazer, a. B.; Seeman, D.; Minsky, B. B.; Dubin, P. L.; Xu, Y. Protein–Polyelectrolyte Interactions. *Soft Matter* **2013**, *9* (9), 2553. https://doi.org/10.1039/c2sm27002a.

(195) Seyrek, E.; Dubin, P. L.; Tribet, C.; Gamble, E. A. Ionic Strength Dependence of Protein-Polyelectrolyte Interactions. *Biomacromolecules* **2003**, *4* (2), 273–282. https://doi.org/10.1021/bm025664a.

(196) Henzler, K.; Haupt, B.; Lauterbach, K.; Wittemann, A.; Borisov, O.; Ballauff, M. Adsorption of β-Lactoglobulin on Spherical Polyelectrolyte Brushes: Direct Proof of Counterion Release by Isothermal Titration Calorimetry. *J. Am. Chem. Soc.* **2010**, *132* (9), 3159–3163. https://doi.org/10.1021/ja909938c.

(197) Xu, Y.; Mazzawi, M.; Chen, K.; Sun, L.; Dubin, P. L. Protein Purification by Polyelectrolyte Coacervation: Influence of Protein Charge Anisotropy on Selectivity. *Biomacromolecules* **2011**, *12* (5), 1512–1522. https://doi.org/10.1021/bm101465y.

(198) Record, M. T.; Anderson, C. F.; Lohman, T. M. Thermodynamic Analysis of Ion Effects on the Binding and Conformational Equilibria of Proteins and Nucleic Acids: The Roles of Ion Association or Release, Screening, and Ion Effects on Water Activity. *Q. Rev. Biophys.* **1978**, *11* (2), 103–178. https://doi.org/10.1017/S003358350000202X.

(199) Record, M. T.; Lohman, T. M.; Haseth, P. de. Ion Effects on Ligand-Nucleic Acid Interactions. *J. Mol. Biol.* **1976**, *107* (2), 145–158. https://doi.org/10.1016/S0022-2836(76)80023-X.

(200) Bergqvist, S.; Williams, M. A.; O'Brien, R.; Ladbury, J. E. Heat Capacity Effects of Water Molecules and Ions at a Protein–DNA Interface. *J. Mol. Biol.* **2004**, *336* (4), 829–842. https://doi.org/10.1016/j.jmb.2003.12.061.

(201) Mascotti, D. P.; Lohman, T. M. Thermodynamic Extent of Counterion Release upon Binding Oligolysines to Single-Stranded Nucleic Acids. *Proc. Natl. Acad. Sci.* **1990**, *87* (8), 3142–3146. https://doi.org/10.1073/pnas.87.8.3142.

(202) Bergqvist, S.; O'Brien, R.; Ladbury, J. E. Site-Specific Cation Binding Mediates TATA Binding Protein−DNA Interaction from a Hyperthermophilic Archaeon. *Biochemistry* **2001**, *40* (8), 2419–2425. https://doi.org/10.1021/bi002488m.

(203) de Vos, W. M.; Leermakers, F. A. M.; de Keizer, A.; Cohen Stuart, M. A.; Kleijn, J. M. Field Theoretical Analysis of Driving Forces for the Uptake of Proteins by Like-Charged Polyelectrolyte Brushes: Effects of Charge Regulation and Patchiness. *Langmuir* **2010**, *26* (1), 249–259. https://doi.org/10.1021/la902079u.

(204) Evers, F.; Reichhart, C.; Steitz, R.; Tolan, M.; Czeslik, C. Probing Adsorption and Aggregation of Insulin at a Poly(Acrylic Acid) Brush. *Phys. Chem. Chem. Phys.* **2010**, *12* (17), 4375. https://doi.org/10.1039/b925134k.

(205) Uhlmann, P.; Houbenov, N.; Brenner, N.; Grundke, K.; Burkert, S.; Stamm, M. In-Situ Investigation of the Adsorption of Globular Model Proteins on Stimuli-Responsive Binary Polyelectrolyte Brushes †. *Langmuir* **2007**, *23* (1), 57–64. https://doi.org/10.1021/la061557g.

(206) Uhlmann, P.; Merlitz, H.; Sommer, J.-U.; Stamm, M. Polymer Brushes for Surface Tuning. *Macromol. Rapid Commun.* **2009**, *30* (9–10), 732–740. https://doi.org/10.1002/marc.200900113.

(207) Czeslik, C.; Jackler, G.; Hazlett, T.; Gratton, E.; Steitz, R.; Wittemann, A.; Ballauff, M. Salt-Induced Protein Resistance of Polyelectrolyte Brushes Studied Using Fluorescence Correlation Spectroscopy and Neutron Reflectometry. *Phys. Chem. Chem. Phys.* **2004**, *6* (24), 5557. https://doi.org/10.1039/b410805a.

(208) He, S.-Z.; Merlitz, H.; Sommer, J.-U.; Wu, C.-X. Counterion-Mediated Protein Adsorption into Polyelectrolyte Brushes. *Eur. Phys. J. E. Soft Matter* **2015**, *38* (9), 101. https://doi.org/10.1140/epje/i2015-15101-9.

(209) Olsson, T. S. G.; Ladbury, J. E.; Pitt, W. R.; Williams, M. A. Extent of Enthalpy-Entropy Compensation in Protein-Ligand Interactions. *Protein Sci.* **2011**, *20* (9), 1607–1618. https://doi.org/10.1002/pro.692.

(210) Torres, F. E.; Recht, M. I.; Coyle, J. E.; Bruce, R. H.; Williams, G. Higher Throughput Calorimetry: Opportunities, Approaches and Challenges. *Curr. Opin. Struct. Biol.* **2010**, *20* (5), 598–605. https://doi.org/10.1016/j.sbi.2010.09.001.

(211) Becktel, W. J.; Schellman, J. A. Protein Stability Curves. *Biopolymers* **1987**, *26* (11), 1859–1877. https://doi.org/10.1002/bip.360261104.

(212) Frank, H. S.; Evans, M. W. Free Volume and Entropy in Condensed Systems III. Entropy in Binary Liquid Mixtures; Partial Molal Entropy in Dilute Solutions; Structure and Thermodynamics in Aqueous Electrolytes. *J. Chem. Phys.* **1945**, *13* (11), 507–532. https://doi.org/10.1063/1.1723985.

(213) Kauzmann, W. Some Factors in the Interpretation of Protein Denaturation. In *Advances in Protein Chemistry*; 1959; pp 1–63. https://doi.org/10.1016/S0065-3233(08)60608-7.

(214) Mizoue, L. S.; Tellinghuisen, J. Calorimetric vs. van't Hoff Binding Enthalpies from Isothermal Titration Calorimetry: Ba2+-Crown Ether Complexation. *Biophys. Chem.* **2004**, *110* (1–2), 15–24. https://doi.org/10.1016/j.bpc.2003.12.011.

(215) Tellinghuisen, J. Van't Hoff Analysis of K°(T): How Good…or Bad? *Biophys. Chem.* **2006**, *120* (2), 114–120. https://doi.org/10.1016/j.bpc.2005.10.012.

(216) KRUG, R. R.; HUNTER, W. G.; GRIEGER, R. A. Statistical Interpretation of Enthalpy–Entropy Compensation. *Nature* **1976**, *261* (5561), 566–567. https://doi.org/10.1038/261566a0.

(217) Kozlov, A. G.; Lohman, T. M. Large Contributions of Coupled Protonation Equilibria to the Observed Enthalpy and Heat Capacity Changes for SsDNA Binding ToEscherichia Coli SSB Protein. *Proteins Struct. Funct. Genet.* **2002**. https://doi.org/10.1002/1097-0134(2000)41:4+<8::aid-prot20>3.0.co;2-h.

(218) Jen-Jacobson, L.; Engler, L. E.; Jacobson, L. A. Structural and Thermodynamic Strategies for Site-Specific DNA Binding Proteins. *Structure* **2000**, *8* (10), 1015–1023. https://doi.org/10.1016/S0969-2126(00)00501-3.

(219) Dunitz, J. D. Win Some, Lose Some: Enthalpy-Entropy Compensation in Weak Intermolecular Interactions. *Chem. Biol.* **1995**, *2* (11), 709–712. https://doi.org/10.1016/1074-5521(95)90097-7.

(220) Potoyan, D. A.; Zhuravlev, P. I.; Papoian, G. A. Computing Free Energy of a Large-Scale Allosteric Transition in Adenylate Kinase Using All Atom Explicit Solvent Simulations. *J. Phys. Chem. B* **2012**, *116* (5), 1709–1715. https://doi.org/10.1021/jp209980b.

(221) Xu, X.; Ran, Q.; Haag, R.; Ballauff, M.; Dzubiella, J. Charged Dendrimers Revisited: Effective Charge and Surface Potential of Dendritic Polyglycerol Sulfate. *Macromolecules* **2017**, *50* (12), 4759–4769. https://doi.org/10.1021/acs.macromol.7b00742.

(222) Xu, X.; Ballauff, M. Interaction of Lysozyme with a Dendritic Polyelectrolyte: Quantitative Analysis of the Free Energy of Binding and Comparison to Molecular Dynamics Simulations. *J. Phys. Chem. B* **2019**, *123* (39), 8222–8231. https://doi.org/10.1021/acs.jpcb.9b07448.

(223) Lohman, T. M.; DeHaseth, P. L.; Record, M. T. Pentalysine-Deoxyribonucleic Acid Interactions: A Model for the General Effects of Ion Concentrations on the Interactions of Proteins with Nucleic Acids. *Biochemistry* **1980**, *19* (15), 3522–3530. https://doi.org/10.1021/bi00556a017.

(224) Overman, L. B.; Bujalowski, W.; Lohman, T. M. Equilibrium Binding of Escherichia Coli Single-Strand Binding Protein to Single-Stranded Nucleic Acids in the (SSB)65 Binding Mode. Cation and Anion Effects and Polynucleotide Specificity. *Biochemistry* **1988**, *27* (1), 456–471. https://doi.org/10.1021/bi00401a067.

(225) Bujalowski, W.; Lohman, T. M. Escherichia Coli Single-Strand Binding Protein Forms Multiple, Distinct Complexes with Single-Stranded DNA. *Biochemistry* **1986**, *25* (24), 7799–7802. https://doi.org/10.1021/bi00372a003.

(226) Overman, L. B.; Lohman, T. M. Linkage of PH, Anion and Cation Effects in Protein-Nucleic Acid Equilibria. *J. Mol. Biol.* **1994**, *236* (1), 165–178. https://doi.org/10.1006/jmbi.1994.1126.

(227) Ladbury, J. E.; Chowdhry, B. Z. Sensing the Heat: The Application of Isothermal Titration Calorimetry to Thermodynamic Studies of Biomolecular Interactions. *Chem. Biol.* **1996**, *3* (10), 791–801. https://doi.org/10.1016/S1074-5521(96)90063-0.

(228) Baier, G.; Costa, C.; Zeller, A.; Baumann, D.; Sayer, C.; Araujo, P. H. H.; Mailänder, V.; Musyanovych, A.; Landfester, K. BSA Adsorption on Differently Charged Polystyrene Nanoparticles Using Isothermal Titration Calorimetry and the Influence on Cellular Uptake. *Macromol. Biosci.* **2011**, *11* (5), 628–638. https://doi.org/10.1002/mabi.201000395.

(229) Duff, M. R.; Kumar, C. V. Protein−Solid Interactions: Important Role of Solvent, Ions, Temperature, and Buffer in Protein Binding to α-Zr(IV) Phosphate. *Langmuir* **2009**, *25* (21), 12635–12643. https://doi.org/10.1021/la901901k.

(230) Rieger, J.; Freichels, H.; Imberty, A.; Putaux, J.-L.; Delair, T.; Jérôme, C.; Auzély-Velty, R. Polyester Nanoparticles Presenting Mannose Residues: Toward the Development of New Vaccine Delivery Systems Combining Biodegradability and Targeting Properties. *Biomacromolecules* **2009**, *10* (3), 651–657.

https://doi.org/10.1021/bm801492c.

(231) Wang, W.; Li, L.; Henzler, K.; Lu, Y.; Wang, J.; Han, H.; Tian, Y.; Wang, Y.; Zhou, Z.; Lotze, G.; et al. Protein Immobilization onto Cationic Spherical Polyelectrolyte Brushes Studied by Small Angle X-Ray Scattering. *Biomacromolecules* **2017**, *18* (5), 1574–1581. https://doi.org/10.1021/acs.biomac.7b00164.

(232) Ciulli, A. Biophysical Screening for the Discovery of Small-Molecule Ligands. In *Methods in Molecular Biology*; 2013; pp 357–388. https://doi.org/10.1007/978-1-62703-398-5_13.

(233) Ladbury, John E. & Doyle, M. *Biocalorimetry 2*; Ladbury, J. E., Doyle, M. L., Eds.; John Wiley & Sons, Ltd: Chichester, UK, 2004. https://doi.org/10.1002/0470011122.

(234) Turnbull, W. B.; Daranas, A. H. On the Value of c : Can Low Affinity Systems Be Studied by Isothermal Titration Calorimetry? *J. Am. Chem. Soc.* **2003**, *125* (48), 14859–14866. https://doi.org/10.1021/ja036166s.

(235) Indyk, L.; Fisher, H. F. [17] Theoretical Aspects of Isothermal Titration Calorimetry. In *Methods in Enzymology*; 1998; pp 350–364. https://doi.org/10.1016/S0076-6879(98)95048-0.

(236) Lin, L. N.; Mason, A. B.; Woodworth, R. C.; Brandts, J. F. Calorimetric Studies of the Binding of Ferric Ions to Human Serum Transferrin. *Biochemistry* **1993**, *32* (36), 9398–9406. https://doi.org/10.1021/bi00087a019.

(237) Yigit, C.; Welsch, N.; Ballauff, M.; Dzubiella, J. Protein Sorption to Charged Microgels: Characterizing Binding Isotherms and Driving Forces. *Langmuir* **2012**. https://doi.org/10.1021/la303292z.

(238) Xu, X.; Dzubiella, J. Probing the Protein Corona around Charged Macromolecules: Interpretation of Isothermal Titration Calorimetry by Binding Models and Computer Simulations. *Colloid Polym. Sci.* **2020**. https://doi.org/10.1007/s00396-020-04648-x.

(239) Marx, K. A. Quartz Crystal Microbalance: A Useful Tool for Studying Thin Polymer Films and Complex Biomolecular Systems at the Solution−Surface Interface. *Biomacromolecules* **2003**, *4* (5), 1099–1120. https://doi.org/10.1021/bm020116i.

(240) Richter, R. P.; Bérat, R.; Brisson, A. R. Formation of Solid-Supported Lipid Bilayers: An Integrated View. *Langmuir* **2006**, *22* (8), 3497–3505. https://doi.org/10.1021/la052687c.

(241) Steinmetz, N. F.; Bock, E.; Richter, R. P.; Spatz, J. P.; Lomonossoff, G. P.; Evans, D. J. Assembly of Multilayer Arrays of Viral Nanoparticles via Biospecific Recognition: A Quartz Crystal Microbalance with Dissipation Monitoring Study. *Biomacromolecules* **2008**, *9* (2), 456–462. https://doi.org/10.1021/bm700797b.

(242) Tellechea, E.; Johannsmann, D.; Steinmetz, N. F.; Richter, R. P.; Reviakine, I. Model-Independent Analysis of QCM Data on Colloidal Particle Adsorption. *Langmuir* **2009**, *25* (9), 5177–5184. https://doi.org/10.1021/la803912p.

(243) Eisele, N. B.; Frey, S.; Piehler, J.; Görlich, D.; Richter, R. P. Ultrathin Nucleoporin Phenylalanine–Glycine Repeat Films and Their Interaction with Nuclear Transport Receptors. *EMBO Rep.* **2010**, *11* (5), 366–372. https://doi.org/10.1038/embor.2010.34.

(244) Reviakine, I.; Johannsmann, D.; Richter, R. P. Hearing What You Cannot See and Visualizing What You Hear: Interpreting Quartz Crystal Microbalance Data from Solvated Interfaces. *Anal. Chem.* **2011**, *83* (23), 8838–8848. https://doi.org/10.1021/ac201778h.

(245) Jaiswal, A.; Smoukov, S.; Poggi, M.; Grzybowski, B. Quartz Crystal Microbalance with Dissipation Monitoring (QCM-D): Real-Time Characterization of Nano-Scale Interactions at Surfaces. In *Technical Proceedings of the 2008 NSTI Nanotechnology Conference and Trade Show, NSTI-Nanotech, Nanotechnology 2008*; 2008.

(246) Su, X.; Wu, Y.-J.; Knoll, W. Comparison of Surface Plasmon Resonance Spectroscopy and Quartz Crystal Microbalance Techniques for Studying DNA Assembly and Hybridization. *Biosens. Bioelectron.* **2005**, *21* (5), 719–726. https://doi.org/10.1016/j.bios.2005.01.006.

(247) Ozeki, T.; Morita, M.; Yoshimine, H.; Furusawa, H.; Okahata, Y. Hydration and Energy Dissipation Measurements of Biomolecules on a Piezoelectric Quartz Oscillator by Admittance Analyses. *Anal. Chem.*

2007, *79* (1), 79–88. https://doi.org/10.1021/ac060873x.

(248) Macakova, L.; Blomberg, E.; Claesson, P. M. Effect of Adsorbed Layer Surface Roughness on the QCM-D Response: Focus on Trapped Water. *Langmuir* **2007**, *23* (24), 12436–12444. https://doi.org/10.1021/la7014308.

(249) Carton, I.; Brisson, A. R.; Richter, R. P. Label-Free Detection of Clustering of Membrane-Bound Proteins. *Anal. Chem.* **2010**, *82* (22), 9275–9281. https://doi.org/10.1021/ac102495q.

(250) Bingen, P.; Wang, G.; Steinmetz, N. F.; Rodahl, M.; Richter, R. P. Solvation Effects in the Quartz Crystal Microbalance with Dissipation Monitoring Response to Biomolecular Adsorption. A Phenomenological Approach. *Anal. Chem.* **2008**, *80* (23), 8880–8890. https://doi.org/10.1021/ac8011686.

(251) Rojas, E.; Gallego, M.; Reviakine, I. Effect of Sample Heterogeneity on the Interpretation of Quartz Crystal Microbalance Data: Impurity Effects. *Anal. Chem.* **2008**, *80* (23), 8982–8990. https://doi.org/10.1021/ac8012829.

(252) Ward, M. D.; Buttry, D. A. In Situ Interfacial Mass Detection with Piezoelectric Transducers. *Science (80-.).* **1990**, *249* (4972), 1000–1007. https://doi.org/10.1126/science.249.4972.1000.

(253) Mason, W. P.; Baerwald, H. Piezoelectric Crystals and Their Applications to Ultrasonics. *Phys. Today* **1951**, *4* (5), 23–24. https://doi.org/10.1063/1.3067231.

(254) Rodahl, M.; Höök, F.; Krozer, A.; Brzezinski, P.; Kasemo, B. Quartz Crystal Microbalance Setup for Frequency and Q -factor Measurements in Gaseous and Liquid Environments. *Rev. Sci. Instrum.* **1995**, *66* (7), 3924–3930. https://doi.org/10.1063/1.1145396.

(255) Tsortos, A.; Papadakis, G.; Mitsakakis, K.; Melzak, K. A.; Gizeli, E. Quantitative Determination of Size and Shape of Surface-Bound DNA Using an Acoustic Wave Sensor. *Biophys. J.* **2008**, *94* (7), 2706–2715. https://doi.org/10.1529/biophysj.107.119271.

(256) Sauerbrey, G. Verwendung von Schwingquarzen Zur Wägung Dünner Schichten Und Zur Mikrowägung. *Zeitschrift für Phys.* **1959**, *155* (2), 206–222. https://doi.org/10.1007/BF01337937.

(257) Kanazawa, K. K.; Gordon, J. G. Frequency of a Quartz Microbalance in Contact with Liquid. *Anal. Chem.* **1985**, *57* (8), 1770–1771. https://doi.org/10.1021/ac00285a062.

(258) Johannsmann, D. Viscoelastic, Mechanical, and Dielectric Measurements on Complex Samples with the Quartz Crystal Microbalance. *Phys. Chem. Chem. Phys.* **2008**, *10* (31), 4516. https://doi.org/10.1039/b803960g.

(259) Voinova, M. V.; Jonson, M.; Kasemo, B. 'Missing Mass' Effect in Biosensor's QCM Applications. *Biosens. Bioelectron.* **2002**, *17* (10), 835–841. https://doi.org/10.1016/S0956-5663(02)00050-7.

(260) Alexander, S.; Chaikin, P. M.; Grant, P.; Morales, G. J.; Pincus, P.; Hone, D. Charge Renormalization, Osmotic Pressure, and Bulk Modulus of Colloidal Crystals: Theory. *J. Chem. Phys.* **1984**, *80* (11), 5776–5781. https://doi.org/10.1063/1.446600.

(261) Belloni, L. Ionic Condensation and Charge Renormalization in Colloidal Suspensions. In *Colloids and Surfaces A: Physicochemical and Engineering Aspects*; 1998. https://doi.org/10.1016/S0927-7757(97)00281-1.

(262) van de Steeg, H. G. M.; Stuart, M. A. C.; de keizer, A.; Bijsterbosch, B. H. Polyelectrolyte Adsorption: A Subtle Balance of Forces. *Langmuir* **1992**. https://doi.org/10.1021/la00046a030.

(263) Dahlgren, M. A. G.; Waltermo, Å.; Blomberg, E.; Claesson, P. M.; Sjöström, L.; Åkesson, T.; Jönsson, B. Salt Effects on the Interaction between Adsorbed Cationic Polyelectrolyte Layers - Theory and Experiment. *J. Phys. Chem.* **1993**. https://doi.org/10.1021/j100147a033.

(264) Netz, R. R.; Joanny, J. F. Complexation Behavior of Polyampholytes and Charged Objects. *Macromolecules* **1998**. https://doi.org/10.1021/ma980115b.

(265) Hariharan, R.; Biver, C.; Mays, J.; Russel, W. B. Ionic Strength and Curvature Effects in Flat and Highly Curved Polyelectrolyte Brushes. *Macromolecules* **1998**. https://doi.org/10.1021/ma971818g.

(266) Gittins, D. I.; Caruso, F. Tailoring the Polyelectrolyte Coating of Metal Nanoparticles. *J. Phys. Chem. B* **2001**. https://doi.org/10.1021/jp0111665.

(267) Caruso, F. Hollow Capsule Processing through Colloidal Templating and Self-Assembly. *Chem. - A Eur. J.* **2000**. https://doi.org/10.1002/(SICI)1521-3765(20000204)6:3<413::AID-CHEM413>3.0.CO;2-9.

(268) Decher, G.; Hong, J. D.; Schmitt, J. Buildup of Ultrathin Multilayer Films by a Self-Assembly Process: III. Consecutively Alternating Adsorption of Anionic and Cationic Polyelectrolytes on Charged Surfaces. *Thin Solid Films* **1992**. https://doi.org/10.1016/0040-6090(92)90417-A.

(269) Dubas, S. T.; Schlenoff, J. B. Swelling and Smoothing of Polyelectrolyte Multilayers by Salt. *Langmuir* **2001**. https://doi.org/10.1021/la0112099.

(270) Hugerth, A.; Caram-Lelham, N.; Sundelöf, L.-O. The Effect of Charge Density and Conformation on the Polyelectrolyte Complex Formation between Carrageenan and Chitosan. *Carbohydr. Polym.* **1997**, *34* (3), 149–156. https://doi.org/10.1016/S0144-8617(97)00088-X.

(271) Rusu-Balaita, L.; Desbrières, J.; Rinaudo, M. Formation of a Biocompatible Polyelectrolyte Complex: Chitosan-Hyaluronan Complex Stability. *Polym. Bull.* **2003**. https://doi.org/10.1007/s00289-003-0144-1.

(272) Winkler, R. G.; Steinhauser, M. O.; Reineker, P. Complex Formation in Systems of Oppositely Charged Polyelectrolytes: A Molecular Dynamics Simulation Study. *Phys. Rev. E - Stat. Physics, Plasmas, Fluids, Relat. Interdiscip. Top.* **2002**. https://doi.org/10.1103/PhysRevE.66.021802.

(273) Kudlay, A.; Olvera de la Cruz, M. Precipitation of Oppositely Charged Polyelectrolytes in Salt Solutions. *J. Chem. Phys.* **2004**, *120* (1), 404–412. https://doi.org/10.1063/1.1629271.

(274) Mende, M.; Petzold, G.; Buchhammer, H. M. Polyelectrolyte Complex Formation between Poly(Diallyldimethyl-Ammonium Chloride) and Copolymers of Acrylamide and Sodium-Acrylate. *Colloid Polym. Sci.* **2002**. https://doi.org/10.1007/s00396-001-0614-7.

(275) de Kruif, C. G.; Weinbreck, F.; de Vries, R. Complex Coacervation of Proteins and Anionic Polysaccharides. *Curr. Opin. Colloid Interface Sci.* **2004**, *9* (5), 340–349. https://doi.org/10.1016/j.cocis.2004.09.006.

(276) Wittemann, A.; Ballauff, M. Interaction of Proteins with Linear Polyelectrolytes and Spherical Polyelectrolyte Brushes in Aqueous Solution. *Phys. Chem. Chem. Phys.* **2006**, *8* (45), 5269. https://doi.org/10.1039/b609879g.

(277) Xu, X.; Ran, Q.; Haag, R.; Ballauff, M.; Dzubiella, J. Charged Dendrimers Revisited: Effective Charge and Surface Potential of Dendritic Polyglycerol Sulfate. *Macromolecules* **2017**. https://doi.org/10.1021/acs.macromol.7b00742.

(278) Türk, H.; Haag, R.; Alban, S. Dendritic Polyglycerol Sulfates as New Heparin Analogues and Potent Inhibitors of the Complement System. *Bioconjug. Chem.* **2004**, *15* (1), 162–167. https://doi.org/10.1021/bc034044j.

(279) Licha, K.; Welker, P.; Weinhart, M.; Wegner, N.; Kern, S.; Reichert, S.; Gemeinhardt, I.; Weissbach, C.; Ebert, B.; Haag, R.; et al. Fluorescence Imaging with Multifunctional Polyglycerol Sulfates: Novel Polymeric near-IR Probes Targeting Inflammation. *Bioconjug. Chem.* **2011**, *22* (12), 2453–2460. https://doi.org/10.1021/bc2002727.

(280) Rubinstein, M.; Papoian, G. A. Polyelectrolytes in Biology and Soft Matter. *Soft Matter* **2012**, *8* (36), 9265. https://doi.org/10.1039/c2sm90104h.

(281) Israelachvili, J. *Intermolecular and Surface Forces*; Elsevier, 2011. https://doi.org/10.1016/C2009-0-21560-1.

(282) Adamson, a W. Physical Chemistry of Surfaces. *J. Electrochem. Soc.* **1977**, *124* (5), 192C. https://doi.org/10.1149/1.2133374.

(283) Verwey, E. J. W. Theory of the Stability of Lyophobic Colloids. *J. Phys. Colloid Chem.* **1947**. https://doi.org/10.1021/j150453a001.

(284) Borukhov, I.; Andelman, D.; Orland, H. Adsorption of Large Ions from an Electrolyte Solution: A

Modified Poisson-Boltzmann Equation. *Electrochim. Acta* **2000**. https://doi.org/10.1016/S0013-4686(00)00576-4.

(285) Nikam, R.; Xu, X.; Ballauff, M.; Kanduč, M.; Dzubiella, J. Charge and Hydration Structure of Dendritic Polyelectrolytes: Molecular Simulations of Polyglycerol Sulphate. *Soft Matter* **2018**, *14* (21), 4300–4310. https://doi.org/10.1039/C8SM00714D.

(286) Wall, F. T.; Berkowitz, J. Numerical Solution to the Poisson-Boltzmann Equation for Spherical Polyelectrolyte Molecules. *J. Chem. Phys.* **1957**. https://doi.org/10.1063/1.1743234.

(287) Ohshima, H. Donnan Potential and Surface Potential of a Spherical Soft Particle in an Electrolyte Solution. *J. Colloid Interface Sci.* **2008**. https://doi.org/10.1016/j.jcis.2008.03.021.

(288) Ohshima, H.; Healy, T. W.; White, L. R. Accurate Analytic Expressions for the Surface Charge Density/Surface Potential Relationship and Double-Layer Potential Distribution for a Spherical Colloidal Particle. *J. Colloid Interface Sci.* **1982**, *90* (1), 17–26. https://doi.org/10.1016/0021-9797(82)90393-9.

(289) Kalcher, I.; Schulz, J. C. F.; Dzubiella, J. Ion-Specific Excluded-Volume Correlations and Solvation Forces. *Phys. Rev. Lett.* **2010**, *104* (9), 097802. https://doi.org/10.1103/PhysRevLett.104.097802.

(290) Kalcher, I.; Schulz, J. C. F.; Dzubiella, J. Electrolytes in a Nanometer Slab-Confinement: Ion-Specific Structure and Solvation Forces. *J. Chem. Phys.* **2010**. https://doi.org/10.1063/1.3490666.

(291) Chudoba, R.; Heyda, J.; Dzubiella, J. Tuning the Collapse Transition of Weakly Charged Polymers by Ion-Specific Screening and Adsorption. *Soft Matter* **2018**, *14* (47), 9631–9642. https://doi.org/10.1039/C8SM01646A.

(292) Moncho-Jordá, A.; Adroher-Benítez, I. Ion Permeation inside Microgel Particles Induced by Specific Interactions: From Charge Inversion to Overcharging. *Soft Matter* **2014**, *10* (31), 5810. https://doi.org/10.1039/C4SM00243A.

(293) Ahualli, S.; Martín-Molina, A.; Quesada-Pérez, M. Excluded Volume Effects on Ionic Partitioning in Gels and Microgels: A Simulation Study. *Phys. Chem. Chem. Phys.* **2014**. https://doi.org/10.1039/c4cp03314k.

(294) Hachim, D.; Whittaker, T. E.; Kim, H.; Stevens, M. M. Glycosaminoglycan-Based Biomaterials for Growth Factor and Cytokine Delivery: Making the Right Choices. *J. Control. Release* **2019**, *313*, 131–147. https://doi.org/10.1016/j.jconrel.2019.10.018.

(295) Kjellén, L.; Lindahl, U. Specificity of Glycosaminoglycan–Protein Interactions. *Current Opinion in Structural Biology*. Elsevier Ltd June 2018, pp 101–108. https://doi.org/10.1016/j.sbi.2017.12.011.

(296) Gao, Q.; Yang, J. Y.; Moremen, K. W.; Flanagan, J. G.; Prestegard, J. H. Structural Characterization of a Heparan Sulfate Pentamer Interacting with LAR-Ig1-2. *Biochemistry* **2018**, *57* (15), 2189–2199. https://doi.org/10.1021/acs.biochem.8b00241.

(297) Mulloy, B.; Hogwood, J.; Gray, E.; Lever, R.; Page, C. P. Pharmacology of Heparin and Related Drugs. *Pharmacol. Rev.* **2015**, *68* (1), 76–141. https://doi.org/10.1124/pr.115.011247.

(298) Lu, G.; Deguzman, F. R.; Hollenbach, S. J.; Karbarz, M. J.; Abe, K.; Lee, G.; Luan, P.; Hutchaleelaha, A.; Inagaki, M.; Conley, P. B.; et al. A Specific Antidote for Reversal of Anticoagulation by Direct and Indirect Inhibitors of Coagulation Factor Xa. *Nat. Med.* **2013**, *19* (4), 446–451. https://doi.org/10.1038/nm.3102.

(299) Kalathottukaren, M. T.; Creagh, A. L.; Abbina, S.; Lu, G.; Karbarz, M. J.; Pandey, A.; Conley, P. B.; Kizhakkedathu, J. N.; Haynes, C. Comparison of Reversal Activity and Mechanism of Action of UHRA, Andexanet, and PER977 on Heparin and Oral FXa Inhibitors. *Blood Adv.* **2018**, *2* (16), 2104–2114. https://doi.org/10.1182/bloodadvances.2016003616.

(300) Fischer, P. M. Design of Small-Molecule Active-Site Inhibitors of the S1A Family Proteases as Procoagulant and Anticoagulant Drugs. *J. Med. Chem.* **2018**, *61* (9), 3799–3822. https://doi.org/10.1021/acs.jmedchem.7b00772.

(301) Winzor, D. J.; Carrington, L. E.; Deszczynski, M.; Harding, S. E. Extent of Charge Screening in Aqueous Polysaccharide Solutions. *Biomacromolecules* **2004**, *5* (6), 2456–2460. https://doi.org/10.1021/bm040054r.

(302) Minsky, B. B.; Atmuri, A.; Kaltashov, I. A.; Dubin, P. L. Counterion Condensation on Heparin Oligomers. *Biomacromolecules* **2013**, *14* (4), 1113–1121. https://doi.org/10.1021/bm400006g.

(303) Xu, X.; Angioletti-Uberti, S.; Lu, Y.; Dzubiella, J.; Ballauff, M. Interaction of Proteins with Polyelectrolytes: Comparison of Theory to Experiment. *Langmuir* **2019**, *35* (16), 5373–5391. https://doi.org/10.1021/acs.langmuir.8b01802.

(304) Velázquez Campoy, A.; Freire, E. ITC in the Post-Genomic Era...? Priceless. *Biophys. Chem.* **2005**, *115* (2–3), 115–124. https://doi.org/10.1016/j.bpc.2004.12.015.

(305) Vega, S.; Abian, O.; Velazquez-Campoy, A. A Unified Framework Based on the Binding Polynomial for Characterizing Biological Systems by Isothermal Titration Calorimetry. *Methods* **2015**, *76*, 99–115. https://doi.org/10.1016/j.ymeth.2014.09.010.

(306) Mascotti, D. P.; Lohman, T. M. Thermodynamics of Charged Oligopeptide-Heparin Interactions. *Biochemistry* **1995**, *34* (9), 2908–2915. https://doi.org/10.1021/bi00009a022.

(307) Datta, K.; LiCata, V. J. Salt Dependence of DNA Binding by Thermus Aquaticus and Escherichia Coli DNA Polymerases. *J. Biol. Chem.* **2003**, *278* (8), 5694–5701. https://doi.org/10.1074/jbc.M208133200.

(308) Nadine, L.; Lucas, S.; Elke, W.; Passant, A.; Inka, F.; Uwe, F.; Carsten, W.; Jan, S.; Sandra, F. StarPEG-Heparin Hydrogels as Chemokine Scavenger to Improve Aberrant Wound Healing Processes. *Front. Bioeng. Biotechnol.* **2016**, *4*. https://doi.org/10.3389/conf.FBIOE.2016.01.00956.

(309) Atallah, P.; Schirmer, L.; Tsurkan, M.; Putra Limasale, Y. D.; Zimmermann, R.; Werner, C.; Freudenberg, U. In Situ-Forming, Cell-Instructive Hydrogels Based on Glycosaminoglycans with Varied Sulfation Patterns. *Biomaterials* **2018**, *181*, 227–239. https://doi.org/10.1016/j.biomaterials.2018.07.056.

(310) Freudenberg, U.; Atallah, P.; Limasale, Y. D. P.; Werner, C. Charge-Tuning of Glycosaminoglycan-Based Hydrogels to Program Cytokine Sequestration. *Faraday Discuss.* **2019**, *219*, 244–251. https://doi.org/10.1039/C9FD00016J.

(311) Olson, S. T.; Halvorson, H. R.; Bjork, I. Quantitative Characterization of the Thrombin-Heparin Interaction: Discrimination between Specific and Nonspecific Binding Models. *J. Biol. Chem.* **1991**, *266* (10), 6342–6352.

(312) Kayitmazer, a. B.; Quinn, B.; Kimura, K.; Ryan, G. L.; Tate, A. J.; Pink, D. a.; Dubin, P. L. Protein Specificity of Charged Sequences in Polyanions and Heparins. *Biomacromolecules* **2010**, *11*, 3325–3331. https://doi.org/10.1021/bm1008074.

(313) Xu, Y.; Seeman, D.; Yan, Y.; Sun, L.; Post, J.; Dubin, P. L. Effect of Heparin on Protein Aggregation: Inhibition versus Promotion. *Biomacromolecules* **2012**, *13* (5), 1642–1651. https://doi.org/10.1021/bm3003539.

(314) Pichert, A.; Samsonov, S. A.; Norsieck, K.; Beck-Sickinger, A. G.; Pisabarro, M. T.; Huster, D. Investigation of the Influence Glycosaminoglycan Sulfation on the Interaction with Interleukin-8 by Fluorescence and Solution NMR Spectroscopy. *Biophys. J.* **2012**, *102* (3), 464a. https://doi.org/10.1016/j.bpj.2011.11.2545.

(315) Scharnweber, D.; Hübner, L.; Rother, S.; Hempel, U.; Anderegg, U.; Samsonov, S. A.; Pisabarro, M. T.; Hofbauer, L.; Schnabelrauch, M.; Franz, S.; et al. Glycosaminoglycan Derivatives: Promising Candidates for the Design of Functional Biomaterials. *J. Mater. Sci. Mater. Med.* **2015**, *26* (9). https://doi.org/10.1007/s10856-015-5563-7.

(316) Nguyen, K.; Rabenstein, D. L. Interaction of the Heparin-Binding Consensus Sequence of β-Amyloid Peptides with Heparin and Heparin-Derived Oligosaccharides. *J. Phys. Chem. B* **2016**, *120* (9), 2187–2197. https://doi.org/10.1021/acs.jpcb.5b12235.

(317) Corredor, M.; Carbajo, D.; Domingo, C.; Pérez, Y.; Bujons, J.; Messeguer, A.; Alfonso, I. Dynamic Covalent Identification of an Efficient Heparin Ligand. *Angew. Chemie Int. Ed.* **2018**, *57* (37), 11973–11977. https://doi.org/10.1002/anie.201806770.

(318) Minsky, B. B.; Nguyen, T. V.; Peyton, S. R.; Kaltashov, I. A.; Dubin, P. L. Heparin Decamer Bridges a Growth Factor and an Oligolysine by Different Charge-Driven Interactions. *Biomacromolecules* **2013**, *14*

(11), 4091–4098. https://doi.org/10.1021/bm401227p.

(319) Courtenay, E. S.; Capp, M. W.; Anderson, C. F.; Record, M. T. Vapor Pressure Osmometry Studies of Osmolyte-Protein Interactions: Implications for the Action of Osmoprotectants in Vivo and for the Interpretation of "osmotic Stress" Experiments in Vitro. *Biochemistry* **2000**, *39* (15), 4455–4471. https://doi.org/10.1021/bi9928871.

(320) Vander Meulen, K. A.; Saecker, R. M.; Record, M. T. Formation of a Wrapped DNA-Protein Interface: Experimental Characterization and Analysis of the Large Contributions of Ions and Water to the Thermodynamics of Binding IHF to H′ DNA. *J. Mol. Biol.* **2008**, *377* (1), 9–27. https://doi.org/10.1016/j.jmb.2007.11.104.

(321) Kayitmazer, A. B. Thermodynamics of Complex Coacervation. *Adv. Colloid Interface Sci.* **2017**, *239*, 169–177. https://doi.org/10.1016/j.cis.2016.07.006.

(322) Pavlov, G.; Finet, S.; Tatarenko, K.; Korneeva, E.; Ebel, C. Conformation of Heparin Studied with Macromolecular Hydrodynamic Methods and X-Ray Scattering. In *European Biophysics Journal*; 2003; Vol. 32, pp 437–449. https://doi.org/10.1007/s00249-003-0316-9.

(323) Delben, F.; Paoletti, S.; Porasso, R. D.; Benegas, J. C. Potentiometric Titrations of Maleic Acid Copolymers in Dilute Aqueous Solution: Experimental Results and Theoretical Interpretation. *Macromol. Chem. Phys.* **2006**, *207* (24), 2299–2310. https://doi.org/10.1002/macp.200600479.

(324) Manning, G. S. Approximate Solutions to Some Problems in Polyelectrolyte Theory Involving Nonuniform Charge Distributions. *Macromolecules* **2008**, *41* (16), 6217–6227. https://doi.org/10.1021/ma800628v.

(325) Thompson, L. D.; Pantoliano, M. W.; Springer, B. A. Energetic Characterization of the Basic Fibroblast Growth Factor-Heparin Interaction: Identification of the Heparin Binding Domain. *Biochemistry* **1994**, *33* (13), 3831–3840. https://doi.org/10.1021/bi00179a006.

(326) Winzor, D. J.; Jackson, C. M. Interpretation of the Temperature Dependence of Equilibrium and Rate Constants. *J. Mol. Recognit. 19* (5), 389–407. https://doi.org/10.1002/jmr.799.

(327) Liu, Y.; Sturtevant, J. M. Significant Discrepancies between van't Hoff and Calorimetric Enthalpies. III. *Biophys. Chem.* **1997**, *64* (1–3), 121–126. https://doi.org/10.1016/S0301-4622(96)02229-6.

(328) Ricard-Blum, S.; Lisacek, F. Glycosaminoglycanomics: Where We Are. *Glycoconj. J.* **2017**, *34* (3), 339–349. https://doi.org/10.1007/s10719-016-9747-2.

(329) Cagno, V.; Tseligka, E. D.; Jones, S. T.; Tapparel, C. Heparan Sulfate Proteoglycans and Viral Attachment: True Receptors or Adaptation Bias? *Viruses*. MDPI AG July 2019. https://doi.org/10.3390/v11070596.

(330) Loftsson, T. Cyclodextrins and the Biopharmaceutics Classification System of Drugs. In *Journal of Inclusion Phenomena*; 2002. https://doi.org/10.1023/A:1023088423667.

(331) Challa, R.; Ahuja, A.; Ali, J.; Khar, R. K. Cyclodextrins in Drug Delivery: An Updated Review. *AAPS PharmSciTech* **2005**, *6* (2), E329–E357. https://doi.org/10.1208/pt060243.

(332) Miyajima, K.; Sawada, M.; Nakagaki, M. Viscosity B -Coefficients, Apparent Molar Volumes, and Activity Coefficients for α- and γ-Cyclodextrins in Aqueous Solutions. *Bull. Chem. Soc. Jpn.* **1983**, *56* (12), 3556–3560. https://doi.org/10.1246/bcsj.56.3556.

(333) Coleman, A. W.; Nicolis, I.; Keller, N.; Dalbiez, J. P. Aggregation of Cyclodextrins: An Explanation of the Abnormal Solubility of?-Cyclodextrin. *J. Incl. Phenom. Mol. Recognit. Chem.* **1992**, *13* (2), 139–143. https://doi.org/10.1007/BF01053637.

(334) Szejtli, J. *CYCLODEXTRIN TECHNOLOGY*; 2013. https://doi.org/10.1017/CBO9781107415324.004.

(335) Connors, K. A. The Stability of Cyclodextrin Complexes in Solution. *Chem. Rev.* **1997**. https://doi.org/10.1021/cr960371r.

(336) Sun, D. Z.; Li, L.; Qiu, X. M.; Liu, F.; Yin, B. L. Isothermal Titration Calorimetry and 1H NMR Studies on Host-Guest Interaction of Paeonol and Two of Its Isomers with β-Cyclodextrin. *Int. J. Pharm.* **2006**.

https://doi.org/10.1016/j.ijpharm.2006.02.020.

(337) Rodriguez-Perez, A. I.; Rodriguez-Tenreiro, C.; Alvarez-Lorenzo, C.; Taboada, P.; Concheiro, A.; Torres-Labandeira, J. J. Sertaconazole/Hydroxypropyl-β-Cyclodextrin Complexation: Isothermal Titration Calorimetry and Solubility Approaches. *Journal of Pharmaceutical Sciences*. 2006. https://doi.org/10.1002/jps.20661.

(338) Perry, C. S.; Charman, S. A.; Prankerd, R. J.; Chiu, F. C. K.; Scanlon, M. J.; Chalmers, D.; Charman, W. N. The Binding Interaction of Synthetic Ozonide Antimalarials with Natural and Modified β-Cyclodextrins. *J. Pharm. Sci.* **2006**. https://doi.org/10.1002/jps.20525.

(339) Merkus, F. W. H. M.; Verhoef, J. C.; Marttin, E.; Romeijn, S. G.; Van Der Kuy, P. H. M.; Hermens, W. A. J. J.; Schipper, N. G. M. Cyclodextrins in Nasal Drug Delivery. *Advanced Drug Delivery Reviews*. 1999. https://doi.org/10.1016/S0169-409X(98)00054-4.

(340) Ballauff, M. *Spherical Polyelectrolyte Brushes*; 2007; Vol. 32, pp 1135–1151. https://doi.org/10.1016/j.progpolymsci.2007.05.002.

(341) Lu, Y.; Ballauff, M.; Wittemann, A. Spherical Polymer Brushes. In *Polymer Science: A Comprehensive Reference, 10 Volume Set*; 2012; Vol. 6, pp 265–292. https://doi.org/10.1016/B978-0-444-53349-4.00165-5.

(342) Wittemann, A.; Ballauff, M. Temperature-Induced Unfolding of Ribonuclease A Embedded in Spherical Polyelectrolyte Brushes. *Macromol. Biosci.* **2005**, *5* (1), 13–20. https://doi.org/10.1002/mabi.200400133.

(343) Wittemann, A.; Haupt, B.; Ballauff, M. Adsorption of Proteins on Spherical Polyelectrolyte Brushes in Aqueous Solution. *Phys. Chem. Chem. Phys.* **2003**, *5* (8), 1671–1677. https://doi.org/10.1039/b300607g.

(344) Matyjaszewski, K.; Xia, J. Atom Transfer Radical Polymerization. *Chem. Rev.* **2001**, *101* (9), 2921–2990.

(345) Baek, K.-Y.; Kamigaito, M.; Sawamoto, M. Core-Functionalized Star Polymers by Transition Metal-Catalyzed Living Radical Polymerization. 1. Synthesis and Characterization of Star Polymers with PMMA Arms and Amide Cores 1. *Macromolecules* **2001**, *34* (22), 7629–7635. https://doi.org/10.1021/ma010973z.

(346) Coessens, V.; Pintauer, T.; Matyjaszewski, K. Functional Polymers by Atom Transfer Radical Polymerization. *Prog. Polym. Sci.* **2001**, *26* (3), 337–377. https://doi.org/10.1016/S0079-6700(01)00003-X.

(347) Bittrich, E.; Rodenhausen, K. B.; Eichhorn, K.-J.; Hofmann, T.; Schubert, M.; Stamm, M.; Uhlmann, P. Protein Adsorption on and Swelling of Polyelectrolyte Brushes: A Simultaneous Ellipsometry-Quartz Crystal Microbalance Study. *Biointerphases* **2010**, *5* (4), 159–167. https://doi.org/10.1116/1.3530841.

(348) Wong, V. N.; Fernando, G.; Wagner, A. R.; Zhang, J.; Kinsel, G. R.; Zauscher, S.; Dyer, D. J. Separation of Peptides with Polyionic Nanosponges for MALDI-MS Analysis. *Langmuir* **2009**, *25* (3), 1459–1465. https://doi.org/10.1021/la802723r.

(349) Liu, G.; Zhang, G. Periodic Swelling and Collapse of Polyelectrolyte Brushes Driven by Chemical Oscillation. *J. Phys. Chem. B* **2008**, *112* (33), 10137–10141. https://doi.org/10.1021/jp801533r.

(350) Aulich, D.; Hoy, O.; Luzinov, I.; Brücher, M.; Hergenröder, R.; Bittrich, E.; Eichhorn, K.-J.; Uhlmann, P.; Stamm, M.; Esser, N.; et al. In Situ Studies on the Switching Behavior of Ultrathin Poly(Acrylic Acid) Polyelectrolyte Brushes in Different Aqueous Environments. *Langmuir* **2010**, *26* (15), 12926–12932. https://doi.org/10.1021/la101762f.

(351) Welsch, N. Interactions of Proteins with Soft Polymeric Surfaces, Humboldt-Universität zu Berlin, Mathematisch-Naturwissenschaftliche Fakultät I, 2012. https://doi.org/http://dx.doi.org/10.18452/16633.

(352) Lide, D. R. *CRC Handbook of Chemistry and Physics 86TH Edition 2005-2006*; 2005.

(353) Stockmayer, W. H. Macromolecules in Solution (High Polymers, Volume XXI). HERBERT MORAWETZ. Interscience, New York, 1965. Xvi + 495. $16.50. *J. Polym. Sci. Part A-2 Polym. Phys.* **1967**, *5* (1), 235–236. https://doi.org/10.1002/pol.1967.160050120.

(354) Ballauff, M.; Borisov, O. Polyelectrolyte Brushes. *Curr. Opin. Colloid Interface Sci.* **2006**, *11* (6), 316–

323. https://doi.org/10.1016/j.cocis.2006.12.002.

(355) Lu, Y.; Wittemann, A.; Ballauff, M. Supramolecular Structures Generated by Spherical Polyelectrolyte Brushes and Their Application in Catalysis. *Macromol. Rapid Commun.* **2009**, *30* (9–10), 806–815. https://doi.org/10.1002/marc.200800789.

(356) Jusufi, A.; Likos, C. N.; Löwen, H. Counterion-Induced Entropic Interactions in Solutions of Strongly Stretched, Osmotic Polyelectrolyte Stars. *J. Chem. Phys.* **2002**, *116* (24), 11011–11027. https://doi.org/10.1063/1.1480007.

(357) Brandrup, J.; Immergut, E. H. *Polymer Handbook, 3rd*; 1989. https://doi.org/10.1002/actp.1990.010410614.

(358) Pan, F.; Wang, P.; Lee, K.; Wu, A.; Turro, N. J.; Koberstein, J. T. Photochemical Modification and Patterning of Polymer Surfaces by Surface Adsorption of Photoactive Block Copolymers. *Langmuir* **2005**, *21* (8), 3605–3612. https://doi.org/10.1021/la0477439.

(359) Matyjaszewski, K.; Miller, P. J.; Shukla, N.; Immaraporn, B.; Gelman, A.; Luokala, B. B.; Siclovan, T. M.; Kickelbick, G.; Vallant, T.; Hoffmann, H.; et al. Polymers at Interfaces: Using Atom Transfer Radical Polymerization in the Controlled Growth of Homopolymers and Block Copolymers from Silicon Surfaces in the Absence of Untethered Sacrificial Initiator. *Macromolecules* **1999**, *32* (26), 8716–8724. https://doi.org/10.1021/ma991146p.

(360) ONYON, P. F. Polymer Handbook. *Nature* **1972**, *238* (5358), 56–56. https://doi.org/10.1038/238056a0.

(361) Sokolowski, M.; Bartsch, C.; Spiering, V. J.; Prévost, S.; Appavou, M.-S.; Schweins, R.; Gradzielski, M. Preparation of Polymer Brush Grafted Anionic or Cationic Silica Nanoparticles: Systematic Variation of the Polymer Shell. *Macromolecules* **2018**, *51* (17), 6936–6948. https://doi.org/10.1021/acs.macromol.8b01019.

(362) Haag, R.; Sunder, A.; Stumbé, J.-F. An Approach to Glycerol Dendrimers and Pseudo-Dendritic Polyglycerols. *J. Am. Chem. Soc.* **2000**, *122* (12), 2954–2955. https://doi.org/10.1021/ja994363e.

(363) Cesàro, A.; Delben, F.; Flaibani, A.; Paoletti, S. Polyelectrolytic Effects in Carboxylic Derivatives of Natural Polysaccharides. *Carbohydr. Res.* **1987**. https://doi.org/10.1016/0008-6215(87)80323-3.

(364) Paoletti, S.; Gilli, R.; Navarini, L.; Crescenzi, V. Effect of Monomer Composition on Proton Dissociation of Weak Polyacids. *Glycoconjugate Journal*. 1997. https://doi.org/10.1023/A:1018515905407.

(365) Porasso, R. D.; Benegas, J. C.; Van Den Hoop, M. A. G. T.; Paoletti, S. Analysis of Potentiometric Titrations of Heterogeneous Natural Polyelectrolytes in Terms of Counterion Condensation Theory: Application to Humic Acid. *Biophys. Chem.* **2000**. https://doi.org/10.1016/S0301-4622(00)00159-9.

List of Abbreviations

AAc	acrylic acid
AFM	atomic force microscopy
ARGET	activator regenerated by electron transfer
ATR	attenuated total reflection
ATRP	atom transfer radical polymerization
BamHI	Bacillus amyliquetaciens
β-CD	beta-cyclodextrine
β-CD-S	beta-cyclodextrine-sulfated
BLG	beta-Lactoglobulin
BSA	bovine serum albumin
CD	circular dichroism
CDs	cyclodextrins
Cryo-TEM	cryogenic transmission electron miscroscopy
dPGS	dendritic polyglycerol sulfate
DLS	dynamic light scattering
DNA	deoxyribonucleic acid
DTBU	Bis[2-(2-bromoisobutyryloxy)undecyl]disulfide
EEC	enthalpy-entropy cancellation
FT-IR	Fourier transform infrared spectroscopy
GAG	glycoaminoglycan
Hep	heparin
HMEM	2-[p-(2-hydroxy-2-methylpropiophenone)]-ethylene glycol-methacrylate
HSA	human serum albumin
ITC	isothermal titration calorimetry
KPS	potassium peroxodisulfate
Lys	lysozyme
MD	molecular dynamics
MOPS	3-(N-morpholino)propane sulfonic acid

MSE	mean square error
NEXAFS	near-edge X-ray absorption fine spectrum
PAA	poly(acrylic acid)
PAEMH	poly-(2-aminoethylmetacrylate)
PDB	protein data bank
PE	polyelectrolyte
PE-P	polyelectrolyte-protein
pI	isoelectric point
PMDETA	N,N,N',N",N"-Pentamethyldiethylenetriamine
PPB	penetrable Poisson-Boltzmann model
PPBs	planar polyelectrolyte brushes
PS	polystyrene
P*t*BA	poly(tert-butyl acrylate)
QCM	quartz crystal microbalance
QCM-D	quartz crystal microbalance with dissipation monitoring
RNA	ribonucleic acid
RNase	ribonuclease
SANS	small angle neutron scattering
SAXS	small angle X-ray scattering
SDS	sodium dodecyl sulfate
SPBs	spherical polyelectrolyte brushes
SSIS	single set of identical binding sites
SWCA	static water contact angle
*t*BA	tart-butyl acrylate
TCLB	two component ligand binding model
TSIS	two sets of independent binding sites
UV-vis	ultraviolet-visible light

List of Figures

List of Tables

List of Publications

- Walkowiak, J.; Lu, Y.; Gradzielski, M.; Zauscher, S.; Ballauff, M. Thermodynamic Analysis of the Uptake of a Protein in a Spherical Polyelectrolyte Brush. *Macromol. Rapid Commun.* **2020,** *41* (1), 1900421.
- Walkowiak, J.; Zimmermann, R.; Freudenberg, U.; Werner, C.; Ballauff, M. Thermodynamic Analysis of the Interaction of Heparin with Lysozyme. Under revision by *Biomacromolecules.* **2020**.
- Walkowiak, J.; Gradzielski, M.; Zauscher, S.; Ballauff, M. Interaction of Proteins with a planar Poly(acrylic acid) Brush: Analysis by Quartz Crystal Microbalance with Dissipation Monitoring (QCM-D). To be submitted.

Presentations at Conferences and Meetings

- IRTG 1524 „Self-Assembled Soft-Matter Nanostructures at Interfaces", Annual Meeting 2016. Oral presentation: „*Interaction of spherical polyelectrolyte brushes with proteins*". Neuruppin, Germany, 07-10.10.2016

- Helmholtz Virtual Institute Symposium (HVI 2016). Poster presentation: „*Interaction of spherical polyelectrolyte brushes with proteins*". Berlin, Germany, 27-29.11.2016

- IRTG 1524 „Self-Assembled Soft-Matter Nanostructures at Interfaces", Spring School 2017 „Self Assembly in Soft Matter Systems". Poster presentation: „*Interaction of spherical polyelectrolyte brushes with proteins*". Boston, MA, USA, 5-11.03.2017

- IRTG 1524 „Self-Assembled Soft-Matter Nanostructures at Interfaces", Annual Meeting 2017. Oral presentation: „*Interaction of spherical polyelectrolyte brushes with proteins*". Raleigh, NC, USA, 07-10.10.2017

- Nano S&T-2018 Conference. Oral presentation: „*Interaction of polyelectrolytes with proteins*". Potsdam, Germany, 24-26.10.2018

- 5. International Symposium of the SFB 765 „Multivalency in Chemistry and Biology". Poster presentation: „*Proteins interacting with polyelectrolytes*". Berlin, Germany, 30.09-02.10.2019.

Acknowledgments

I would like to thank my supervisor Prof. Dr. Matthias Ballauff for the opportunity to work on an interesting and challenging topic, for his guidance, support and professionalism. I owe special thanks to Prof. Michael Gradzielski, Prof. Yan Lu, Prof. Rainer Haag, Prof. Joachim Dzubiella and Rohit Nikam for the great collaboration and for the time they spend on fruitful discussions which led to the successful publication of our study. I would like to thank Prof. Stefan Zauscher for our collaboration, for hosting my at his research group and for an opportunity to pursue my research ideas.

I am truly grateful to my friends at Technische Universität Berlin, Helmholtz Zentrum Berlin and Duke University: Miriam Simon for sharing her expertise on dynamic light scattering with me. Dr. Sasa Gu, Dr. Shilin Mei, Dr. Shun Yu, Dr. Qidi Ran, Dr. Zehra Parlak, Luis Navarro and Daniel French for their help and great discussions regarding polymer synthesis, isothermal titration calorimetry and quartz crystal microbalance.

I am indebted to the financial support from the: Internationale Graduiertenkolleg (IRTG) 1524 “Self-Assembled Soft Matter Nano-Structures at Interfaces, Sonderforschungsbereich (SFB) 765 “ Multivalency in Chemistry and Biology” and Sonderforschungsbereich (SFB) 1349 “Fluor-Specific Interactions: Fundamentals and Functions”. I would like to thank my colleagues from AG Risse at Freie Universität Berlin for the joyful time we spend during these past two years.

I sincerely thank my family.